

## 5 RESEARCH ACTIVITIES

### 5.1 NUCLEAR PHYSICS

N. Madhavan

The National array of Neutron detectors (NAND) facility has been commissioned, cross-talk and response of array to mono-energetic gamma rays have been simulated and first set of experiments have been successfully carried out. The HYbrid Telescope ARray for reaction dynamics (HYTAR) was used for quasi elastic back-scattering experiments to extract fusion barrier distribution in  $^{48}\text{Ti} + ^{232}\text{Th}$  system for a possible formation of heavy, Copernicium ( $^{280}\text{Cn}^*$ ) compound nucleus.

HYbrid Recoil mass Analyzer (HYRA) was used in gas-filled mode, in conjunction with TIFR  $4\pi$  Spin Spectrometer, to carry out evaporation residue (ER) fusion excitation function and ER-gated spin (l) distributions in several heavy systems ( $A_{\text{CN}} > 190$  amu) in order to study shell closure, target deformation and entrance channel effects on the survival of heavy residues and on the limits of l-distributions. HYRA transmission efficiency has been experimentally extracted for two systems. The identification of a new isomer in  $^{195}\text{Bi}$ , above an existing known isomer, in the very first experiment on search for microsecond isomers using HYRA, has resulted in a plan for a longer campaign. A new setup has been designed, for the focal plane of first stage of HYRA, to accommodate up to seven HPGe Clover detectors.

The Indian National Gamma Array (INGA) detectors from various Indian institutes arrived at IUAC following a long campaign at TIFR, Mumbai. The detectors have been put in operation in the existing INGA structure and initial experiments have started. INGA will be coupled to HYRA, during the present campaign, for ER-tagged gamma spectroscopy of heavy residues surviving fission.

Several experiments, a large part of them being students' theses related ones, have been performed using all the nuclear physics facilities last year. Some of the interesting results include observation of co-existing asymmetric and symmetric fission at lower excitation energies, shell closure and target deformation effects in the survival and l-distribution of heavy ERs, detailed information on the  $2^+$  and  $4^+$  states in several nuclei in collaboration with Warsaw, GSI and RIKEN groups, higher order coupling effects in sub-barrier fusion, dependence of incomplete fusion, etc.

Ms. Ruchi Mahajan (research scholar from Panjab University) won an award for one of ten best posters in DAE symposium on Nuclear Physics 2015 for her research work using NAND facility. We congratulate her and wish her many more laurels.

#### 5.1.1 Transfer and fusion measurements for $^{28}\text{Si}+^{92,96}\text{Zr}$ systems

Khushboo<sup>1</sup>, S. Mandal<sup>1</sup>, S. Nath<sup>2</sup>, N. Madhavan<sup>2</sup>, J. Gehlot<sup>2</sup>, A. Banerjee<sup>1</sup>, N. Kumar<sup>1</sup>, Tathagata Banerjee<sup>2</sup>, G. Kaur<sup>3</sup>, K. Rojeeta<sup>1</sup>, Unnati<sup>1</sup>, A. Jhingan<sup>2</sup>, T. Varughese<sup>2</sup>, Indu Bala<sup>2</sup>, S. Muralithar<sup>2</sup>, R. P. Singh<sup>2</sup>, Visakh A. C.<sup>4</sup>, Ch. Vikar<sup>1</sup>, A. Chaudhury<sup>1</sup>, H. Arora<sup>3</sup>, Sandeep Singh<sup>1</sup>, Sarvesh<sup>5</sup>, S. Kumar<sup>1</sup> and S. Verma<sup>1</sup>

<sup>1</sup>Department of Physics and Astrophysics, University of Delhi, Delhi 110007, India

<sup>2</sup>Inter University Accelerator Centre, Aruna Asaf Ali Marg, New Delhi 110067, India

<sup>3</sup>Department of Physics, Panjab University, Chandigarh 160014, India

<sup>4</sup>Department of Physics, Central University of Kerala, Nilesishwar 671314, India

<sup>5</sup>Department of Physics, Kalindi College, University of Delhi, New Delhi 110008, India

Fusion dynamics in low energy region is governed by quantum tunneling through Coulomb barrier. In sub-barrier region, fusion cross-sections show large enhancement with respect to theoretical predictions based on one dimensional barrier penetration model. It is well known that the enhancement occurs due to nuclear vibration,

deformation and nucleon transfer. The influence of nuclear vibration and deformation is well described within the framework of coupled channels (CC) calculations [1, 2]. However, the role of neutron transfer is still not completely understood. Study of transfer reactions provides useful information on pairing correlation and its effect on fusion reaction mechanism [3]. Therefore, to investigate sub-barrier fusion and transfer reactions, experiments were performed with two systems  $^{28}\text{Si}+^{92,96}\text{Zr}$ . Both systems,  $^{28}\text{Si}+^{92}\text{Zr}$  and  $^{28}\text{Si}+^{96}\text{Zr}$ , favour neutron transfer due to positive Q-values up to two and six neutron pick up channels, respectively. Therefore, multi-neutron transfer and its effect on fusion cross-sections can be studied.

The experiment was performed in the Heavy Ion Reaction Analyzer (HIRA) facility at IUAC [4]. HIRA was kept at  $0^\circ$  with respect to the beam axis with 5 mSr entrance aperture for fusion and 1 mSr for transfer measurements. HIRA was rotated to  $6^\circ$  during transfer experiment to improve beam rejection.  $^{28}\text{Si}$  pulsed beam was used to bombard the enriched  $^{92,96}\text{Zr}$  targets (thickness  $\sim 230 \mu\text{g}/\text{cm}^2$ ) which were prepared by electron beam evaporation method at the target laboratory of IUAC. A multi-wire proportional counter (MWPC) with active area of  $152.4 \times 50.8 \text{ mm}^2$  was used at the focal plane of HIRA to detect the evaporation residues (ERs) or the transfer products. A position sensitive silicon detector with effective area of  $21 \times 21 \text{ mm}^2$  was mounted at the appropriate backward angle inside the target chamber to detect the back scattered particles during transfer measurements. In order to get the contribution of excited states of reaction products, a 13-element BGO (Bismuth Germanate) multiplicity filter was mounted at top and bottom of the target chamber. Kinematic coincidence was set up between focal plane MWPC, position sensitive silicon detector and/or BGO. Two silicon surface barrier detectors (SSBD) were placed inside the target chamber at angles of  $\pm 15^\circ$  with respect to beam direction for beam monitoring and for normalization of cross-sections. A time of flight (TOF) signal was set up between the anode of MWPC and the RF signal used for pulsed beam to separate beam-like particles from ERs. A raw spectrum between energy loss in MWPC and TOF is shown in Fig. 1. ER-gated gamma multiplicity spectrum with BGO is shown in Fig. 2. Fusion measurements were performed in the beam energy ( $E_{\text{lab}}$ ) range of 82 MeV to 111 MeV. Transfer measurements were carried out at  $E_{\text{lab}} = 88, 91$  and  $94$  MeV, for both systems. A two-dimensional spectrum between TOF and MWPC position of transfer recoil products for  $^{28}\text{Si}+^{96}\text{Zr}$  at  $E_{\text{lab}} = 88$  MeV is shown in Fig. 3.

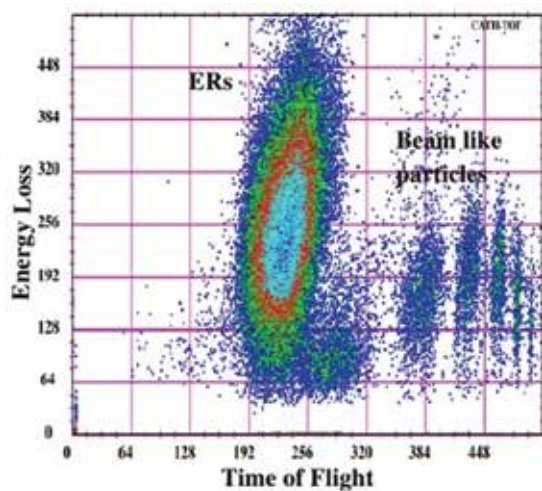


Fig. 1: Two-dimensional spectrum of TOF versus Energy loss for  $^{28}\text{Si}+^{92}\text{Zr}$  at  $E_{\text{lab}} = 96$  MeV.

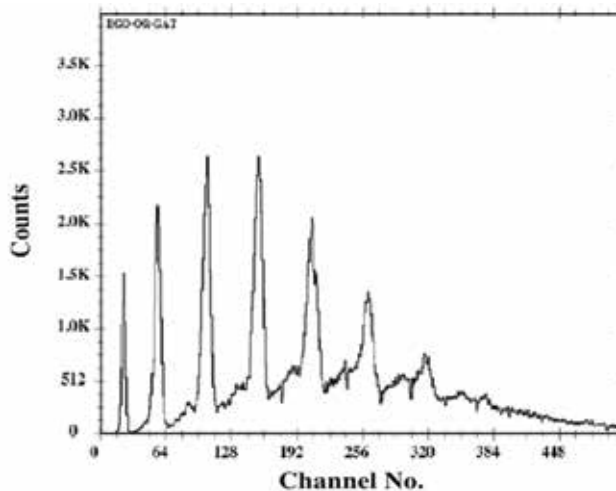


Fig. 2: ER-gated BGO multiplicity spectrum for  $^{28}\text{Si}+^{92}\text{Zr}$  at  $E_{\text{lab}} = 111$  MeV.

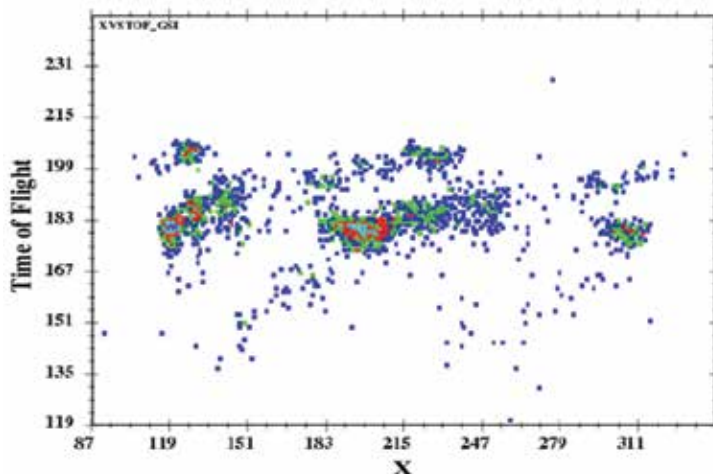


Fig. 3: Two-dimensional spectrum between TOF (y-axis) and MWPC position (x-axis) of transfer recoil products for  $^{28}\text{Si}+^{96}\text{Zr}$  at  $E_{\text{lab}} = 88$  MeV.

## References

- [1] S. Kalkalet *et al.*, Phys. Rev. C **81**, 044610 (2010).
- [2] H. Q. Zhang *et al.*, Phys. Rev. C **82**, 054609 (2010).
- [3] S. Kalkalet *et al.*, Phys. Rev. C **83**, 054607 (2011).
- [4] A. K. Sinha *et al.*, Nucl. Instrum. Meth. A **339**, 543 (1994).

### 5.1.2 Nuclear structure study of $^{104}\text{Pd}$ using Coulomb excitation at heavy ion laboratory, Warsaw

S. Dutt<sup>1,2</sup>, P. J. Napiorkowski<sup>2</sup>, T. Abraham<sup>2</sup>, L. Janiak<sup>3</sup>, S. M. Kisielinski<sup>2,4</sup>, M. Komorowska<sup>2,5</sup>, M. Kowalczyk<sup>2,5</sup>, R. Kumar<sup>6</sup>, T. Marchlewski<sup>2,5</sup>, M. Matejska-Minda<sup>2</sup>, M. Palacz<sup>2</sup>, W. Piatek<sup>2</sup>, L. Prochniak<sup>2</sup>, I. A. Rizvi<sup>1</sup>, J. Samorajczyk<sup>2,3</sup>, M. Saxena<sup>7</sup>, J. Srebrny<sup>2</sup>, A. Tucholski<sup>2</sup>, W. Wroblewski<sup>3</sup>, K. Wrzosek-Lipska<sup>2</sup> and M. Zielinska<sup>2,8</sup>

<sup>1</sup>Department of Physics, Aligarh Muslim University, Aligarh, India

<sup>2</sup>Heavy Ion Laboratory, Warsaw University, Pasteura 5a, 02-093 Warsaw, Poland

<sup>3</sup>Faculty of Physics and Applied Computer Science, University of Lodz, Lodz, Poland

<sup>4</sup>National Centre for Nuclear Research, Swierk, Poland

<sup>5</sup>Faculty of Physics, University of Warsaw, Warsaw, Poland

<sup>6</sup>Inter University Accelerator Centre, New Delhi, India

<sup>7</sup>Department of Physics and Astrophysics, University of Delhi, India

<sup>8</sup>MIRFU/SPhN, CEA Saclay, Gif-Sur-Yvette, France

Experimental data on electromagnetic structure of  $^{104}\text{Pd}$  are scarce as compared to the experimental information available for the other even-even Pd-isotopes. Earlier, level structures of even-even stable Pd isotopes were considered as being examples of quadrupole vibrational spectra [1]. However, Coulomb excitation investigations of  $^{106-110}\text{Pd}$  have demonstrated that these nuclei show rather complicated structures [2,3], which may be explained as a result of the interplay of collective and single particle effects. In particular, the relatively low-lying  $0^+$  states in this isotopic chain may arise from collective excitations, but some of them were suggested as built from the single-particle intruder states [3].

The Coulomb excitation experiment of  $^{104}\text{Pd}$  was carried out at the Heavy Ion Laboratory, Warsaw using 91 MeV  $^{32}\text{S}$  beam.  $^{104}\text{Pd}$  target of 2 mg/cm<sup>2</sup> thickness was used in the present experiment. The  $\gamma$ -rays depopulating Coulomb excited states were detected by using the EAGLE gamma-ray spectrometer [4] in coincidence with scattered projectiles. 48 PIN-diodes of 0.5×0.5 cm<sup>2</sup> active area, covering the backward angles from 120-170° in Munich chamber [5], were used to detect the back-scattered projectiles. The data were collected in particle-gamma coincidence mode for 5 days.

As the gamma-rays detected by the HPGe detectors were Doppler-broadened, appropriate corrections were incorporated. Timing gates for prompt and random events were applied for each individual PIN-diode and HPGe detector combination. Random events were subtracted from the prompt events to normalize the 511 keV -annihilation peak. The prompt-gated and random subtracted gamma-ray spectra, for individual PIN-diode-HPGe detector combination, were summed over all the PIN-diodes and HPGe detectors to get the total statistics, as shown in Fig. 4. In the present experiment, states up to 6+ in the ground state band along with the low lying non-yrast bands were also populated. Gamma-rays for other stable Pd isotopes  $^{105,106,108,110}\text{Pd}$  were also observed as isotopic contaminations in the target and are tagged in the spectrum presented here. Further analysis of the data is in progress to determine the matrix elements of different levels by using the least square fitting code GOSIA [6].

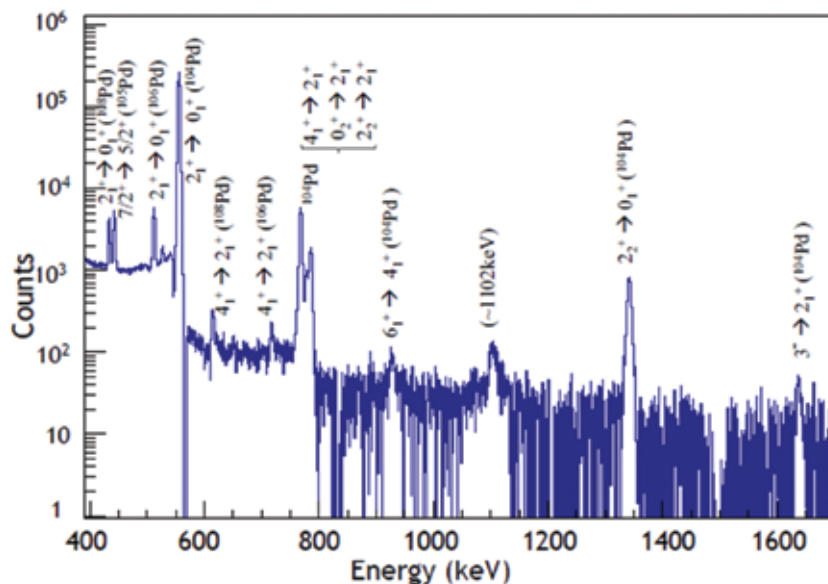


Fig. 4: Energy-calibrated, Doppler corrected and random subtracted gamma-ray spectrum resulting from the Coulomb excitation of highly enriched  $^{104}\text{Pd}$  target with 91 MeV  $^{32}\text{S}$  beam.

## References

- [1] David J. Rowe, John L. Wood, *Fundamentals of Nuclear Models*, World Scientific (2010).
- [2] L. E. Svensson *et al.*, *Nucl. Phys. A* **584**, 547 (1995).
- [3] K. Zajac *et al.*, *Nucl. Phys. A* **653**, 71 (1999).
- [4] J. Mierzejewski *et al.*, *Nucl. Instrum. Meth. A* **659**, 84 (2011).
- [5] M. B. Warkner *et al.*, *Nucl. Phys. A* **725**, 3 (2003).
- [6] T. Czosnyka *et al.*, *Bull. Amer. Phys. Soc.* **28**, 745 (1983).

### 5.1.3 Study of static quadrupole moments in $^{120}\text{Te}$

R. Kumar<sup>1</sup>, M. Saxena<sup>2</sup>, P. Napiorkowski<sup>3</sup>, A. Stolarz<sup>3</sup>, M. Komorowska<sup>3</sup>, K. Wrzosek-Lipska<sup>3</sup>, J. Srebrny<sup>3</sup>, S. Dutt<sup>4</sup> and H.-J. Wollersheim<sup>5</sup>

<sup>1</sup>Inter-University Accelerator Centre, New Delhi 110067, India

<sup>2</sup>Department of Physics and Astrophysics, University of Delhi, Delhi 110007, India

<sup>3</sup>Heavy Ion Laboratory, University of Warsaw, Pasteura 5a, 02-093 Warsaw, Poland

<sup>4</sup>Department of Physics, Bareilly College, India

<sup>5</sup>GSI Helmholtzzentrum für Schwerionenforschung GmbH, D-64291 Darmstadt, Germany

In recent years, the region in the vicinity of Sn isotopes has been intensively investigated both from experimental and theoretical perspectives. In particular, the excitation energies and the reduced transition probabilities across

the  $Z=50$  chain has been examined in detail. In Te nuclei with two protons outside the major shell, the partial level schemes are dominated by the  $1g_{7/2}$  orbit leading to  $6^+$  isomers in the vicinity of  $N=82$  shell closure. The Te nuclei with 52 protons lies in the transitional region between the spherical nuclei at  $Z = 50$  and deformed Xe and Ba nuclei. At low spin, the Te nuclei are considered to be one of the best examples of quadrupole vibrators. For any nuclei to be vibrational, three criteria must be satisfied: (i) the  $R_{4/2}$  ratio should be equal to 2, (ii) it should have a nearly degenerate two-phonon triplet of  $0^+$ ,  $2^+$  and  $4^+$  states and (iii) it should exhibit collective electric quadrupole transitions between states differing by one phonon and strong hindrance of E2 transition between states differing by more than one phonon.

For the mid-shell  $^{120,122,124}\text{Te}$  nuclei, the partial level schemes depicted in Fig. 5 show the expected vibrational-like structure with equal energy spacing between the phonon states.

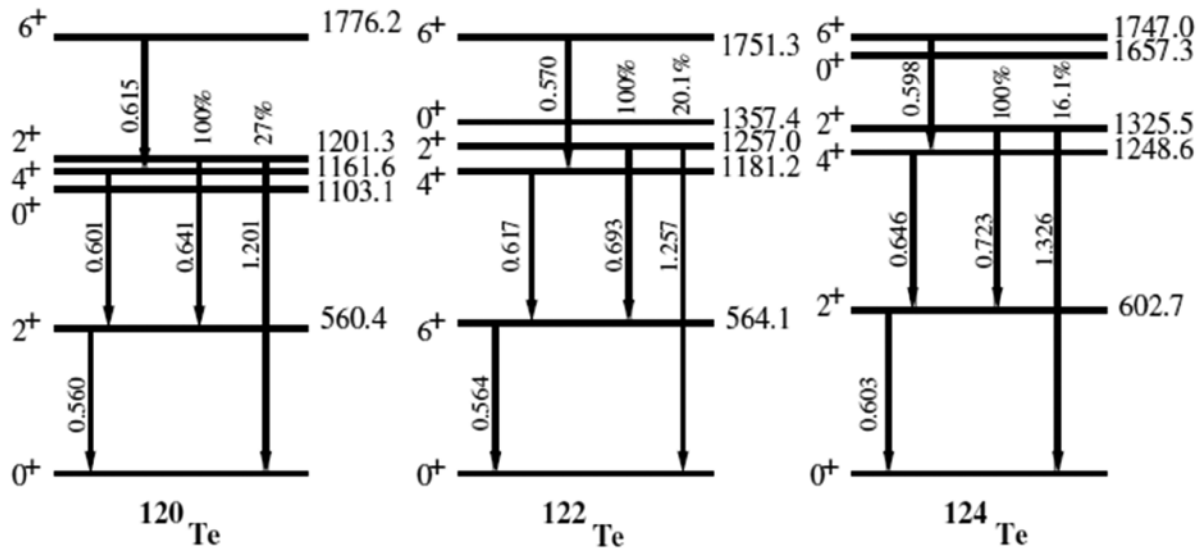


Fig. 5: Partial level schemes of  $^{120}\text{Te}$ ,  $^{122}\text{Te}$  and  $^{124}\text{Te}$ .

This observation is in contrast to the measured quadrupole moments ( $Q_{2^+}$ ) in  $^{122,124}\text{Te}$  isotopes [1,2]. The experimental quadrupole moments reach almost 60% of the rigid rotor values.

In our recent Coulomb excitation experiment [3] at IUAC, we used  $^{58}\text{Ni}$  beam at  $E_{\text{lab}} = 175$  MeV to excite  $^{120,122,124}\text{Te}$  isotopes. In these measurements, the scattered particles were detected at forward angles. The  $B(E2; 0^+ \rightarrow 2^+)$  value in  $^{120}\text{Te}$  was re-measured with a much higher precision to allow a comparison with the predictions of the large scale shell model (LSSM) calculations. In addition, the nuclear structures of  $^{120,122,124}\text{Te}$  were also investigated by measuring the absolute  $B(E2^+)$  values to higher lying states. Based on all experimental findings, level schemes and reduced transition probabilities for  $^{120,122,124}\text{Te}$ , one obtains the best agreement with an asymmetric rotor behaviour. The aim of the present experiment was to measure the quadrupole moments ( $Q_{2^+}$ ) of the first excited states of the stable  $^{120}\text{Te}$ , using the reorientation effect.



## REFERENCES

- [1] A. Bockisch and A.M. Kleinfeld, Nucl. Phys. A **261**, 498 (1976).  
 [2] J. Barrette, M. Barrette, R. Haroutunian, G. Lamoureux and S. Monaro, Phys. Rev. C **10**, 1166 (1974).  
 [3] <http://www.nndc.bnl.gov/ensdf/>  
 [4] M. Saxena *et al.*, Phys. Rev. C **90**, 024316 (2014).  
 [5] D. Cline, *et al.*, Bull. Amer. Phys. Soc. **14**, 726 (1983).  
 [6] T. Czosnyka, D. Cline and C.Y. Wu *et al.*, Bull. Amer. Phys. Soc. **28**, 745 (1983).

5.1.4 Study of multiple Coulomb excitation of  $^{132}\text{Ba}$ 

R. Kumar<sup>1</sup>, S. Dutt<sup>2</sup>, Mansi Saxena<sup>3</sup>, A. Jhingan<sup>1</sup>, R. K. Bhowmik<sup>4</sup>, A. Banerjee<sup>3</sup>, J. Kaur<sup>5</sup>, C. Joshi<sup>6</sup>, V. Mishra<sup>7</sup>, P. J. Napiorkowski<sup>8</sup>, M. Matejska-Minda<sup>8</sup>, A. Stolarz<sup>8</sup>, A. Tyagi<sup>7</sup>, A. Agarwal<sup>9</sup>, S. Prajapati<sup>9</sup>, I. Rizvi<sup>2</sup> and H. J. Wollersheim<sup>10</sup>

<sup>1</sup>Inter University Accelerator Centre, New Delhi, India

<sup>2</sup>Department of Physics, Aligarh Muslim University, Aligarh, India

<sup>3</sup>Department of Physics and Astrophysics, University of Delhi, India

<sup>4</sup>Formerly with Inter University Accelerator Centre, New Delhi, India

<sup>5</sup>National Institute for Physics and Nuclear Engineering (IFIN-HH), 30 Reactorului, 077125 Bucharest-Magurele, Romania

<sup>6</sup>Department of Physics, MS University of Baroda, India

<sup>7</sup>Department of Physics, Banaras Hindu University, India

<sup>8</sup>Heavy Ion Laboratory, Warsaw University, Pasteura 5a, 02-093 Warsaw, Poland

<sup>9</sup>Department of Physics, Bareilly College, India

<sup>10</sup>GSI Helmholtzzentrum für Schwerionenforschung, Darmstadt, Germany

Numerous experimental and theoretical studies are currently focused on nuclear shell structure far from the line of stability [1]. Nuclei in the vicinity of doubly-magic  $^{100,132}\text{Sn}$  are of key importance for the understanding of the nuclear shell structure as a function of increasing neutron number. Especially, the proton-neutron interaction will play an important role for these nuclei. In the mass region  $A \approx 130$ , the Xe and Ba nuclei develop a transitional path from spherical shapes to strong deformations (see Fig.8).

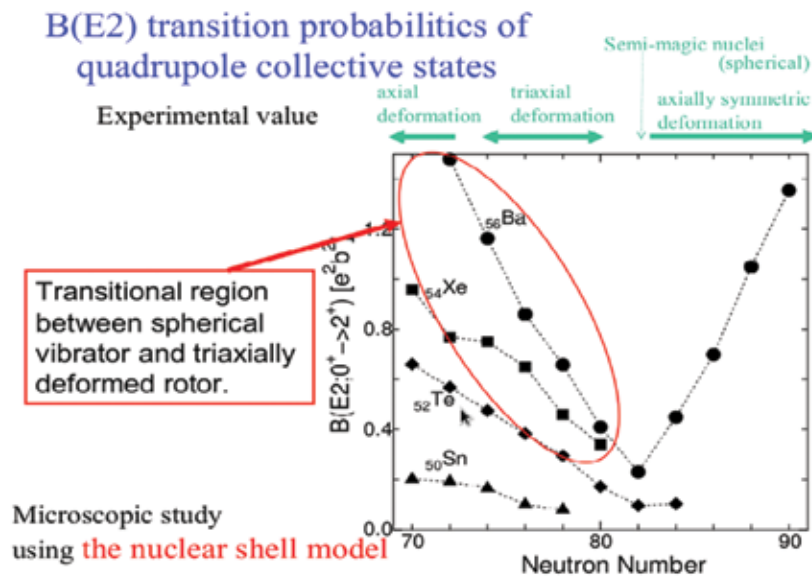


Fig. 8: B(E2) transition probabilities of quadrupole collective states.

The isotones with  $N = 82$ , which are semi-magic nuclei, show the feature of spherical vibrator with a small collective strength. With increasing neutron number, the  $B(E2)$  value for Ba isotopes (and hence the collectivity) increases. The same trend is also visible for nuclei with decreasing neutron number. From the additional knowledge of the  $4^+$  state, the nuclear structure can be extracted. For the structure of heavy isotopes, one finds an axially symmetric rotor, while nuclei with  $N < 82$  show features of triaxial deformation. One obtains a triaxiality parameter of  $\gamma \approx 30^\circ$  [2,3] and a rather soft potential. Fig. 9 shows the  $E_4/E_2$  ratio plot of Ba isotopes which clearly indicates the signature of triaxiality.

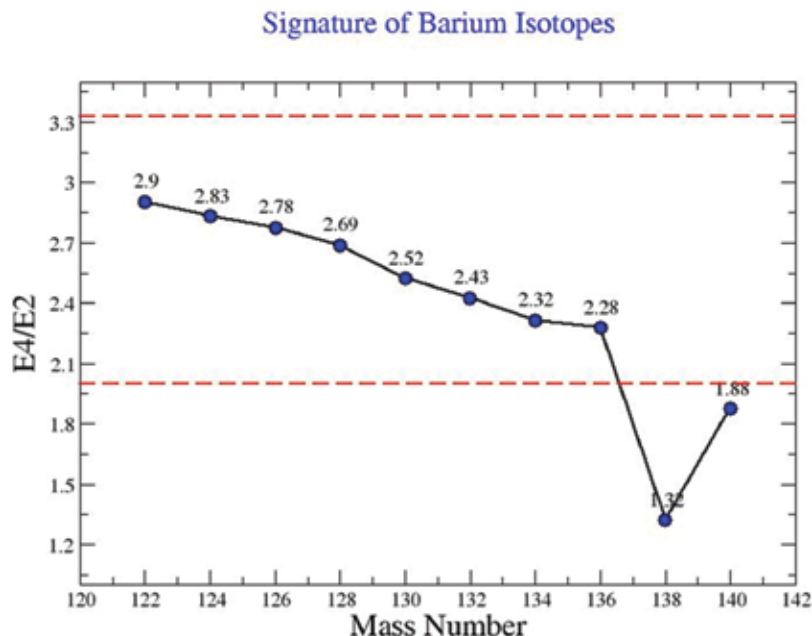


Fig. 9:  $E_4/E_2$  ratio of Barium isotopes are between the vibrator and rotor limits with a clear signature of triaxiality.

Fig. 10 (a and b) illustrates the observed level energies and  $B(E2\uparrow)$  values in stable Ba isotopes, respectively. The  $B(E2\uparrow)$  values are predicted to follow a parabolic behavior between the shell closures. In case of  $^{132}\text{Ba}$ , the measurements for the  $2^+$  state were performed in 1985 [4] and 1958 [5], but no measurement is available for the  $4^+$  state. As we have shown for the stable Sn isotopes, very accurate data are needed to be compared with current microscopic [6] and macroscopic theories. Therefore, it is important to improve our experimental knowledge on the collectivity and determine the nuclear structure of  $^{132}\text{Ba}$ .

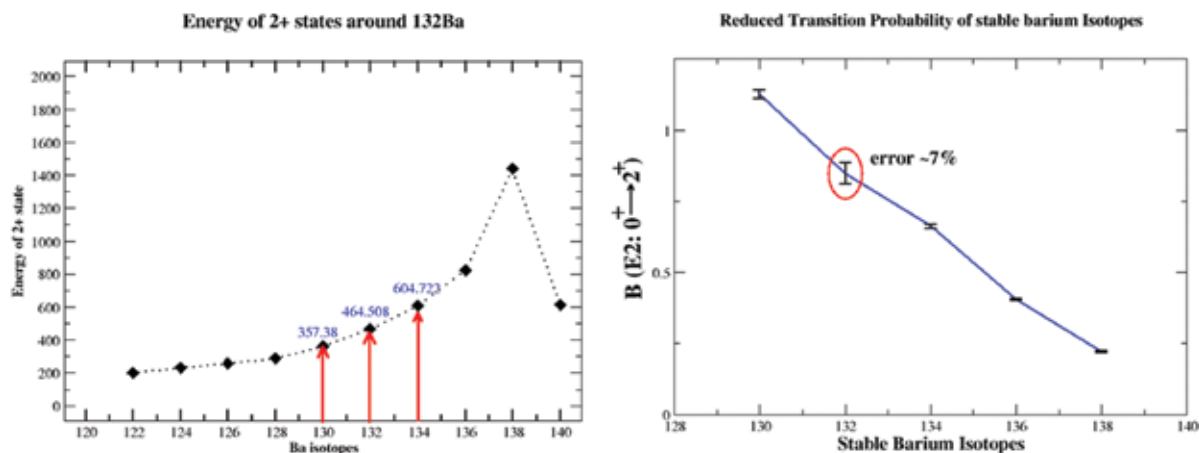


Fig. 10. (a) Observed level energies, and (b) experimental  $B(E2\uparrow)$  values for the stable Ba isotopes.

Two sets of complementary experiments were performed to study the nuclear structure of  $^{132}\text{Ba}$  using Coulomb excitation. The first experiment was performed at Heavy Ion Laboratory, Warsaw and the second one was performed at IUAC, New Delhi.

Experiment at IUAC, New Delhi: The experiment was carried out using  $^{58}\text{Ni}$  beam at  $E_{\text{lab}} = 175$  MeV from the 15UD tandem accelerator. Stable targets of  $^{132}\text{Ba}$  (thickness  $0.25$  mg/cm $^2$  with a  $10\text{-}20\mu\text{g/cm}^2$  carbon backing) were used. The scattered beam-like particles and the recoils were detected in an annular gas-filled parallel plate avalanche counter (PPAC), having a mylar entrance window of  $10$   $\mu\text{m}$ . The PPAC was placed  $11$  cm downstream from the target position, covering an angular range of  $15^\circ \leq \theta_{\text{lab}} \leq 45^\circ$  in the forward direction. The PPAC was position sensitive for both the azimuthal  $\phi$  and the polar  $\theta$  angles. The azimuthal angle was obtained from the anode foil which was divided into  $20$  radial sections of  $18^\circ$  each. The polar angle was determined from the cathode which was patterned in concentric conductor rings of constant  $\tan\theta$ , each  $1$  mm wide, with an insulating gap of  $0.5$  mm between them.

The de-exciting  $\gamma$ -rays were detected in the four Clover detectors, having an energy resolution  $\sim 2.5$  keV, mounted at angle  $\sim 145^\circ$  relative to the beam direction. The  $\phi$  angles for the Clover detectors were  $\sim 50^\circ$  and  $\sim 130^\circ$  relative to the vertical direction. The present data analysis has been performed using a dedicated code written using GO4 software package. Fig. 11 shows an example of energy calibrated spectrum for one of the Ge detectors.

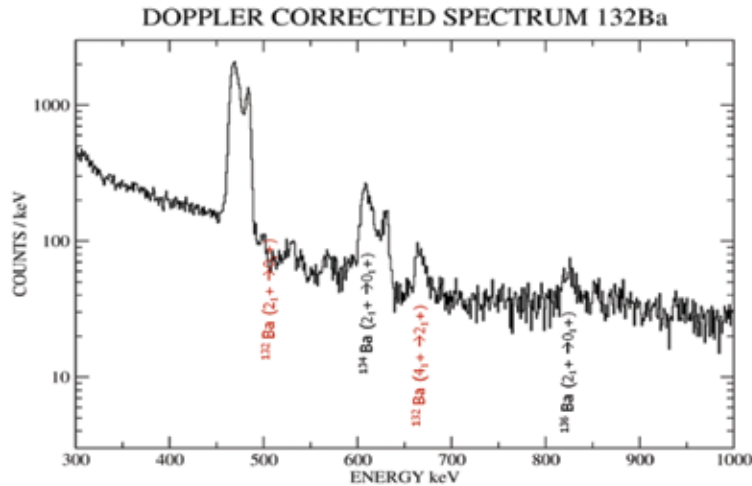


Fig. 11: Energy-calibrated, Doppler-corrected  $\gamma$ -ray spectrum resulting from the Coulomb excitation of highly enriched  $^{132}\text{Ba}$  target with  $175$  MeV  $^{58}\text{Ni}$  beam.

Experiment at HIL, Warsaw: Coulomb excitation experiment of  $^{132}\text{Ba}$  was performed in May-June campaign at the Heavy Ion Laboratory, University of Warsaw.  $^{132}\text{Ba}$  target (thickness  $\approx 0.5$  mg/cm $^2$ , 40% enrichment) was prepared at the Heavy Ion Laboratory. Energy calibration of Ge-detectors were done by using  $^{152}\text{Eu}$  source. Prompt and random timing gates were applied for each individual combination of Germanium and PIN-diode detectors.

Data were collected in particle-gamma coincidence mode. To remove the background radiation, random events were subtracted from prompt events by selecting the proper timing gates, and the results are shown in Fig. 12.

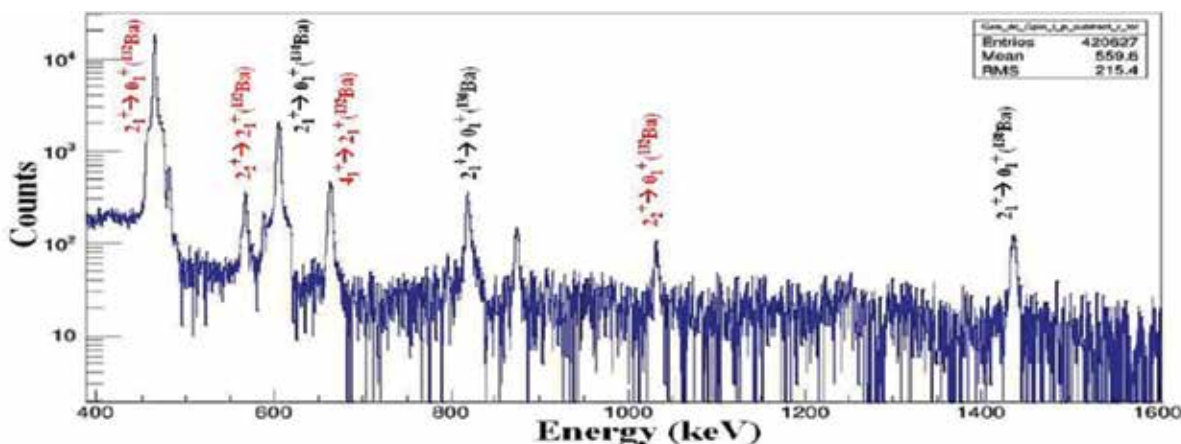


Fig-12 : Energy calibrated, Doppler-corrected and random-subtracted  $\gamma$ -ray spectrum resulting from Coulomb excitation of highly enriched  $^{132}\text{Ba}$  with 91 MeV  $^{32}\text{S}$  beam.

## REFERENCES

- [1] H. Grawe and M. Lewitowicz, Nucl. Phys. A **693**, 116 (2001), and references therein
- [2] J. Yan, O. Vogel, P. von Brentano and A. Gelberg, Phys. Rev. C **48**, 1046 (1993).
- [3] O. Vogel, P. van Isacker, A. Gelberg, P. von Brentano and A. Dewald, Phys. Rev. C **53**, 1660 (1996).
- [4] S. M. Burnett *et al.*, Nucl. Phys. A **432**, 524 (1985).
- [5] L. W. Fagg *et al.*, Phys. Rev. **109**, 100 (1958).
- [6] L. Próchniak, K. Zając, K. Pomorski, S. G. Rohoziński, J. Srebrny, Nucl. Phys. A **648**, 181 (1999).
- [7] T. Czosnyka *et al.*, Bull. Am. Phys. Soc. **28**, 745 (1986), <http://www.slj.uw.edu.pl/gosia>
- [8] Brookhaven ENDSF database, <http://www.nndc.bnl.gov/endsf>

### 5.1.5 Re-measurement of transition probability of Sn isotopes using Coulomb excitation method

R. Kumar<sup>1</sup>, P. Doornenbal<sup>2</sup>, Mansi Saxena<sup>3</sup>, A. Jhingan<sup>1</sup>, R. K. Bhowmik<sup>4</sup>, A. Banerjee<sup>3</sup>, S. Dutt<sup>5</sup>, Ritika Garg<sup>1</sup>, C. Joshi<sup>6</sup>, V. Mishra<sup>7</sup>, P. J. Napiorkowski<sup>8</sup>, S. Prajapati<sup>9</sup>, P. A. Soederstroem<sup>1</sup> and H. J. Wollersheim<sup>10</sup>

<sup>1</sup>Inter University Accelerator Centre, New Delhi, India

<sup>2</sup>Riken Nishina Centre for Accelerator Based Science Saitama 3510198, Japan

<sup>3</sup>Department of Physics and Astrophysics, University of Delhi, India

<sup>4</sup>Formerly with Inter University Accelerator Centre, New Delhi, India

<sup>5</sup>Accelerator Laboratory, Department of Physics, Aligarh Muslim University, India

<sup>6</sup>Department of Physics, MS University of Baroda, India

<sup>7</sup>Department of Physics, Banaras Hindu University, India

<sup>8</sup>Heavy Ion Laboratory, Warsaw University, Pasteura 5a, 02-093 Warsaw, Poland

<sup>9</sup>Department of Physics, Bareilly College, India

<sup>10</sup>GSI Helmholtzzentrum für Schwerionenforschung, Darmstadt, Germany

Numerous experimental and theoretical studies are currently focused on nuclear shell structure far from the line of stability [1]. In particular, the evolution of basic nuclear properties, e.g., the energy of the first excited state ( $2^+$ ) and the reduced transition probability, i.e.  $B(E2; 0^+ \rightarrow 2^+)$  value, along closed shells mark an area of great interest. The longest isotopic chain, between two doubly magic nuclei, are the Sn isotopes which are accessible for nuclear structure studies. Even-even nuclei along closed proton or neutron shells are often well described by the seniority scheme. (see, e.g., Ref. [2]). For the seniority scheme one expects a symmetric distribution of the  $B(E2)$  values between the two doubly magic nuclei  $^{100}\text{Sn}$  and  $^{132}\text{Sn}$ , with a maximum collectivity at mid-shell ( $^{116}\text{Sn}$ ).

While the almost constant  $2^+$  excitation energies are well described by the seniority scheme between the two doubly magic nuclei, the  $B(E2\uparrow)$  values follow a deviating pattern. The a priori expectation is a curve showing

maximum collectivity at mid-shell. However, several experimental findings in recent years have put this pattern into question. While the neutron-rich isotopes ( $^{126-130}\text{Sn}$ ) smoothly decrease in collectivity, proton-rich nuclei are almost constant and not mirror-symmetric with respect to  $^{116}\text{Sn}$ , as shown in Fig. 13. Most of the neutron deficient nuclei were measured at radioactive isotope facilities [3-8,12-14], except for  $^{112,114}\text{Sn}$  [9,10]. For the latter nucleus, the  $B(E2\uparrow)$  values were extracted relative to  $^{116}\text{Sn}$  in order to obtain an accuracy of better than 3%. A recent Doppler shift attenuation (DSA) measurement [11] yields, however, low  $B(E2\uparrow)$  values (up to 20%) than previously found in the literature [15]. Therefore, we performed a series of Coulomb excitation experiments at IUAC in order to excite all stable Sn isotopes ( $^{112,116,118,120,122,124}\text{Sn}$ ) with a  $^{58}\text{Ni}$  beam. Both projectile and target nuclei were excited and from the  $2^+$  intensities the  $B(E2)$  ratios could be determined in a straight forward manner.

The experiment was carried out using  $^{58}\text{Ni}$  beam at  $E_{\text{lab}} = 175$  MeV from the 15UD Pelletron accelerator at IUAC. Six stable targets, namely  $^{112}\text{Sn}$ ,  $^{116}\text{Sn}$ ,  $^{118}\text{Sn}$ ,  $^{120}\text{Sn}$ ,  $^{122}\text{Sn}$  and  $^{124}\text{Sn}$ , each of thickness  $0.45$  mg/cm $^2$  with a  $10\text{-}20$   $\mu\text{g}/\text{cm}^2$  carbon backing were used. The scattered beam-like particles and the recoils were detected in an annular gas filled parallel plate avalanche counter (PPAC), having an entrance mylar window of  $10$   $\mu\text{m}$  thickness. The PPAC was placed  $11$  cm downstream from the target position, covering an angular range of  $15^\circ \leq \theta_{\text{lab}} \leq 45^\circ$  in the forward direction. The PPAC was position-sensitive for both the azimuthal  $\phi$  and the polar  $\theta$  angles. The azimuthal angle was obtained from the anode foil which was divided into  $20$  radial sections of  $18^\circ$  each. The polar angle was determined from the cathode which was patterned in concentric conductor rings of constant  $\tan \theta$ , each  $1$  mm wide, with an insulating gap of  $0.5$  mm between them.

The de-exciting gamma-rays were detected in the four Clover detectors, having an energy resolution  $\sim 2.5$  keV, mounted at angle  $\sim 145^\circ$  relative to the beam direction. The  $\phi$  angles for the Clover detectors were  $\sim 50^\circ$  and  $\sim 130^\circ$  relative to the vertical direction.

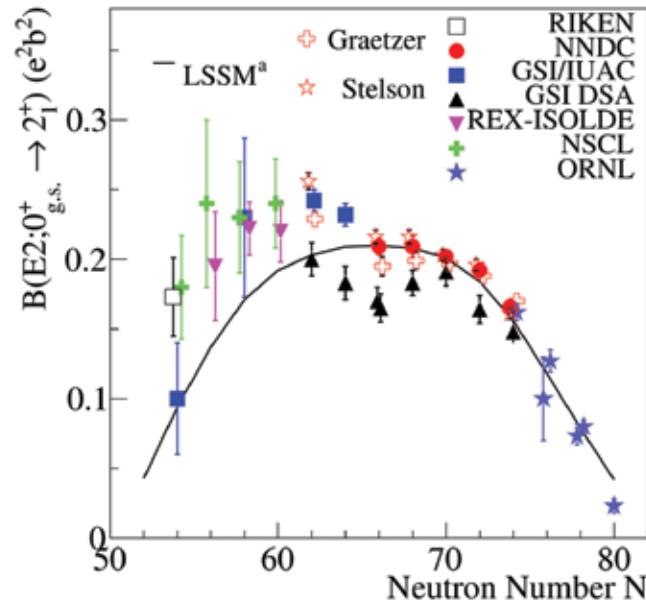


Figure-13: Evolution of  $B(E2\uparrow)$  values for Sn isotopes. An increasing deviation from  $^{124}\text{Sn}$  to  $^{112}\text{Sn}$  is visible for the latest Coulex results [9,10,16,17] and the DSA measurements [11] on stable nuclei. Shell model calculations using a  $^{100}\text{Sn}$  core are shown for comparison [5]. Values labeled with NNDC are the adopted ones from Ref. [15].

The present data analysis has been performed using a dedicated code written using GO4 software package. Fig. 14 shows an example of Doppler-corrected and energy-calibrated spectrum for one of the Ge detectors.

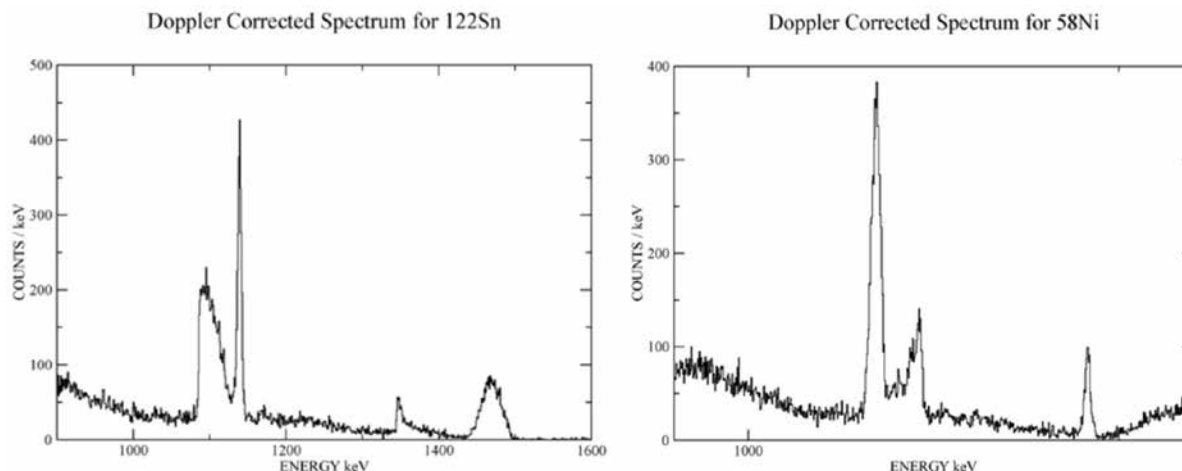


Fig. 14 : (a) Doppler shift corrected  $\gamma$ -ray spectra for the  $2^+ \rightarrow 0^+$  transition measured for the system  $^{58}\text{Ni}+^{122}\text{Sn}$  assuming  $^{58}\text{Ni}$  being detected in the PPAC. The broad distribution on left hand side results from close collisions events, when Sn recoils are detected in PPAC (b) Doppler shift corrected  $\gamma$ -ray spectra for  $^{58}\text{Ni}$  excitation.

## REFERENCES

- [1] H. Grawe and M. Lewitowicz, Nucl. Phys. A **693**, 116 (2001) and references therein.
- [2] R. Casten, Nuclear Structure from a Simple Perspective (Oxford University Press, 2001).
- [3] D. Radford *et al.*, Nucl. Phys. A **746**, 83c (2004).
- [4] J. Allmond *et al.*, Phys. Rev. C **84**, 061303(R) (2011).
- [5] A. Banu *et al.*, Phys. Rev. C **72**, 061305 (2005).
- [6] A. Ekström *et al.*, Phys. Rev. Lett. **101**, 012502 (2008).
- [7] J. Cederkäll *et al.*, Phys. Rev. Lett. **98**, 172501 (2007).
- [8] C. Vamanet *et al.*, Phys. Rev. Lett. **99**, 162501 (2007).
- [9] P. Doornenbal *et al.*, Phys. Rev. C **78**, 031303 (2008).
- [10] R. Kumar *et al.*, Phys. Rev. C **81**, 024306 (2010).
- [11] A. Jungclauss *et al.*, Phys. Lett. B **110**, 695 (2011).
- [12] G. Guastalla *et al.*, Phys. Rev. Lett. **110**, 172501 (2013).
- [13] V. Bader *et al.*, Phys. Rev. C **88**, 051301(R) (2013).
- [14] P. Doornenbal *et al.*, submitted to Phys. Rev. C.
- [15] S. Raman, C. W. Nestor Jr., and P. Tikkanen, Atom. Data Nucl. Data Tab. **78**, 1 (2001).
- [16] P. H. Stelson *et al.* Phys. Rev. C **2**, 2015 (1970).
- [17] R. Graetzer *et al.*, Phys. Rev. C **12**, 1462 (1975).

### 5.1.6 Observation of incomplete fusion contribution below $I_{\text{crit}}$

Harish Kumar<sup>1</sup>, Suhail A Tali<sup>1</sup>, Siddharth Parashari<sup>1</sup>, Asif Ali<sup>1</sup>, M. Afzal Ansari<sup>1</sup>, D. Singh<sup>2</sup>, Rahbar Ali<sup>3</sup>, Kamal Kumar<sup>1</sup>, N. P. M. Sathik<sup>4</sup>, R. Dubey<sup>5</sup>, Indu Bala<sup>5</sup>, Rakesh Kumar<sup>5</sup>, R. P. Singh<sup>5</sup> and S. Muralithar<sup>5</sup>

<sup>1</sup>Department of Physics, Aligarh Muslim University, Aligarh 202002, India

<sup>2</sup>Centre for Applied Physics, Central University of Jharkhand, Ranchi 835205, India

<sup>3</sup>Department of Physics, G. F. (P. G.) College, Shahjahanpur 242001, India

<sup>4</sup>Department of Physics, Jamal Mohammed College, Tiruchirappalli 620020, India

<sup>5</sup>Inter-University Accelerator Centre, New Delhi 110067, India

Incomplete fusion process (ICF) shows significant contribution in competition with the complete fusion (CF) at lower projectile energies  $\approx 4\text{-}8$  MeV/nucleon [1-3]. Several models [4-6] have been proposed to explain the ICF reactions. Unfortunately, all these existing models are not applicable to fit the experimental data below 10 MeV/nucleon energies. In Sum-rule model [4], Wilczynski *et al.* approached a sharp cutoff approximation to explain

ICF reactions according to which the CF probability is assumed to be unity for  $l \leq l_{\text{crit}}$  and zero in case of  $l > l_{\text{crit}}$ . Barker *et al.* [7] also observed the ICF process for  $l$  values greater than  $l_{\text{crit}}$ . However, Tricoire *et al.* [8] found the ICF existence for  $l \leq l_{\text{crit}}$ . Later on, Singh *et al.* [2] and Ali *et al.* [3] also claimed the ICF contribution below the  $l_{\text{crit}}$  values in contradiction to the sumrule model assumptions. In order to have a better insight into the role of fusion  $l$ -distribution on ICF reaction dynamics, the excitation functions (EFs) of residues produced in  $^{13}\text{C} + ^{175}\text{Lu}$  system have been measured at  $\approx 4-7$  MeV/nucleon energies.

The experiment was performed at IUAC and recoil catcher activation technique followed by off-line  $\gamma$ -ray spectroscopy was adopted for the EFs measurement. The target as well as Al-catcher foils were fabricated by rolling. Two stacks of four self-supporting  $^{175}\text{Lu}$  target foils having thickness ranges  $\approx 1.0-1.5$  mg/cm<sup>2</sup> backed by Al-catcher foils of thickness  $\approx 1.4-2.0$  mg/cm<sup>2</sup> were irradiated with  $^{13}\text{C}$  beam. The experiment was carried out in the General Purpose Scattering Chamber (GPSC) for about 7-10 hours to cover the energy range 4-7 MeV/nucleon. The induced  $\gamma$ -ray activities in each target-catcher assembly was recorded by using the pre-calibrated HPGe detector coupled to CAMAC based FREEDOM software.

Several evaporation residues (ERs) produced in  $^{13}\text{C} + ^{175}\text{Lu}$  system were measured. The individual cross-sections have been deduced by using the Cavinato *et al.* formalism [9] for any higher charge isobar precursor decay. The experimental EFs were compared with theoretical predictions based on statistical model code PACE-4 [10], which calculated only the CF contribution. Any enhancement in the measured cross sections of  $\alpha\text{xn}-2\alpha\text{xn}$  channels from the theoretical predictions was attributed to the ICF contribution leading to the production of these residues via ICF along with CF. The sum of all measured  $\alpha\text{xn}-2\alpha\text{xn}$  channel cross-sections ( $\sigma_{\text{exp}}$ ) was compared with that estimated by PACE4 ( $\sigma_{\text{CF}}$ ) with level density parameter  $K = 10$  for  $^{13}\text{C} + ^{175}\text{Lu}$  system. The comparison is shown in Fig. 15(a). This graph provides better visualization of ICF contribution and PACE4 predictions are found to underestimate significantly throughout the studied energy region. The ICF cross-section was also found to increase with increasing projectile energy. In order to enlighten the underlying discrepancies of fusion  $l$ -distribution, the theoretical calculations based on Sum-rule model were performed for  $^{13}\text{C} + ^{175}\text{Lu}$  by retaining the same set of parameters as those were incorporated by Wilczynski *et al.* in Sum-rule model [4]. The experimentally measured cross sections for  $\alpha\text{xn}$  and  $2\alpha\text{xn}$  channels are  $\approx 171$  mb and  $\approx 96$  mb, however, the Sum-rule predictions for these channels are  $\approx 82$  mb and  $\approx 4$  mb, respectively, at 87.5 MeV energy. Similarly, the Sumrule model based  $\alpha\text{xn}$  and  $2\alpha\text{xn}$  channel cross sections were calculated at 83.7, 79.9 and 75.9 MeV and compared with experimental cross-sections of these channels at the respective energy. The comparison between experimentally measured and theoretically predicted cross-sections for  $\alpha\text{xn}-2\alpha\text{xn}$  evaporation channels is demonstrated in Fig. 15(b). This Figure clearly shows that the Sum-rule model predictions highly underestimate the measured cross sections for  $\alpha\text{xn}-2\alpha\text{xn}$  evaporation channels. The obtained results supplement the findings of Singh *et al.* [2] and Ali *et al.* [3] and indicate the inconsistency of Sum-rule model calculations with low-energy ICF reaction dynamics. To understand the role of  $l_{\text{crit}}$  window in a better way, the critical angular momentum ( $l_{\text{crit}}$ ) and maximum angular momentum ( $l_{\text{max}}$ ) values were calculated for the present system. The ' $l_{\text{max}}$ ' is a maximum limit of  $l$  for which fusion may occur. By using Wilczynski *et al.* prescription [4], the  $l_{\text{crit}}$  value is found to be  $\approx 50\hbar$  for  $^{13}\text{C} + ^{175}\text{Lu}$ . However, the  $l_{\text{max}}$  value based on CCFULL calculations [11] is  $\approx 45\hbar$  at the highest projectile energy ( $\approx 87.5$  MeV). It may be pointed out that the  $l_{\text{max}}$  value is not as high as  $l_{\text{crit}}$  for fusion at the highest projectile energy, but the significant ICF contribution was observed for the present system at this energy. The present work indicates that ICF may occur even below  $l_{\text{crit}}$  i.e.  $l \leq l_{\text{crit}}$  for  $^{13}\text{C} + ^{175}\text{Lu}$ . The ICF contributions at  $l \leq l_{\text{crit}}$  values have also been claimed in recent studies [2, 3], contrary to the Sum-rule model. Moreover, it may be concluded that more experimental studies are needed to get any definite conclusion about the refinement in the basic assumptions of this model below 8 MeV/nucleon energies.

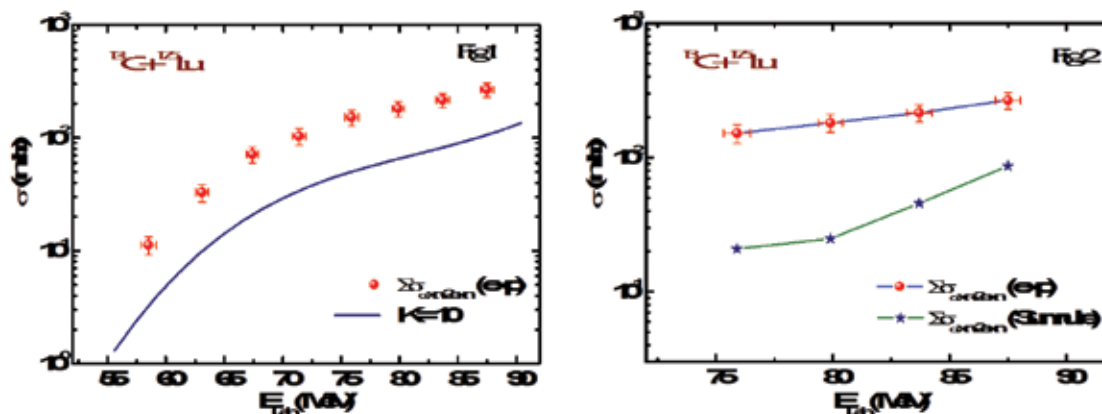


Fig. 15

## REFERENCES

- [1] B. S. Tomar et al., Phys. Rev. C **49**, 941 (1994); Phys. Rev. C **58**, 3478 (1998).
- [2] D. Singh et al., Nucl. Phys. A **879**, 107 (2012); Phys. Rev. C **83**, 054604 (2011).
- [3] Rahbar Ali et al., J. Phys. G: Nucl. Part. Phys. **37**, 115101 (2010).
- [4] T. Udagawa, T. Tamura, Phys. Rev. Lett. **45**, 1311 (1980).
- [5] J. Wilczynski et al., Nucl. Phys. A **373**, 109 (1982).
- [6] J. P. Bondroff et al., Nucl. Phys. A **333**, 285 (1980).
- [7] J. H. Barker et al., Phys. Rev. Lett. **45**, 424 (1980).
- [8] H. Tricoire et al., Z. Phys. A-Atomic Nuclei **323**, 163 (1986).
- [9] M. Cavinato et al., Phys. Rev. C **52**, 2577 (1995).
- [10] A. Gavron, Phys. Rev. C **21**, 230 (1980).
- [11] K. Hagino et al., Comput. Phys. Commun. **123**, 143 (1999).

5.1.7 Systematic study of incomplete fusion reactions in  $^{19}\text{F}+^{159}\text{Tb}$  at energies  $\approx 4\text{-}7\text{MeV/A}$ 

Mohd. Shuaib<sup>1</sup>, Vijay R. Sharma<sup>1,2</sup>, Abhishek Yadav<sup>2</sup>, Pushpendra P. Singh<sup>3</sup>, Manoj Kumar Sharma<sup>4</sup>, Devendra P. Singh<sup>5</sup>, R. Kumar<sup>2</sup>, S. Muralithar<sup>2</sup>, R. P. Singh<sup>2</sup>, B. P. Singh<sup>1</sup> and R. Prasad<sup>1</sup>

<sup>1</sup>Nuclear Physics Laboratory, Department of Physics, Aligarh Muslim University, Aligarh 202002, India

<sup>2</sup>Inter University Accelerator Centre, Aruna Asaf Ali Marg, New Delhi 110067, India

<sup>3</sup>Department of Physics, Indian Institute of Technology Ropar, Punjab 140001, India

<sup>4</sup>Physics Department, S. V. College, Aligarh 202002, India

<sup>5</sup> Physics Department, University of Petroleum and Energy Studies, Dehradun 248007, India

In heavy-ion (HI) induced reactions from Coulomb barrier to well above it, the complete fusion (CF) process is considered as a sole contributor. However, in recent reports, the incomplete fusion (ICF) process has also been found to be a competing mode of reaction at these energies [1, 2]. To get a proper visualization of reaction dynamics of ICF, the onset and strength of ICF in terms of various entrance channel parameters are needed to be systematically explored. Several theoretical models [1] have been employed to understand the reaction dynamics of ICF at energies  $\geq 10.5$  MeV/A, but none of them is found to reproduce the ICF data at low incident energies  $\approx 4\text{-}7$  MeV/A. At present, there is no theoretical model available which can explain the low energy ICF data precisely. In the present report, the excitation functions (EFs) of reaction residues populated via CF and/ or ICF in the interaction of  $^{19}\text{F}+^{159}\text{Tb}$  at energies  $\approx 4\text{-}7\text{MeV/A}$ , measured using the off-line  $\gamma$ -ray spectroscopy, are presented. The reaction residues were identified on the basis of characteristic  $\gamma$ -rays and confirmed by decay-curve analysis. Fig. 16 shows the EFs of individual reaction residues i.e.,  $^{174, 173, 172}\text{W}$  and  $^{173}\text{Ta}$  populated via 4n, 5n, 6n, and p4n channels, respectively, and compared with the theoretical predictions of statistical model code PACE4 [3]. As can be seen from this Figure, the experimental EFs are found to be in good agreement with the

results of PACE4 for the level density parameter  $a = A/10$ , which confirms the production of these residues solely via CF process. The residues  $^{173}\text{Ta}$  formed via p4n channel are found to be strongly fed from its higher charge isobar (precursor, hereafter)  $^{173}\text{W}$  (5n) through  $\beta^+$  emission. The independent cross-section of  $^{173}\text{Ta}$  was deduced using the successive radioactive decay formulations presented in Ref. [16].

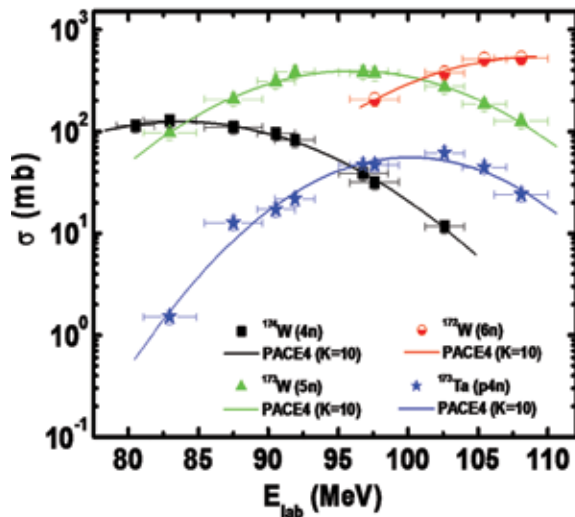


Fig. 16: Experimental EFs of individual reaction residues populated via xn and pxn channels. The solid colour lines represent the PACE4 predictions.

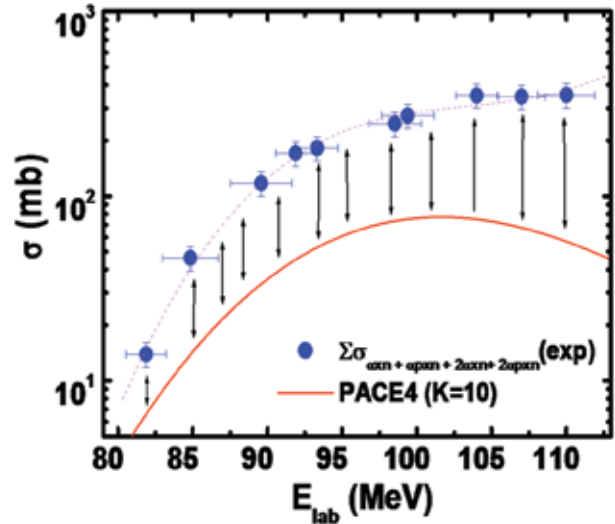


Fig.17: The sum of experimental EFs of  $\alpha$ -emitting channels compared with the predictions of PACE4. The dashed line through the data points is drawn to guide the eye.

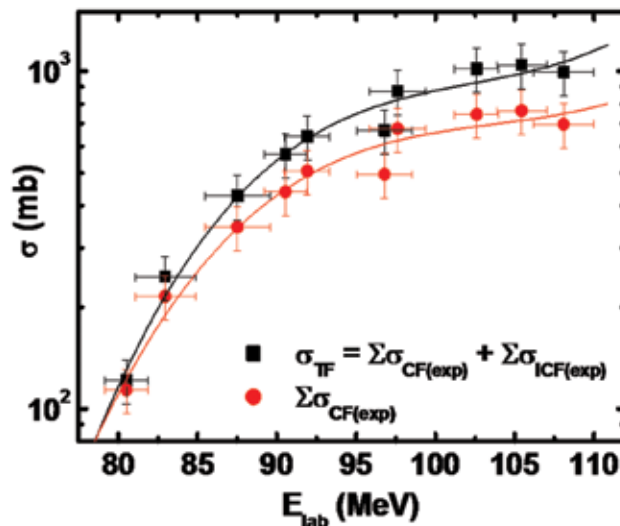


Fig. 18: A comparison of total reaction cross section as a function of incident laboratory energy. The solid colour lines are drawn to guide the eye.

To Figure out, if the  $\alpha$ -emitting channels were formed via CF and/or ICF process, the PACE4 calculations were done by using the same input parameters which were used to reproduce the EFs of xn and pxn channels. The sum of experimental EFs of all  $\alpha$ -emitting channels i.e.,  $^{171}\text{Hf}$  ( $\alpha 3n$ ),  $^{170}\text{Hf}$  ( $\alpha 4n$ ),  $^{170}\text{Lu}$  ( $\alpha p 3n$ ),  $^{167}\text{Yb}$  ( $2\alpha 3n$ ),  $^{167}\text{Tm}$  ( $2\alpha p 2n$ ), and  $^{165}\text{Tm}$  ( $2\alpha p 4n$ ) are compared with the predictions of corresponding PACE4 calculations and presented in Fig. 17. As can be seen from this Figure, the experimental EFs of  $\alpha$ -emitting channels show a

systematic enhancement over the predictions of PACE4 which may be attributed due to the ICF process at studied range of energy. In order to see, how ICF influence the total reaction cross-section, the total reaction cross-section has been plotted with (sum of all xn and pxn channels) as a function of incident lab energy and shown in Fig. 18. As can be seen from this Figure, the increasing gap indicates the presence of ICF in the total reaction cross-section. Further, to get detailed knowledge of ICF reaction dynamics at low energy, it will be interesting to compare the present work with various entrance channel parameters which may give some conclusive picture of ICF data [5].

## REFERENCES

- [1] Vijay R. Sharma et al., Phys. Rev. C **89**, 024608 (2014).
- [2] Abhishek Yadav et al., Phys. Rev. C **86**, 014603 (2012).
- [3] A. Gavronet *et al.*, Phys. Rev. C **21**, 230 (1980).
- [4] M. Cavinato *et al.*, Phys. Rev. C **52**, 2577 (1995).
- [5] Mohd. Shuaib *et al.*, IUAC Conference on Recent Trends In Nuclear Physics 2015, Book of Abstract, p31 (2015).

### 5.1.8 Evaporation residue excitation function for $^{35,37}\text{Cl}+^{181}\text{Ta}$ reaction

P. V. Laveen<sup>1</sup>, E. Prasad<sup>1</sup>, N. Madhavan<sup>2</sup>, J. Gehlot<sup>2</sup>, S. Nath<sup>2</sup>, A. M. Vinodkumar<sup>3</sup>, A. Shamlath<sup>1</sup>, M. Shareef<sup>1</sup>, Tathagata Banerjee<sup>2</sup>, A. Jhingan<sup>2</sup>, T. Varughese<sup>2</sup>, D. V. G. R. K. S. Kumar<sup>4</sup>, P. Sandya Devi<sup>4</sup>, Khushboo<sup>5</sup>, P. Jisha<sup>3</sup>, Priya Sharma<sup>6</sup>, Neeraj Kumar<sup>5</sup> and M.M. Hosamani<sup>7</sup>

<sup>1</sup>Department of Physics, School of Mathematical and Physical Sciences, Central University of Kerala, Kasaragod, 671314, India

<sup>2</sup>Inter University Accelerator Centre, Aruna Asaf Ali Marg, New Delhi, 110067, India

<sup>3</sup>Department of Physics, University of Calicut, Calicut 673653, India

<sup>4</sup>Department of Nuclear Physics, Andhra University, 530003, India

<sup>5</sup>Department of Physics, Delhi University, Delhi 110007, India

<sup>6</sup>Department of Physics, Panjab University, Chandigarh 160014, India

<sup>7</sup>Department of Physics, Karnatak University, Dharwad, 580003, India

Study of evaporation residue (ER) cross section provides valuable information about the formation and decay of the compound nucleus in heavy ion collisions. ER cross sections have been measured for the  $^{35,37}\text{Cl}+^{181}\text{T}$  reactions populating  $^{216,218}\text{Th}$  in the laboratory energy (after correcting the energy loss) range 169.7-235.9 MeV for the  $^{35}\text{Cl}$  beam and 170.3-236.6 MeV for the  $^{37}\text{Cl}$  beam using LINAC+Pelletron accelerator and there coil mass separator HYRA [1] at IUAC. Pulsed beams with  $2\mu\text{s}$  pulse separation were used to bombard the  $^{181}\text{T}$  target of thickness  $170\mu\text{g}/\text{cm}^2$  on  $20\mu\text{g}/\text{cm}^2$  carbon backing.

The gas-filled mode of HYRA (first stage) with He gas at 0.15 Torr was used for the ER cross section measurements in this work. In the focal plane chamber, a position sensitive MWPC of active area  $6\times 2\text{ inch}^2$  followed by a strip detector of active area  $2.4\times 2.4\text{ inch}^2$  we reused to detect the ERs reaching the focal plane. Two monitor detectors mounted at  $25^\circ$ , on either side, with respect to the beam direction inside the target chamber were used to record the Rutherford-scattered beam-like particles. These elastic events were used for absolute cross section normalization. A time-of-flight (TOF) spectrum was generated by taking the MWPC anode signal as start and RF signal as stop, which enabled unambiguous separation of the ERs from the beam-like and target-like contaminants. The TOF versus energy loss spectrum for  $^{35}\text{Cl}+^{181}\text{T}$  reaction for 205.3 MeV is shown in Fig. 19. The HYRA transmission efficiency was obtained using the calibration reaction  $^{30}\text{Si}+^{186}\text{W}$  [2] and TERS code [3] following the method discussed in Ref. [4].

The total ER cross section as a function of center-of-mass energy are shown in Fig. 20. Present measurements indicate similar trends in ER cross sections for both reactions populating  $^{216,218}\text{Th}$ , contradicting the results reported in Ref. [5] & [6]. The detailed theoretical calculations are in progress.

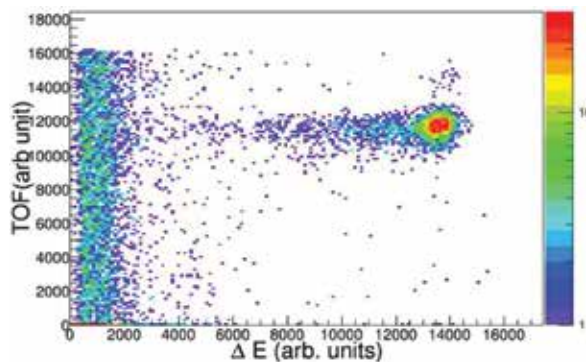


Fig. 19: The  $\Delta E$  versus TOF spectrum of  $^{35}\text{Cl}+^{181}\text{Ta}$  at 205.3 MeV beam energy.

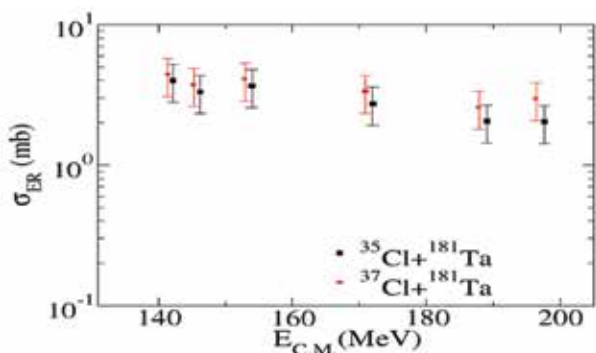


Fig. 20: ER cross section for  $^{35,37}\text{Cl}+^{181}\text{Ta}$  reaction.

## REFERENCES

- [1] N.Madhavan *et al.*, *Pramana***81**, 317 (2010).
- [2] A. C. Berrimean *et al.*, *Nature(London)* **413**, 144 (2001).
- [3] S.Nath, *Comput. Phys. Commun.* **179**, 492 (2008).
- [4] E.Prasad *et al.*, *Phy. Rev C***84**, 064606 (2011).
- [5] S.Mitsuoka *et al.*, *Phys. Rev. C***62**, 054603 (2000).
- [6] B.B.Back *et al.*, *Phy. Rev C***60**, 044602 (1999).

### 5.1.9 Measurement of mass-gated neutron multiplicity for nuclei near super-heavy region

Meenu Thakur<sup>1</sup>, B. R. Behera<sup>1</sup>, Ruchi Mahajan<sup>1</sup>, N. Saneesh<sup>2</sup>, Gurpreet Kaur<sup>1</sup>, Priya Sharma<sup>1</sup>, R. Dubey<sup>2</sup>, Kushal Kapoor<sup>1</sup>, A. Yadav<sup>2</sup>, Neeraj Kumar<sup>3</sup>, S. Kumar<sup>4</sup>, Kavita Rani<sup>1</sup>, P. Sugathan<sup>2</sup>, A. Jhingan<sup>2</sup>, A. Chatterjee<sup>2</sup>, M.B. Chatterjee<sup>2</sup>, S. Mandal<sup>3</sup>, A. Saxena<sup>5</sup> and S. Kailas<sup>5</sup>

<sup>1</sup>Department of Physics, Panjab University, Chandigarh 160014, India

<sup>2</sup>Inter University Accelerator Centre, Aruna Asaf Ali Marg, New Delhi 110067, India

<sup>3</sup>Department of Physics and Astrophysics, University of Delhi 110007, India

<sup>4</sup>Department of Nuclear Physics, Andhra University 530003, India

<sup>5</sup>Nuclear Physics Division, Bhabha Atomic Research Centre, Mumbai 400085, India

To understand the reaction mechanism of fusion-fission and quasi-fission processes, mass distributions, mass-energy distributions and mass-gated neutron multiplicities have been measured for the system  $^{48}\text{Ti}+^{208}\text{Pb}$ , populating the near super-heavy compound nucleus  $^{256}\text{Rf}$  at an excitation energy of 56.4 MeV. These measurements have been carried out with  $^{48}\text{Ti}$  beam from 15UD Pelletron+LINAC booster using NAND [1] facility at IUAC. Thin  $^{208}\text{Pb}$  target of thickness  $250 \mu\text{g}/\text{cm}^2$  with carbon backing of thickness  $20 \mu\text{g}/\text{cm}^2$  were kept at the center of a thin-walled (4 mm thickness) spherical scattering chamber. The target ladder was tilted to an angle of  $40^\circ$  with respect to the beam axis in order to minimize the shadowing to position-sensitive multi-wire proportional counters (MWPC). Neutrons were detected using 100 organic liquid scintillators (BC501A) in coincidence with the fission fragments detected using two large area ( $5''\times 3''$ ) MWPCs. MWPCs were kept at folding angle of  $127^\circ$  and at distance of 25 cm from the target. Along with this, two silicon surface barrier detectors (SSBD), kept at  $\pm 13.5^\circ$  with respect to the beam direction on either side, were used to monitor the beam flux. All the detector signals were acquired by using VME based data acquisition system. A fission fragment detected in any of the MWPCs in coincidence with RF was used as trigger for list mode data collection with LAMPS as the acquisition software. The neutron TOF was converted to neutron energy by considering the prompt gamma peak in the TOF spectrum as the time reference. Efficiency correction for the neutron detectors was performed using FLUKA [2] code.

The main motive of the data analysis was to measure mass distributions and total kinetic energy (TKE) of the binary fragments and to correlate them with the number of emitted neutrons. The velocity vectors of the detected fragments were constructed using the measured TOF and emission polar and azimuthal angles ( $\theta$ ,  $\phi$ ). From these

velocity vectors, masses and kinetic energies [3] of fission fragments were calculated assuming binary kinematics, linear momentum and mass conservation relationships. Mass distribution is shown on the left panel of Fig. 21. The right panel of Fig. 21 indicates obtained mass-energy distribution, where central region corresponds to symmetric and asymmetric fission and side wings describe projectile-like and target-like fragments, respectively. Since FF and QF events may result in similar mass distributions with significant yield in symmetric mass region, one can identify the contribution of the fusion-fission through neutron multiplicities in correlation with binary fragments. For this purpose, we have analysed the neutron data by dividing the mass-TKE distribution into three different mass splits: symmetric ( $A_{FF} = A_{CN}/2 \pm 20$ ), asymmetric ( $68 < A_{FF} < 108$ ) and projectile like fragments (PLF) ( $38 < A_{FF} < 68$ ).

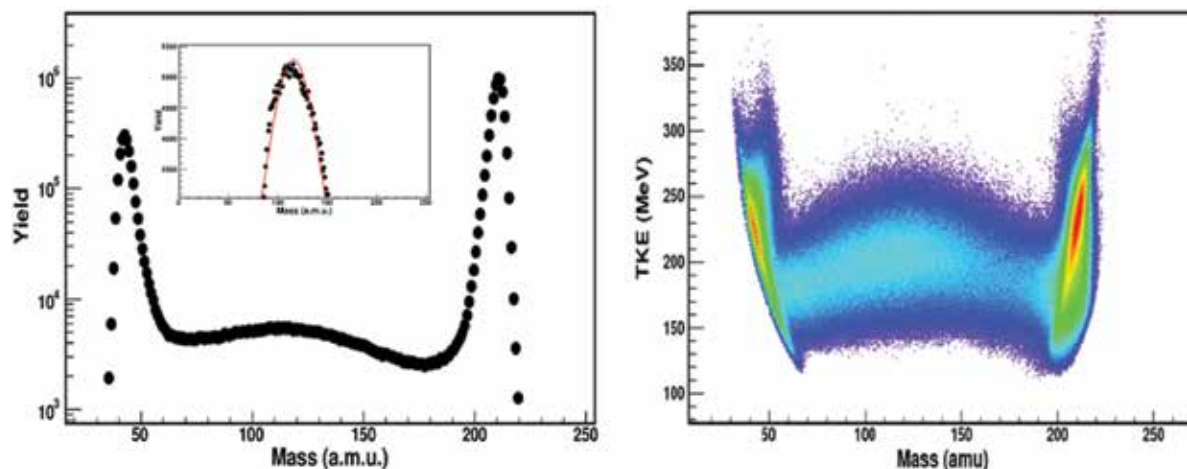


Fig. 21: Mass distribution of Fission fragments (left panel) and mass vs TKE scatter plot (right panel).

The observed neutron energy spectra were fitted with three moving source components to obtain the correct pre-scission and post-scission neutron multiplicities. The theoretical expression for the total neutron energy spectrum can be given as the sum of all three sources in the form:

where  $E_n$  is the measured neutron energy in the laboratory frame and  $A_i$ ,  $E_i$ ,  $T_i$ ,  $M_{ni}$  are mass, energy, temperature and multiplicity of the neutron emitting source.  $\theta_i$  is the angle between the neutron and its emitting source. The angular acceptance of both neutron detectors and fission detectors were taken into consideration in fitting procedure. In addition, to avoid angular uncertainty caused by the finite size of fission detectors, MWPC was sliced into four pieces.  $T_i$ ,  $M_{ni}$  are free parameters of the fits.

**Table 5.1.1 : Neutron multiplicity as a function of mass of fission fragments.**

	<b>PLF mass cut</b> $38 < A_{FF} < 68$	<b>Asymmetric mass cut</b> $68 < A_{FF} < 108$	<b>Symmetric mass cut</b> $A_{FF} = A_{CN}/2 \pm 20$
$v_{pre}$	$0.10 \pm 0.02$	$1.76 \pm 0.22$	$2.28 \pm 0.06$
$v_{FF1}$	$0.06 \pm 0.01$	$1.86 \pm 0.09$	$2.99 \pm 0.05$
$v_{FF2}$	$0.15 \pm 0.01$	$3.35 \pm 0.13$	$2.99 \pm 0.05$
$v_{total} = v_{pre} + v_{FF1} + v_{FF2}$	$0.31 \pm 0.09$	$6.91 \pm 0.27$	$8.26 \pm 0.09$

This analysis was done using ROOT software and fitting was done using MINUIT. The extracted values of multiplicity, corresponding to each mass cut are given in Table 5.1.1. From Table 5.1.1, one can observe that  $v_{\text{total}}$  increases from  $0.31 \pm 0.09$  to  $8.26 \pm 0.09$  while moving from PLF to symmetric mass cut. Similarly,  $v_{\text{pre}}$  increases going from PLF to symmetric mass cut indicating an increase of the available excitation energy.

## REFERENCES

- [1] P. Sugathan *et al.*, *Pramana* **83**, 807 (2014).
- [2] FLUKA, A multi particle transport code, CERN.
- [3] D. J. Hinde *et al.*, *Phys. Rev. C* **53**, 1290 (1996).

### 5.1.10 Study of the fission dynamics of $^{192,202}\text{Po}$ using NAND facility

Ruchi Mahajan<sup>1</sup>, B. R. Behera<sup>1</sup>, Meenu Thakur<sup>1</sup>, N. Saneesh<sup>2</sup>, Gurpreet Kaur<sup>1</sup>, Priya Sharma<sup>1</sup>, Kushal Kapoor<sup>1</sup>, R. Dubey<sup>2</sup>, A. Yadav<sup>2</sup>, Neeraj Kumar<sup>3</sup>, P. Sugathan<sup>2</sup>, A. Jhingan<sup>2</sup>, Hardev Singh<sup>4</sup>, A. Kumar<sup>1</sup>, A. Saxena<sup>5</sup>, A. Chatterjee<sup>2</sup> and Santanu Pal<sup>6,\*</sup>

<sup>1</sup>Department of Physics, Panjab University, Chandigarh 160014, India

<sup>2</sup>Inter University Accelerator Centre, Aruna Asaf Ali Marg, New Delhi 110067, India

<sup>3</sup>Department of Physics and Astrophysics, University of Delhi, Delhi 110007, India

<sup>4</sup>Department of Physics, Kurukshetra University, Kurukshetra 136119, India

<sup>5</sup>Nuclear Physics Division, Bhabha Atomic Research Centre, Mumbai 400085, India

<sup>6</sup>CS-6/1, Golf Green, Kolkata 700095, India

\*Formerly with Variable Energy Cyclotron Centre, Kolkata

For nuclear reactions with heavy systems, along with fusion-fission (FF) process there is significant contribution from non-compound nuclear processes such as quasi-fission (QF) [1]. Several experimental as well as theoretical approaches have been adopted to understand the dynamics of FF process in heavy nuclei. It is well established that the pre-scission neutron multiplicity is one of the most efficient probes to study the dynamics of heavy-ion induced fusion-fission (FF) reactions [2]. Measurement of pre-scission neutron multiplicities from an isotopic chain will be a suitable tool to disentangle FF and QF processes. This is because FF and QF reactions have their own characteristic reaction times implying that each reaction process is associated with different pre-scission neutron multiplicity. With this motivation, we have measured pre-scission neutron multiplicities from two compound nuclei, namely,  $^{192,202}\text{Po}$ , populated using  $^{48}\text{Ti}+^{144,154}\text{Sm}$  systems at 260 and 230 MeV of laboratory energy using National Array of Neutron Detectors (NAND) facility at IUAC. This experiment was performed using 15 UD Pelletron+LINAC facility of IUAC. Pulsed beam of  $^{48}\text{Ti}$  having pulse separation of 250 ns was bombarded on sandwiched targets of  $^{144,154}\text{Sm}$  of thickness 250 and 270  $\mu\text{g}/\text{cm}^2$ , respectively. Targets were placed at the centre of a thin-walled, spherical scattering chamber of 1 m diameter. Fission fragments were detected using a pair of multi-wire proportional counters (MWPCs) (6.4'' $\times$ 4.4'') kept at fission fragment folding angle of  $\pm 60^\circ$  on both sides with respect to the beam direction, at a distance of 30 cm from the target. Two silicon PIPS detectors were also placed inside the chamber at  $\pm 13^\circ$  with respect to the beam direction for beam monitoring. The neutrons emitted were detected by an array of 100 organic liquid scintillators (BC501A) of dimension 5'' $\times$ 5'' mounted on a geodesic dome structure with both in-plane and out-of-plane positions having a flight path of 175 cm [3]. Hardware thresholds were adjusted to 0.5 MeV neutron energy using  $^{137}\text{Cs}$  and  $^{60}\text{Co}$  sources. The trigger of the data acquisition was generated by setting up a coincidence between RF of the beam pulse and either of the fission detectors. VME based data acquisition using LAMPS software was used to acquire event mode data. The pre- and post-scission components of neutron multiplicities are obtained from the measured neutron energy spectra by using a multiple source least-square fitting procedure, using the Watt expression [4]. The fitted energy spectra from one of the neutron detectors are shown in Fig. 22.

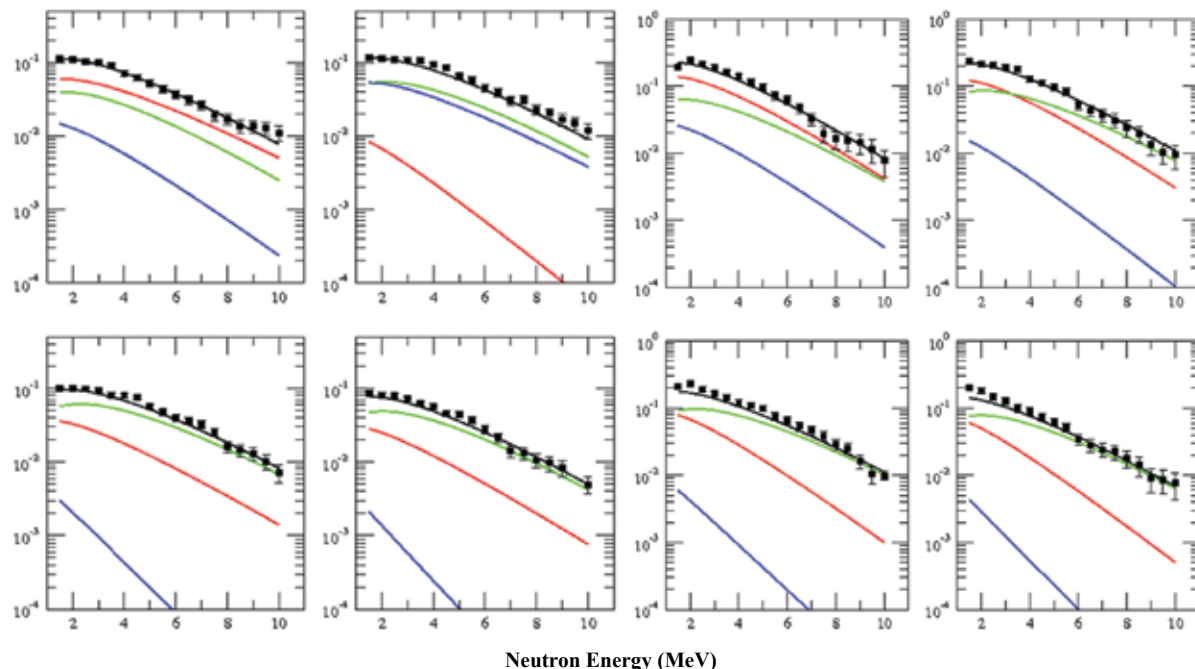


Fig. 22: Neutron multiplicity spectra for  $^{48}\text{Ti}+^{144,154}\text{Sm}$  system at 70 MeV of excitation energy for six of the neutron detectors. The fits for the pre-scission (dashed-dotted line) and post-scission contribution from one fragment (dotted line) and that from the other fragment (dashed line) are shown. The solid black line represents the sum of the different contributions.

The measured neutron multiplicities are further analyzed with the statistical model of nuclear decay using Bohr Wheeler as well as Kramer's formalism [5]. The disagreement of the statistical model results with the experimental values even at higher  $\beta$  value may point towards the presence of QF and fast-fission.

## REFERENCES

- [1] D. Jacquet *et al.*, Nucl. Phys. A **63**, 155 (2009).
- [2] D. J. Hinde *et al.*, Phys. Rev. C **39**, 2268 (1989).
- [3] P. Sugathan, Proc. DAE Symp. Nucl. Phys. **58**, 37 (2013).
- [4] A. Saxena *et al.*, Phys. Rev. C **49**, 932 (1994).
- [5] Jhilam Sadhukhan and Santanu Pal, Phys. Rev. C **79**, 019901 (2009).

### 5.1.11 Probing quasi-fission in reactions forming Rn nucleus

A. Shamlath<sup>1</sup>, E. Prasad<sup>1</sup>, P. V. Laveen<sup>1</sup>, N. Madhavan<sup>2</sup>, J. Gehlot<sup>2</sup>, A. M. Vinod Kumar<sup>3</sup>, S. Nath<sup>2</sup>, M. Shareef<sup>1</sup>, Tathagata Banerjee<sup>2</sup>, A. Jhingan<sup>2</sup>, T. Varughese<sup>2</sup>, D.V.G.R.K.S. Kumar<sup>4</sup>, P. Sandya Devi<sup>4</sup>, Khushboo<sup>5</sup>, P. Jisha<sup>3</sup>, Neeraj Kumar<sup>5</sup>, M. M. Hosamani<sup>6</sup> and S. Kailas<sup>7</sup>

<sup>1</sup> Department of Physics, Central University of Kerala, Nilleshwar 671314, India

<sup>†</sup> Department of Nuclear Physics, Australian National University, Canberra ACT, Australia

<sup>2</sup> Inter University Accelerator Centre, Aruna Asaf Ali Marg, New Delhi 110067, India

<sup>3</sup> Department of Physics, University of Calicut, Calicut 673635, India

<sup>4</sup> Department of Nuclear Physics, Andhra University 530003, India

<sup>5</sup> Department of Physics Astrophysics, University of Delhi, Delhi 110007, India

<sup>6</sup> Department of Physics, Karnatak University, Dharwad 580003, India

<sup>7</sup> UM-DAE Centre for Excellence in Basic Sciences, University of Mumbai, Mumbai 400098, India

The ER excitation function measurements were performed using the pulsed beams from the 15UD Pelletron+LINAC accelerator facility at IUAC.  $^{28,30}\text{Si}$  beams with pulse separation of 2  $\mu\text{s}$  were used to bombard the isotopically

enriched  $^{180}\text{Hf}$  target of thickness  $150 \mu\text{g}/\text{cm}^2$  on  $40 \mu\text{g}/\text{cm}^2$  thick carbon backing. The ER cross sections were measured for the  $^{30}\text{Si}+^{180}\text{Hf}$  and  $^{28}\text{Si}+^{180}\text{Hf}$  reactions in the beam energy range 138.7 to 178.8 MeV and 138.4 to 200.0 MeV, respectively. ERs were separated from the intense beam background using HYbrid Recoil mass Analyzer (HYRA) [1]. Two silicon detectors were used inside the target chamber, placed at  $\theta = 25^\circ$  on either side of the beam direction, to detect the Rutherford-scattered beam-like particles for absolute normalization of ER cross sections. These detectors were also used for positioning the beam at the centre of the target. The ERs reaching the focal plane were detected using a position sensitive, multi wire proportional counter (MWPC) of active area 6 inch  $\times$  2 inch followed by a silicon strip detector of active area 2.4 inch  $\times$  2.4 inch. A time-of-flight (TOF) spectrum was generated with the timing pulse from the MWPC anode as start and the radio frequency (RF) signal, delayed suitably, as stop. The energy loss ( $\Delta E$ ) vs TOF spectrum helped in unambiguous identification of ERs from the beam-like and the target-like contaminations. Fig. 23(a) shows the two-dimensional plot of  $\Delta E$  versus TOF for the reaction  $^{28}\text{Si}+^{180}\text{Hf}$  at 138.4 MeV beam energy.

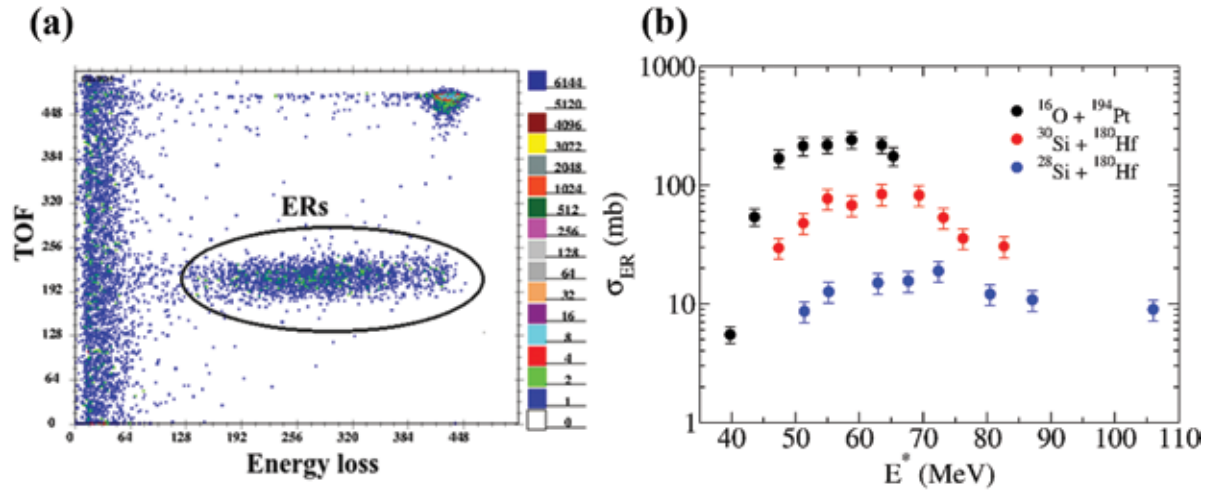


Fig. 23: (a) Two-dimensional plot of  $\Delta E$  vs TOF for the reaction  $^{28}\text{Si}+^{180}\text{Hf}$  at 138.4 MeV beam energy and (b) the experimental ER cross sections for the  $^{16}\text{O}+^{194}\text{Pt}$  and  $^{28,30}\text{Si}+^{180}\text{Hf}$  reactions as a function of  $E^*$ .

Total ER cross sections ( $\sigma_{\text{ER}}$ ) were calculated using the relation [2]  $\sigma_{\text{ER}} = \frac{Y_{\text{ER}}}{Y_{\text{mon}}} \left( \frac{d\sigma}{d\Omega} \right)_R \Omega_M \frac{1}{\varepsilon_{\text{HYRA}}}$ . We

calculated  $\varepsilon_{\text{HYRA}}$  using  $^{30}\text{Si} + ^{186}\text{W}$  reaction [3] as the calibration system following the method described in Ref. [2]. The ER angular distributions for the two reactions were simulated using TERS [4] and were compared within the angular acceptance of HYRA. Fig. 23(b) shows the total ER cross sections of the present measurements compared with that of  $^{16}\text{O}+^{194}\text{Pt}$ , populating the compound nucleus  $^{210}\text{Rn}$  at similar excitation energies. Reduction in ER cross sections in more symmetric systems and the larger fission fragment mass widths reported [5] in the  $^{30}\text{Si}+^{180}\text{Hf}$  reaction compared with the  $^{16}\text{O}+^{194}\text{Pt}$  reaction clearly demonstrate the presence of quasi-fission in Si+Hf reactions.

## REFERENCES

- [1] N. Madhavan *et al.*, *Pramana - J. Phys.* **75**, 317 (2010).
- [2] E. Prasad *et al.*, *Phys. Rev. C* **84**, 064606 (2011).
- [3] D. J. Hinde *et al.*, *J. Nucl. Radiochem. Sci.* **3**, 31 (2002).
- [4] S. Nath, *Comput. Phys. Commun.* **180**, 2392 (2009).
- [5] A. Shamlath *et al.*, *Nucl. Phys. A* **945**, 67 (2016).

### 5.1.12 Quasi-elastic scattering measurements for $^{48}\text{Ti}+^{232}\text{Th}$ system leading to super-heavy element $^{280}\text{Cn}$

Gurpreet Kaur<sup>1</sup>, B. R. Behera<sup>1</sup>, A. Jhingan<sup>2</sup>, R. Dubey<sup>2</sup>, T. Banerjee<sup>2</sup>, N. Saneesh<sup>2</sup>, Meenu Thakur<sup>1</sup>, Ruchi Mahajan<sup>1</sup>, Priya Sharma<sup>1</sup>, Khushboo<sup>3</sup>, A. Yadav<sup>2</sup>, Kushal Kapoor<sup>1</sup>, N. Kumar<sup>3</sup>, Kavita<sup>1</sup>, B. K. Nayak<sup>4</sup>, A. Saxena<sup>4</sup> and P. Sugathan<sup>2</sup>

<sup>1</sup>Department of Physics, Panjab University, Chandigarh 160014, India

<sup>2</sup>Inter University Accelerator Centre, Aruna Asaf Ali Marg, New Delhi 110067, India

<sup>3</sup>Department of Physics and Astrophysics, Delhi University, New Delhi 110067, India

<sup>4</sup>Nuclear Physics Division, Bhabha Atomic Research Centre, Mumbai 400085, India

The existence of super-heavy elements (SHE) has been confirmed through nuclear fusion reactions [1]. Classically, for fusion to occur, the incident particle has to overcome the fusion barrier. As the choice of target-projectile combination and the bombarding energy greatly influence the fusion probability, the quantitative information of the fusion barrier plays a vital role in the synthesis of SHE. In case of heavy systems, because of coupling to many degrees of freedom, the single uncoupled barrier splits to distribution of barriers called barrier distribution (BD). Here, average value of the distribution gives the fusion barrier, which may be different from the theoretically proposed values. To extract the BD, one has to measure the fusion cross section and take second derivative of its product with energy with respect to energy [2]. However, for heavy systems, due to very low cross sections ( $\sim$ nb), measuring the fusion cross section is a very time consuming process. Hence, the remedial complementary way to do the same is through first derivative of the quasi-elastic (QE) cross section [3]. In the present study, we have performed the quasi-elastic scattering measurements for the  $^{48}\text{Ti}+^{232}\text{Th}$  system leading to super heavy element,  $^{280}\text{Cn}$ . The aim is to extract the information about the fusion barrier from experimental BD and study the role of nuclear structure in the reaction dynamics.

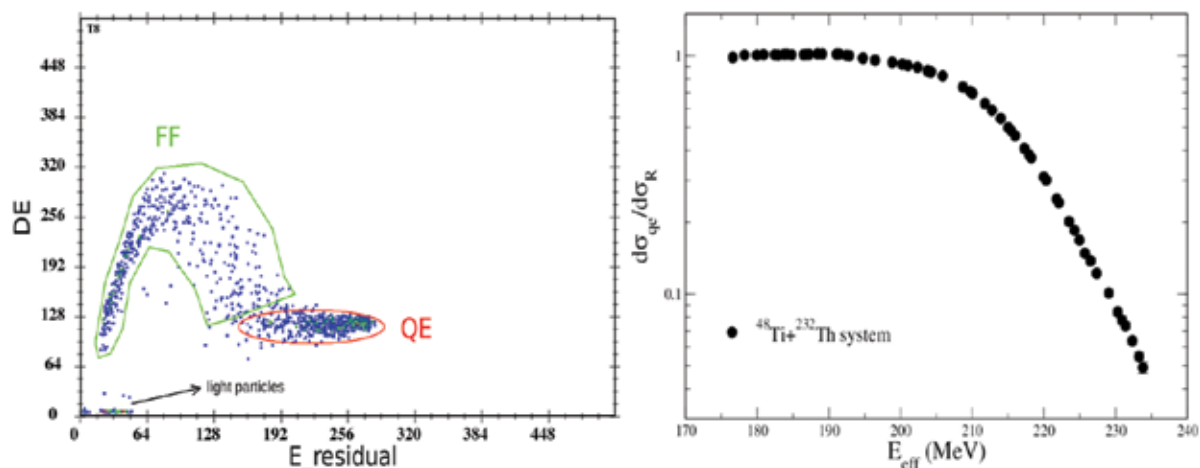


Fig. 24 : E- $\Delta E$  spectrum obtained at lab angle of  $120^\circ$  with respect to beam direction for beam energy  $E_{\text{lab}} = 275\text{MeV}$ (left)and the extracted quasi-elastic excitation functions suitably normalized(right).

Measurements were performed in the National Array of Neutron Detectors (NAND) Chamber using LINAC boosted  $^{48}\text{Ti}$  beam from 15UD Pelletron at IUAC. The target of  $^{232}\text{Th}$  having typical thickness  $\sim 150\ \mu\text{g}/\text{cm}^2$  with carbon backing of thickness  $\sim 30\ \mu\text{g}/\text{cm}^2$  was used. Measurements were performed employing a facility of sixteen hybrid telescope detectors (HYTAR) consisting of gas ionisation ( $\Delta E$ ) and silicon (E) detectors [4]. Four telescopes, two in-plane and two out-of-plane, each at an angle of  $173^\circ$ , were placed in a ring arrangement for the QE measurements at backward angles. Eight telescopes were placed at angles from  $160^\circ$  to  $90^\circ$  with an angular pitch of  $10^\circ$ . Other four telescopes were placed at angles of  $105^\circ$  to  $75^\circ$  with an angular pitch of  $10^\circ$ . The spectra were recorded in the bombarding energy range from 220 to 280 MeV in steps of 5 MeV. Two silicon surface barrier detectors of thickness  $300\ \mu\text{m}$  were positioned at  $\pm 130^\circ$  with respect to the beam direction to monitor the beam and to determine the absolute values of the cross sections. For all the detectors, home-made pre-amplifiers were used in vacuum to improve the signal to noise ratio.

Typical particle identification spectrum obtained for the  $^{48}\text{Ti}+^{232}\text{Th}$  reaction at  $\theta_{\text{lab}} = 120^\circ$  for  $E_{\text{lab}} = 275\ \text{MeV}$  has been shown in the left panel of Fig. 24. For such a heavy system, probability of fission is very high at energies above the Coulomb barrier. It can be observed from the Figure that QE events, which are sum of all peripheral

processes (elastic, in-elastic and transfer etc.), are well separated from fission events (FF). The right panel of Fig. 24 shows the excitation function as a function of  $E_{\text{eff}}$ , where  $E_{\text{eff}} = 2E_{\text{c.m.}}/(1+\text{cosec}(\theta_{\text{c.m.}}/2))$  corrects for centrifugal effects. In addition to it, the angular distributions of the QE events at energies from 220 to 280 MeV in steps of 5 MeV were also measured. The measured QE events will be used to extract the experimental BD for the  $^{48}\text{Ti}+^{232}\text{Th}$  system. From angular distribution measurements, the nuclear potential parameters will be extracted.

## REFERENCES

- [1] J. Khuyagbaatar *et al.*, Phys. Rev. Lett. **112**, 172501 (2014).
- [2] M. Dasgupta *et al.*, Annu. Rev. Nucl. Part. Sci. **48**, 401(1998).
- [3] H. Timmers *et al.*, Nucl. Phys. A **584**, 190 (1995).
- [4] A. Jhingan *et al.*, Proc. DAE Symp. Nucl. Phys. **59**, 830 (2014).

### 5.1.13 Shell closure and target deformation effects probed using evaporation residue cross section and spin distribution measurements

Priya Sharma<sup>1</sup>, B. R. Behera<sup>1</sup>, N. Madhavan<sup>2</sup>, I. Mazumdar<sup>3</sup>, Ruchi Mahajan<sup>1</sup>, Meenu Thakur<sup>1</sup>, Gurpreet Kaur<sup>1</sup>, Kushal Kapoor<sup>1</sup>, Kavita Rani<sup>1</sup>, J. Gehlot<sup>2</sup>, S. Nath<sup>2</sup>, M. Dhibar<sup>5</sup>, S. M. Patel<sup>3</sup>, M. M. Hosamani<sup>4</sup>, Khushboo<sup>6</sup>, R. Dubey<sup>2</sup>, A. Shamlath<sup>7</sup>, N. Kumar<sup>6</sup>, G. Mohanto<sup>8</sup> and S. Pal<sup>9,\*</sup>

<sup>1</sup>Department of Physics, Panjab University, Chandigarh 160014, India

<sup>2</sup>Inter University Accelerator Centre, Aruna Asaf Ali Marg, New Delhi 110067, India

<sup>3</sup>Tata Institute of Fundamental Research, Mumbai 400005, India

<sup>4</sup>Department of Physics, Karnatak University, Dharwad 580003, India

<sup>5</sup>Department of Physics, Indian Institute of Technology Roorkee 247667, India

<sup>6</sup>Department of Physics and Astrophysics, University of Delhi 110007, India

<sup>7</sup>Department of Physics, Central University of Kerala, Kasaragod 671314, India

<sup>8</sup>Nuclear Physics Division, Bhabha Atomic Research Centre, Mumbai 400085, India

<sup>9</sup>CS-6/1 Golf Green, Kolkata 700095, India

\*Formerly with Variable Energy Cyclotron Centre, Kolkata

For understanding the shell closure and target deformation effects in the formation and survival of a heavy compound nucleus (CN), we have performed the evaporation residue (ER) cross-section and spin distribution measurements for the (i)  $^{48}\text{Ti}+^{150}\text{Nd}\rightarrow^{198}\text{Pb}$ , (ii)  $^{48}\text{Ti}+^{142}\text{Nd}\rightarrow^{190}\text{Pb}$  and (iii)  $^{48}\text{Ti}+^{144}\text{Sm}\rightarrow^{192}\text{Po}$  systems leading to compound nuclei around  $Z_{\text{CN}}=82$ . Here, we investigate the effect of proton shell closure  $Z_{\text{CN}}=82$  and target deformation effects through the ER cross-section and ER gated spin distribution measurements. It is conjectured that [1] proton shell closure  $Z_{\text{CN}}=82$  may lead to enhanced ER production and may help in the synthesis of heavy nuclei. Such effect can be deciphered by studying the high-spin region of spin distributions. A clear signature would be enhancement of the high spin part of the ER spin distributions. A high spin population may also be possible due to target deformation effect. Shell effects are expected to affect the survival probability in a fusion-fission reaction.

The experiments were carried out using HYbrid Recoil mass Analyzer (HYRA) [2] + TIFR 4 $\pi$  spin spectrometer [3] and the 15 UD Pelletron + LINAC facility at IUAC. ER cross-section measurements were performed using pulsed  $^{48}\text{Ti}$  beam with 1  $\mu\text{s}$  pulse separation at laboratory energies ranging from 185 - 270 MeV (taking into account the energy loss from 650  $\mu\text{g}/\text{cm}^2$  carbon window foil and half thickness of target) with an average current of 0.5 pA. Thin, isotopically enriched, targets of  $^{150,142}\text{Nd}$  (thickness = 150  $\mu\text{g}/\text{cm}^2$  and 100  $\mu\text{g}/\text{cm}^2$ , respectively) and  $^{144}\text{Sm}$  (thickness = 120  $\mu\text{g}/\text{cm}^2$ ) sandwiched [4] between two very thin carbon layers were used in the experiment. Two silicon surface barrier detectors (SSBD) were placed inside the target chamber and kept at 45 mm from the target, at angles of  $\pm 25^\circ$ . The helium gas pressure in the gas-filled mode of HYRA was set at 0.3 Torr. The ERs were separated from the other contaminants using HYRA and were detected by a position sensitive multi wire proportional counter (MWPC) of dimension 6 inch  $\times$  2 inch followed by a strip detector of dimension 6 cm  $\times$  6 cm at the focal plane. The spin distribution measurements were carried out using the TIFR 4 $\pi$  spin spectrometer

consisting of 29 NaI detectors. A time of flight (TOF) spectrum was generated using anode of MWPC as start and RF of beam as stop. A time to amplitude (TAC) spectrum was generated using MWPC anode as a start and timing OR as a stop. A two dimensional plot was generated using TOF and energy loss ( $\Delta E$ ) signal of MWPC which provided clean separation of ERs, as shown in Fig. 25.

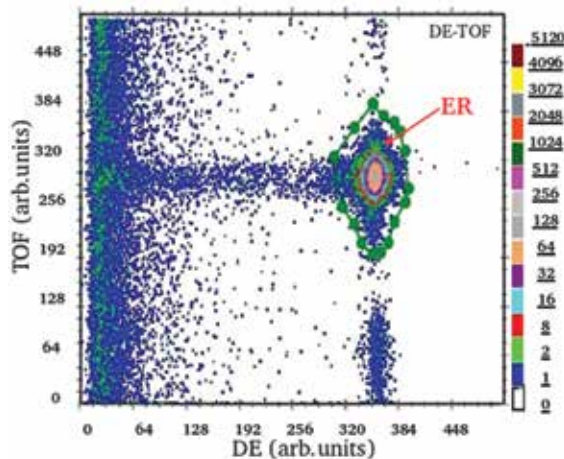


Fig. 25 : Two-dimensional spectrum of  $\Delta E$  (cathode) vs TOF for  $^{48}\text{Ti}+^{150}\text{Nd}$  at  $E_{\text{lab}} = 208.3$  MeV.

For measurement of transmission efficiency of HYRA, we performed calibration run of the reaction  $^{48}\text{Ti}+^{122}\text{Sn}$ . Experimentally extracted efficiency of HYRA for the reaction  $^{48}\text{Ti}+^{122}\text{Sn}$  was 28.7% ( $\pm 6\%$ ). The ER angular distribution was calculated using the semi-microscopic Monte Carlo simulation code TERS [5] and compared within the angular acceptance of HYRA ( $9.5^\circ$  half angle). The efficiency value of the calibration reaction was further normalized for the other systems to obtain the ER cross-sections. The ER excitation functions for  $^{48}\text{Ti}+^{150,142}\text{Nd}$ ,  $^{144}\text{Sm}$  systems are shown in Fig. 26.

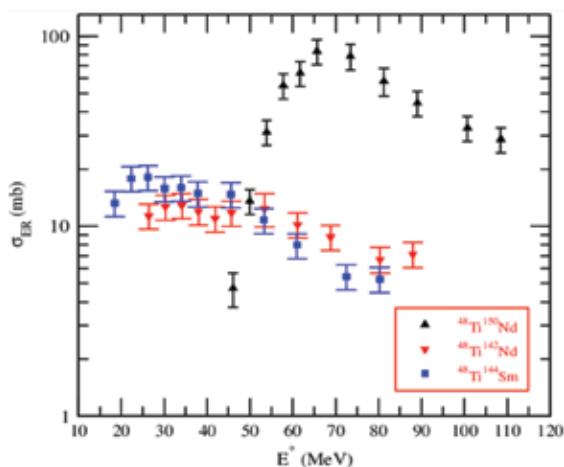


Fig. 26 : ER cross-section for  $^{48}\text{Ti}+^{150}\text{Nd}$ ,  $^{48}\text{Ti}+^{142}\text{Nd}$  and  $^{48}\text{Ti}+^{144}\text{Sm}$  systems as a function of excitation energy.

Statistical model calculations were performed using Bohr-Wheeler (BW) formalism [6] for  $\Gamma_f$  including shell correction in the level density and the fission barrier. In the input, macro-micro model was incorporated using calculated values of fission barrier [7]. We performed CCFULL calculations at every energy point and fitted the fusion excitation function by adjusting the potential parameters  $V_0$ ,  $r_0$  and  $a_0$  where,  $V_0$  is the depth parameter of the Woods-Saxon potential,  $r_0$  is the radius parameter and  $a_0$  is the surface diffuseness parameter. The CN spin distributions obtained from CCFULL calculations, at each energy, was subsequently used as the input in the statistical model code. Subsequently, we performed the statistical model calculations and adjusted  $k_f$  to reproduce the ER cross-sections. Further analysis is in progress.

## REFERENCES

- [1] D. Ackermann *et al.*, Eur. Phys. J. A **20**, 151 (2004).
- [2] N. Madhavan *et al.*, Pramana - J. Phys. **75**, 317 (2010).
- [3] G. Anil kumar *et al.*, Nucl. Instr. Meth. A **611**, 76 (2009).
- [4] P. Sharma *et al.*, Proc. Int. Symp. Nucl. Phys. **59**, 910 (2014).
- [5] S. Nath, Comput. Phys. Commun. **180**, 2392 (2009).
- [6] N. Bohr and J. A. Wheeler, Phys. Rev. **56**, 426 (1936).
- [7] P. Moller *et al.*, Phys. Rev. C **91**, 024310 (2015).

## 5.2 MATERIALS SCIENCE

A. Tripathi

The materials science research programmes in areas of ion beam induced materials modification and characterization are being carried out in a wide range of energies varying from tens of keV to hundreds of MeV. Studies on various type of materials: metallic, semi conducting and insulating and in different forms: nanostructures, thin film and bulk, are undertaken. This year there have been 58 user experiments with over 192 shifts and these included 21 runs spread over 71 shifts which were BTA experiments associated with students' Ph.D. programmes. The experiments are mostly performed in the irradiation chamber in the materials science beam lines in beam hall-I, though experiments utilizing in-situ XRD facility were performed in materials science beam line in beam hall-II and experiments requiring low fluence irradiation were performed in GPSC. The users also utilized various synthesis techniques and offline characterization facilities such as XRD, AFM, SEM, Raman, UV-Vis, I-V, Hall measurement.

It has been demonstrated that 80 MeV Ni ion irradiation results in significant enhancement in the photocatalytic efficiency of ZnO–CuO nanocomposites and has been attributed to improved sun light utilization and suppression of the recombination of photogenerated charge carriers. The robustness of the spontaneously formed superconducting order of NiBi<sub>3</sub> phase in thermally evaporated Ni-Bi bilayer film was demonstrated by unchanged transition temperature and upper critical field, up to an ion dose of 100 MeV Au ions. 150 MeV Ag<sup>+</sup> ions induced inter mixing in W/Si multilayers has been studied using in situ x-ray reflectivity to monitor the evolution of interface mixing and internal stresses and finite intermixing was observed even though the system has a positive heat of mixing. A systematic change in nature of charge carriers from p- to n-type in nitrogen doped zinc oxide (ZnO:N) thin films and about four orders of magnitude enhancement of n-type conductivity is reported with increase in the fluence of irradiation. Modification of magnetic anisotropy induced by swift heavy ion irradiation in cobalt ferrite thin was reported. Ion beam induced annealing; shifting of charge neutrality point in graphene and reduction of graphene oxide was also reported.

Low energy Ar ion irradiation on the optical properties of gold nanogratings and its application in biological sensing was demonstrated. The radiation stability of nano-crystalline cubic zirconia films was demonstrated under low energy irradiation. The sensitivity for cholesterol detection of the L-MMT electrode formed through H<sup>+</sup> ion implantation clearly exhibited a strong dependence on the fluence with possible applications in enzymes-free strip sensor. Influence of SHI irradiation on the surface and structural properties of C<sub>70</sub> fullerene and resulting increase

in hydrophobicity at lower fluencies is also shown. Low energy ion beams induced reduction of grapheme oxide and investigation of blistering process in Hydrogen implanted GaSb for a potential layer transfer application is shown. Effect of  $\text{Ag}^{9+}$  and  $\text{O}^{7+}$  ion irradiation on the structural and magnetic properties of FeGa thin films inducing magnetic anisotropy has been demonstrated.

Electronic excitation induced modifications of optical and morphological properties of PCBM thin films; structural, topographical and magnetic properties in zinc ferrite films; structure sensitive properties of Zr-based bulk amorphous alloys showing formation of nano-crystallites and phase change memory properties of SHI irradiated metal chalcogenide thin films are also studied. Irradiation temperature dependence of shape elongation of vanadium nanoparticles (V NPs) in silica was evaluated between 100 and 750 K after 120 MeV  $\text{Ag}^{9+}$  ion irradiation. SHI induced ion beam mixing occurs in  $\text{Pd}_{1-x}\text{Ni}_x$  alloy thin layer and Si is studied complimenting the earlier studies at keV energies.

In-situ investigation of 80 MeV N, 100 MeV P ion irradiation on the electrical characterizations of NPN *rf* power transistors, and subsequent degradation in electrical characteristics of advanced 200 GHz SiGe HBTs is shown. The studies included SHI induced radiation effects at Si/SiO<sub>2</sub> interface of MOS devices. Defects and junction characteristics of keV ion irradiated ZnO are studied Low temperature PL and XPS studies show significant increase of zinc interstitial ( $\text{I}_{\text{Zn}}$ ) related defects at high fluence and sharp decrease of its sheet resistance.

The 18<sup>th</sup> International Conference on Radiation Effects in Insulators (REI 18), which is one of the most prominent and long-running international conferences in the field of ion irradiation effects in materials conferences in the field of ion radiation effects in materials, was organized in Jaipur from 26<sup>th</sup> to 31<sup>st</sup> October 2015. The REI conference was held in India for the first time and was jointly organized by IUAC, New Delhi, MNIT, Jaipur and VGU, Jaipur. An International School on ‘Simulation of ion beam radiation effects on materials’ was also organised from 24<sup>th</sup> to 26<sup>th</sup> Oct 2015, in MNIT, Jaipur. The International Conference on Nanostructuring with ion beams (ICNIB), was organized in Agra from 23<sup>rd</sup> to 25<sup>th</sup> November 2015.

### 5.2.1 Study on SHI Induced Hydrogen Desorption from Porous Silicon Measured by Online ERDA

V.S. Vendamani<sup>1</sup>, Saif A. Khan<sup>2</sup>, M. Dhanunjaya<sup>1</sup>, A.P. Pathak<sup>1</sup> and S.V.S. Nageswara Rao<sup>1</sup>

<sup>1</sup>School of Physics, University of Hyderabad, Hyderabad, 500 046, India

<sup>2</sup>Inter-University Accelerator Centre, Aruna Asaf Ali Marg, New Delhi-110 067, India

Hydrogen is an important impurity in crystalline semiconductors, and its properties have been studied extensively both, experimentally and theoretically [1]. The most prominent property of hydrogen in semiconductor is its ability to passivate the deep and shallow defects [2]. Moreover, in silicon-based electronic and optoelectronic devices, hydrogen plays a significant role by eliminating the pre-existing dangling bonds. This improves the device performance and reliability by producing high quality Si-SiO<sub>2</sub> interfaces (eg. Si nanocrystals that are embedded in SiO<sub>2</sub>). In semiconductors, the elemental hydrogen is invariably incorporated during crystal growth or processing steps such as wafer polishing, wet chemical etching or reactive ion etching etc. [3]. The elemental H is one of the important and inevitable constituent elements present in the porous silicon. The porous silicon (pSi) is one of the silicon compatible photonic materials that can be used in the fields of information and communication technologies.

Hydrogen depth profiles and desorption from porous silicon (pSi) layers have been studied by online elastic recoil detection analysis (ERDA) by using high energy heavy (100 MeV Ag) ions [4]. p-type, B-doped (1-30 Ω-cm) single crystalline silicon (100) wafers were anodically etched for 15 min with the volumetric ratio of 1:1:2:: HF: H<sub>2</sub>O: ethanol solution at various current densities ( $J= 5, 10, 15, 20$  and  $25 \text{ mA/cm}^2$ ). The hydrogen depth profiles of pSi layers prepared at various etching current densities have been presented in Fig. 27(9). It is found that the concentration of H is more prominent in the near surface region and falls down significantly in the deeper layers. Further, to understand the desorption process of H present in the pSi layers as a function of irradiation fluence, a theoretical fitting has been done.

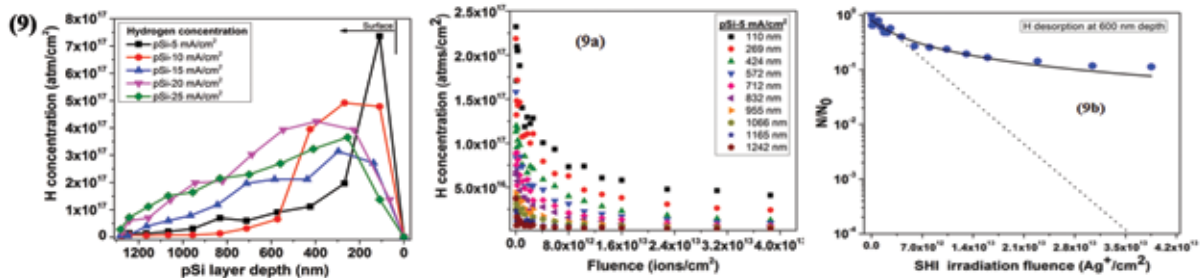


Figure 27 : (9) Depth profiles of hydrogen in pSi layers, (9a) H concentrations at diff. depths and (9b) Second-order and exponential decay fittings for desorption of hydrogen present in the pSi layer ( $J= 5\text{mA}/\text{cm}^2$ ) sample

Fig. 27 (9a) shows the concentration of H at different depths of pSi samples as a function of irradiation fluence. The energy loss by ionization/excitation of electrons under high energy ion irradiation is expected to cause non-thermal dissociation of Si-H bonds around pores in pSi. The solid line in Fig. 27(9b) represents a second order fit obtained by the eq.  $N/N_0 = 1/(1+B\phi)$ . Whereas the dashed line represents the exponential decay obtained by eq.  $N=N_0 \exp(-k\phi)$ . This implies that the hydrogen is leaving the pSi surface in molecular ( $\text{H}_2$ ) form. This is also consistent with the other observations mentioned above that the rate of decay is higher in deeper layers as compared to that of surface layers.

## REFERENCES

- [1] V. S. Vendamani, A. P. Pathak, and S. V. S. Nageswara Rao, Nucl. Inst. Meth. B **315** (2013) 188-1915.
- [2] S. V. S. Nageswara Rao, S. K. Dixit, G. Lüpke, N. H. Tolk and L. C. Feldman, Phys. Rev. B **75** (2007) 235202.
- [3] H. F. Arrand, T. M. Benson, P. Sewell and A. Loni, J. Lumin. **80** (1998) 199.
- [4] An Online ERDA Study on SHI-Induced Desorption of Hydrogen from Porous Silicon Prepared by Anodic Etching of H-implanted Silicon; V.S. Vendamani, Saif A. Khan, M. Dhanunjaya, A.P. Pathak, and S.V.S. Nageswara (under Review).
- [5] Study on SHI-Induced Hydrogen Desorption from Porous Silicon Measured by Online ERDA; V.S. Vendamani, Saif A. Khan, M. Dhanunjaya, A.P. Pathak, and S.V.S. Nageswara Rao (under consideration).

### 5.2.2 *In-situ* structural investigations on $(\text{La,Gd})\text{PO}_4$ solid solution series under swift heavy ion irradiation

S. Neumeier<sup>1</sup>, P.K. Kulriya<sup>2,3</sup>, Y. Arinicheva<sup>1</sup>, G. Deissmann<sup>1</sup>, D. Bosbach<sup>1</sup>

<sup>1</sup>Forschungszentrum Jülich GmbH; Institute of Energy and Climate Research – Nuclear Waste Management (IEK-6), 52425 Jülich, Germany

<sup>2</sup>Inter-University Accelerator Centre, Aruna Asaf Ali Marg, New Delhi-110 067, India

<sup>3</sup>Rensselaer Polytechnic Institute, Dept. of Mechanical, Aerospace & Nuclear Engineering, Troy, New York, USA

Phosphate based ceramics with monazite structure ( $\text{LnPO}_4$ ,  $\text{Ln} = \text{La} - \text{Gd}$ ) are considered as promising nuclear waste forms for the conditioning of trivalent actinides such as Pu(III). Radiation damages due to  $\alpha$ -decay of the incorporated radionuclide will cause damages in crystal structure and thus might affect the long-term stability of the waste form.

Single phase  $\text{La}_{0.2}\text{Gd}_{0.8}\text{PO}_4$  and  $\text{La}_{0.8}\text{Gd}_{0.2}\text{PO}_4$  monazite-type solid solutions have been irradiated with 100 MeV Au ions at room temperature and above the critical temperature (500 K) in a fluence range of  $10^{12} - 10^{14}$  ions/cm<sup>2</sup>. Exemplarily, the results are presented in Fig. 28 for the  $\text{La}_{0.8}\text{Gd}_{0.8}\text{PO}_4$  solid solution since no significant influence of the composition was observed.

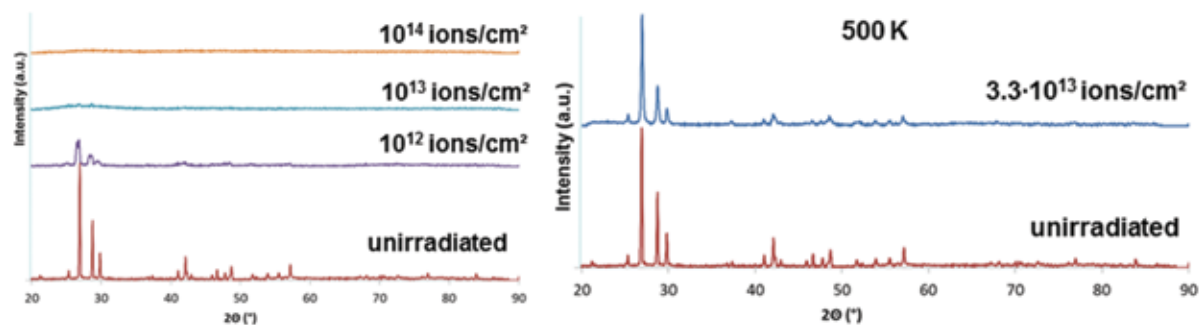


Figure 28 : XRD patterns of  $\text{La}_{0.2}\text{Gd}_{0.8}\text{PO}_4$  pellets before and after irradiation applying different fluences at RT (left) and 500 K (right).

It was found that both compositions show similar response to the Au irradiation at different fluences. At RT, they went amorphous after irradiation to fluence of  $10^{13}$  ions/cm<sup>2</sup>. An irradiation fluence of  $10^{12}$  ions/cm<sup>2</sup> yields already a loss of crystallinity indicating a partial amorphisation.

The influence of temperature was investigated by irradiating the samples to fluences  $> 10^{13}$  ions/cm<sup>2</sup> while heating to 500 K. The fluence was selected from the *in-situ* experiments, where complete amorphisation of both materials occurred. The temperature was selected from the literature. Both samples remained crystalline under these conditions even after irradiation at high fluences, indicating that 500 K is definitely above the critical temperature for these materials where no amorphisation takes place.

These results definitely prove the stability and radiation resistance of monazite-type waste forms which is unique so far. The results of that beamtime have been presented at several international conferences and meetings and pounced on wide interests [2].

## REFERENCES

- [1] A. Meldrum, L. A. Boatner, and R. C. Ewing, Phys. Rev. B, 56(21) (1997) 13805-13814.
- [2] S. Neumeier, P. K. Kulriya, Y. Arinicheva, G. Deissmann, D. K. Avasthi, and D. Bosbach, In-situ structural investigations on monazite-type  $\text{La}_{0.2}\text{Gd}_{0.8}\text{PO}_4$  ceramics under heavy ion irradiation, Scientific Basis for Nuclear Waste Management XXXIX, Montpellier (France), 2nd -6th Nov 2015.

### 5.2.3 An *in-situ* Investigation of 100 MeV Phosphorous ion irradiation on the Electrical Characteristics of NPN *rf* Power Transistors

T. M. Pradeep<sup>1</sup>, N. H. Vinayakaprasanna<sup>1</sup>, K. C. Praveen<sup>2</sup>, B.C. Hemaraju<sup>1</sup>, A. Anjum<sup>1</sup>, N. Pushpa<sup>3</sup>, K. Asokan<sup>4</sup>, A. Tripathi<sup>4</sup>, K.G. Bhushan<sup>5</sup> and A. P. Gnana Prakash<sup>1</sup>,

<sup>1</sup>Department of Studies in Physics, University of Mysore, Manasagangotri, Mysore-570 006, India

<sup>2</sup>Semiconductor Laboratory, Department of Space, Govt. of India, Punjab-160 071, India

<sup>3</sup>Department of PG Studies in Physics, JSS College, Ooty Road, Mysore-570 025, India

<sup>4</sup>Inter-University Accelerator Centre, Aruna Asaf Ali Marg, New Delhi-110 067, India

<sup>5</sup>Technical Physics Division, Bhabha Atomic Research Center, Mumbai-400 085, India

Bipolar Junction Transistors (BJTs) and bipolar circuits have become the most important components for advanced integrated circuits which can be used in many fields including space applications and other radiation rich environments like large hadron collider (LHC). When bipolar transistors and circuits are exposed to radiation environment, the resulting effects can cause significant degradation in the performance of the device [1]. Incident particles, such as Co-60 gamma rays, electrons, protons and heavy ions can induce ionization damage in the oxide layer or displacement damage in silicon bulk of BJTs. In order to understand the high dose effects, NPN Transistors

were irradiated with 100 MeV Phosphorous ions in the dose range of 600 krad(Si) to 100 Mrad(Si) with a beam current of 0.25 p-nA (particle-nano ampere) at IUAC, New Delhi. The different electrical characteristics like Gummel characteristics, excess base current ( $\Delta I_B = I_{B-Post} - I_{B-Pre}$ ), DC current gain ( $h_{FE}$ ) and output characteristics were studied before and after ion irradiation. Some of the important results are discussed in this report. Fig. 29(a) illustrates the Gummel characteristics for 100 MeV Phosphorous ion irradiated transistors. From the Figure it can be seen that  $I_B$  at lower  $V_{BE}$  is increasing with increase in dose. This indicates that the  $I_B$  of the transistor is very sensitive to ionizing radiation. The increase in the  $I_B$  is the result of increased recombination current in the E-B depletion region due to radiation induced (G-R) centers. In addition to G-R centers, high energy ions can also create various types of defects and their complexes in the transistor structure and they reduce the minority carrier lifetime and this in turn increases the  $I_B$  of the transistor [2]. Fig. 29(b) illustrates the DC current gain ( $h_{FE}$ ) for 100 MeV P ion irradiated transistors. From the Figure, it is clear that the  $h_{FE}$  of the irradiated transistors reduces almost to a negligible value after a total dose of 100 Mrad(Si). The degradation in peak  $h_{FE}$  is around 99% after 100 Mrad(Si) of total dose. The output characteristics of 100 MeV P ion irradiated transistors measured at  $I_B = 0.75$  mA is shown in Fig. 29(c). From Figure, it can be seen that the  $I_C$  at saturation region ( $I_{CSat}$ ) and active region decreases with increase in ion dose. The radiation induced defects are responsible for the increase in the collector series resistance and in turn reduce  $I_C$  in saturation region.

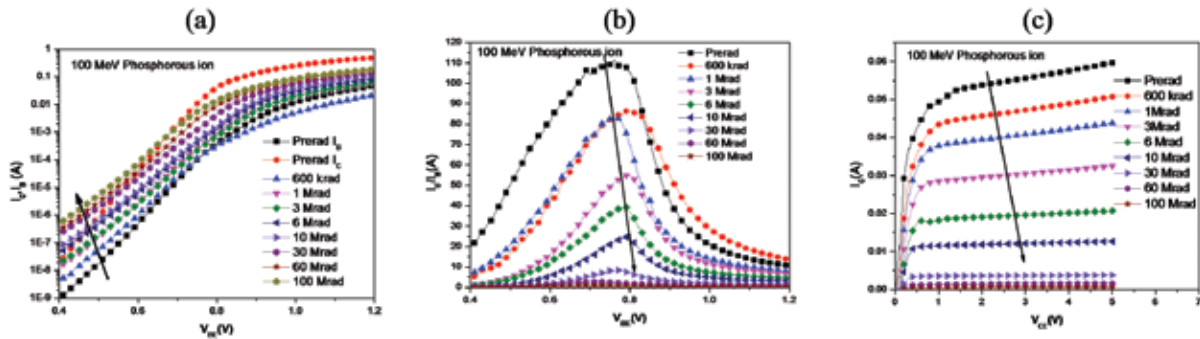


Figure 29: (a) Gummel characteristics of 100 MeV P ion irradiation, (b) The variation in dc current gain after 100 MeV P ion irradiation, and (c) The output characteristics of 100 MeV P ion irradiation.

## REFERENCES

- [1] A. P. Gnana Prakash *et al.*, Semiconductor Science and Technology. 19 (2004) 1029
- [2] N. Pushpa *et al.*, Nucl. Instrum. Meth. B. 273 (2012) 36

### 5.2.4 100 MeV Phosphorous Ion Induced Degradation in Electrical Characteristics of Advanced 200 GHz SiGe HBTs: An In-Situ Reliability Study

N. H. Vinayak Prasanna<sup>1</sup>, K. C. Praveen<sup>2</sup>, T. M. Pradeep<sup>1</sup>, B. C. Hemaraju<sup>1</sup>, A. Anjum<sup>1</sup>, N. Pushpa<sup>3</sup>, John D. Cressler<sup>4</sup>, A. Tripathi<sup>5</sup>, K. Asokan<sup>5</sup>, K.G. Bhushan<sup>6</sup> and A. P. Gnana Prakash<sup>1</sup>

<sup>1</sup>Department of Studies in Physics, University of Mysore, Manasagangotri, Mysore-570006, India

<sup>2</sup>Semiconductor Laboratory, Department of Space, ISRO, Mohali-160071, India

<sup>3</sup>Department of PG Studies in Physics, JSS College, Ooty Road, Mysore-570 025, India

<sup>4</sup>School of Electrical and Computer Engineering, Georgia Institute of Technology, Atlanta, GA, 30332, USA

<sup>5</sup>Inter-University Accelerator Centre, Aruna Asaf Ali Marg, New Delhi-110 067, India

<sup>6</sup>Technical Physics Division, Bhabha Atomic Research Center, Mumbai-400 085, India

Silicon-germanium heterojunction bipolar transistor (SiGe HBT) is an attractive candidate for operation in extreme environments, including: in radiation-intense surroundings (e.g., space) and at different temperature conditions (e.g., 77.3 K to 300 °C). The excellent cryogenic performance and significant improvement in unity-gain cutoff frequency ( $f_T$ ), current gain ( $\beta$ ) and early voltage ( $V_A$ ) of SiGe HBTs, can potentially facilitate their extension

into a diverse set of emerging applications such as, cooled sensors and detectors, semiconductor-superconductor hybrid electronic systems. Electronics employing in such applications must be hardened against radiation to operate reliably, since electronic systems operated in space environment experience persistent exposure to large and potentially lethal fluxes of high-energy protons, neutrons, electrons, gamma rays, X-rays and high-energy heavy ions [1, 2]. In order to examine the reliability of SiGe HBTs were irradiated with 100 MeV P ions up to a total dose of 100 Mrad. The dc I-V characteristics such as Gummel characteristics, excess base current ( $\Delta I_{IB} = I_{B-Post} - I_{B-Pre}$ ), current gain ( $\beta$ ), output characteristics, neutral base recombination (NBR) and avalanche multiplication of carriers (M-1) were studied before and after irradiation. The typical forward Gummel characteristics of 200 GHz SiGe HBTs subjected to 100 MeV P ion irradiation is shown in the Fig. 30(a). The increase in forward mode base current ( $I_B$ ) at lower  $V_{BE}$  was observed after 100 MeV P ion irradiation. The negligible change in collector current ( $I_C$ ) was observed even after 100 Mrad of total dose. The degradation in IB is the result of increased recombination current in the emitter-base (EB) depletion region due to radiation-induced generation-recombination (G/R) traps near the EB spacer oxide. The Fig. 30(b) shows the degradation in current gain ( $h_{FE}$ ) for 100 MeV P ion irradiated SiGe HBT. It can be seen that  $h_{FE}$  decreases with increase in radiation total dose. As ion dose increases the peak current gain shifts towards higher  $I_C$  or higher  $V_{BE}$ . The current gain curves for different ion doses tend to merge as  $I_C$  increases and it indicates that the gain degradation is small at higher  $I_B$  and quasi-neutral base recombination is not significantly affected by ion irradiation. The radiation-induced G/R centers decrease the minority-carrier lifetime which in turn decrease the current gain. The decrease in minority carrier lifetime is the dominant mechanism for gain degradation in addition to G/R centers created in the EB spacer oxide. Fig. 30(c) illustrates the measured multiplication factor i.e., the number of electron-hole pairs created in the collector-base (CB) space-charge region as a function of  $V_{CE}$ . The decrease in the M-1 is very small even after 100 Mrad of total dose, hence the electron/hole pairs created in the CB space-charge region is unable to multiply the impact ionization with lattice atoms due to the formation of displacement damages by phosphorous ion irradiation. The parameters of ion irradiated SiGe HBTs is acceptable even after 100 Mrad of total dose. The SiGe HBTs show better anti-radiation performance; hence they can be used in radiation rich environments.

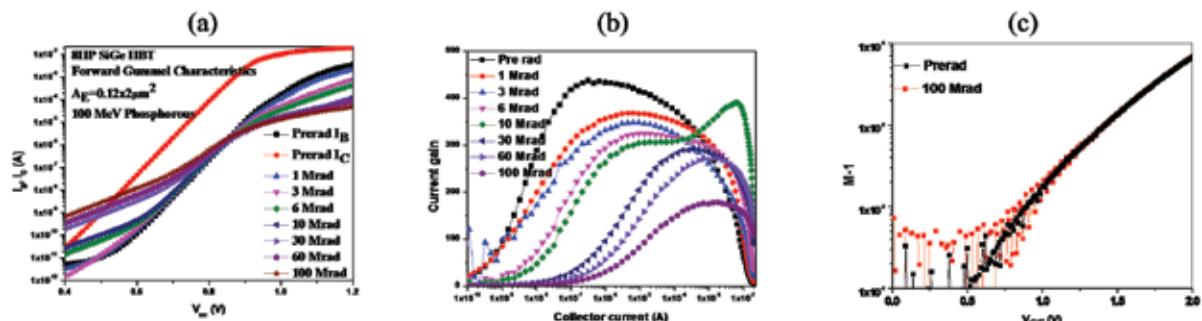


Figure 30 : (a) Forward mode Gummel characteristics, (b) Variation of current gain after irradiation, and (c) Avalanche multiplication of carriers (M-1)

## REFERENCES

- [1] J. D. Cressler, G. Niu, "Silicon Germanium Heterojunction Bipolar Transistors" Artech House, Norwood (MA), (2003)
- [2] K.C. Praveen *et al.*, Radiation Effects and Defects in Solids, 166 (2011) 710

### 5.2.5 In-situ electrical properties of HfO<sub>2</sub> based MOSCAPs under SHI irradiation

N. Manikanthababu<sup>1</sup>, S. Vajandar<sup>2</sup>, K. Asokan<sup>3</sup>, A. P. Pathak<sup>1</sup>, T. Osipowicz<sup>2</sup> and S. V. S. Nageswara Rao<sup>1</sup>

<sup>1</sup>School of Physics, University of Hyderabad, Hyderabad, India 500046.

<sup>2</sup>Department of Physics, National University of Singapore, Singapore 117542, Singapore.

<sup>3</sup>Inter-University Accelerator Centre, Aruna Asaf Ali Marg, New Delhi-110 067, India

Thermodynamic instability and the lower band offsets are the practical limitations which normally restrict the applicability of high-k dielectric materials in device fabrication [1-2].  $\text{HfO}_2$  has evolved as the commercial materials despite the trade-off between the dielectric constant and the band offsets [3]. Swift heavy ion induced mixing / modifications at the interfaces can yield relatively new materials [4]. In-situ measurements evade any environment induced modifications of the electrical characteristics in the device. Hence, a thorough investigation on the electrical response of these devices and the interfaces as a function of irradiation fluences has been performed.

ALD grown ultra-thin device quality  $\text{HfO}_2/\text{SiO}_2/\text{Si}$  samples, obtained from SEMATECH, USA, have been used for 120 MeV Ag ion irradiation. The typical sample structure of ALD grown samples is " $\text{HfO}_2$  (2.7 nm) /  $\text{SiO}_2$  (0.6 nm) / Si (substrate)". These samples were termed as H3 series samples. H3 series samples were mounted on a specially designed ladder for SHI irradiation to measure I-V and C-V characteristics. On an average, there were four devices connected on each sample for in-situ measurements. SHI irradiation was performed at room temperature at IUAC, New Delhi. Low beam currents have been preferred for reducing the damage of the device. 0.5 pA was maintained throughout the experiments and the ion fluence has been varied from  $1 \times 10^{10}$  to  $1 \times 10^{14}$  ions/cm<sup>2</sup>. HRBS and TEM measurements were performed on these samples at NUS, Singapore.

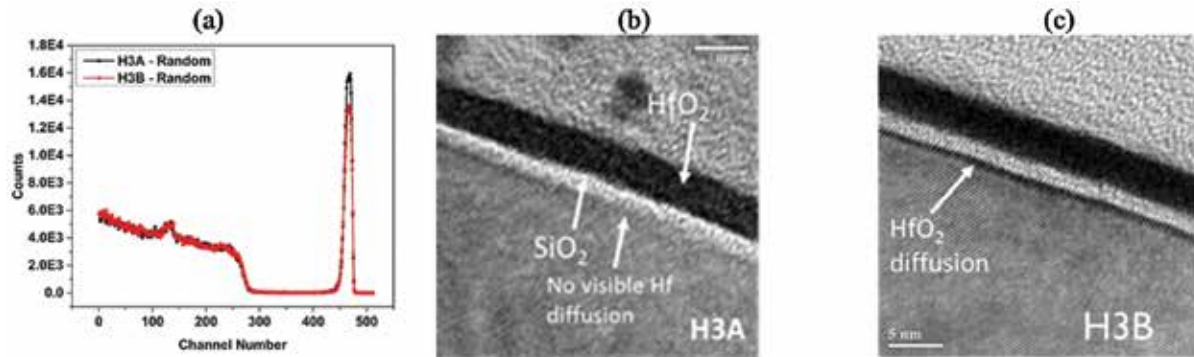


Figure 31 : (a) Random HRBS spectra of H3 pristine and irradiated sample, (b) XTEM on H3A sample, (c) XTEM of H3B sample indicating Hf diffusion

Random HRBS spectra of pristine sample (H3A) and irradiated sample (H3B) are shown in Fig. 31(a). The yield of Hf seems to be less everywhere in the irradiated sample as compared to that of pristine sample. The width of this peak is also slightly higher in irradiated sample. This indicates possible increase in the thickness and decrease in the density of the irradiated samples. XTEM images in Fig. 31(b) and Fig. 31(c) show a clear indication of Hf diffusion across  $\text{HfO}_2/\text{SiO}_2$  interface.

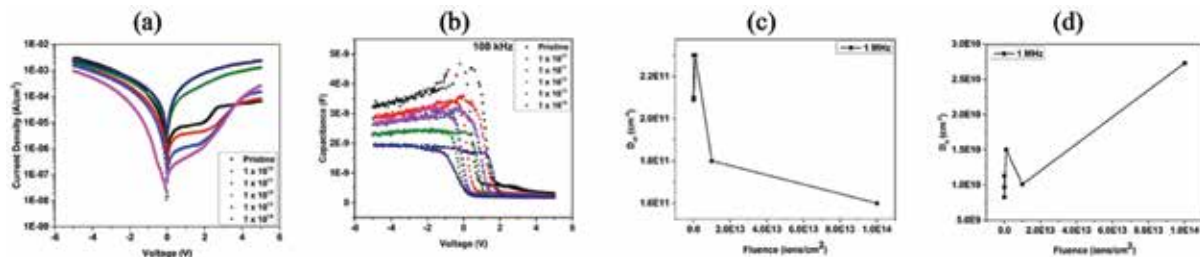


Figure 32 : (a) In-situ I-V characteristics of sample (fluence unit: ions/cm<sup>2</sup>), (b) In-situ C-V characteristics of H3 series sample, (c)  $D_{ox}$  as function of irradiation fluence at 1 MHz frequency in H3 sample, (d)  $D_{it}$  as function of irradiation fluences at 1 MHz frequency in H3 sample.

The in-situ I–V and C–V characteristics of H3 sample at various fluences are shown in Fig. 32(a) and 32(b). The reduction in leakage current density can be attributed to the improvement of the device as the defects get annealed during SHI irradiation. However, after  $1 \times 10^{12}$  ions/cm<sup>2</sup> fluence, the leakage current has been observed to increase up to the fluence of  $1 \times 10^{14}$  ions/cm<sup>2</sup>. The sustenance and device tolerance have been evicted from these higher fluences. At the higher fluences, the degradation of the device performance has been observed in terms of its increase in the leakage current. On the other hand, in the negative bias region, the leakage currents are found to be less because the device is in depletion region. It is also important that the depletion region is not observed at higher dose indicating that the device is driven to inversion region. This is possible because the presence of defects can influence carrier recombination process. These defects cause defect-assisted tunneling of electrons across the interface. A systematic decrease in the accumulation capacitance with increase in the irradiation fluence has been observed. This can be attributed to the possible increase in physical thickness and changes in the composition of the interlayer (HfSiO) layer which can affect its dielectric constant. Further, the density of these oxide traps has been estimated which is shown in Fig. 32(c). The oxide trap density ( $D_{ot}$ ) increases up to  $1 \times 10^{12}$  ions/cm<sup>2</sup> fluence, thereafter there is a decrease in the oxide trap density. It is known that the slope of C–V curves can be altered by the interface traps (see Fig. 32(d)). The density of interface traps ( $D_{it}$ ) is directly proportional to the change in the flat band and mid-gap voltages. A behavior similar to the  $D_{ot}$  changes has been observed in the density of interface ( $D_{it}$ ).

The in-situ electrical measurements were performed on the H3 series MOSCAPs using 120 MeV Ag ion irradiation to understand the ion induced intermixing effects, annealing and creation of defects. Leakage current density has been found to decrease at lower fluences, but an increase at higher fluences. The density of oxide traps has been found to decrease whereas the density of interface traps has been found to increase with the irradiation fluence.

## REFERENCES

- [1] Y.H. Kim and J.C. Lee, *Microelectronics & Reliab.*, 44 (2004) 183.
- [2] H. Kim, P.C. McIntyre and K.C. Saraswat, *Appl. Phys. Lett.*, 82 (2003) 106.
- [3] Byoung Hun Lee, Laegu Kang, Renee Nieh and Jack C. Lee, *Appl. Phys. Lett.*, 76 (2000) 1926.
- [4] N. Manikantbabu, *et al.* varaju, N. Srinivasa Rao, P. Yang, M. B. H. Breese, T. Osipowicz, S. V. S. Nageswara Rao, *Nucl. Inst. and Meth. in Phys. Res. B*, 332 (2014) 389.

### 5.2.6 Observation of swift heavy ion induced mixing in Pd<sub>1-x</sub>Ni<sub>x</sub>/Si interfaces

Paramita Patra<sup>1</sup>, S. A. Khan<sup>2</sup>, D. Kabiraj<sup>2</sup>, Manju Bala<sup>2</sup>, D. K. Avasthi<sup>2</sup>, and S. K. Srivastava<sup>1</sup>

<sup>1</sup>Department of Physics, Indian Institute of Technology Kharagpur, Kharagpur, 721302

<sup>2</sup>Inter-University Accelerator Centre, Aruna Asaf Ali Marg, New Delhi-110 067, India

Irradiation of thin film systems with energetic ions often leads to atomic displacements due to the ion-matter interaction resulting in intermixing of the layer with its substrate. The occurrence of thermal spikes via Electron Phonon Coupling (EPC) mediated transfer of electronic energy to lattice [1,2] has been identified as the primary cause of all observed SHI-matter interaction related phenomena in metals and insulators alike. In the case of Ni/Si and Pd/Si system, intermixing or silicide phase formation has been observed only in low energy ion bombardment [3,4]. But there is no such experimental evidence of mixing of Ni or Pd in Si substrate in swift heavy ion irradiation. The aim of our study is to check whether ion beam mixing occurs in Pd<sub>1-x</sub>Ni<sub>x</sub> alloy thin layer and Si.

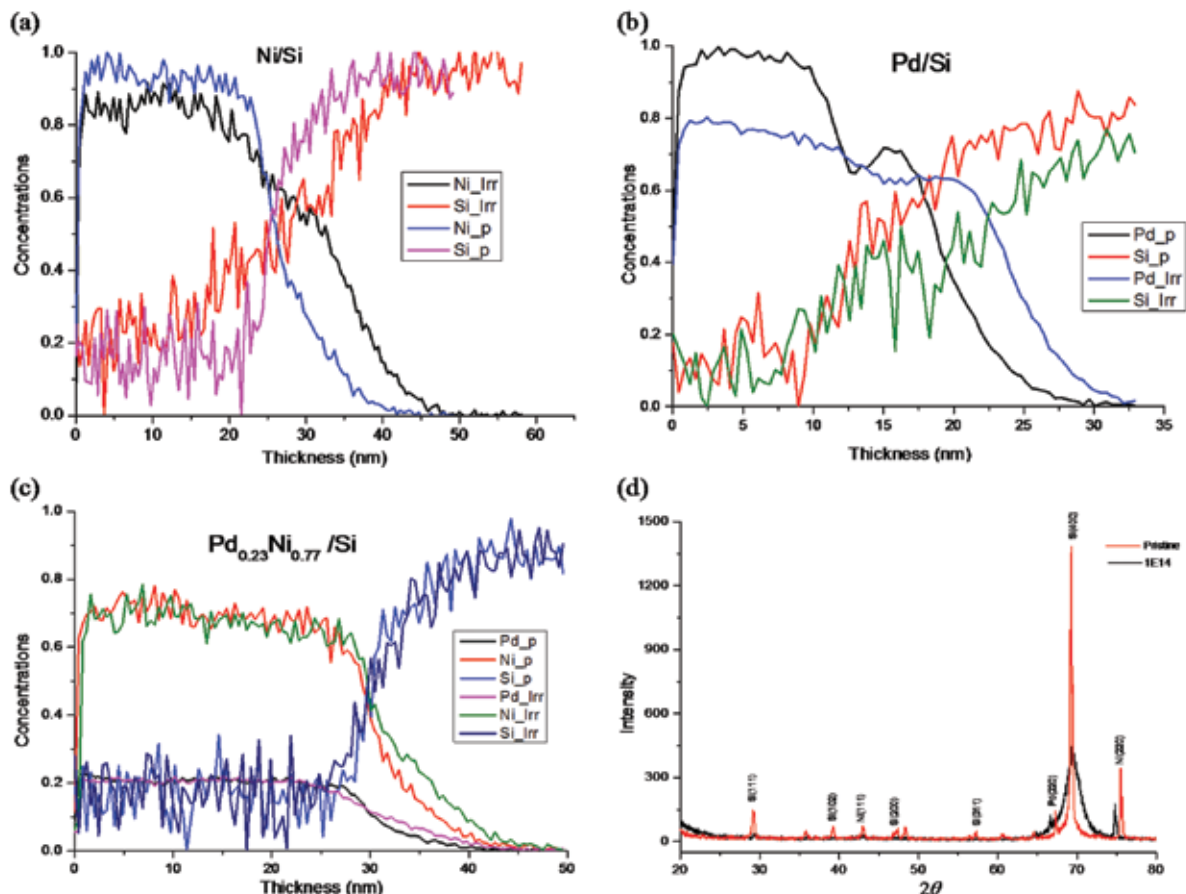


Figure 33 : XPS depth profile (a) pristine and irradiated Ni/Si system (b) pristine and irradiated Pd/Si system (c) pristine and irradiated Pd<sub>0.23</sub>Ni<sub>0.77</sub>/Si system. (d) XRD spectra of Pd<sub>0.23</sub>Ni<sub>0.77</sub>/Si system for pristine and irradiated sample

In this work, Pd<sub>1-x</sub>Ni<sub>x</sub> alloys were prepared by melting pure elemental metals in an arc furnace in argon atmosphere. Then Pd<sub>(1-x)</sub>Ni<sub>x</sub> alloy thin films were deposited from the melts onto Si substrates using multi-target electron beam evaporation system at Inter-University Accelerator Center (IUAC), New Delhi. Pd<sub>1-x</sub>Ni<sub>x</sub>/Si samples were irradiated with 100 MeV Au ions with fluence  $1 \times 10^{13}$  to  $1 \times 10^{14}$  ions/cm<sup>2</sup> using 15 UD Pelletron accelerator at IUAC, New Delhi. The pristine and irradiated samples were characterised to study the structure and interfacial mixing in Pd<sub>1-x</sub>Ni<sub>x</sub> alloy thin films and Si substrate using X-ray diffraction (XRD), Rutherford backscattering spectrometry (RBS) and X-ray photoelectron spectroscopy (XPS).

The RBS spectra of Pd<sub>1-x</sub>Ni<sub>x</sub> alloy thin films on Si do not show any significant mixing at interface or it might be the limitation of resolution of RBS ~10nm. The thicknesses of the films as derived from RBS data are ~25nm. XPS was used for studying the interface profile. The XPS depth profile for Ni/Si, Pd/Si and Pd<sub>0.23</sub>Ni<sub>0.77</sub>/Si for pristine and irradiated ( $1 \times 10^{14}$  ions/cm<sup>2</sup>) samples are shown in Fig. 33(a-c). From these Figures, mixing at interface is clearly seen. The mixing rate of pure Pd and Ni in Si is higher than the intermediate composition of Pd and Ni. Fig. 33(d) shows XRD spectra of the pristine and irradiated (fluence  $1 \times 10^{14}$  ions/cm<sup>2</sup>) Pd<sub>0.23</sub>Ni<sub>0.77</sub> sample. In case of pristine sample there are many sharp peaks but in irradiated sample only broad Si Bragg peak is observed. It is due to the inter-diffusion of Si atoms into the Pd-Ni layer. So it can be concluded from XRD result that the intermixing is occurring due to the inter diffusion of atoms. Further analysis of the data is underway.

**REFERENCES**

- [1] Z.G. Wang, C. Dufour, E. Paumier and M. Toulemomde, *J. Phys: Condensed Matter* 6 (1994) 6733
- [2] S.K. Srivastava, et al., *Phys. Rev. B* 71 (2005) 193405.
- [3] B. Y. Tsaur, Z. L. Liao, and J. W. Mayer, *Appl. Phys. Lett.* 34 (1979) 168.
- [4] Y. Chimi Iwase et al., *Nucl. Instr. and Meth. in Phys. Res. B* 245 (2006) 141–144.

**5.2.7 Irradiation temperature dependence of shape elongation of metal nanoparticles induced by swift heavy ion irradiation**

Hiro Amekura<sup>1</sup>, Saif Ahmad Khan<sup>2</sup>, Sonu Hooda<sup>2</sup>, Ramcharan Meena<sup>2</sup>, Devesh Kumar Avasthi<sup>2,3</sup>

<sup>1</sup>National Institute for Materials Science (NIMS), Tsukuba 305-0003, Japan.

<sup>2</sup>Inter-University Accelerator Centre, Aruna Asaf Ali Marg, New Delhi-110 067, India

<sup>3</sup>Amity University, Noida 201313, India.

Irradiation temperature dependence of shape elongation of vanadiumnanoparticles (VNPs) in silica was evaluated between 100 and 750 K after 120 MeV Ag<sup>9+</sup> ion irradiation to a fluence of  $1 \times 10^{14}$  ions/cm<sup>2</sup>. The V NPs were formed in silica (amorphous SiO<sub>2</sub>) as an embedded form by 60 keV V<sup>+</sup> ion implantation to a fluence of  $1.0 \times 10^{17}$  ions/cm<sup>2</sup>. Silica glass of KU-1 type (high OH concentration of ~1000 ppm) was used. Cross-sectional transmission electron microscopy (XTEM) showed that the most of the NPs were observed between 10 and 70 nm in depth [1], and that the mean diameter and the standard deviation was 9.0 nm and 2.9 nm, respectively [2]. The samples were irradiated with 120 MeV Ag<sup>9+</sup> ions with an incident angle of 45°, in order to detect the shape elongation as anisotropic optical absorption [3]. The irradiations were carried out at five different temperatures 100, 300, 450, 600, and 750K, using either the low-temperature chamber in the beam hall I or the high-temperature chamber in the beam hall II. To exclude purely thermal effects during the irradiation, a pair of samples was set to the irradiation chamber at every irradiation temperature. Then, one was irradiated but the other was not. After the irradiation experiments, the unirradiated party was evaluated with the absorption spectroscopy. The spectra were not identical but nearly the same. This fact justifies that the present experimental result is reliable as the irradiation temperature dependence.

Fig. 34(L) shows optical density spectra of V NPs in silica irradiated with 120 MeV Ag<sup>9+</sup> ions at different irradiation temperatures between 100 and 750K. The measurements were carried out using linearly polarized light. The solid and broken curves denote the polarization angle of 0 and 90°, respectively, where the polarization angle is defined as angle between a plane including trajectory of individual incident ion and that of the light polarization. Around 5 eV, a peak is clearly detected at 100 and 300K, and disappears with increasing the irradiation temperature higher. This peak can be ascribed to point-defects of silica matrix, called B<sub>2</sub> center [4]. We have confirmed that this peak is observed in silica without any NPs after irradiation of swift heavy ions [3] or even low energy light dimmer ions of 60 keV B<sub>2</sub><sup>-</sup> [5]. Also we have studied isochronal annealing effects on this peak: The peak steeply decreased at 200 °C (473K) and mostly disappeared at 400 °C (673K) [6]. This observation is consistent with the present result.

The difference between the solid curve and the broken curve at each temperature corresponds to contribution from the shape elongation of NPs. The contribution from the B<sub>2</sub> centers cancelled out between the polarization angles of 0 and 90°. The difference was integrated over the wavelength and plotted against the irradiation temperature as shown in Fig. 34(R). The difference of the optical density, i.e., the shape elongation, decreases gradually from 100K to 450K, but slightly increases again from 450K to 750K. However, it can be described that the change is moderate and could be regarded as almost constant. Further discussion will be given elsewhere.

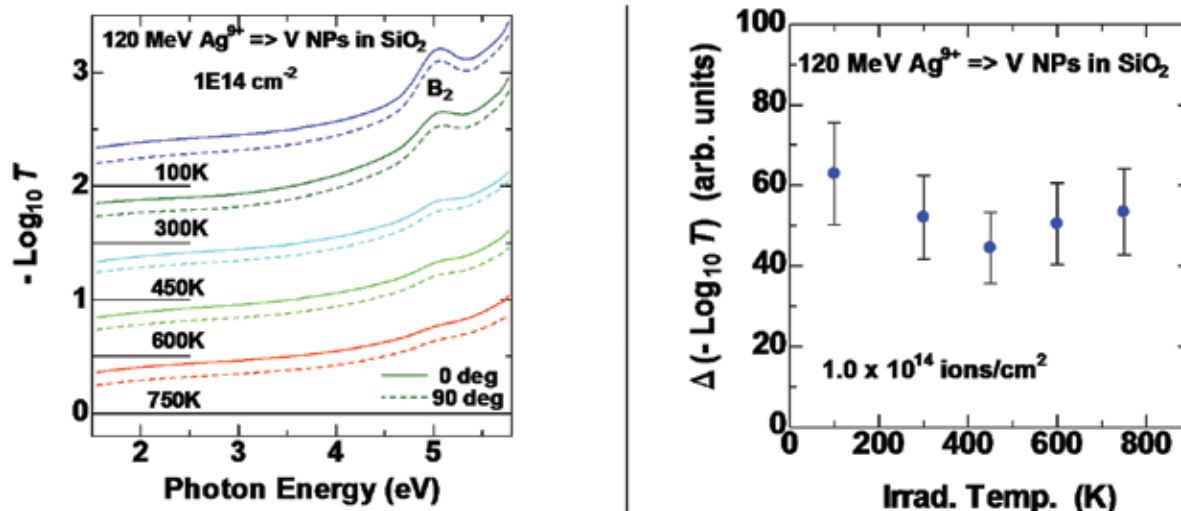


Figure 34 : (L) Optical density spectra of vanadium nanoparticles in silica irradiated with 120 MeV Ag<sup>9+</sup> ions, at various irradiation temperatures between 100 and 750K, where  $T$  denotes the optical transmittance. The measurements were carried out using linearly polarized light. The solid and broken curves denote the polarization angle of 0 and 90°, respectively, where the polarization angle is defined as angle between a plane including trajectory of individual incident ion and that of the light polarization. The spectra were shifted vertically between different irradiation temperatures, but not between the pair at the same irradiation temperatures. The zero levels were indicated by horizontal bars. (R) The integrated difference between the spectrum at 0° and that at 90° was plotted against the irradiation temperature.

## REFERENCES

- [1] H. Amekura, *et al.*, Thin Solid Films 520 (2012) 5528
- [2] H. Amekura, *et al.*, Nucl. Instr. and Methods in Phys. Res. B 269 (2011) 2730
- [3] H. Amekura, *et al.*, Phys. Rev. B 83 (2011) 205401
- [4] D.L. Griscom, J. Ceram. Soc. Jpn. 99 (1991) 923
- [5] H. Amekura, *et al.*, J. Appl. Phys. 104 (2008) 063509
- [6] H. Amekura, *et al.*, unpublished.

### 5.2.8 Influence of Swift Heavy Ion Irradiation on the Surface and Structure Properties of C<sub>70</sub> Fullerene

P. Sharma<sup>1</sup>, R. Singhal<sup>1</sup>, M.K. Banerjee<sup>2</sup>

<sup>1</sup>Department of Physics, Malaviya National Institute of Technology, Jaipur 302017, India.

<sup>2</sup>Department of Metallurgical & Materials Engineering, Malaviya National Institute of Technology Jaipur 302017, India

This research work is focused to observe the effect of 90 MeV Si ion irradiation on the surface and structural properties of C<sub>70</sub> thin films. For this, C<sub>70</sub> thin films were developed on double side polished silicon substrate by resistive heating of C<sub>70</sub> powder. These films were irradiated with 90 MeV Si<sup>7+</sup> ions to different fluences in the range from  $1 \times 10^{12}$  to  $6 \times 10^{13}$  ions cm<sup>-2</sup>. Pristine as well as irradiated thin films were characterized by Raman spectroscopy and atomic force microscopy (AFM) for the investigation of structural and surface modifications, respectively. Raman spectroscopy studies reveal that C<sub>70</sub> is not completely transformed into amorphous carbon at a fluence of  $6 \times 10^{13}$  ions cm<sup>-2</sup>. The breakage of C<sub>70</sub> molecules was explained on the basis of Thermal Spike Model [1-2]. Swift heavy ion irradiation generates nanometer size conducting tracks in fullerenes. For 90 MeV Si ions irradiated C<sub>70</sub> fullerene, the damage cross-section ( $\sigma$ ) and radius of damaged cylindrical zone were estimated (from Raman spectra) to be  $\sim 0.32 \times 10^{-13}$  cm<sup>2</sup> and  $\sim 1.01$  nm, respectively, using vibrational modes of C<sub>70</sub>. It was observed that the value of roughness (Fig. 35(I)) increases up to a fluence of  $3 \times 10^{12}$  ions cm<sup>-2</sup>. Also the average particle size becomes larger after irradiation. This may be due to the agglomeration of smaller particles into larger ones; since the smaller particles have higher surface free energy, there is an urge for its agglomeration to form bigger particles which decreases surface free energy owing to lower specific surface area of larger particles. The average particle size at highest fluence ( $6 \times 10^{13}$  ions cm<sup>-2</sup>) is reduced to a value of  $26 \pm 0.8$  nm which is attributed

to the large overlapping of ions at this fluence. Contact angle measurements (Fig. 35(II)) have been performed to investigate about hydrophilic or hydrophobic nature of fullerene  $C_{70}$  thin films. The contact angle first increases and then decreases with fluence. This demonstrates that the hydrophobic nature of fullerene  $C_{70}$  increases with fluence up to  $3 \times 10^{12}$  ions  $\text{cm}^{-2}$  but it decreases as the fluence reaches to  $1 \times 10^{13}$  ions  $\text{cm}^{-2}$  [3].

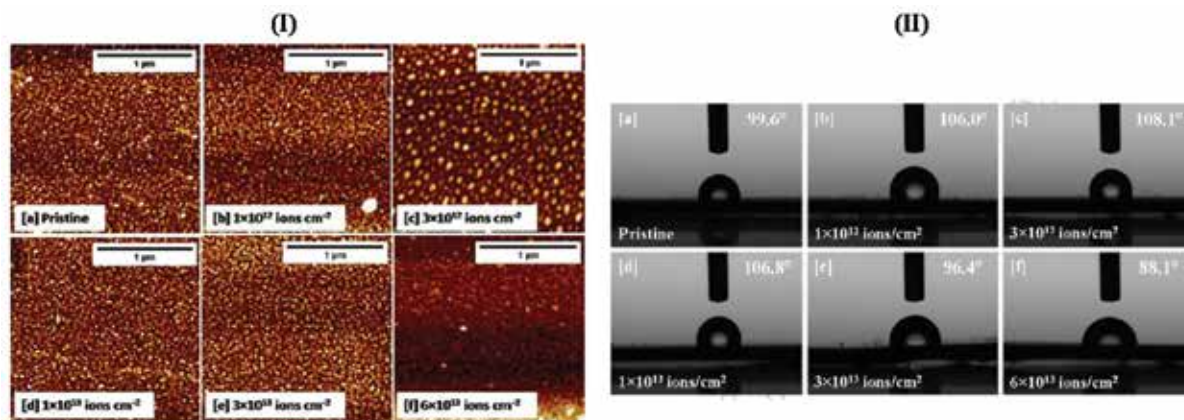


Figure 35 : (a) Two dimensional (2D) AFM images of pristine as well as 90 MeV Si ion irradiated films at different fluences and (b) Represents the snapshots of the contact angle measurement for the pristine and 90 MeV ion irradiated samples.

## REFERENCES

- [1] D. K. Avasthi and G. K. Mehta: 'Swift heavy ions for materials engineering and nanostructuring', 2011, Springer Science & Business Media.
- [2] S. K. Srivastava *et al.*, Phys. Rev. B 71 (2005) 193405
- [3] P. Sharma *et al.*, Surface Engineering (2016) DOI 10.1080/02670844.2016.1185838

### 5.2.9 Electronic structure modification and Fermi level shifting in Niobium doped anatase Titanium dioxide thin films: A comparative study of NEXAFS, work function and stiffening of phonons

Subodh K. Gautam<sup>1</sup>, Arkaprava Das<sup>1</sup>, S. Ojha<sup>1</sup>, D. K. Shukla<sup>2</sup>, D.M. Phase<sup>2</sup>, and Fouran Singh<sup>1</sup>

<sup>1</sup>Inter-University Accelerator Centre, Aruna Asaf Ali Marg, New Delhi-110 067, India

<sup>2</sup>UGC-DAE Consortium for Scientific Research, University Campus, Khandwa Road, Indore 452017, India

The study of Swift Heavy Ions (SHIs) irradiation effect on nano-crystalline Nb doped  $\text{TiO}_2$  (NTO) thin films has generated great interest for the fundamental understanding of phase transformation and the response of their physio-chemistry properties due to change in crystallite size, structural defects and stoichiometry and lattice parameters. NTO is a unique semiconductor oxide material which exhibit salient superior properties and can be used as transparent conductor, solar cells, and photo-catalytic applications [1]. In the present study, SHIs irradiation induced modification of structural optical and electronic structure properties along with the tuning of work function (WF), stiffening in low frequency  $E_{\text{lg}}$  Raman mode and Fermi level shifting at different density of electronic excitations (EEs) has been investigated. Hence, the investigations were carried out on 5 at.% Nb doped nanocrystalline NTO thin films synthesized by sol-gel spin coating technique. The densities of EEs were varied by using 80 MeV O, 130 MeV Ni and 120 MeV Ag ions for irradiation. Structural investigations were carried out using grazing incidence X-ray diffraction, micro-Raman spectroscopy and the EEs induced modification in electronic structure were studied using near edge x-ray absorption fine structure (NEXAFS) spectroscopy. NEXAFS results reveal the reduction of hybridized O 2p and Ti 3d unoccupied states in conduction band with a decrease in energy of crystal field strength  $\sim 480$  meV and correlated effect on decrease in the WF value of  $\sim 520$  meV upon increasing the density of EEs. WF value is calculated using Scanning Kelvin Probe Microscopy (SKPM) study. The stiffening in low frequency Raman mode (LFRM) of  $\sim 9$   $\text{cm}^{-1}$  is observed as increasing the

total energy deposited to the lattice which validates the electronic structure modification under the influence of EEs induced strain in  $\text{TiO}_6$  octahedra [2]. The reduction of hybridized electronic state and stiffening behavior of  $E_{\text{lg}}$  Raman mode are explained in terms of nano-crystallization followed by amorphization in NTO lattice induced by continuous and discontinuous amorphous ion tracks containing intentionally created defects and non-stoichiometry in the lattice. The  $S_{\text{eth}}$  value of anatase  $\text{TiO}_2$  is calculated and found to be  $\approx 15.0$  keV/nm. Ag ion irradiation, having  $S_e > S_{\text{eth}}$ , produced the continuous amorphous ion track of radius  $\sim 3.6$  nm surrounded by damaged region and it is quite consistent with the value reported in the literature [3]. Ni ions, have  $S_e$  value less than the  $S_{\text{eth}}$ , are only liable to create discontinuous tracks in the lattice. However, O ion irradiation is unable to produce amorphous track, but creates point defect and thermal annealing in lattice due to much lower  $S_e$  as compared to  $S_{\text{eth}}$ . XRD and Raman results have shown that such ion tracks induce major modification in NTO films which leads to reduction of crystallite size and produce large density of disorder/defects in crystalline lattice. The intentionally created defects and non-stoichiometry in NTO lattice are liable to modification in the Ti 3d occupancies and directly influence the sensitive local structure of  $t_{2g}$  and  $e_g$  orbitals. These studies are very appropriate for better insights of electronic structure modification during phase transformation and controlled Fermi level shifting, which plays a crucial role in controlling the charge carrier injection efficiency in optoelectronic applications. Moreover, this fundamental understanding of ion interaction, involved processes and their tailoring capabilities will be exploited for the development of new class of materials. For details, see the published paper [Subodh K. Gautam, *et al.*, Phys. Chem. Chem. Phys. 18, (2016) 3618].

## REFERENCES

- [1] V. L. Kuznetsov, Mrs Bull., 25, (2011) 15
- [2] Subodh K. Gautam, Fouran Singh, *et al.*, J. Appl. Phys. 115, (2014) 143504
- [3] K. Awazu, *et al.*, J. Appl. Phys., 2006, 100, 10–15

### 5.2.10 Band gap engineering and low temperature transport phenomenon in highly conducting antimony doped tin oxide thin films

M.P.S. Rana<sup>1</sup>, Fouran Singh<sup>2</sup>, Sandhya Negi<sup>1</sup>, Subodh K. Gautam<sup>2</sup>, R.G. Singh<sup>3</sup>, R.C. Ramola<sup>1</sup>

<sup>1</sup>Department of Physics, H.N.B. Garhwal University, Tehri, Garhwal-249199, India

<sup>2</sup>Inter-University Accelerator Centre, Aruna Asaf Ali Marg, New Delhi-110 067, India

<sup>3</sup>UGC-DAE Consortium for Scientific Research, University Campus, Khandwa Road, Indore- 452017

Highly transparent, conducting and smooth antimony doped tin oxide thin films were successfully deposited using cost effective sol-gel spin coating technique. A huge band gap tuning and low temperature transport phenomenon in highly transparent antimony doped tin oxide thin film ( $\text{Sb}:\text{SnO}_2$ ) under the influence of swift heavy ions irradiation (SHII) is reported. Structural analysis shows an enhancement in crystallinity at initial fluence of irradiation followed by amorphization at higher fluences. Films were also well studied for their surface morphology by atomic force microscopy and scanning electron microscopy. Band gap analysis reveals a drastic band gap narrowing around 1.1 eV upon SHI irradiation. Transport measurements show that the conductivity and the carrier concentration decrease upon increase in the fluence of irradiation. The mechanism of charge carrier transport investigated at low temperature is attributed to nearest neighbour hopping (NNH) and variable range hopping (VRH) in different temperature regimes. Origin of the band gap tuning is understood in framework of Burstein–Moss (BM) shift, quantum confinement (QC) effect and band-tailing states in amorphous semiconductors. Finally, such band gap tuning and understanding of activation processes may play a crucial role for the development of optoelectronic devices. For details, see the published paper [M.P.S. Rana *et al.*, Ceramics International 42 (2016) 5932–5941].

### 5.2.11 Micro-Raman, optical and morphological study of swift heavy ion irradiated ZnO thin films

Naina Gautam<sup>1</sup>, Fouran Singh<sup>2</sup>, Subodh K. Gautam<sup>2</sup>, R. G. Singh<sup>3</sup>, S. Ojha<sup>2</sup>, A. Kapoor<sup>1</sup>

<sup>1</sup>Department of Electronic Science, University of Delhi South Campus, New Delhi-110023,India.

<sup>2</sup>Inter-University Accelerator Centre, Aruna Asaf Ali Marg, New Delhi-110 067, India

<sup>3</sup>Department of Physics, Bhagini Nivedita College University of Delhi, New Delhi -110043, India.

Low energy ion irradiation has proven to be a very simple and versatile tool for surface nano-structuring, while Swift Heavy Ion (SHI) is very efficient method for modifying the structural and optical properties of materials in narrow cylindrical volume along their straight path [1]. When a highly energetic ion strikes on the ZnO thin film target, it loses most of its energy in exciting electrons and/or ionizing atoms. The large value of energy transferred induces an unusual density of defects in the material. Therefore, the changes in structural, optical properties and surface modification of the ZnO thin film induced by the defect production require detailed investigation. The Raman spectra of pristine and irradiated films are shown in Fig. 36. The spectrum of pristine film has peaks at  $\sim 302$ ,  $\sim 436$ ,  $\sim 620$   $\text{cm}^{-1}$  and a very broad band around  $\sim 578$   $\text{cm}^{-1}$ . The peak at  $\sim 436$   $\text{cm}^{-1}$  is attributed to  $E_2$  (high) and the band at  $578$   $\text{cm}^{-1}$  can be ascribed to  $A_1$ (LO) mode. The peaks at about  $302$  and  $620$   $\text{cm}^{-1}$  are due to the Si substrate [2]. There is shift observed in the  $A_1$ (LO) peak with increase in fluence showing that stress is created in the films due to introduction of defects whereas  $E_2$ (H) mode peak confirms hexagonal wurtzite structure of ZnO. The shift of  $A_1$ (LO) peak is tabulated in Table 5.2.1.

The dependence of the transmission spectra in the visible region post irradiation is shown in Fig. 36(centre). Here the transmittance decreases from  $\sim 88$  % to  $\sim 75$  % for pristine and for fluence of  $1 \times 10^{13}$  ions/ $\text{cm}^2$  respectively. Additionally there is variation of the optical absorption edge which has been investigated using Tauc's plot. The dependence of absorption coefficient on the photon energy was fitted to the relation:  $\alpha h\nu = A(h\nu - E_g)^n$ , where A is a constant,  $\alpha$  is the absorption coefficient,  $h\nu$  is the photon energy,  $E_g$  is the optical band gap of the thin film. Here exponent n depends on the type of transition allowed in the material ( $n=1/2$ ). The absorption edge shifts to shorter wavelengths with increase in fluence. This blue shift can be explained by Burstein-Moss effect. The AFM image of ZnO thin film irradiated at dose of  $1 \times 10^{13}$  ions/ $\text{cm}^2$  is shown in Fig. 36(right). The irradiated film is uniform having surface roughness of  $\sim 16$  nm which is less as compared to the pristine sample. The effect of swift heavy ion irradiation on ZnO thin films prepared by the chemical route of sol-gel method have been studied in terms of structural, morphological and optical properties. The Raman and XRD (not shown) findings are in sync as Raman data reveals that irradiated films exhibit stable hexagonal wurtzite structure (intense  $E_2$  (H) mode peak) along with defect formation post irradiation. Also, band-gap tuning (blue shift) can be achieved by irradiation at certain optimum dose without losing high transparency in the visible region.

**Table 5.2.1: Values of transmittance, band-gap and Raman shift measured for the different samples**

Sample	Transmittance (%)	Band-gap (eV)	Raman shift ( $\text{cm}^{-1}$ )
Pristine	$\sim 88$	3.27	--
$1 \times 10^{12}$ ions/ $\text{cm}^2$	$\sim 80$	3.26	$\sim 584$
$1 \times 10^{13}$ ions/ $\text{cm}^2$	$\sim 75$	3.29	$\sim 577$

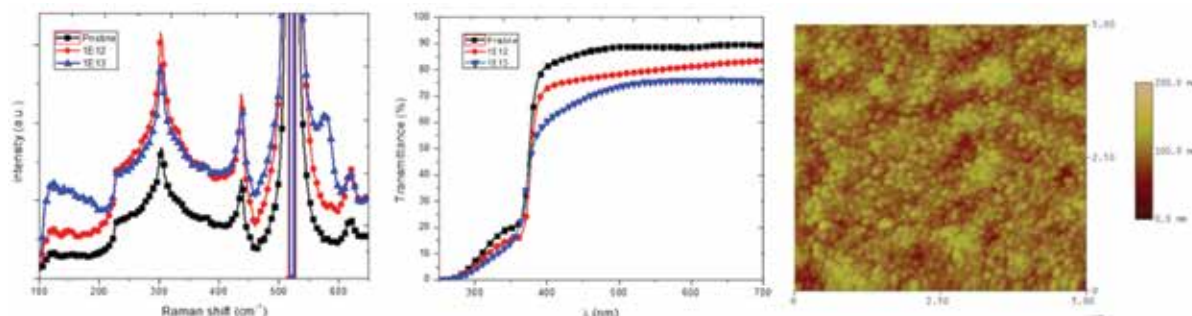


Figure 36 : (left) Raman plot, (centre) transmission for pristine and irradiated film and (right) AFM image of the film irradiated to dose of  $1 \times 10^{13}$  ions/ $\text{cm}^2$

## REFERENCES

- [1] R. Krishna et al., Nucl Instru Method B 78 (2006) 244  
 [2] Ratheesh Kumar P.M. *et al.* J Appl Phys, 97 (2005) 013509

### 5.2.12 Modified structural, surface morphological and optical studies of $\text{Li}^{3+}$ swift heavy ions irradiation on zinc oxide nanoparticles

H. A. Khawal<sup>1</sup>, U. P. Gawai<sup>1</sup>, K. Asokan<sup>2</sup> and B. N. Dole<sup>1</sup>

<sup>1</sup>Advanced Materials Research Laboratory, Department of Physics, Dr. Babasaheb Ambedkar Marathwada University, Aurangabad-431 004, India

<sup>2</sup>Inter-University Accelerator Centre, Aruna Asaf Ali Marg, New Delhi-110 067, India

Nanoparticles of ZnO were synthesized by a co-precipitation method. The samples of ZnO were irradiated with 50 MeV  $\text{Li}^{3+}$  ions to fluences i.e.  $5 \times 10^{11}$  and  $1 \times 10^{13}$  ions/cm<sup>2</sup> with constant current of 1 pA. Structural parameters of pristine and SHI irradiated ZnO nanoparticles have been intervened by XRD. It was explicitly confirmed from XRD data that pristine and SHI irradiated ZnO samples show wurtzite structures. The particle size of pristine and SHI irradiated ZnO samples was estimated using XRD data and found in the range 20 nm to 22 nm. SEM images outline that pristine sample show spherical shapes, whereas SHI irradiated with  $5 \times 10^{11}$  ions/cm<sup>2</sup> fluence ZnO sample exhibit enlargement in grain size and  $1 \times 10^{13}$  ions/cm<sup>2</sup> fluence ZnO sample reflects rod like structure. The UV-Vis spectroscopy results show that reduction in the energy band gap which gives red shift with enhancing the  $\text{Li}^{3+}$  swift heavy ions irradiation on the ZnO nanoparticles.

The structural analysis of pristine and 50 MeV  $\text{Li}^{3+}$  ion irradiated with fluence  $5 \times 10^{11}$  and  $1 \times 10^{13}$  ions/cm<sup>2</sup> ZnO nanoparticles was carried out by using XRD technique as shown in Fig. 37(a). The X-ray diffraction peaks at (100), (002), (101), (103), (200), (112), (201) and (004) exhibit the formation of hexagonal wurtzite structure [1]. These diffraction peaks are well matched with Joint Committee on Powder Diffraction Standard (JCPDS) card no. 01-089-0510 with lattice constant  $a = 0.3296$ ,  $c = 0.52065$  nm. Peak broadening in the XRD pattern clearly indicates that small nanocrystals are present in the samples. Prominent peaks, (100), (002) and (101) appear at

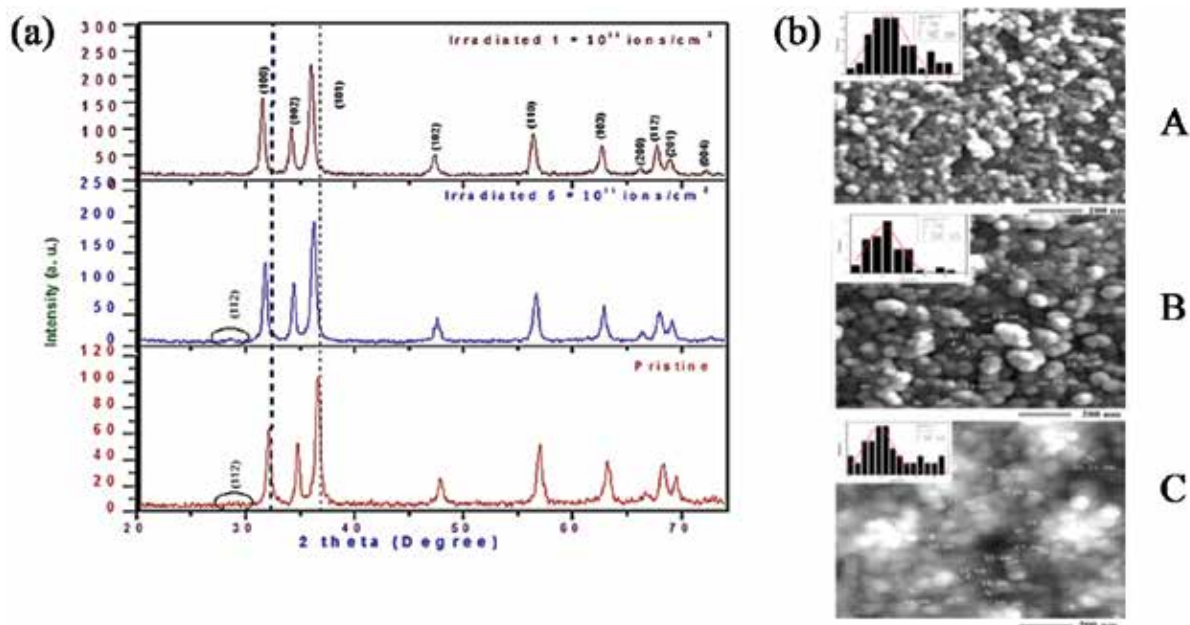


Figure 37 : (a) XRD patterns of pristine and irradiated of ZnO pellets. (b) SEM micrographs of ZnO pellets (A) Pristine (B) Irradiated at  $5 \times 10^{11}$  ions/cm<sup>2</sup> fluence (C) Irradiated at  $1 \times 10^{13}$  ions/cm<sup>2</sup> fluence.

$2\theta = 32.34, 34.83$  and  $36.59$  degrees respectively, which indicate that the samples are crystalline. One weaker peak (112) at  $2\theta = 28.73^\circ$  can also be seen at fluence  $5 \times 10^{11}$  ions/cm<sup>2</sup> in the XRD pattern, it is due to the  $\text{Mn}_2\text{O}_4$  impurity of the samples [2]. However, this peak disappeared at fluence  $1 \times 10^{13}$  ions/cm<sup>2</sup>. It is seen from XRD data, the peaks of a ZnO shift towards lower angles with increasing fluences on ZnO samples. Such shifts of the XRD peaks reveal a lattice expansion due to the irradiation of  $\text{Li}^{3+}$  ions on ZnO pellets. It was observed from XRD patterns that peak intensity increases as fluence is increased because for pristine ZnO sample intensity was 120 but for the sample irradiated to the fluences  $5 \times 10^{11}$  ions/cm<sup>2</sup> and  $1 \times 10^{13}$  ions/cm<sup>2</sup> the intensities are 250 and 300 respectively. Also, there is a decrease in the full width at half-maximum (FWHM) corresponding to all observed peaks in irradiated samples as compared to pristine ZnO. It was observed that there is small enhancement in lattice constant.

Scanning Electron Microscopic (SEM) images of pristine and  $\text{Li}^{3+}$  ion irradiated with different fluences of ZnO samples are shown in Fig. 37(b). Before irradiation, the pellets are observed to have regular uniform grain size nanoparticles (Fig. 37(A)). The pellets irradiated to a fluence of  $5 \times 10^{12}$  ions/cm<sup>2</sup> and  $1 \times 10^{13}$  ions/cm<sup>2</sup> show maximum change in the morphology, which is due to the inelastic collisions between the electrons of the target samples and the high energy ions. Sample irradiated to  $5 \times 10^{11}$  ions/cm<sup>2</sup> show that big spherical shape of grains as shown in Fig. 37(b)B. Fig. 37(b)C shows the irradiated pellets at high fluence  $1 \times 10^{13}$  ions/cm<sup>2</sup>. Here grains of the sample are arranged in a regular manner on the surface as a result of surface morphology, leading to the formation of pores and small rod like structures. Abhirami et al. [3] reported that SHI irradiated ZnO pellets exhibit agglomeration but in our investigation SHI irradiated ZnO samples at  $1 \times 10^{13}$  ions/cm<sup>2</sup> fluence evidently show rod like structure. The particle size of pristine and irradiated ZnO samples observed from SEM is in good agreement with particle size obtained by XRD data.

UV-visible absorption spectroscopy is widely being used technique to examine the optical properties of nanosized particles. The absorption spectra are recorded in the range of 300-800 nm at room temperature as shown in Fig. 38. Exciton absorption peak at 351, 352 and 354 nm are observed for pristine,  $5 \times 10^{11}$  ions/cm<sup>2</sup> fluence and  $1 \times 10^{13}$  ions/cm<sup>2</sup> fluence of  $\text{Li}^{3+}$  SHI irradiated respectively, which lie below the band gap wavelength of bulk ZnO particles of 358 nm ( $E_g = 3.46$  eV). It evidently reflects that the exciton absorption peaks are shifted towards the higher wavelengths on increasing the fluences. The energy band gap of pristine and irradiated at  $5 \times 10^{11}$  ions/cm<sup>2</sup> and  $1 \times 10^{13}$  ions/cm<sup>2</sup> fluences are calculated using Tauc's plots and their values are 3.11, 3.07 and 2.91 eV respectively. SHI irradiation resulted in the decrease in the band gap with an increase in the ion fluences, which confirms red shifting of the absorption edge due to the quantum confinement and size effects. This can be attributed to creation of cascade in the material after SHI irradiation, which in turn leads to the introduction of defect within the band gap. It must be pointed out here that a decrease in the energy band gap facilitates an easy passage of electrons from the conduction band and therefore leads to an increase in the electron flow in the irradiated samples as compared to the pristine sample. This property can be employed in various optoelectronic devices.

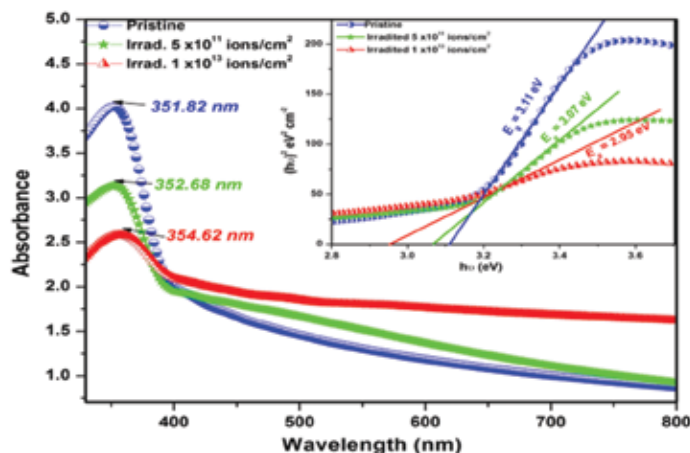


Figure 38 : UV-Vis absorbance spectra of (inset shows the Tauc's plot) pristine and  $5 \times 10^{11}$  ions/cm<sup>2</sup> and  $1 \times 10^{13}$  ions/cm<sup>2</sup>  $\text{Li}^{3+}$  ion irradiation on ZnO nanoparticles.

## REFERENCES

- [1] N.S. Ridhuan, R. K. Abdul, Z. Lockman, A. A. Abdul, PLoS ONE 7(11) (2012) e50405  
 [2] V. D. Mote, B. N. Dole, Advanced Materials Research 678, (2013) 234-238  
 [3] K. Abhirami, P. Matheswaran, B. Gokul, R. Sathyamoorthy and K. Asokan, IOP Conf. Ser.: Mater. Sci. Eng., 73 (2015) 012113

### 5.2.13 Synthesis, characterization and radiation response of HfO<sub>2</sub> based high-k dielectric materials

N. Manikanthababu, A. P. Pathak, and S. V. S. Nageswara Rao

School of Physics, University of Hyderabad, Hyderabad, India 500046.

In this work, we have studied the synthesis, characterization, radiation response and reliability of HfO<sub>2</sub> based MOS devices. HfO<sub>2</sub> samples prepared by ALD, RF magnetron sputtering (RF) and e-beam evaporation (EB) methods have been studied in this work. One of the main reasons for employing different growth techniques in this thesis has been to investigate the influence of growth techniques on the nature of defects and their evolution during irradiation studies. In brief, we have performed our studies on 1) the optimization of synthesis of HfO<sub>2</sub> thin films by a newly established RF magnetron sputtering system under different deposition conditions on different substrates. These samples have been characterized by several well established techniques [1], 2) the effects of gamma irradiation on the electrical properties of HfO<sub>2</sub>/Si MOSCAPs fabricated by both the RF magnetron sputtering and e-beam evaporation techniques [2,3] and 3) SHI induced diffusion of Hf across HfO<sub>2</sub>/SiO<sub>2</sub>/Si and HfO<sub>2</sub>/Si interfaces and the consequent effects on their electrical properties [4,5].

Good quality HfO<sub>2</sub> thin films were deposited on Si and quartz substrates after the optimization of the synthesis parameters. Au/HfO<sub>2</sub>/Si MOSCAPs have been fabricated by e-beam evaporation (EB) and RF magnetron sputtering techniques to study the gamma irradiation effects on their electrical properties [2,3]. Structural and electrical characterizations were performed on both sets of these samples. EB series samples have shown the presence of negatively trapped charges, whereas RF series samples have shown positively trapped charges. Both the sets of samples have shown similar behavior with gamma irradiation. Both the leakage current and accumulation capacitance have been found to increase with increase in the irradiation dose. Flat-band shift and increase in the width of the hysteresis in the C-V characteristics clearly indicate the increase of oxide trapped charge densities and changes in the slopes of these curves show the increase of interface traps. These studies provide useful information for understanding the gamma irradiation response of HfO<sub>2</sub> based MOSCAPs in view of their applications in radiation environments.

On the other hand, SHI induced intermixing effects on the structural properties and consequent effects on the electrical properties of HfO<sub>2</sub> based MOS devices have been studied [4,5]. ALD grown (H1, H2 and H3 series) HfO<sub>2</sub>/SiO<sub>2</sub>/Si and HfO<sub>2</sub>/Si samples deposited by RF magnetron sputtering technique (RF series) have been used for this study. In H2 (HfO<sub>2</sub>(2.5 nm)/SiO<sub>2</sub> (1 nm)/Si) series samples, the effects of 80 MeV Ni ion irradiation on this interface have been studied [4]. The thickness of this interlayer is also found to increase with increase in fluence. Corresponding changes in the composition of these interlayers have also been estimated. These observations together with XRR analysis confirm that SHI can induce inter-diffusion of Hf and Si across HfSiO/HfO<sub>2</sub> interface. The studies on H1 (HfO<sub>2</sub>(3 nm)/SiO<sub>2</sub> (0.6 nm)/Si) series also yielded similar results, wherein the thickness of the interlayer (HfSiO) has been found to increase with increase in the irradiation fluence as evidenced by HRBS and XRR measurements. In addition, the leakage current is found to decrease by one order upon irradiation, which can be attributed to the increase in the physical thickness of the interlayer. The samples were further processed by RTA at 600° C in N<sub>2</sub> atmosphere for 60 s for studying the annealing kinetics. The increase in the density of the defects during RTA processing might be responsible for the observed increase in leakage currents during the device operation. Further, 80 MeV Ni ion irradiation induced effects have been studied on the electrical properties of HfO<sub>2</sub>/Si samples. A systematic decrease in the leakage current density as a function of irradiation fluence has been observed. The effects of the defects together with the SHI induced intermixing effects on HfO<sub>2</sub>/Si MOS devices have been studied.

Promising and reliable in-situ electrical measurements were performed on the H3 ( $\text{HfO}_2(2.7 \text{ nm})/\text{SiO}_2(0.6 \text{ nm})/\text{Si}$ ) series samples using 120 MeV Ag ion irradiation and RF series samples by 120 MeV Au ion irradiation. These results unambiguously reveal the influence of SHI induced intermixing effects and the defect dynamics on the electrical properties of these devices. A systematic decrease in the leakage current and capacitance are evident from electrical properties. These in-situ measurements were further strengthened by HRBS measurements. Defects annealing/creation and SHI induced mixing have been observed. Hence, SHI can be used as an important tool in material modification with spatial selectivity to tune the structural and electrical properties. In essence, these studies provide some useful information for understanding the influence of swift heavy ion and gamma irradiation on the structural and electrical properties of  $\text{HfO}_2$  based high-k dielectric materials. The observed reduction in the leakage current and accumulation capacitance with increase in fluence under SHI irradiation are in contrast with the observed increase in these parameters with increase in dose in similar samples under gamma irradiation. Here it is important to note that the ion irradiation can induce structural modifications, like inter-diffusion of constituent elements, in addition to beam induced creation and annealing of defects. . This implies that the effects of structural modification caused by ions dominates the effects caused by simple point defects. Hence, these results are distinctly different from those of gamma irradiation effects. Both the ion and gamma irradiation together give the complete picture of possible modifications of the electrical properties of  $\text{HfO}_2$  based MOS devices when used in radiation environments.

## REFERENCES

- [1] K. C. Das *et al.*, *J. Mat. Sci.* 26 (2015) 6025
- [2] N. Manikanthababu *et al.*, *Rad. Eff. Def. Solids.* 170 (2015) 207
- [3] N. Manikanthababu, N. Arun, M. Dhanunjaya, S. V. S. Nageswara Rao and A. P. Pathak, *Rad. Eff. Def. Solids.* 171 (1-2) (2016) 77
- [4] N. Manikanthababu *et al.*, *Nucl. Inst. and Meth. in Phys. Res. B* 332 (2014) 389
- [5] N. Manikanthababu, M. Dhanunjaya, S. V. S. Nageswara Rao and A. P. Pathak, *Nucl. Inst. and Meth. in Phys. Res. B* 379 (2016) 230.

### 5.2.14 Synthesis of Nano-Crystalline Hafnium Oxide Thin Films by RF Magnetron Sputtering Technique and Ion Irradiation Effects

M. Dhanunjaya<sup>1</sup>, V. S. Vendamani<sup>1</sup>, S. V. S. Nageawara Rao<sup>1</sup>, D K Avasthi<sup>2</sup> and A. P. Pathak<sup>1</sup>

<sup>1</sup>School of Physics, University of Hyderabad, Hyderabad- 500046, India.

<sup>2</sup>Inter-University Accelerator Centre, Aruna Asaf Ali Marg, New Delhi-110 067, India

Nano-crystalline Hafnium Oxide thin-films have been successfully prepared by RF Magnetron Sputtering method. The  $\text{HfO}_2$  Nano-particles (NPs) / grains observed in these thin-films have been characterized by using High Resolution Transmission Electron Microscopy (HRTEM), Field Emission Scanning Electron Microscope (FESEM), UV-visible Absorption, Photo Luminescence (PL) measurements. These measurements were performed before and after Swift Heavy Ion (SHI) irradiation with 100 MeV Ag ions. HRTEM measurements confirm that the particles are non-spherical in nature with average particle size of 2.8 nm. Particle size is found to increase from 2.8 to 4.3 nm with fluence as shown in Fig. 39. The Selected Area Electron Diffraction (SAED) patterns confirms d spacing is 0.28 and 0.31 nm which correspond to (-111) and (111) directions as shown in Fig. 39(e) and 1(f).

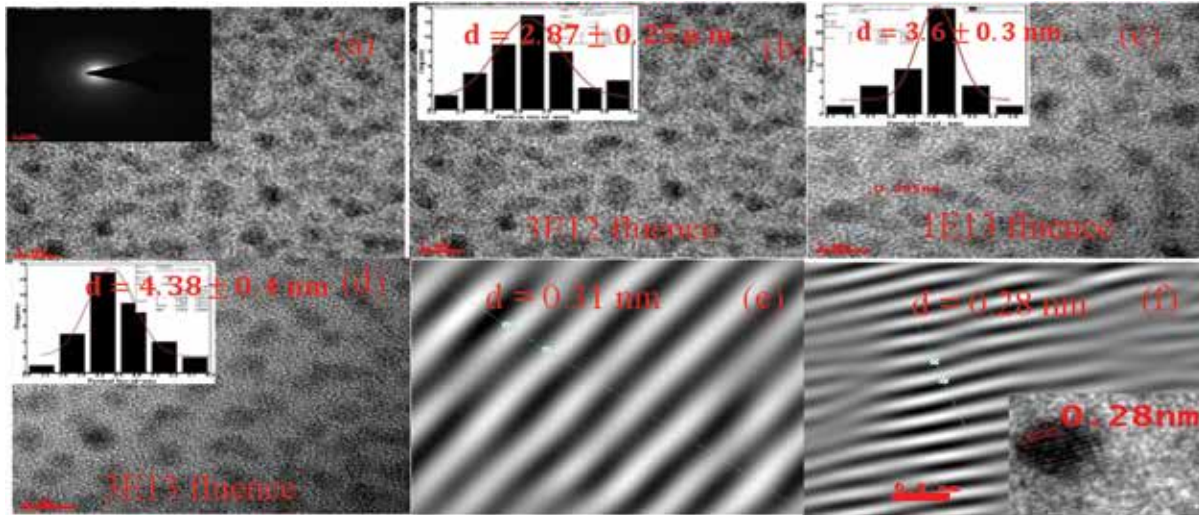


Figure 39 : HRTEM images of HfO<sub>2</sub> NPs: (a) as deposited sample (inset shows that Diffraction pattern) (b) with fluence  $3 \times 10^{12}$  ions/cm<sup>2</sup> (c) with fluence  $1 \times 10^{13}$  ions/cm<sup>2</sup> (d) with fluence  $3 \times 10^{13}$  ions/cm<sup>2</sup>, (e) inverse Fast Fourier Transform (FFT) of HfO<sub>2</sub> NPs for <-111> plane (f) inverse Fast Fourier Transform (FFT) of HfO<sub>2</sub> NPs for <111> plane (inset shows HRTEM image of HfO<sub>2</sub> NPs).

Before irradiation the PL measurement shows a broad emission peak around 410 to 450 nm. After irradiation the dominant emission peak is shifted to 390 nm and the intensity increases with increase in fluence as shown in Fig. 40(a)-(d). This PL emission is attributed to “O” related point defects [1-3]. The increase in the intensity of emission indicates an increase of defects in HfO<sub>2</sub> NPs. The orientation of the particles specifically at (-111), (111) directions and inter-planar spacing’s confirm the monoclinic phase. Further, GIXRD spectra confirm the same and increase in intensity of (-111) peak with increase of fluence is observed as shown in Fig. 40(e).

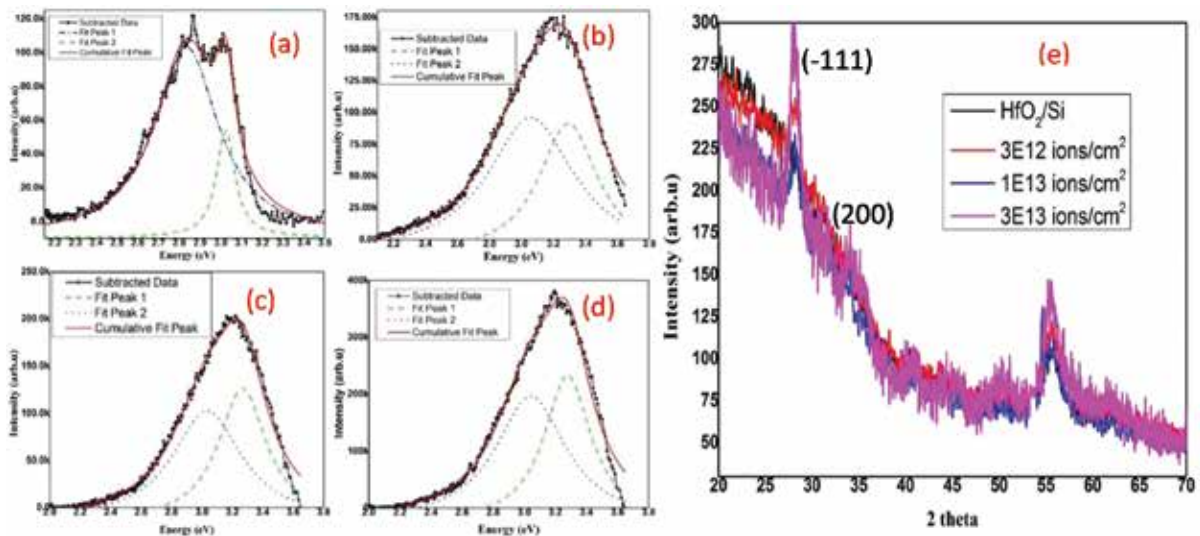


Figure 40 : Photoluminescence spectra: (a) as deposited (b) with fluence  $3 \times 10^{12}$  ions/cm<sup>2</sup> (c) with fluence  $1 \times 10^{13}$  ions/cm<sup>2</sup> (d) with fluence  $3 \times 10^{13}$  ions/cm<sup>2</sup>, (e) GIXRD pattern of as deposited and irradiated HfO<sub>2</sub> NPs on Si substrates.

We have synthesized thin-films of  $\text{HfO}_2$  NPs by using RF Magnetron sputtering method. As grown  $\text{HfO}_2$  NPs were amorphous and non-spherical. HRTEM measurements confirm the particle size as 2.8 nm. After irradiation the same particles become crystalline non-agglomerated and well dispersed. The HRTEM and SAED measurements confirm the mono-clinic phase of NPs. GIXRD measurements also confirm the same mono-clinic phase after irradiation. The particle size increases with irradiation fluence. PL emission band confirms the O vacancy defects. Before irradiation a broad emission band is observed in the visible range 2.2 to 3.1 eV. After irradiation, the emission peak shifted to a particular peak position and intensity is found to increase with increase in fluence. These observations confirm that irradiation induces a particular type of O vacancy defects.

## REFERENCES

- [1] G. Znamenski and V. A. Marchenko, Tech. Phys. 43 (1998) 766
- [2] Ran Jiang, Xianghao Du, Weideng Sun, Zuyin Han and Zhengran Wu, Scientific Reports 5 (2015) 15574
- [3] K.-H. Xue et al, Appl. Phys. Lett. 102 (2013) 201908.

### 5.2.15 Swift heavy ion induced modifications in $\text{GeO}_2$ thin films prepared by Pulsed Laser Deposition

Mahendra Singh Rathore<sup>1</sup>, Arun Vinod<sup>1</sup>, A P Pathak<sup>2</sup>, D K Avasthi<sup>3</sup>, F Singh<sup>3</sup>, A Rambabu<sup>4</sup>, and N.Srinivasa Rao<sup>1</sup>

<sup>1</sup>Department of Physics, Malaviya National Institute of Technology Jaipur, J.L.N. Marg, Jaipur-302017, India

<sup>2</sup>School of Physics, University of Hyderabad, Hyderabad- 500046, India

<sup>3</sup>Inter-University Accelerator Centre, Aruna Asaf Ali Marg, New Delhi-110 067, India

<sup>4</sup>Jawaharlal Nehru Centre for advanced Scientific Research, Bangalore- 560 064, India

$\text{GeO}_2$  is a very promising material due to its wide band gap (5.4-5.9 eV) which makes it a potential material for various applications in diverse fields such as fiber optics, thin film field effect transistors and optoelectronics devices [1]. There has been a great scientific interest to modify the properties of  $\text{GeO}_2$  thin films & Nano Crystals (NCs) to make them suitable for desired applications and tuning the properties using different methods plays an important role. Swift heavy ion (SHI) beam irradiation is one of the best techniques to tune and modify the properties of materials, nanocrystals and thin films by choosing appropriate ion energy and fluence [2,3]. Here, we report the effects of deposition parameters and 100 MeV Ag<sup>+7</sup> ions irradiation induced modification of structural properties of nanocrystalline  $\text{GeO}_2$  films.

The  $\text{GeO}_2$  thin films were prepared onto silicon substrate by pulsed laser deposition (PLD) technique, using 1 inch diameter of  $\text{GeO}_2$  target, in presence of oxygen pressure 300 mTorr at various substrate temperatures (varied from 100 to 500°C). Pristine samples were irradiated at fixed fluence  $1 \times 10^{13}$  ions/cm<sup>2</sup> with 100MeV Ag<sup>+7</sup> ions by using the 15UD Pelletron accelerator at Inter University Accelerator Centre (IUAC), New Delhi. Structural properties of pristine and irradiated films were characterized by X-ray diffraction. The functional group and phonon modes of samples have been investigated by FTIR spectroscopy and Raman Spectroscopy.

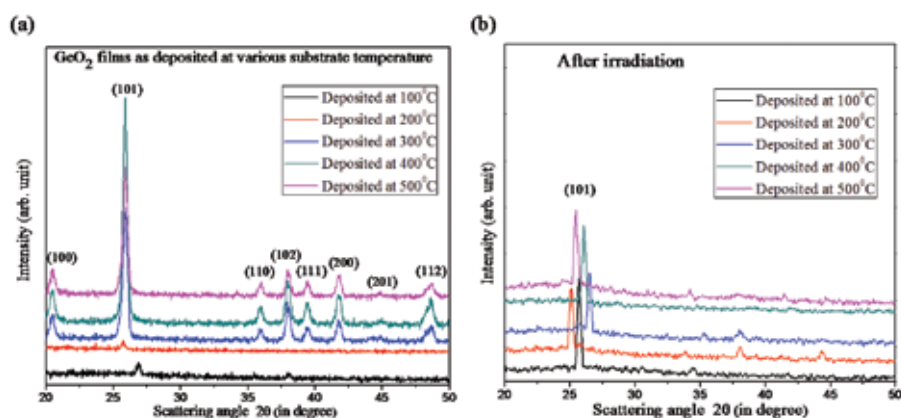


Figure 41 : XRD pattern of (a) as-deposited films at various substrate temperatures (before irradiation) (b) After irradiation

XRD pattern of as-deposited samples at various substrate temperatures have been shown here in Fig. 41(a). The film deposited at 100°C shows early stage crystallization, which gradually increases with an increase in substrate temperature. The spectra reveal that the films show hexagonal phase of crystalline GeO<sub>2</sub>. The XRD pattern of the SHI irradiated samples is presented in Fig. 41(b). It is observed that the SHI irradiated samples show shift in the peak position due to strain in the films. Some diffraction peaks have disappeared and intensity of few planes has reduced which indicates the partial amorphization of films due to higher fluence resulting in overlapping of the ion tracks [4]. Crystalline to partial amorphization of GeO<sub>2</sub> upon irradiation may be due to induced oxygen vacancies and non-stoichiometry in lattice. Further analysis and complementary investigations besides optical studies to validate the aforementioned results are under progress.

## REFERENCES

- [1] C.V. Ramana et al., Materials Science and Engineering B 174 (2010) 279-284
- [2] Swift Heavy Ions for Mat. Eng. and Nanostructuring, Springer Series in Mat. Sci. by D. K. Avasthi, G.K. Mehta, 145 (2011) 1
- [3] A. V. Krashennnikov and F. Banhart, Nature Materials 6 (2007) 723
- [4] S.X. Wang, Nucl. Instr. And Meth. B 615 (2001) 175–177

### 5.2.16 Swift Heavy Ion induced modification of structural, topographical and magnetic properties in zinc ferrite films

Lisha Raghavan<sup>1</sup>, Indra Sulania<sup>2</sup>, D K Avasthi<sup>2</sup>, M R Anantharaman<sup>1</sup>

<sup>1</sup>Department of Physics, Cochin University of Science and Technology, Cochin-682022, India

<sup>2</sup>Inter-University Accelerator Centre, Aruna Asaf Ali Marg, New Delhi-110 067, India

Zinc ferrite is a normal spinel and known for its antiferromagnetic properties with a Neel temperature of 10K [1]. In the nanoregime, zinc ferrite exhibits altogether different properties and the magnetic property changes from antiferromagnet to ferrimagnetic, superparamagnetic or spin glass [2-4]. These anomalies make zinc ferrite an interesting candidate to study. Swift heavy ion irradiation offers unique possibilities to modify material properties and can result in track formation in ferrites when the electronic energy loss exceeds a threshold value [5]. Ion irradiation can cause amorphisation of zinc ferrite thin films and the role of crystallinity on magnetism can be examined.

In the present study, zinc ferrite films prepared by RF sputtering were subjected to 100MeV Ag ion irradiation to fluences of  $1 \times 10^{12}$ ,  $1 \times 10^{13}$  and  $3 \times 10^{13}$  ions/cm<sup>2</sup>. Structural characterization was carried out using Glancing X Ray Diffractometer (GXRD). The topographical studies were conducted using Atomic Force Microscope (AFM). Both room temperature and low temperature magnetic measurements were performed using SQUID VSM.

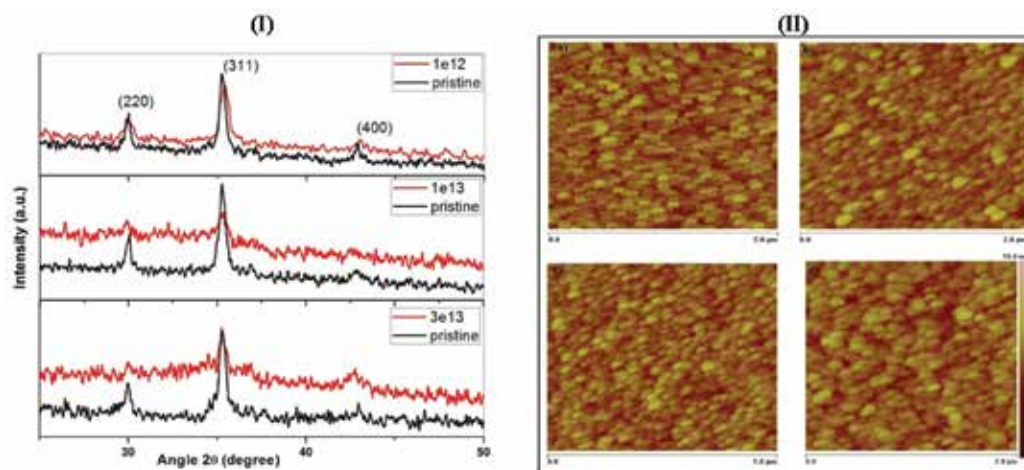


Figure 42 : (I) GXRD images of pristine and irradiated films, and (II) AFM images of a) pristine and film irradiated at fluences b)  $1 \times 10^{12}$  c)  $1 \times 10^{13}$  and d)  $3 \times 10^{13}$  ions/cm<sup>2</sup>

Structural characterization (Fig. 42 (I)) indicated amorphisation and subsequent reduction in particle size. At highest fluence of  $3 \times 10^{13}$  ions/cm<sup>2</sup>, crystallite size increased. The AFM images are shown in Fig. 42(II). The rms roughness decreases at lower fluence and thereafter increases for the highest fluence. At the highest fluence, the grains are agglomerated and cause an increase in surface roughness. The high energy imparted to the material initially breaks the grain and at higher fluence they diffuse through the surface and the grains are agglomerated. M-H loops were measured at room temperature and at 5K of pristine and irradiated films (Fig. 43). The pristine films show near saturation with a magnetisation of 45 emu/cc indicating ferrimagnetic behaviour of films. The  $1 \times 10^{12}$  ions/cm<sup>2</sup> irradiated samples show almost similar behaviour as that of pristine sample. On irradiating the sample to a fluence of  $1 \times 10^{13}$  ions/cm<sup>2</sup>, magnetisation reduced and at fluence of  $3 \times 10^{13}$  ions/cm<sup>2</sup> magnetisation increased to 22 emu/cc. Contrary to room temperature ferrimagnetic behaviour, the loops of pristine and film irradiated at  $1 \times 10^{12}$  ions/cm<sup>2</sup> were not saturating even at the maximum applied field of 60000 Oe. However films irradiated at  $1 \times 10^{13}$  ions/cm<sup>2</sup> and  $3 \times 10^{13}$  ions/cm<sup>2</sup> saturated at a field of 15000 Oe. The variation of magnetisation with fluence at 5K was similar to that of room temperature magnetisation with the pristine sample exhibiting higher value of saturation magnetisation.

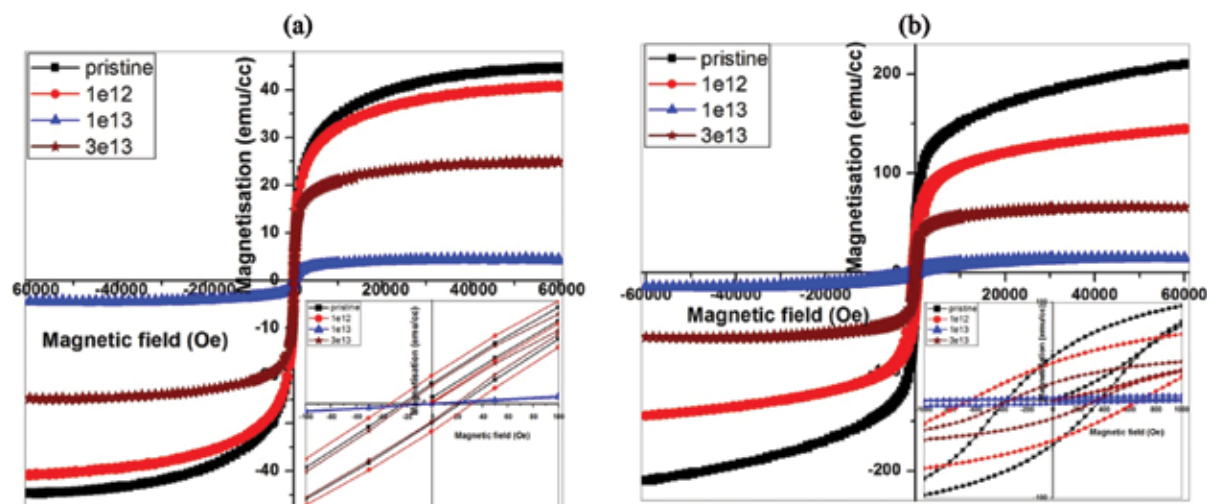


Figure 43 : MH loops of pristine and irradiated films a) at room temperature and b) at 5K

## REFERENCES

- [1] F. G Brockman, Phys. Rev.77 (1950) 841-842
- [2] S. Nakashima, K. Fujita, K. Tanaka and K. Hirao, J. Phys. Condens. Matter 17 (2005) 137-149
- [3] Y. Liang and H. Hsia, Nanoscale Research Letters 1 (2013) 1-8
- [4] S. D. Shenoy, P. A. Joy and M. R. Anantharaman, J. Magn. Magn. Mater. 269 (2004) 217-226
- [5] F. Studer et al., Nucl. Instr. and Meth. B82 (1993) 91-102

### 5.2.17 Effect of swift heavy ion irradiation on structure sensitive properties of Zr-based bulk amorphous alloys

Poonam Sharma<sup>1,2</sup>, A. Dhawan<sup>2</sup>, S. F. Naqvi<sup>2</sup> and S. K. Sharma<sup>1</sup>

<sup>1</sup>Department of Physics, Malaviya National Institute of Technology, Jaipur-302017, India

<sup>2</sup>Department of Physics, Anand International College of Engineering, Jaipur-303012, India

The effect of high energy heavy ion beam irradiation (100 MeV Ni<sup>7+</sup>) was studied on Zr-based amorphous alloys Zr<sub>59</sub>Nb<sub>3</sub>Cu<sub>20</sub>Al<sub>10</sub>Ni<sub>8</sub> and Zr<sub>59</sub>Ti<sub>3</sub>Cu<sub>20</sub>Al<sub>10</sub>Ni<sub>8</sub> at room and elevated temp. (200°C). The irradiation was carried out on the amorphous alloys using self-ions Ni<sup>7+</sup> to fluence of  $1 \times 10^{13}$  ions/cm<sup>2</sup> and  $1 \times 10^{14}$  ions/cm<sup>2</sup>. It was expected to get significant changes in the structure sensitive and mechanical properties of the alloys after irradiation at room and elevated temperature.

Fig. 44(a-b) shows the XRD pattern of as spun and irradiated  $Zr_{59}Nb_3Cu_{20}Al_{10}Ni_8$  ribbon alloys at different fluence rate and temp. Fig. 44(a) exhibited the presence of a broad halo peak, which indicates the amorphous nature of the alloy. Fig. 44(b) is a XRD pattern of  $Ni^{+7}$  ion irradiated  $Zr_{59}Nb_3Cu_{20}Al_{10}Ni_8$  ribbon sample with doses of  $1 \times 10^{13}$  and  $1 \times 10^{14}$  ions/cm<sup>2</sup> at room and elevated temperature i.e. 200 °C. It showed that no significant changes have been observed in the microstructure of glassy alloy at low fluence rate, whereas at higher fluence, comparatively sharp peak was observed which is possibly due to formation of nanocrystalline structure. To further elucidate the surface morphology of the alloy after irradiation, FE-SEM was carried out at high fluence rate.

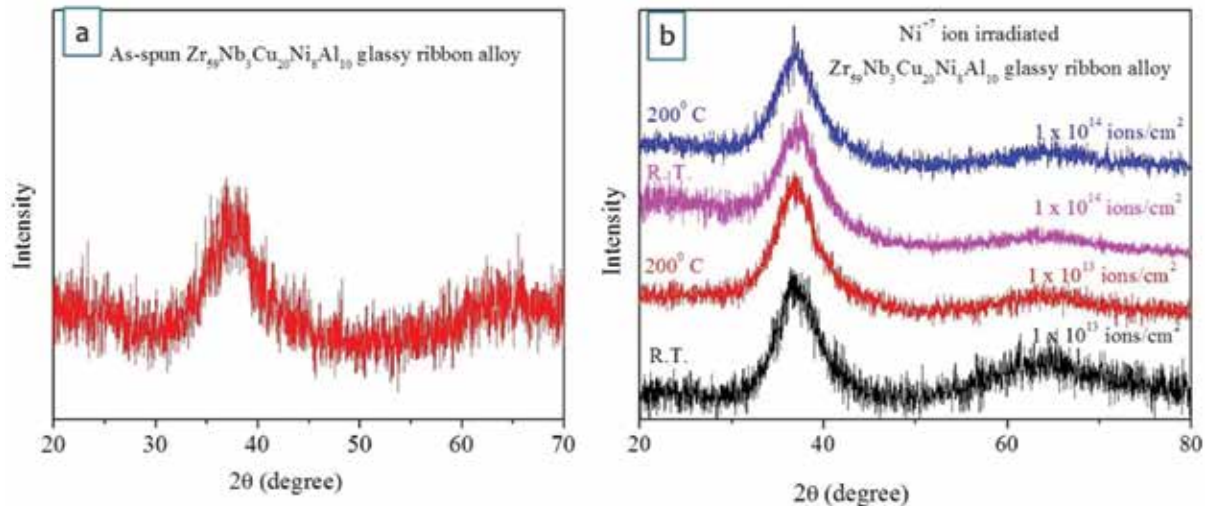


Figure 44 : XRD pattern of (a) as spun and  $Ni^{+7}$  ion irradiated  $Zr_{59}Nb_3Cu_{20}Al_{10}Ni_8$  glassy ribbon at (b)  $1 \times 10^{13}$  and  $1 \times 10^{14}$  ions/cm<sup>2</sup> dose at room and elevated temperature

Fig. 45 (a) revealed that the surface of as-spun glassy ribbon was smooth and clean. Fig. 45(b) shows the surface of irradiated  $Zr_{55}Cu_{30}Ni_5Al_{10}$  glassy ribbon to  $1 \times 10^{14}$  ions/cm<sup>2</sup> fluence at room temperature. Irradiation affected area can be seen in this micrograph. High magnification image of marked area is shown in Fig. 45(c) which indicates the initiation of nano-crystal formation. Fig. 45(d) is a micrograph of  $Ni^{+7}$  ion irradiated surface of  $Zr_{55}Cu_{30}Ni_5Al_{10}$  glassy ribbon at  $1 \times 10^{14}$  ions/cm<sup>2</sup> fluence at elevated temperature. It is found that at elevated temperature, micrographs exhibit the formation of nano-crystal structures which were clearly visible in high magnification image (Fig. 45(e)).

The electrochemical behavior and the mechanical properties of the alloy will be further carried out for selecting the material in the engineering applications.

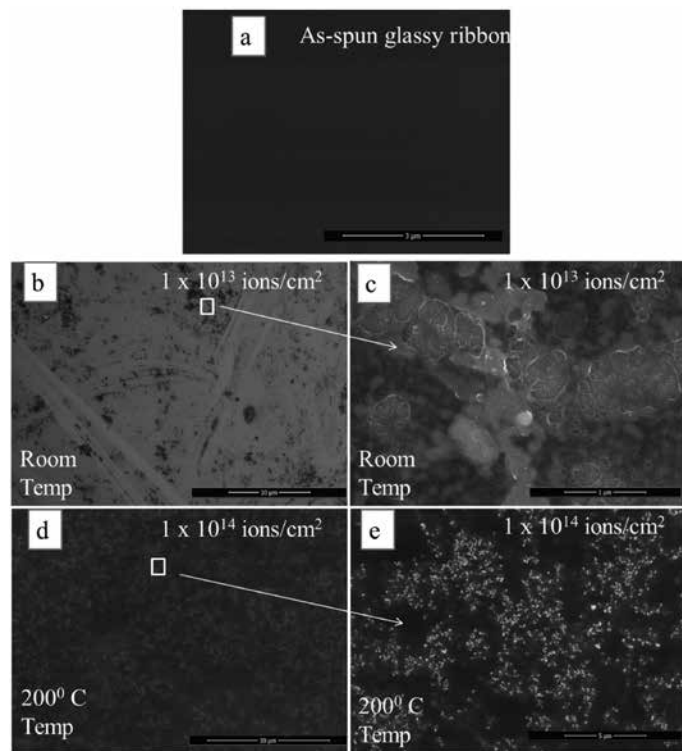


Figure 45 : The FE-SEM micrographs of as spun and irradiated  $Zr_{55}Cu_{30}Ni_5Al_{10}$  glassy ribbon to  $1 \times 10^{13}$  ions/cm<sup>2</sup> and  $1 \times 10^{14}$  ions/cm<sup>2</sup> fluence at room and elevated temperature (200°C).

### 5.2.18 Effect of Ag<sup>9+</sup> and O<sup>7+</sup> ion irradiation on the structural and magnetic properties of FeGa thin films

Nivedita L. Raveendran<sup>1</sup>, K. Asokan<sup>2</sup>, R. T. Rajendrakumar<sup>3</sup>

<sup>1</sup>Department of Physics, Bharathiar University, Coimbatore – 641046, India

<sup>2</sup>Inter-University Accelerator Centre, Aruna Asaf Ali Marg, New Delhi-110 067, India

<sup>3</sup>Department of Nanoscience and Technology, Bharathiar University, Coimbatore – 641046, India

FeGa thin films are of utmost importance in the research fraternity for their vast potentiality in numerous areas like actuators, sensors, transducers, spintronics etc. Thin films of Gallenol (FeGa) were prepared using two methods, DC magnetron Sputtering and Pulsed Laser Deposition (PLD). These films were subjected to high energy irradiation using Ag and O irradiation (Energy 120 MeV and 100 MeV respectively). The irradiation was carried out using the 15UD Pelletron accelerator with a beam current set at 1pna for both availed ion beams. The films were irradiated over five fluences ranging from  $5 \times 10^{10}$  to  $5 \times 10^{12}$  ions/cm<sup>2</sup>. It was found that the irradiation amorphized the thin films. The XRD data gives evidence to the irradiation induced amorphosity in the films with decreased intensity of the characteristic peaks with them being almost nonexistent at the highest fluence.

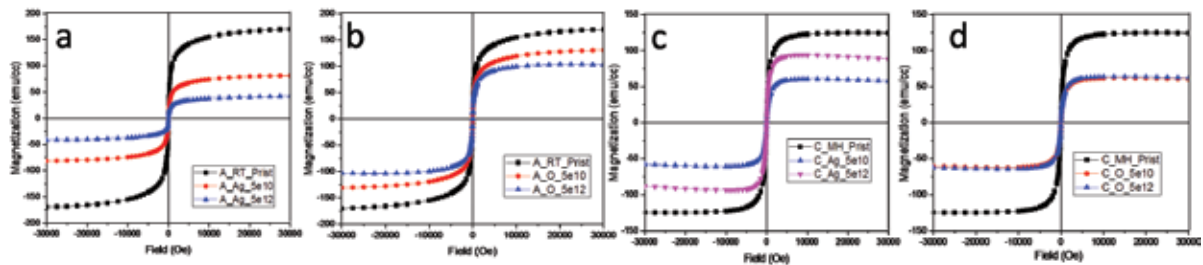


Figure 46 : In plane VSM hysteresis loops for the pristine and SHI irradiated FeGa films; a- RT Ag irradiated, b – RT O irradiated, c- 250 °C Ag irradiated, d- 250 °C O irradiated

The effect of irradiation is more prominent in the case of Ag ion irradiation than O, as expected. Analysis of magnetic moment (Fig. 46) with respect to applied field (sputtered samples) shows that post irradiation, the magnetic moment has reduced but the saturation field remains nearly the same. The magnetization of the pristine samples of room temperature and 250 °C deposited samples are 160 emu/cc and 120 emu/cc respectively. After irradiation, the magnetization values have come down to as low as 38 emu/cc for Ag ion irradiated samples.

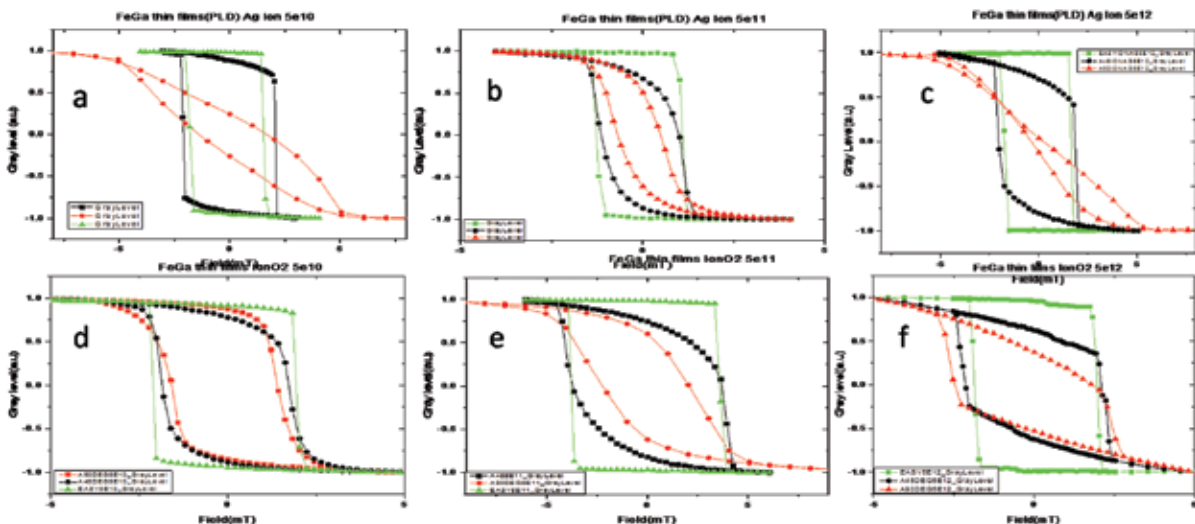


Figure 47 : MOKE hysteresis curves of pristine and Ag (a- $5 \times 10^{10}$ , b- $5 \times 10^{11}$ , c- $5 \times 10^{12}$ ) and O (d- $5 \times 10^{10}$ , e- $5 \times 10^{11}$ , f- $5 \times 10^{12}$ ) irradiated thin films

The surface magnetization properties of the PLD deposited films were measured using MOKE and interesting results have been obtained. There is noticeable reduction in the coercivity of the films post irradiation (Fig. 47). However, the intriguing result appears in the fact that the hysteresis loops measured are of different shapes for each samples post irradiation measured along hard axis of magnetization. This is because irradiation has induced anisotropy in the films. Detailed studies have to be carried out to understand more about the irradiation induced effects on these samples. Further analysis of the irradiation effects on the magnetic anisotropy and magnetostriction of these thin films are underway.

### 5.2.19 Comparison of thermoluminescence characteristics in $\gamma$ -ray and $C^{5+}$ ion beam-irradiated $LiCaAlF_6:Ce$ phosphor

M. M. Yerpude<sup>1</sup>, N. S. Dhoble<sup>2</sup>, S. P. Lochab<sup>3</sup>, and S. J. Dhoble<sup>4</sup>

<sup>1</sup>Department of Physics, RTM Nagpur University, Nagpur 440033, India.

<sup>2</sup>Department of Chemistry, Sevadal Mahila Mahavidyalaya, Nagpur 440009, India

<sup>3</sup>Inter-University Accelerator Centre, Aruna Asaf Ali Marg, New Delhi-110 067, India

In this work, a study on some thermoluminescence characteristics of  $LiCaAlF_6:Ce$  phosphor is presented. The samples in the form of pellets were irradiated at room temperature by a  $C^{5+}$  ion beam at energies of 50MeV and 75MeV for different ion fluences in the range of  $1.5 \times 10^{11}$  to  $3.0 \times 10^{13}$  ions per  $cm^2$ , using a 16MV Pelletron at IUAC. The full details of this set up are given by Kanjilal et al. [1]. Thermoluminescence (TL) measurements with heating rate 5 K/s were taken using Harshaw (3500) TLD reader. TL glow curve of  $C^{5+}$  ion beam irradiated phosphor at different fluences is shown in Fig. 48. A simple glow curve peaking at 330 °C was observed indicating that various types of defect centres are present in  $LiCaAlF_6:Ce$ . The LCAF doped with 1.0 mol% of Ce showed 8 times more sensitivity than commercially available  $CaSO_4:Dy^{3+}$  phosphor when irradiated with a carbon ion beam (Fig. 48 B).

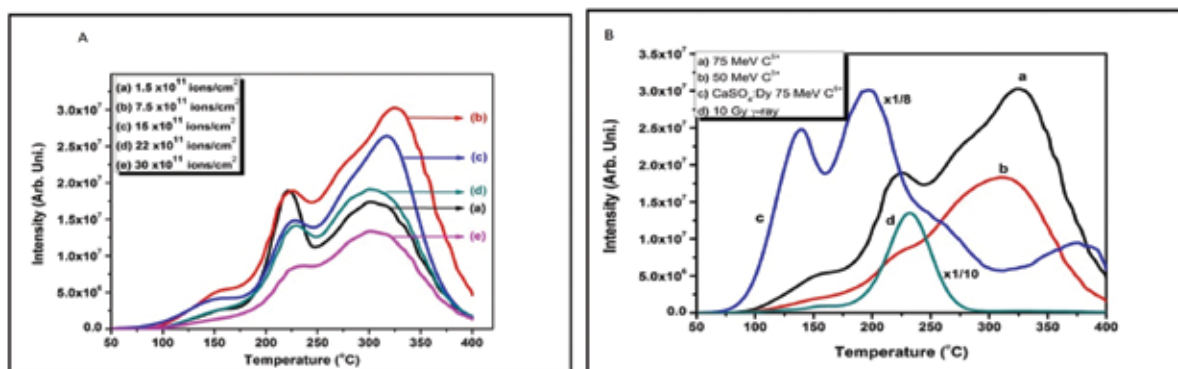


Figure 48 : A) TL glow curves of LCAF:Ce exposed to  $1.5 \times 10^{12}$  ions/ $cm^2$  fluence of (a) 75 MeV, (b) 50 MeV carbon ion beam and (d) 10 Gy  $\gamma$ -ray from  $^{60}Co$ . Curve (c) denotes TL glow curve of  $CaSO_4:Dy$  exposed to  $1.5 \times 10^{12}$  ions/ $cm^2$  fluence of (a) 75 MeV carbon ion beam. Curve (c) and (d) to be multiplied by the numbers at the curve to get the relative intensity. B) TL glow curve of LCAF:Ce(1 mole%) exposed to the different fluences of 75 MeV  $C^{5+}$  ion beam.

TL showed variation with enhancement in amount of dose imparted to LCAF:Ce phosphor. To study the effect of different doses on  $LiCaAlF_6:Ce$  phosphor, dose exposure was varied and it was observed that highest TL intensity occurred at around 1kGy irradiation followed by drop in TL intensity on further enhancement in doses. Also SRIM based calculations were performed to study the effect of  $C^{5+}$  ion beams on the samples of LCAF:Ce. SRIM calculation shows that F vacancies are highest in number. The range of 75MeV carbon ion beam inside the phosphor was calculated using SRIM and is shown in Fig. 49.A. From calculations it was observed that 75MeV C ion beam penetrates deeply and linear energy transfer (LET) value is 287 (MeV)/(mg/ $cm^2$ ) for 75 MeV C ion

beam. The vacancy distribution profile of carbon ion irradiated phosphor at 75MeV energy of C ion beam is shown in Fig. 49.B. The depth for maximum vacancies formation is 165.5  $\mu\text{m}$  at 75MeV energy of  $\text{C}^{5+}$  ion beam.

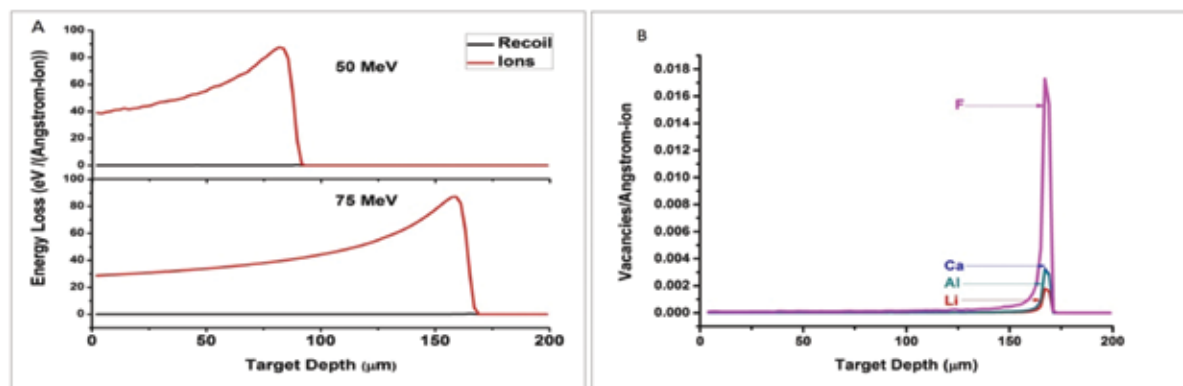


Figure 49 : A) Target ionization due to  $\text{C}^{5+}$  ion beam irradiation, at 50 and 75 MeV, as calculated by SRIM-2013. B) Vacancies formation in target LCAF:Ce after  $\text{C}^{5+}$  ion irradiation, as calculated by SRIM-2013.

## REFERENCES

- [1] D. Kanjilal, S. Chopra, M. M. Narayanan, I .S. Iyer, J .J. R .Vandana, S.K. Datta, Nucl. Instrum. Methods A 328 (1993) 97-100

### 5.2.20 $\text{Ni}^{12+}$ SHI irradiation induced modifications in morphology, structural and optical properties of polypyrrole nanotubes doped with *p*-TSA.

J. Hazarika and A. Kumar

Department of Physics, Tezpur University, Tezpur 784028, Assam, India

Polypyrrole (PPy) nanotubes doped with *p*-TSA have been synthesized using self-assembly polymerization method. Thin films of PPy nanotubes of thickness about 30-35  $\mu\text{m}$  mixed with inert polyvinyl alcohol (2 %) as stabilizer have been prepared for irradiation with 160 MeV  $\text{Ni}^{12+}$  ions. The range of the projectile ions has been calculated as 42  $\mu\text{m}$  and five different ion fluences  $10^{10}$ ,  $5 \times 10^{10}$ ,  $10^{11}$ ,  $5 \times 10^{11}$  and  $10^{12}$  ions/ $\text{cm}^2$  have been used for irradiation to investigate the ion fluence dependence on various properties of the irradiated PPy nanotubes.

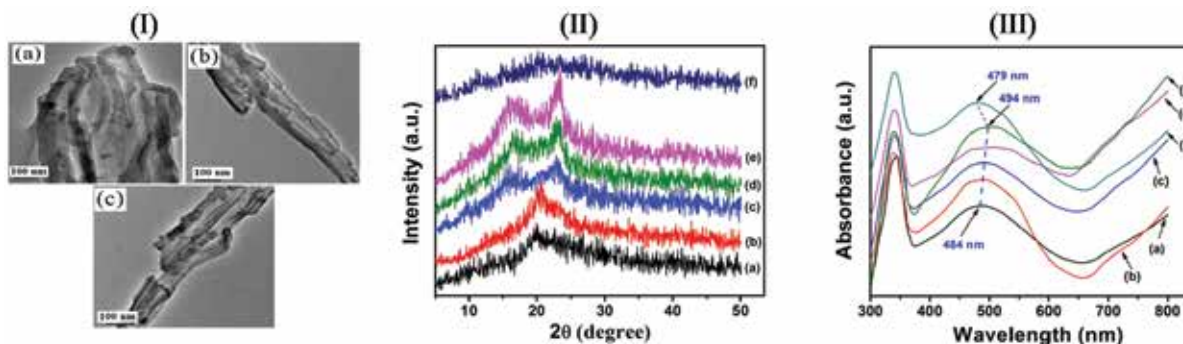


Figure 50 : (I)HRTEM micrographs of (a) pristine and irradiated PPy nanotubes at ion fluence of (b)  $5 \times 10^{11}$  and (c)  $10^{12}$  ions/ $\text{cm}^2$ . (II) XRD patterns of (a) pristine and irradiated PPy nanotubes at ion fluence of (b)  $10^{10}$ , (c)  $5 \times 10^{10}$ , (d)  $10^{11}$ , (e)  $5 \times 10^{11}$  and (f)  $10^{12}$  ions/ $\text{cm}^2$ . (III) UV-vis spectra of (a) pristine and irradiated PPy nanotubes at fluence of (b)  $10^{10}$ , (c)  $5 \times 10^{10}$ , (d)  $10^{11}$ , (e)  $5 \times 10^{11}$  and (f)  $10^{12}$  ions/ $\text{cm}^2$

The HRTEM micrographs as depicted in Fig. 50 (I) show that upon SHI irradiation, PPy nanotubes irradiated at ion fluence of  $5 \times 10^{11}$  ions/cm<sup>2</sup> become more aligned and denser as compared to the pristine PPy nanotubes. However, at the highest ion fluence of  $10^{12}$  ions/cm<sup>2</sup>, breaking or degradation of PPy nanotubes occurs, which results in the random alignments of PPy nanotubes. This happens due to deposition of huge amount of electronic energy ( $\sim 4.5$  keV/nm) along the ion track and whole crystalline domain structure is disrupted. This can originate from either the ion beam generated defects and dislocations or the grain splitting effect at the highest irradiation fluence of  $10^{12}$  ions/cm<sup>2</sup>, which dominates the induced alignment of the PPy nanotubes. In Fig. 50(II), the XRD diffraction patterns show that upon SHI irradiation, the PPy nanotubes form denser structure with enhanced crystallinity as compared to the pristine PPy nanotubes up to the ion fluence of  $5 \times 10^{11}$  ions/cm<sup>2</sup>. However, at and above the critical irradiation fluence of  $5 \times 10^{10}$  ions/cm<sup>2</sup>, new diffraction peak results at lower diffraction angle  $2\theta = 15.9^\circ$  indicating the formation of new crystalline domains with higher d-spacing and this crystallinity increases up to irradiation fluence of  $5 \times 10^{11}$  ions/cm<sup>2</sup>. At the investigated highest irradiation fluence of  $10^{12}$  ions/cm<sup>2</sup>, degradation or breaking of the PPy nanotubes occurs which results in the formation of amorphous structure at the highest ion fluence. The UV-vis absorption spectra as depicts in Fig. 50 (III) show that upon SHI irradiation, the polaron absorption band undergoes a red shift indicating the formation of conjugated structure (i.e. formation of free radicals, carbon-carbon double bonds etc.) and this red shifting increases with increasing the ion fluence up to  $5 \times 10^{11}$  ions/cm<sup>2</sup> [1, 2]. The red shifting of the absorption band indicates reduction in optical band gap energy of the irradiated PPy nanotubes. However, band gap increases at the highest ion fluence of  $10^{12}$  ions/cm<sup>2</sup>. The above results suggest that  $5 \times 10^{11}$  ions/cm<sup>2</sup> is the optimum irradiation fluence to enhance the different properties of PPy nanotubes in the present study.

## REFERENCES

- [1] G Compagnini, G Foti, R Reitano and G Mondio, Appl. Phys. Lett. 57 (1990) 2546  
 [2] H. S. Virk, Nucl. Instrum. Meth. B 183 (2001) 329

### 5.2.21 Effect of MeV ions irradiation on physical properties of polyethylene oxide films

Gnansagar B. Patel<sup>1</sup>, Shilpa Bhavsar<sup>1</sup>, N. L. Singh<sup>1</sup>, F. Singh<sup>2</sup>, P. K. Kulriya<sup>2</sup>

<sup>1</sup>Department of Physics, The M.S. University of Baroda, Vadodara, India-390002

<sup>2</sup>Inter-University Accelerator Centre, Aruna Asaf Ali Marg, New Delhi-110 067, India

Polyethylene oxide (PEO) is a semi crystalline, biodegradable, nontoxic and water soluble polymer having versatile applications [1]. The properties of PEO are being modified by ion beam irradiation for synthesis of hydrogel and to improve the properties of PEO based electrolytes by irradiation in controlled manner [2]. Swift heavy ion (SHI) beam causes irreversible modification of the physical properties due to significant electronic energy loss in PEO at macro-level. The level of modifications strongly depends on irradiation condition. In present report, the effects of 60 MeV carbon and 100 MeV nickel ions over physical properties of PEO film were carried out with two different fluences i.e.,  $1 \times 10^{11}$  and  $1 \times 10^{12}$  ions/cm<sup>2</sup>.

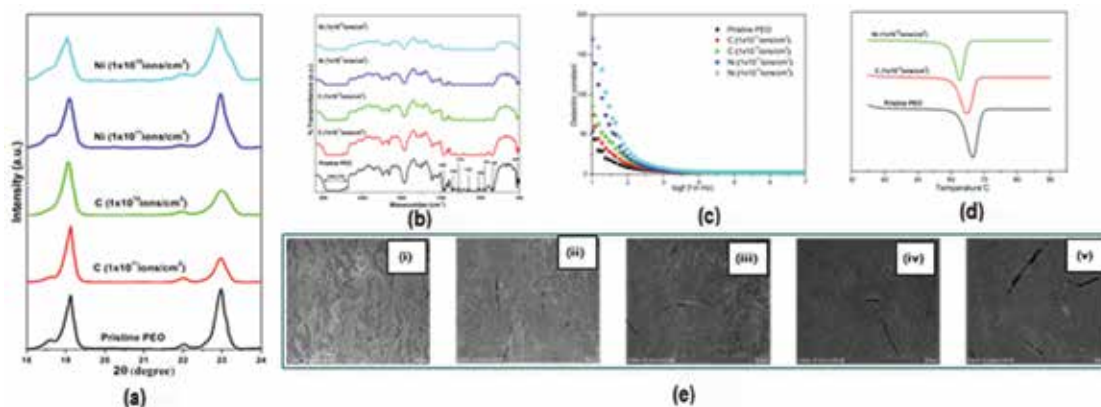


Figure 51 : (a) X-ray diffraction patterns, (b) FTIR spectra, (c) Dielectric constant vs. frequency, (d) DSC curve, and (e) SEM images of pristine and irradiated samples

In the x-ray diffraction patterns (Fig. 51(a)) of pristine and irradiated samples, PEO exhibits diffraction peaks at  $2\theta = 19.12^\circ$  and  $22.98^\circ$ . With the increase in ion fluence, the FWHM of the polymeric peak increases without any shifting in  $2\theta$  position, suggesting a decrease in crystallinity of PEO [1]. UV-vis spectra of the PEO exhibits blue shifting and broadening of the absorption edge. Also, there is a decrease in band gap ( $E_g$ ) and increase in cluster size ( $N$ ) observed upon irradiation attributed to decrease in conjugation length of polymer [3]. The decrease in band gap is about 9.1% and 30.8% due to carbon and nickel ions irradiation, respectively [1]. FTIR spectra (Fig. 51(b)) revealed that upon increase in irradiation fluence for both ions the intensity of prominent vibrational bands of PEO decreases, which is attributed to the scissioning of PEO chain yield and increase in amorphicity [4]. The degradation of PEO caused alteration in the structural properties of PEO due to ion beam induced defects and formation of some ion species [3, 4]. These changes enhanced dielectric properties of PEO as can be seen in Fig. 51(c). The DSC analyses (Fig. 51(d)) indicate degradation/amorphization of PEO upon SHI irradiation. SEM micrographs (Fig. 51(e)) point out decrease in surface roughness and damage of PEO's spherulites structure because of very high electronic energy deposition. At last, it should be noted that the nickel ion caused more impact over physical properties than that of carbon ion. Hence, it can be concluded that the physical properties of polymeric material could be effectively altered by varying the incident MeV ion beam parameter. For more details of the above study, see reference [1].

## REFERENCES

- [1] G. B. Patel, S. Bhavsar, N. L. Singh, F. Singh and P. K. Kuriya, Nucl. Instruments Methods Phys. Res. B 379 (2016) 156
- [2] R. J. Woods and A. K. Pikaev, Applied Radiation Chemistry: Radiation Processing, John Wiley & Sons, 1994
- [3] D. Fink et al., Radiat. Eff. Defects Solids 133 (1995) 193–208
- [4] N. Shah, D. Singh, S. Shah, A. Qureshi, N. L. Singh and K. P. Singh, Bull. Mater. Sci. 30 (2007) 477–480

### 5.2.22 Radiation Induced Effects on Biodegradable Solid Polymer Electrolyte

N. L. Singh<sup>1</sup>, Gnansagar B. Patel<sup>1</sup>, F. Singh<sup>2</sup>

<sup>1</sup>Department of Physics, The M.S. University of Baroda, Vadodara, India-390002

<sup>2</sup>Inter-University Accelerator Centre, Aruna Asaf Ali Marg, New Delhi-110 067, India

In the recent years, investigation on solid polymer electrolyte (SPE) has been attracting much scientific and technological importance in view of their application in electrochemical devices such as supercapacitors, electrochromic display devices, fuel cells, solid-state batteries, and sensors [1]. The main advantage of polymer electrolytes is the easy processing of preferred size and shape and its capability to form suitable electrode/electrolyte contact in electro-chemical devices [1, 2]. In the past decade, extensive efforts have been dedicated to improve the level of amorphosity in polymeric materials, for which many different techniques such as doping, blending, plasticization, and heavy ion radiation were used to moderate the crystallinity phase of polymer [2]. In the present work, swift heavy ion (SHI) beam were used for the modification of the material phase. SHI plays a vital role in the modification of the physical properties of SPE by depositing a large amount of energy within SPE system. In this study, the biodegradable SPE system were subjected to 60 MeV carbon and 100 MeV nickel ions by varying fluences i.e.,  $1 \times 10^{11}$ ,  $1 \times 10^{12}$  ions per  $\text{cm}^2$ .

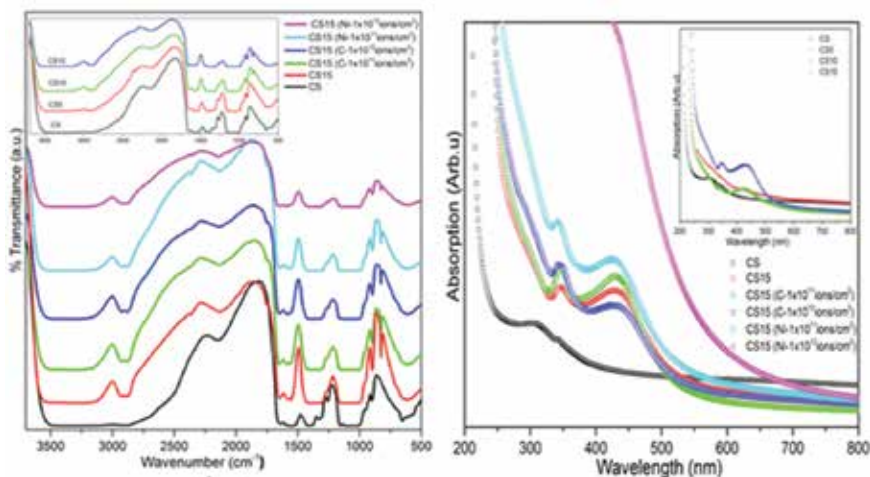


Figure 52 : (left) FTIR spectra and (right) absorption spectra of the pristine and irradiated SPE films

The FTIR spectra of pristine and irradiated SPE films were recorded in the transmission mode. Fig. 52(left) presents the FTIR spectra of the unirradiated and irradiated SPE films using C and Ni-ions. It is observed from the spectra that there is no major shifting of peak and no new mode of vibration appeared upon irradiation. This means that the overall polymeric structure remains same [3]. However, the decrease in transmittance intensity of peaks indicates the occurrence of the chemical bonds scission, formation of lowmolecular radicals and evolution of some gases due to irradiation [2, 3]. Strong Coulombic interactions among these charged species cause realignment of the molecular dipoles into a highly disordered state, reduction in H/C atom ratio and formation of conjugated bond. Fig. 52(right) shows the absorption spectra of the pristine and irradiated SPE films in the wavelength range 200–800 nm. Upon irradiation, absorption edge is initiated to shift monotonically towards longer wavelengths and widening of edge is observed as the irradiation dose increases. These changes can be attributed to the scission of hydrogen and enrichment of carbon rich network [4]. As a result, decrease in optical band gap and increase in carbon cluster size are observed which are responsible for the improvement in electrical properties of SPE system [4]. Also, these results suggest that the effects are more pronounced upon C-ion radiation compared to that of Ni-ion radiation.

Further supporting characterizations like measurement of dielectric properties, surface morphology and data analysis are in progress for drawing more conclusive features in this system.

## REFERENCES

- [1] M. F. Shukur, R. Ithnin and M. F. Z. Kadir, *Ionics* (Kiel) 20, (2014) 977–999
- [2] S. Raghu, K. Archana, C. Sharanappa, S. Ganesh and H. Devendrappa, *J. Non. Cryst. Solids* 426 (2015) 55–62
- [3] G. B. Patel, S. Bhavsar, N. L. Singh, F. Singh and P. K. Kulriya, *Nucl. Instruments Methods Phys. Res. B* 379 (2016) 156
- [4] C. Gavade, N. L. Singh, P. K. Khanna and S. Shah, *J. Nanosci. Nanotechnol.* 15 (2015) 9726–9731

### 5.2.23 Influence of Ion Beam Irradiation in microstructure related properties of polymer blend nano composite solid electrolytes

Subir Kumar Patla<sup>1,2</sup>, R. Ray<sup>2\*</sup>, M. Mukhopadhyay<sup>1</sup>, K. Asokan<sup>3</sup>, and D. Sen<sup>3</sup>

<sup>1</sup>Jadavpur University, Physics Department, Kolkata – 32

<sup>2</sup>Physics Department, Gurudas College, Kolkata – 54

<sup>3</sup>Inter-University Accelerator Centre, Aruna Asaf Ali Marg, New Delhi-110 067, India

Present study investigates the effect of ion beam irradiation on structural, dielectric and microstructure related properties of nano-composite solid polymer electrolytes based on Poly-[Ethylene oxide] (PEO) – Poly[vinylidene fluoride] (PVDF) blend systems. Free standing films (~ 0.1-0.3 mm thickness), designated as *D(1-x)P(x)GIK5S3*, comprising of x% Poly(Ethylene Oxide) (PEO) & (1-x)% Poly[vinylidene fluoride] (PVDF), 1wt% (of polymer) [Poly (Ethylene Glycol) (PEG)] as plasticizer, 3wt% insulating nano (~ 7 – 9 nm) filler (SiO<sub>2</sub>) and 5wt% salt (KBr) dissolved in DMF, has been prepared by solution casting technique. Studies are reported primarily on two polymer blend compositions [PVDF: PEO (80:20) and (20:80)] and these films were irradiated with 80 MeV oxygen ion beam of three different fluences: a) BEAM1-5×10<sup>10</sup> ions/cm<sup>2</sup>, (b) BEAM2 - 1×10<sup>11</sup> ions /cm<sup>2</sup> and (c) BEAM3 - 5×10<sup>11</sup> ions /cm<sup>2</sup> using IUAC Pelletron.

The X-ray diffraction patterns of composite polymer samples as function of PVDF and PEO percentages are presented in Fig. 53(a) and (b) for *D8P2GIK5* systems. New crystalline peaks appear in due to ion beam producing significant enhancement in effective crystallinity. The SEM images for these systems are shown in Fig. 54.

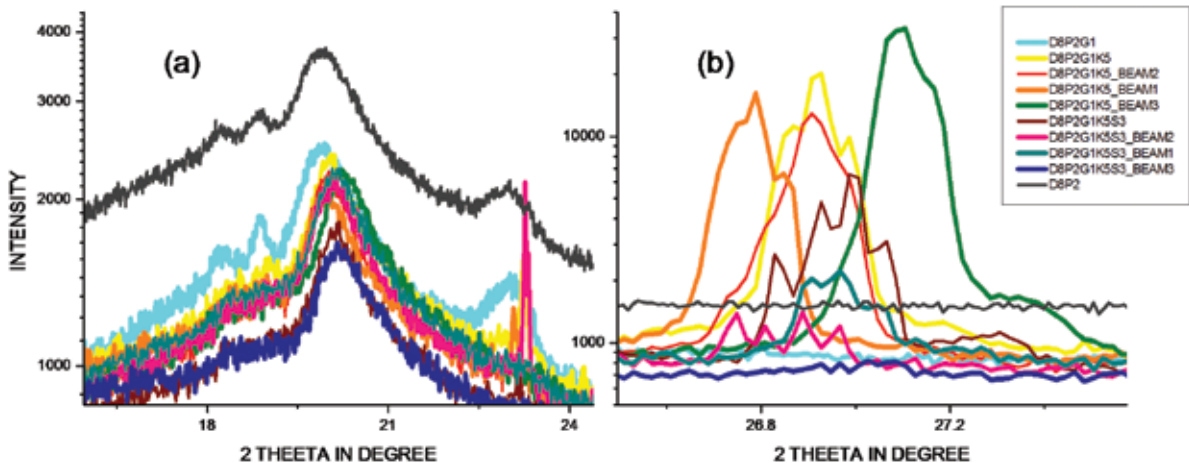


Figure 53 : X-ray diffraction studies of PEO-PVDF nano composite systems: (a) 2θ ~ 20° and (b) 2θ ~ 26°

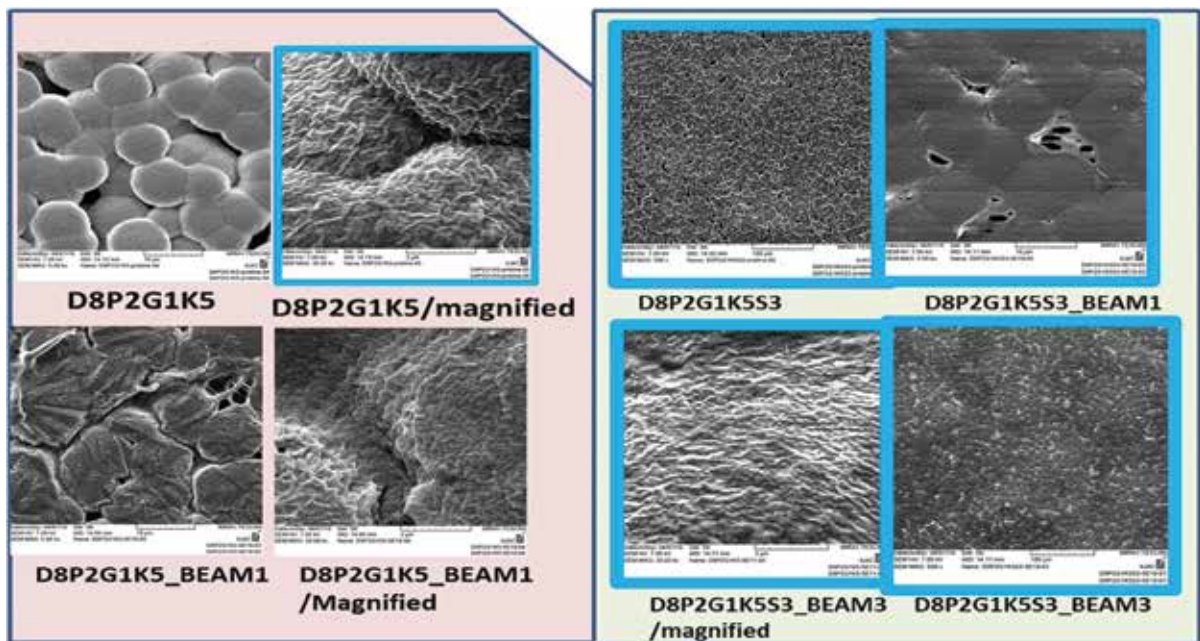


Figure 54 : FESEM micrographs of pristine and ion beam irradiated samples of PEO-PVDF composites

The dc conductivity of the pristine *D8P2G1K5* system appears to be maximum ( $\sim 10^{-7} \text{S/cm}$  at room temperature) and decreases with ion beam irradiation depending on the degree of fluences. Perturbation by high energy beam produces complex morphology inhibiting easy transportation of mobile ions leading to reduction in dc conductivity. The signature of complex morphology of *D8P2* system is reflected by the distributed relaxation time as obtained in Fig. 55.

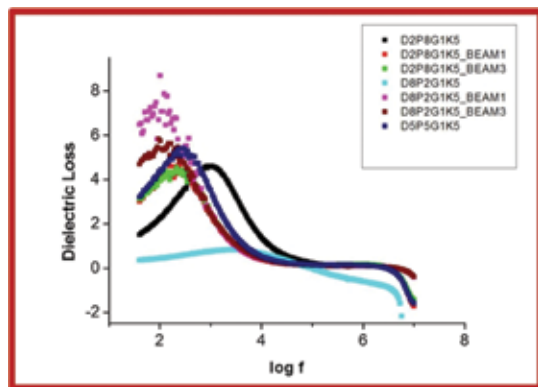


Figure 55 : Dielectric loss as a function of frequency for polymer composites

In summary, the present study have shown the structure – property correlation of PEO-PVDF polymer composite system subjected to high energy ion beam irradiation. Ion irradiation induces complex microstructure of enhanced crystallinity that hinders the ionic pathways and the associated ionic conductivity is found to reduce. The vibrational signatures of PEO-PVDF copolymer is close to the polymer whose content is higher in the matrix. Usage of ion beam in tailored manner could enable the application of such composites for certain specific electrochemical applications with improved dielectric properties.

## REFERENCE

- [1] M. H. A. Rahaman et al., Phys. Chem. Chem. Phys. 16 (2014) 11527-11537
- [2] S. Ramesh, O. P. Ling, Polym. Chem. 1(2010) 702–707
- [3] M. Sethupathy, V. Sethuraman, P. Manisankar, Soft Nanoscience Letters 3(2013) 37–43

### 5.2.24 Electronic Excitation Induced Modifications of Optical and Morphological Properties of PCBM Thin Films

T. Sharma<sup>1</sup>, R. Singhal<sup>1</sup>, R. Vishnoi<sup>2</sup>, P. Sharma<sup>1</sup>, A. Patra<sup>3</sup>, S. Chand<sup>3</sup>, G. B. V. S. Lakshmi<sup>4</sup>, S. K. Biswas<sup>5</sup>

<sup>1</sup>Department of Physics, Malaviya National Institute of Technology, Jaipur-302017, India.

<sup>2</sup>Department of Physics, Vardhman P.G. College, Bijnor- 246701, U.P, India.

<sup>3</sup>National Physical Laboratory, New Delhi 110012, India.

<sup>4</sup>Inter-University Accelerator Centre, Aruna Asaf Ali Marg, New Delhi-110 067, India

<sup>5</sup>Department of Metallurgical and Materials Engineering, Malaviya National Institute of Technology, Jaipur-302017, India

The present work highlights the effect of high energy ion beam irradiation on Phenyl C61 butyric acid methyl ester (PCBM) thin films. PCBM is a fullerene derivative and most commonly used in organic photovoltaic devices both as electron acceptor and transporting material [1] due to high electron mobility and higher electron affinity. PCBM consists of phenyl ring and Butyric acid methyl ester side chain attached to a C<sub>60</sub> cage. This side chain improves the solubility or solution processibility of PCBM molecules in different solvents such as chloroform, chlorobenzene and dichlorobenzene etc. than C<sub>60</sub> molecules [2]. In this study, the spin coated thin films of PCBM (on two different substrates viz. glass and double sided polished silicon) were irradiated using 90 MeV Ni<sup>7+</sup> swift heavy ion beam at low fluences ranging from 1×10<sup>9</sup> to 1×10<sup>11</sup> ions/cm<sup>2</sup> using 15 UD Pelletron accelerator IUAC.

The pristine and irradiated PCBM thin films were characterized using UV-Visible absorption spectroscopy, FTIR spectroscopy and AFM results to investigate the optical and morphological properties. The UV-visible absorption spectra (Fig. 56(a)) shows the intense absorption peak of PCBM films at 335 nm which arises due to interband transition among the  $\pi$  orbitals. The optical band gap calculated using Tauc's relation for the pristine film is 2.1 eV which decreases upto 1.8 eV at the fluences of 1×10<sup>11</sup> ions/cm<sup>2</sup>. The FTIR spectra (Fig. 56(b)) depicted that with ion irradiation at highest fluence (1×10<sup>11</sup> ions/cm<sup>2</sup>), the band intensity corresponding to different vibration is decreased in a fraction with respect to the intensity of pristine film bands. The considerable decrease in the intensity of C-O bond and C=O bond indicates that the side chain of butyric acid methyl ester and phenyl ring were also affected due to high energy ion irradiation but structure is not completely destroyed. The AFM images in Fig. 56(c) indicate that the surface morphology of PCBM thin films is also considerably affected by the high energy ion irradiation. All the observed affect are due to the effective chain reaction due to polymerization which was induced by high energy ion irradiation. The electronic excitation, induced by the high energy ions, produces radicals in C<sub>60</sub> molecules. These radicals initiate the cycloaddition reactions in fullerene molecules which leads to the chain reaction and polymerization in PCBM [3,4].

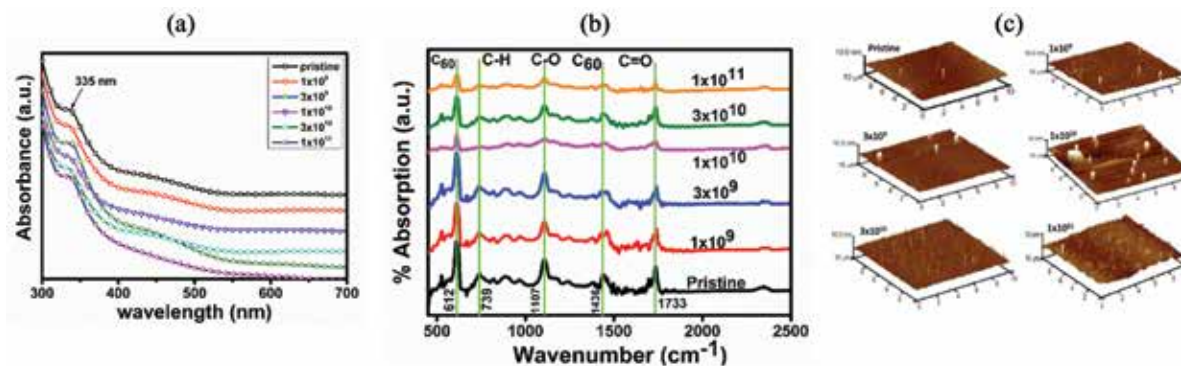


Figure 56 : (a) UV-visible absorption spectra, (b) FTIR spectra and (c) AFM images of pristine and irradiated PCBM thin film

## REFERENCES

- [1] Y. Kim et al., Nat. Mater. 5 (2006) 197
- [2] J.C. Hummelen, B.W. Knight, F. LePeq, F. Wudl, J. Yao, C.L. Wilkins, J. Org. Chem. 60 (1995) 532
- [3] A.M. Rao et al., Science 259 (1993) 955
- [4] P. Zhou, Z.-H. Dong, A.M. Rao, P.C. Eklund, Chem. Phys. Lett. 211 (1993) 337.

### 5.2.25 Structural and optical properties of porous silicon prepared by anodic etching of irradiated silicon

V.S. Vendamani, S.V.S. Nageswara Rao, A.P. Pathak

School of Physics, University of Hyderabad, Hyderabad 500 046, India

Low-dimensional/nanocrystalline silicon finds several technological applications as it can exhibit photoluminescence and electroluminescence in the visible region [1,2]. This work demonstrates a detailed study on the change in structural and optical properties of porous silicon under different experimental conditions. The pSi samples were prepared by anodic etching of Si in aqueous HF based electrolytic solutions. It is possible to tailor the structural and optical properties of pSi by controlling the various etching parameters during anodization [3].

Boron doped (p-type, 1-10  $\Omega$ -cm) single crystalline silicon (100) wafers were used to study the effect of etching current densities on the formation of pSi layers in terms of their structural and optical properties [1-3]. The cleaned Si samples were subjected to Swift heavy ions (SHI) irradiation (80 MeV Ni ions) at various fluences ranging from  $1 \times 10^{11}$  to  $5 \times 10^{13}$  ions/cm<sup>2</sup> prior to anodization process. FESEM measurements confirm the formation of uniform sponge like surface of pSi layers prepared by using pre-irradiated Si with different fluences [4].

To achieve low loss silicon photonic components, it is important to study the underlying mechanisms that can influence the surface roughness of pSi prepared at different *pre-irradiation* fluences. From Fig. 57(a), it can be clearly seen that, the root mean square (RMS) roughness of anodized sample decreases monotonically as a function of *pre-irradiation* dose. The PL spectra of pSi samples have been measured within 24 hrs after the anodization of irradiated crystalline silicon (at different fluences), which are shown in Fig. 57(b). These spectra indicate that, the PL peak position shifts towards higher wavelength (red shift) region as a function of ion fluence. This might be due to increased nanocrystalline skeleton between the pore walls. This observation is in good agreement with the quantum confinement model. The quantitative estimation of layer thickness and refractive index of porous silicon layers fabricated using *pre-irradiated* Si with different fluences, are shown in Fig. 57(c). These measurements have been performed by single wavelength (632 nm) He-Ne laser ellipsometry setup. The thickness of pSi layers is found to decrease as a result of increased defect density in the *pre-irradiated* Si.

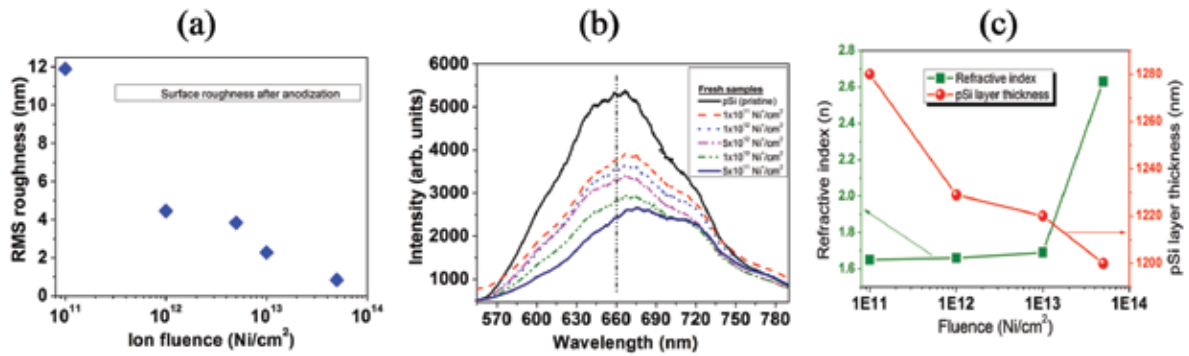


Figure 57 : (a) RMS roughness, (b) PL spectra, and (c) Layer thickness and refractive index (n) of pSi prepared at different pre-irradiation fluences

The increased defect density slows down the formation of porous silicon via reduced hole transport and hence reduces the resulting layer thickness. This study provides useful information for the process of silicon micromachining and optoelectronic applications.

## REFERENCES

- [1] L.T. Canham, Appl. Phys. Lett. 57 (1990) 1046
- [2] V. Lehmann, "Electrochemistry of Silicon: Instrumentation, Science, Materials and Applications", Wiley-VCH Verlag GmbH, Munchen, Germany (2002)
- [3] V. Parkhutik, Solid-State Electron. 43 (1999) 1221
- [4] V. S. Vendamani, A. P. Pathak, and S. V. S. Nageswara Rao, Nucl. Inst. Meth. B 315 (2013) 188-1915

### 5.2.26 Fabrication of porous silicon based tunable distributed Bragg reflectors by anodic etching of irradiated silicon

V.S. Vendamani<sup>1</sup>, Z.Y. Dang<sup>2</sup>, P. Ramana<sup>1</sup>, A.P. Pathak<sup>1</sup>, V.V. Ravi Kanth Kumar<sup>3</sup>, M.B.H. Breese<sup>3</sup>, and S.V.S. Nageswara Rao<sup>1</sup>

<sup>1</sup>School of Physics, University of Hyderabad, Hyderabad 500046, India

<sup>2</sup>Department of Physics, Centre for Ion Beam Applications (CIBA), National University of Singapore, Singapore 117542, Singapore

<sup>3</sup>Department of Physics, Pondicherry University, Puducherry 605014, India

Nanostructured porous silicon is an efficient material to meet the requirements of silicon based industry to integrate many opto-electronic functions on a single chip. Porous silicon (pSi) has been investigated extensively as a possible candidate for developing waveguides, light emitting diodes and distributed Bragg reflectors (DBR) etc. [1-5]. Porous silicon multilayers can be prepared by a stack of alternate pSi layers that are etched with different current densities. Porous silicon multilayers attained much attention for the fabrication of DBR structures because the refractive index and thickness of the layers can be altered by changing the etching parameters during etching process [6].

Porous silicon based DBR structures are fabricated by a stack of alternate high and low refractive index layers [7]. The silicon samples were anodically etched with two alternate current densities viz, 5 and 45 mA/cm<sup>2</sup> to fabricate variable refractive index layers. The optical images of pSi multilayers (DBR) that are designed to reflect different wavelengths have been shown in Fig. 58(a). FESEM cross-sectional images of different wave reflectors

are presented in Fig. 58(b). From this image, it can be clearly seen that the bright and dark strips correspond to low and high porosity layers. The reflection spectra of different wavelength reflectors are presented in Fig. 58(c).

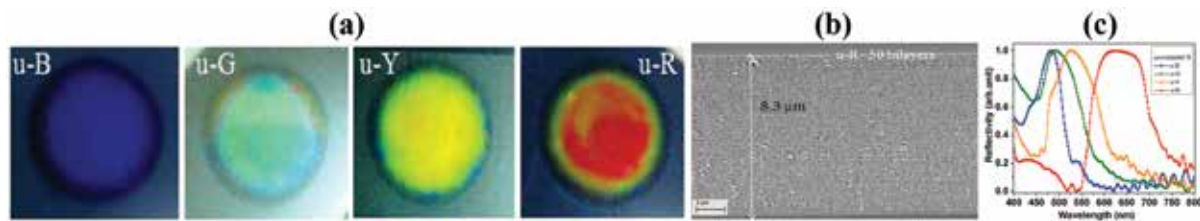


Figure 58 : (a) Optical images of pSi multilayers (DBR) designed at different wavelengths, (b) FESEM images and (c) Reflection of distributed Bragg reflector

To fabricate tunable wave reflectors from pSi based DBR structures, initially a set of Si samples were irradiated by 100 MeV Ag ions at a fluence of  $3 \times 10^{12}$  ions/cm<sup>2</sup> and the other set of samples were irradiated by gamma radiation with dose of 6 kGy. The irradiation induced effects on the reflection spectra (g- and s- series) are shown in Fig. 59.

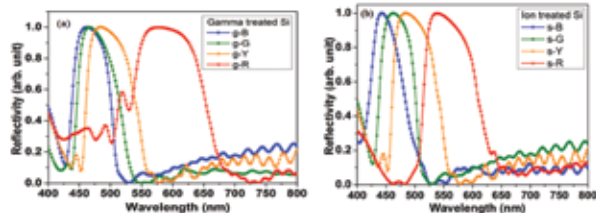


Figure 59 : Reflection spectra of pSi DBRs prepared with DBRs prepared under a) ion and b) gamma irradiated Si samples

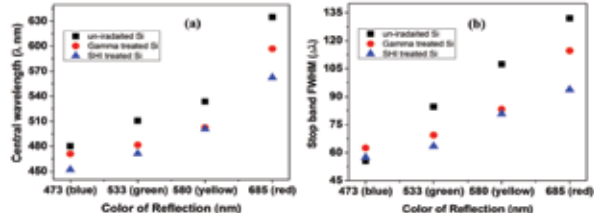


Figure 60 : a) Change in reflection central wavelength b) stop band width of pSi different etching conditions.

As shown in Fig. 60(a), the central wavelengths of irradiated samples are found to shift towards the lower wavelength region as compared to un-irradiated samples (u- series) and the corresponding stopbands are shown in Fig. 60(b). This study is expected to provide useful information for fabricating tunable wave reflectors for optical communication and other device applications.

## REFERENCES

- [1] H. F. Arrand, T. M. Benson, P. Sewell and A. Loni, *J. Lumin.* 80 (1998) 199
- [2] G. Rong, J. J. Saarinen, J. E. Sipe and S. M. Weiss, *Mat. Res. Soc. Symp. Proc.* 934 (2006) 0934-110-04
- [3] K. Nishimura and Y. Nagao, *J. Porous Materials* 7 (2000) 119
- [4] D. Mangaiyarkarasi, M. B. H. Breese, Y. S. Ow and C. Vijila, *Appl. Phys. Lett.* 89 (2006) 021910
- [5] L. Pavesi et al., *Optics and Lasers in Engineering* 39 (2003) 345
- [6] L. Pavesi, "Porous silicon dielectric multilayers and microcavities", *Rivista Del Nuovo Cimento* 20 (1997) 1
- [7] V.S. Vendamani et al., *Nucl. Inst. Meth. B* 358 (2015) 105-111

## 5.2.27 80 MeV Nitrogen ion irradiation effects on the I-V characteristics of NPN rf Power Transistors

T. M. Pradeep<sup>1</sup>, N. H. Vinayakaprasanna<sup>1</sup>, K. C. Praveen<sup>2</sup>, B.C. Hemaraju<sup>1</sup>, Arshiya Anjum<sup>1</sup>, N. Pushpa<sup>3</sup>, K. Asokan<sup>4</sup>, Ambuj Tripathi<sup>4</sup>, K.G. Bhushan<sup>5</sup> and A. P. Gnana Prakash<sup>1</sup>,

<sup>1</sup>Department of Studies in Physics, University of Mysore, Manasagangotri, Mysore-570 006, India

<sup>2</sup>Semiconductor Laboratory, Department of Space, Govt. of India, Punjab-160 071, India

<sup>3</sup>Department of PG Studies in Physics, JSS College, Ooty Road, Mysore-570 025, India

<sup>4</sup>Inter-University Accelerator Centre, Aruna Asaf Ali Marg, New Delhi-110 067, India

<sup>5</sup>Technical Physics Division, Bhabha Atomic Research Center, Mumbai-400 085, India

Silicon BJTs are vulnerable to both ionization and displacement damage. Incident particles, such as Co-60 gamma rays, electrons, protons and heavy ions can induce ionization damage in the oxide layer or displacement damage in silicon bulk of BJTs. Both the ionization and displacement damage can induce the current gain degradation. The ionizing damage could cause interface traps and net positive charges in the oxide overlying the emitter-base junction, leading to an increase in the base recombination current and a decrease in current gain. Displacement damage would produce vacancy defect complexes that are effective recombination and trapping centers, leading to a decrease in minority carrier lifetime. The degradation of minority carrier lifetime results in the degradation of current gain [1-3]. In the present investigation we have studied 80 MeV Nitrogen ion irradiation on the I-V characteristics of NPN transistors in the dose range from 100 krad(Si) to 100 Mrad(Si). The different electrical characteristics like Gummel characteristics, excess base current ( $\Delta I_B$ ), DC current gain ( $h_{FE}$ ) and output characteristics were studied before and after ion irradiation. Fig. 61(a) illustrates the variation in  $\Delta I_B$  for 80 MeV N ion irradiated transistors. We can observe from the Figure that, as the ion dose increases the  $I_B$  also increases to around two orders of magnitude after 100 Mrad (Si) of total dose. The increase in  $I_B$  at low injection is the result of increased recombination current in the emitter-base (E-B) depletion region due to radiation-induced generation-recombination (G-R) centers. In addition to G-R centers, high energy ions can also create various types of defects and their complexes in the transistor structure and they reduce the minority carrier lifetime and this in turn increases the  $I_B$  of the transistor. Fig. 61(b) illustrates the DC current gain ( $h_{FE}$ ) for 80 MeV Nitrogen ion irradiated transistors. From the Figure it is clear that the  $h_{FE}$  of the irradiated transistors reduces almost to a negligible value after a total dose of 100 Mrad. The variation in the  $I_{CSat}$  measured at  $V_{CE} = 3$  V as a function of total dose for 80 MeV Nitrogen ion irradiated transistors is shown in Fig. 61 (c). The  $I_{CSat}$  found to decrease with increase in the ion dose. The heavy ions are capable of producing different defects like vacancies and divacancies in collector region of transistors. These defects are responsible for the increase in collector series resistance and thereby reducing  $I_{CSat}$ .

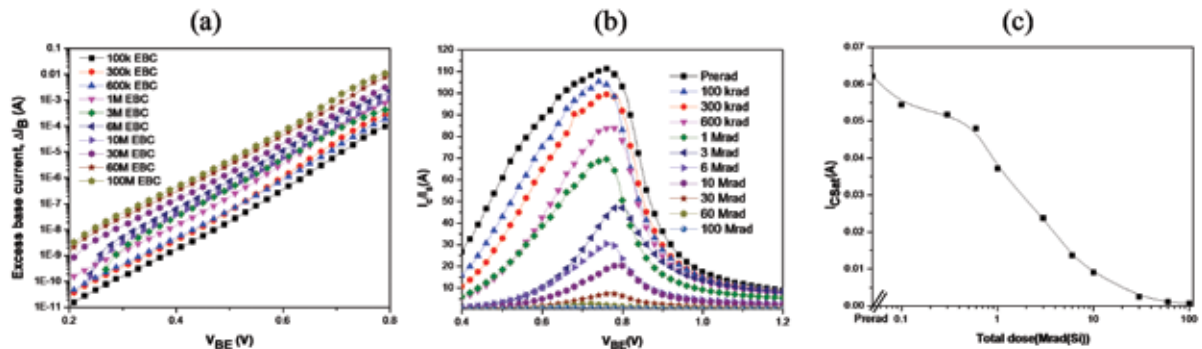


Figure 61 : (a) The variation in excess base current after 80 MeV N ion irradiation, (b) The variation in dc current gain after 80 MeV N ion irradiation, and (c) The variation in the  $I_{CSat}$  measured at  $V_{CE} = 3$  V as a function of total dose for 80 MeV N ion irradiated transistor.

## REFERENCES

- [1] N. Pushpa *et al.*, Radiation Effects & Defects in Solids. 164 (2009) 592
- [2] A. P. Gnana Prakash *et al.*, Nucl. Instrum. Meth. B. 215 (2004) 457
- [3] Xingji Li *et al.*, IEEE Trans. Nucl. Sci. 61 (2014) 630

### 5.2.28 Swift heavy ion induced radiation effects at Si/SiO<sub>2</sub> interface of MOS devices

Arshiya Anjum<sup>1</sup>, N. H. Vinayakprasanna<sup>1</sup>, K. C. Praveen<sup>2</sup>, T. M. Pradeep<sup>1</sup>, B. C. Hemaraju<sup>1</sup>, N. Pushpa<sup>3</sup>, Ambuj Tripathi<sup>4</sup>, K. Asokan<sup>4</sup>, J. B. M. Krishna<sup>5</sup> and A. P. Gnana Prakash<sup>1</sup>

<sup>1</sup>Department of Studies in Physics, University of Mysore, Manasagangotri, Mysore-570006

<sup>2</sup>Semiconductor Laboratory, Department of Space, ISRO, Mohali-160071, India

<sup>3</sup>Department of PG Studies in Physics, JSS College, Ooty Road, Mysore-570 025, India

<sup>4</sup>Inter-University Accelerator Centre, Aruna Asaf Ali Marg, New Delhi-110 067, India

<sup>5</sup>IUC-DAE CSR, Kolkata-700098, India

Metal Oxide Semiconductor Field Effect Transistors (MOSFETs) are extensively used in radiation rich environments such as space, military and large hadron collider (LHC) applications due to their faster switching speed when compared to bipolar transistors. In order to use MOSFETs in radiation rich environments the devices need to withstand few krad to few Mrad of radiation [1]. Hence it is very essential to evaluate the radiation hardness of these devices. In this present work the N-channel MOSFETs were exposed to 80 MeV Nitrogen ions at Inter University Accelerator Centre (IUAC), New Delhi. The MOSFETs were irradiated with 80 MeV Nitrogen ions fluence ranging from  $2.4 \times 10^9$  to  $2.4 \times 10^{12}$  ions/cm<sup>2</sup> at room temperature in an experimental chamber maintained at  $10^{-5}$  torr.

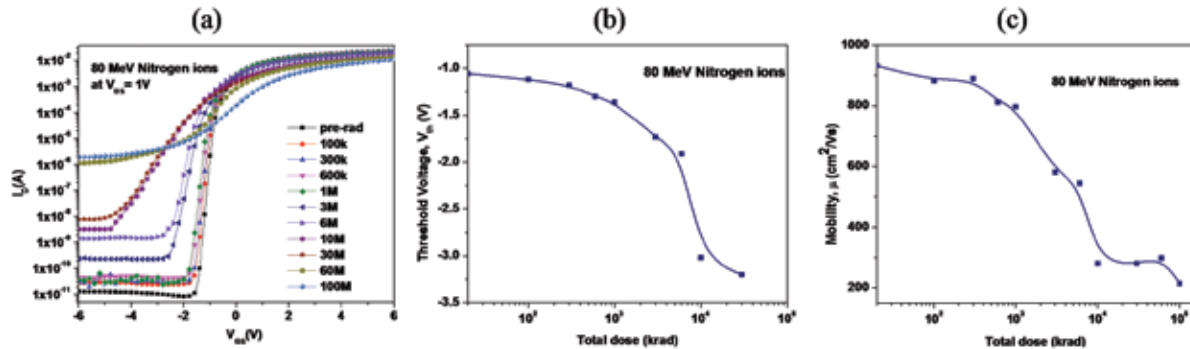


Figure 62 : (a) Transfer characteristics of 80 MeV Nitrogen ion irradiated MOSFET ( $V_{DS} = 1$  V), (b) Variation in  $V_{th}$  after 80 MeV Nitrogen ion irradiation, (c) Variation in  $\mu$  after 80 MeV Nitrogen ion irradiation

Fig. 62(a) shows the transfer characteristics of MOSFETs irradiated with 80 MeV Nitrogen ions. It can be seen from the Figure that as the radiation dose increases the drain current ( $I_D$ ) swings towards the negative gate voltage ( $V_{GS}$ ). This degradation in the electrical characteristics of MOSFETs is due to the creation of interface and oxide trapped charges near the Si/SiO<sub>2</sub> interface. The incident radiation on the device creates electron-hole pairs. When the positive bias is applied to the gate terminal, since the electrons have negligible capturing cross section and high mobility in SiO<sub>2</sub>, they easily sweep out into the external circuit. Whereas the holes have large capturing cross section and very low mobility in SiO<sub>2</sub>, they drift very slowly towards the Si/SiO<sub>2</sub> interface where fraction of them get trapped and induce oxide trapped charges [2]. These positive trapped charges induce a negative shift in the threshold voltage ( $V_{th}$ ) of the MOSFETs which increases the leakage current and hence power consumption will also increase. Fig. 62(b) shows the negative shift induced in  $V_{th}$  after the irradiation of MOS devices. Fig. 62(c) represents the variation in the mobility ( $\mu$ ) of the charge carriers after irradiation. The reduction in the mobility of the charge carriers in the channel is mainly due to the radiation induced trapped charges and these trapped charges act as Coulomb scattering centers, which affect the motion of charge carriers in the channel [3].

## REFERENCES

- [1] N. Pushpa, et al., Nucl. Instrum. Meth. A.613 (2010) 280
- [2] A. P. Gnana Prakash, et al., Indian J. Phys. 78 (11) (2004) 1187–1192.
- [3] S. C. Sun and J. D. Plummer, IEEE Trans. Electron Dev. ED-27 (8) (1980) 1497.

### 5.2.29 80 MeV Nitrogen Ion Irradiation Effects on DC Electrical Characteristics of 200 GHz SiGe HBTs

N. H. Vinayakprasanna<sup>1</sup>, K. C. Praveen<sup>2</sup>, T. M. Pradeep<sup>1</sup>, B. C. Hemaraju<sup>1</sup>, Arshiya Anjum<sup>1</sup>, N. Pushpa<sup>3</sup>, John D. Cressler<sup>4</sup>, Ambuj Tripathi<sup>5</sup>, K. Asokan<sup>5</sup>, K.G. Bhushan<sup>6</sup> and A. P. Gnana Prakash<sup>1</sup>.

<sup>1</sup>Department of Studies in Physics, University of Mysore, Manasagangotri, Mysore-570006

<sup>2</sup>Semiconductor Laboratory, Department of Space, ISRO, Mohali-160071, India

<sup>3</sup>Department of PG Studies in Physics, JSS College, Ooty Road, Mysore-570 025, India

<sup>4</sup>School of Electrical and Computer Engineering, Georgia Institute of Technology, Atlanta, GA, 30332, USA

<sup>5</sup>Inter-University Accelerator Centre, Aruna Asaf Ali Marg, New Delhi-110 067, India

<sup>6</sup>Technical Physics Division, Bhabha Atomic Research Center, Mumbai-400 085, India

Bandgap engineered silicon-germanium heterojunction bipolar transistor (SiGe HBT) technology has recently emerged as a viable candidate for a wide variety of electronics applications operating in space and other extreme environments. The SiGe HBTs are considered for the possible use in the upgrade of the Silicon Strip Detector and Liquid Argon Calorimeter of the ATLAS detector as part of the Large Hadron Collider (LHC), CERN, Geneva, Switzerland [1]. In order to understand the high dose effects, SiGe HBTs were irradiated with 80 MeV Nitrogen ions in the dose of 1Mrad to 100 Mrad. The dc I-V characteristics such as Gummel characteristics, excess base current ( $\Delta I_B = I_{B-Post} - I_{B-Pre}$ ), current gain ( $\beta$ ), output characteristics, neutral base recombination (NBR) and avalanche multiplication of carriers (M-1) were studied before and after irradiation. Some of the important results are discussed in this report. Fig. 63(a) shows the forward mode Gummel characteristics for 80 MeV Nitrogen ion irradiated 200 GHz SiGe HBT. At low injection levels, the base current ( $I_B$ ) increases monotonically with increasing Nitrogen ion total dose. The increase in  $I_B$  shows that the degradation is similar to the conventional degradation mechanism observed in silicon bipolar transistors [2]. The radiation-induced damage in the emitter-base (EB) spacer oxide increases the emitter-base (EB) depletion region. The recombination current in the depletion region can be observed as an additional  $I_B$  in the lower emitter base voltage ( $V_{BE}$ ) regime. However, the collector current ( $I_C$ ) does not change with increase in Nitrogen ion total dose because the recombination in the depletion region does not affect the flow of electrons through the base. Therefore only the pre-irradiation  $I_C$  is shown in the forward-mode Gummel plot. Fig. 63(b) shows the dc current gain ( $\beta$ ) for the 80 MeV Nitrogen ion-irradiated SiGe HBT. As expected, the current gain decreases with Nitrogen ion total dose, because non ideal  $I_B$  increases after Nitrogen ion radiation. Since the  $I_B$  starts increasing for the lower  $V_{BE}$  the peak current gain ( $\beta$ ) shifts towards higher  $V_{BE}$  or higher  $I_C$ . The radiation-induced G/R centers decrease the minority-carrier lifetime which in turn decrease the current gain. The decrease in minority carrier lifetime is the dominant mechanism for gain degradation in addition to G/R centers created in the EB spacer oxide. Fig. 63(c) shows the neutral base recombination for SiGe HBT before and after irradiation. The change in base charge after irradiation can be experimentally estimated by observing the slope of  $I_B$  as a function of  $V_{CB}$  at fixed  $V_{BE}$ . The slope of the NBR curve at lower VCB is almost same for prerad and 100 Mrad curve. There is negligible amount of displacement damage in the base region of SiGe HBT even after 100 Mrad total dose of Nitrogen ion irradiation. The I-V characteristics show that the performance of SiGe HBT is acceptable even after irradiating 80 MeV Nitrogen ion up to 100 Mrad of total dose. Though the degradation observed in electrical characteristics of SiGe HBT is significant after 80 MeV Nitrogen ion irradiation, SiGe HBTs can be considered for use in the design of front-end readout ASICs for use in an upgraded LHC.

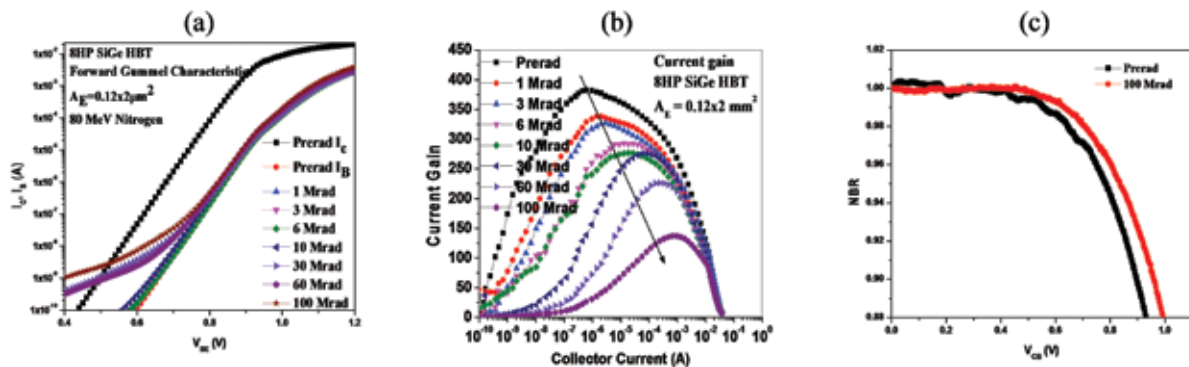


Figure 63 : (a) Forward mode Gummel characteristics, (b) Variation of current gain after irradiation, and (c) NBR

## REFERENCES

- [1] K. C. Praveen *et al.*, Nucl. Instrum. Meth. B. 273 (2011) 43
- [2] A. P. Gnana Prakash *et al.*, IEEE Trans. Nucl. Sci. 53 (2006) 3175

### 5.2.30 Single Event Effects Testing of Microelectronic devices using Swift Heavy Ions

Gaurav Srivastava, S.N. Mittal, Sachin Sharma, Parveen Rana, Thakur Gurmeet Singh, Shammi Verma

Semi-Conductor Laboratory (SCL), Department of Space, Mohali-160071

The intense heavy ions environment encountered in space applications can cause a variety of transient and destructive effects known as single event effects (SEE) which include single event latch-up (SEL), single event transient (SET), single event upset (SEU) and single event burnout (SEB). There are many device conditions and failure modes for a specific device due to SEE depending on the incident energetic particle. Different device effects, hard or soft errors, may or may not be acceptable for a given device design & functionality. The low ion fluence ( $\sim 10^6$  cm<sup>-2</sup>) SEE test facility at GPSC beam line, IUAC, Delhi was used to evaluate the radiation hardness of the digital and mixed signal CMOS ASICs designed and fabricated at SCL. A PC based automatic test setup was developed for SEE testing of ASDR, CMOS Camera Configuration ASIC, LVDS Tx, LVDS Rx, Sigma Delta ADC and 14-bit ADC. The test setup comprised of DUT Board, 3-Channel Power Supply and computer loaded with Test Program. The data was acquired on PC using serial/parallel interface. For SEE testing of these ASICs, various ion beams of Si, Ni, Ti, and Ag with energies 100-140 MeV were used to vary linear energy transfer (LET) from 10-50 MeVcm<sup>2</sup>/mg. Table 5.2.2 summarizes the result highlights of the SEE testing performed on various ASICs. Fig. 64 and Fig. 65 show the cross-section and bit error graphs for CMOS camera configuration ASIC and SEUs observed in ADC output registers respectively.

**Table 5.2.2: Summary of SEE Tests performed on various ASICs and their results**

S r . No.	Device/ASIC Tested	Ion Beam Used	LET (MeV-cm <sup>2</sup> /mg)	Observations	Results
1	CMOS Camera Configuration ASIC	Si	10.15	SEUs increased with LET of ion beam, however no SEU or SET was observed up to LET~10.15 MeV-cm <sup>2</sup> /mg. The ASIC was tolerant to SELs for highest LET of ~50 MeV-cm <sup>2</sup> /mg	ASIC is "pass" up to LET ~10.15 MeV-cm <sup>2</sup> /mg in SEU and up to 50 MeV-cm <sup>2</sup> /mg in SEL
		Ti	20.56		
		Ni	30.51		
		Ag	50.04		
2	ASDR	Ni	30.51	ASIC was tested for ~ 20 mins (Fluence $\sim 0.5 \times 10^6$ ions/cm <sup>2</sup> ) for each beam. No bit error and current latch-up encountered during test	ASICs passed up to LET ~50.04 MeV-cm <sup>2</sup> /mg for SEL and SEU
		Ag	50.04		
3	LVDS Tx & Rx	Ni	30.51	No SET/SEU/SEL were observed till LET ~50.04 MeV-cm <sup>2</sup> /mg	
		Ag	50.04		
4	14-bit ADC	Ti	20.56	No increase in supply current and no SEU/SET/SEL were observed up to LET 50 MeV-cm <sup>2</sup> /mg	
		Ni	30.51		
		Ag	50.04		
5	Sigma-Delta ADC	Si	10.15	Large number of SEUs observed in control & output registers but no SEL was observed up to LET of 30.5 MeV-cm <sup>2</sup> /mg	ASIC was found failed in output and offset registers
		Ti	20.56		
		Ni	30.51		

ASDR- Addressable Synchronous/asynchronous Differential Receiver; LVDS Tx & Rx- Low Voltage Differential Signalling Transmitter and Receiver; ADC- Analog to Digital Convertor

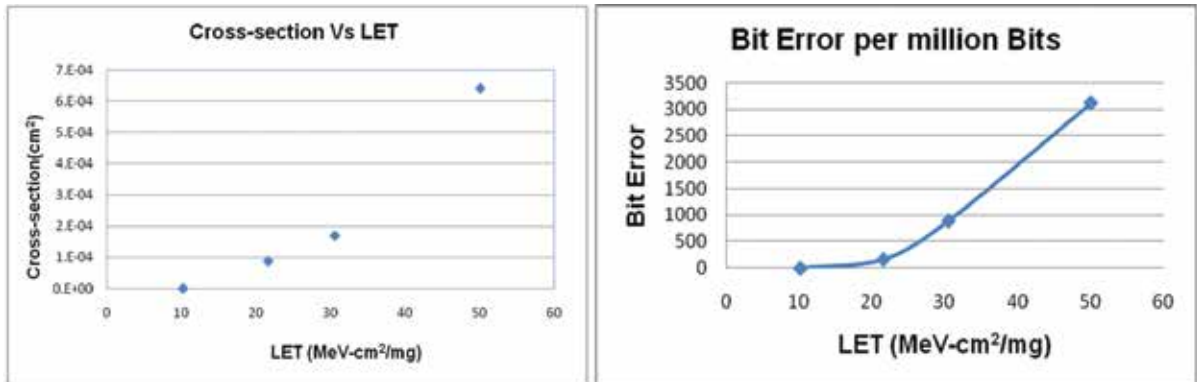


Figure 64 : (left) Cross-section and (right) Bit-error versus LET graphs for CMOS camera configuration ASIC

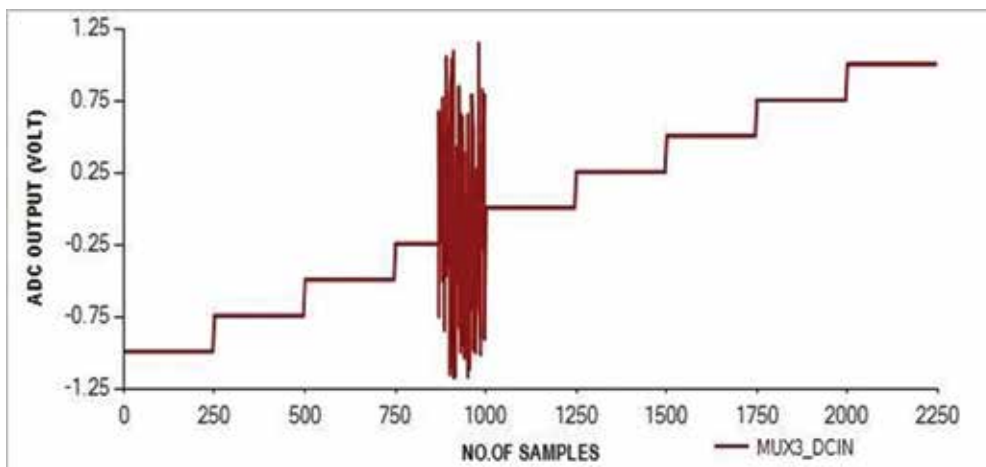


Figure 65 : Observed upsets in Sigma-Delta ADC output register under irradiation with 140 MeV Ti ion beam

### 5.2.31 Radiation induced modification in the properties of nanostructures

Suresh Panchal and R.P. Chauhan

Department of Physics, National Institute of Technology, Kurukshetra-136119, Haryana, India

Nanostructures exhibit distinctive and strange properties superior to their bulk counterparts. These unique properties can be attributed to the controlled motion of electrons in the confined dimensions of the nanostructures. For practical applications, the deeper understanding of utilization and tailoring of the nanomaterials is an area of research interest. A large variety of nanomaterials have been synthesized and incorporated in devices that demonstrate their potential to significantly enhance the performance of currently used technology [1-3]. Radiation interactions with one dimensional nanostructures grab enormous interest of the researchers. The controlled radiation on the nanowires enables one to engineer their properties to great extent. The study of irradiation on nanowires also provides the information about the device operation in harsh environment as well as radiation fluxes. Present study deals with the irradiation induced modification in the electrical properties of the selenium nanowires.

In the present study, selenium nanowires of 80 nm diameter were irradiated with 10 MeV Li<sup>3+</sup> ions for different fluence ranging from  $1 \times 10^{11}$  to  $1 \times 10^{13}$  ions/cm<sup>2</sup>. Electrical properties of pristine and irradiated nanowires were

determined with the help of Keithley 2400 series source meter and a probe station. I-V characteristic shows an increment in conductivity for three fluences and the decrease for next two fluences (Fig. 66(I)). Interaction of ions with a material always results in the creation of charge carrier and defects in it. The increase in the conductivity is mainly due to increase in the carrier concentration, carrier mobility and generation of new intermediate energy levels in the band gap. However, at higher fluence  $5 \times 10^{12}$  and  $1 \times 10^{13}$  ions/cm<sup>2</sup>, irradiation induced defects dominate due to which decrease in the conductivity was observed.

In another study, 80 nm diameter selenium nanowires were exposed to gamma rays for different doses of 50, 100, 150, 200 kGy from Co<sup>60</sup> source in Gamma chamber 1200 BNT. Dose was changed by changing the time of exposure, as activity of the source was 4.533 kGy/hour. Optical band gap ( $E_g$ ) of pristine and irradiated selenium nanowires was calculated using UV-visible spectroscopy. Absorption peak around 580 nm for the pristine nanowires was shifted towards higher wavelength (up to 670 nm) with irradiation dose. The optical band gap decreased from '2.0 eV' to '1.92 eV' as the gamma dose changes from 50 to 200 kGy while for pristine it is '2.01 eV'. I-V characteristics of pristine and gamma irradiated selenium nanowires are shown in Fig. 66(II) and clearly there is an increase in the current with dose rate.

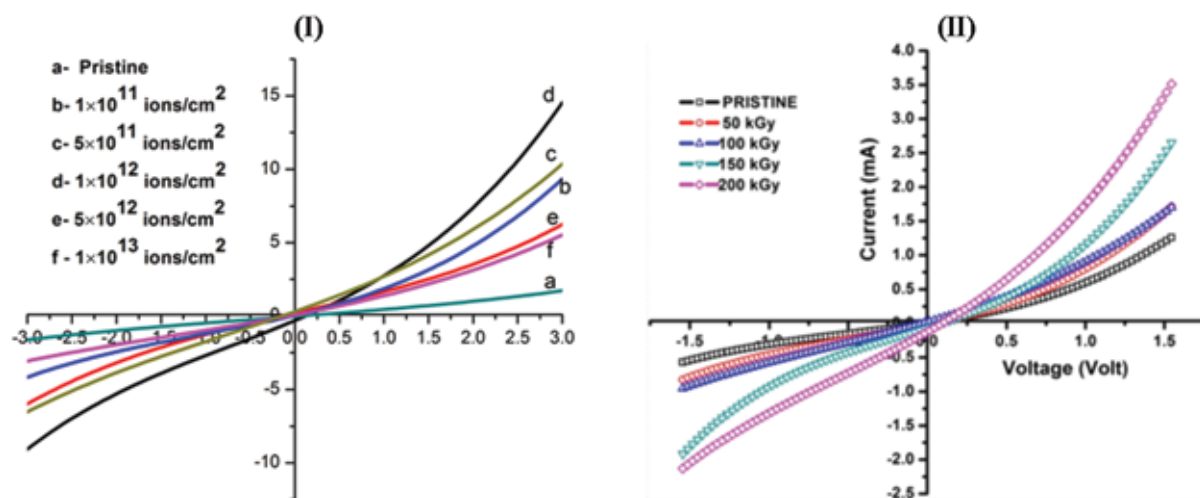


Figure 66 : (I) IVC of pristine and Lithium ion irradiated Se nanowires, and (II) IVC of pristine and gamma irradiated Se nanowires

## REFERENCES

- [1] M.E. Toimil-Molares, Beilstein J. Nanotechnol. 3 (2012) 860
- [2] S. Iijima, Nature 354 (1991) 56
- [3] N. Kumar, R. Kumar, S. Kumar, S.K. Chakarvarti, Curr. Appl. Phys. 14 (2014) 1547

### 5.2.32 Radiation damage of Heavy ions and H irradiated Tungsten – Some Experimental Results

P.M. Raole<sup>1</sup>, Shishir Deshpande<sup>1</sup>, P.N. Maya<sup>1</sup>, S. Khirwadkar<sup>1</sup>, P. Rayjada<sup>1</sup>, M. Mehta<sup>1</sup>, Prashant Sharma<sup>1</sup>, Sai Krishna<sup>1</sup>, P. K. Kularia<sup>2</sup>, Devrani Devi<sup>2</sup>, Ravi Gundakaram<sup>3</sup>, D. Dutta<sup>4</sup>

<sup>1</sup>Institute for Plasma Research, Gandhinagar-382428, India,

<sup>2</sup>Inter-University Accelerator Centre, Aruna Asaf Ali Marg, New Delhi-110 067, India

<sup>3</sup>International Advance Research Centre for Powder Metallurgy and New Materials (ARCI), Balapur P.O. Hyderabad-500005, Telangana, India.

<sup>4</sup>Radiochemistry Division, Bhabha Atomic Research Centre, Mumbai 400085, India

The objectives of this study are to investigate (i) the structural, microstructural and morphological changes in Tungsten after low (0.1 MeV) and High (80 MeV) energy Heavy ion irradiations and (ii) Hydrogen trapped/retained in un-irradiated and pre-irradiated Tungsten [1]. In this study, Electron Back scattered Diffraction

(EBSD) technique has been used to understand the grain structure, size and orientation in the pristine Tungsten samples. EBSD results show that both type of Tungsten samples (Rod and Plate samples with different grain orientations) have equiaxed grains on the surface. However, in the cross section columnar grains are seen. In the Plate samples, it is observed that there are larger grains and lattice is strained. The samples are annealed at 900 °C before irradiation to relieve stress in the samples. The stress and strain (macro and Micro) have been measured before and after Au irradiation by X-ray Diffraction and it has been observed that the pristine and 900 °C annealed samples are tensile strained with respect to standard relaxed Tungsten matrix  $d$ -values. It is progressively relieved with 100 keV Au irradiation and 80 MeV Au irradiation carried out at IUAC, New Delhi. All irradiated samples show that irradiation tends to increase preferred orientation in (200) and (211) direction, and the effect may have been extended in substantial thickness of 10s of microns. Increase in the crystallite size is observed in 80 MeV irradiated gold. Positron Annihilation Lifetime Spectroscopy (PALS) has been carried out at BARC and the results show the effect of annealing in terms of enhanced mono-vacancies at the cost of vacancy clusters. The effect of irradiation is seen in the reduction of mono vacancies.

High and low energy irradiation effects of W/Au ions on retention of Hydrogen in Tungsten samples are planned. As a part of that study, pristine and annealed (at 900 °C) Tungsten samples were subjected to the irradiation of 100 keV H ions with the fluence of  $1 \times 10^{17}$  and  $1 \times 10^{18}$  at LEIBF at IUAC. The characterization using X-ray diffraction (XRD), Positron Annihilation Lifetime Spectroscopy (PALS), Scanning Electron Microscopy (SEM) is in progress. LEIBF at IUAC has also been used to irradiate Tungsten with 100 keV Au ions in order to confirm the earlier results of stress formation, defect structure and surface nano-structuring and to find reasons and mechanism of such phenomena. In the second phase of the study, heavy ion irradiated (with W/Au) tungsten samples will be subjected to hydrogen ion implantation to compare the retention of hydrogen in unirradiated and irradiated tungsten. More investigation in this regard is underway.

## REFERENCES

- [1] P.M. Raole et al. , 2nd Research Coordination Meeting (RCM) of the CRP on Irradiated Tungsten, Seoul, Korea ( 8-11 Sept. 2015)

### 5.2.33 Nanostructure Modifications of Ni-Ti Shape Memory Alloy Thin Films by Ag Implantation

Veeresh Kumar<sup>1</sup>, R. Singhal<sup>1</sup>, R. Vishnoi<sup>1</sup>, M. K. Banerjee<sup>2</sup>, M. Gupta<sup>3</sup>, M. Kumar<sup>4</sup>, K. Asokan<sup>5</sup>, J.C. Pivin<sup>6</sup>

<sup>1</sup>Department of Physics, Malaviya National Institute of Technology Jaipur, JLN Marg, Malviya Nagar, Jaipur-302017, India

<sup>2</sup>Department of Metallurgical & Materials Engineering, Malaviya National Institute of Technology JLN Marg, Malaviya Nagar, Jaipur-302017, India

<sup>3</sup>UGC-DAE Consortium for Scientific Research, University Campus, Khandwa Road, Indore-452001, India

<sup>4</sup>Nanotechnology Application Centre, University of Allahabad, Allahabad-211002, India

<sup>5</sup>Inter-University Accelerator Centre, Aruna Asaf Ali Marg, New Delhi-110 067, India

<sup>6</sup>CSNSM, IN2P3-CNRS, Batiment 108, F-91405 Orsay Campus, France

Ni-Ti based shape memory alloys (SMAs) thin films are interesting materials because they show the shape memory behaviour and superelasticity. These materials are also used to fabricate micro devices for micro-electromechanical systems (MEMS) and Bio-MEMS, such as microwrappers and micro pumps [1-2]. In the present study, thin films of Ni-Ti shape memory alloy were deposited on Si substrate by using dc magnetron co-sputtering technique. These prepared thin films were implanted by 120 keV Ag ions using low energy ion beam facility at Inter University Accelerator Centre (IUAC), New Delhi. Ion fluences were varied from  $3 \times 10^{15}$  to  $3 \times 10^{16}$  ions/cm<sup>2</sup>. The orientation and crystallinity of as deposited and implanted films were studied using a standard x-ray diffractometer (XRD) (Bruker D8 Advance) equipped with Cu K<sub>α</sub> x-rays source in  $\theta$ -2 $\theta$  geometry at a scan speed of 0.6°/minute. The XRD measurement (Fig. 67(left)) reveals presence of the both austenite as well as martensite phases in the films. The mechanical properties of pristine and implanted thin films were

characterized by using Nano-indentation tester (Fig. 67(right)). The mechanical properties such as hardness and elastic modulus increase with increase in the ion fluences up to  $9 \times 10^{15}$  ions/cm<sup>2</sup>, after they slightly decrease due to the defect produced in the film at higher fluence.

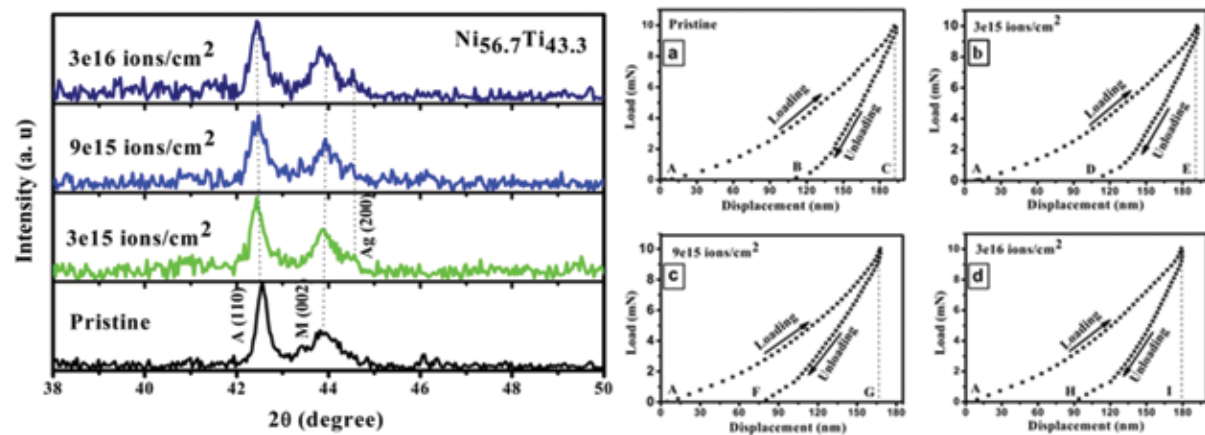


Figure 67 : (left) XRD spectra of pristine and implanted Ni-Ti thin films, and (right) Nano indentation measurement of Ni-Ti thin films

## REFERENCES

- [1] S. Miyazaki et al., Thin film shape memory alloys: fundamental and device application. Cambridge University Press (2009)
- [2] L. C. Chang and T. A. Read, Trans. AIME 47 (1951) 189

### 5.2.34 Ion implantation of FePt thin Films on Si substrate

Rajan Goyal<sup>1</sup>, Ambika Negi<sup>1</sup>, Akanksha Kapoor<sup>1</sup>, S. Lamba<sup>2</sup>, S. Annapoorni<sup>1</sup>

<sup>1</sup>Department of Physics and Astrophysics, University of Delhi, India 110007

<sup>2</sup>Department of Physics, IGNOU, India

Transition metal alloys such FePt are proved to be a promising candidate for the ultra high density magnetic data storage applications due to large magneto crystalline anisotropy and high thermal stability. It exhibits structural and magnetic phase transformation which shows a strong dependence on the atomic composition of the alloy [1-4]. FePt thin films were deposited on Si <100> single crystal substrate using dc magnetron sputtering at 0.03 mbar Ar gas pressure and 30 W dc power.

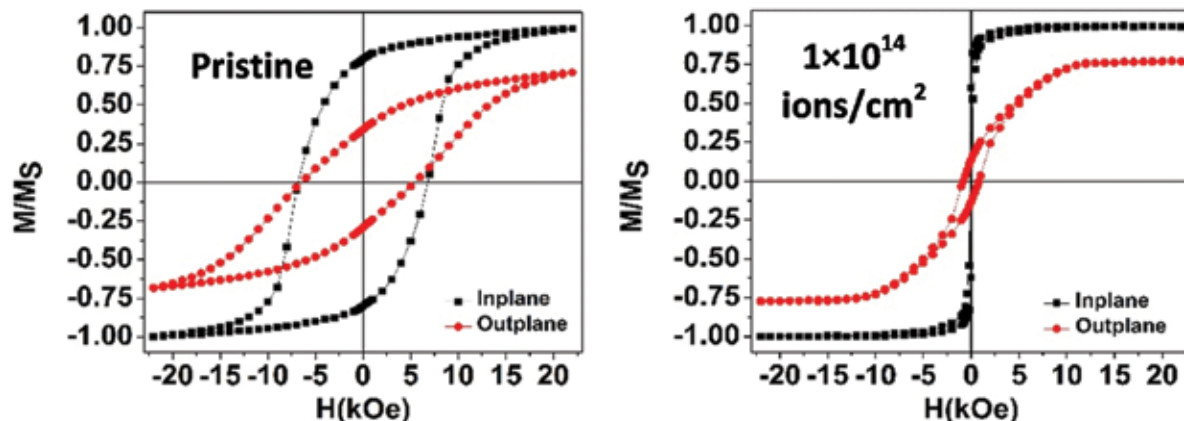


Figure 68 : Hysteresis curve of FePt thin films recorded at room temperature both in the inplane and out of plane configurations for pristine as well as for the sample irradiated at a fluence of  $1 \times 10^{14}$  ions/cm<sup>2</sup>

The as-deposited samples were annealed at 450°C. The 450 °C annealed samples (pristine) were irradiated with 300 keV Ar<sup>+</sup> ions at different fluences viz.  $1 \times 10^{14}$ ,  $1 \times 10^{15}$  and  $1 \times 10^{16}$  ions/cm<sup>2</sup>. The modification of magnetic and structural properties reveals the order-disorder transformation after ion irradiation as shown in Fig. 68 and 69 respectively.

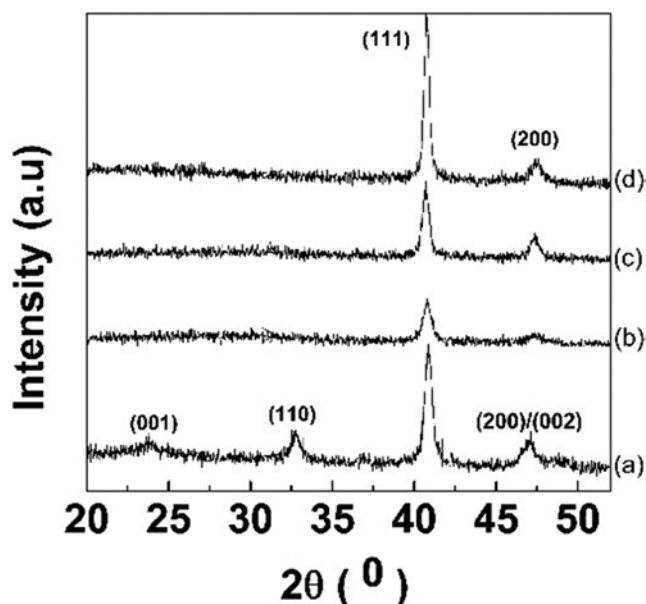


Figure 69 : XRD pattern of FePt thin films (a) pristine, irradiated with 300 keV Ar<sup>+</sup> beam at different fluences (b)  $1 \times 10^{14}$  ions/cm<sup>2</sup> (c)  $1 \times 10^{15}$  ions/cm<sup>2</sup> (d)  $1 \times 10^{16}$  ions/cm<sup>2</sup>

## REFERENCES

- [1] R. Medwal, N. Sehdev, S. Annapoorni, J. Nanoparticle Res. 15 (2013) 1423
- [2] R. Medwal, N. Sehdev, S. Lamba, A. Banerjee, S. Annapoorni, J. Phys. D: Appl. Phys. 47 (2014) 355002
- [3] R. Gupta, R. Medwal, S. Annapoorni, Mater. Res. Bull. 48 (2013) 3881–3886
- [4] R. Gupta, R. Medwal, N. Sehdev, S. Annapoorni, J. Magn. Magn. Mater. 345 (2013) 60–64

### 5.2.35 Oriented Growth of Cobalt Nanoparticle Embedded in Alumina matrix

Rajan Goyal<sup>1</sup>, S. Lamba<sup>2</sup>, S. Annapoorni<sup>1</sup>

<sup>1</sup>Department of Physics and Astrophysics, University of Delhi, India 110007

<sup>2</sup>Department of Physics, IGNOU, India

The soft ferromagnetic material such as cobalt found attractive applications in gas sensors, humidity sensing etc. Metallic cobalt exhibits a phase transformation from hcp to fcc phase at a temperature of about 450 °C [1-4]. Cobalt embedded in alumina matrix thin films were successfully fabricated on Si <100> single crystal substrate using RF magnetron sputtering at 0.03 mbar working pressure of Ar gas and 200 W RF power. The as deposited samples were annealed at 700 °C followed by rapid cooling at room temperature. The 700 °C annealed sample (pristine) were subjected to ion implantation using Ar<sup>+</sup> and Xe<sup>+</sup> 300 keV beam from LEIBF at IUAC with 5 different fluences  $1 \times 10^{14}$ ,  $1 \times 10^{15}$ ,  $5 \times 10^{15}$ ,  $1 \times 10^{16}$  and  $2.5 \times 10^{16}$  ions/cm<sup>2</sup>. The structural and morphological studies have been carried out using X-ray diffraction, scanning electron microscopy (SEM) and scanning probe microscopy (SPM).

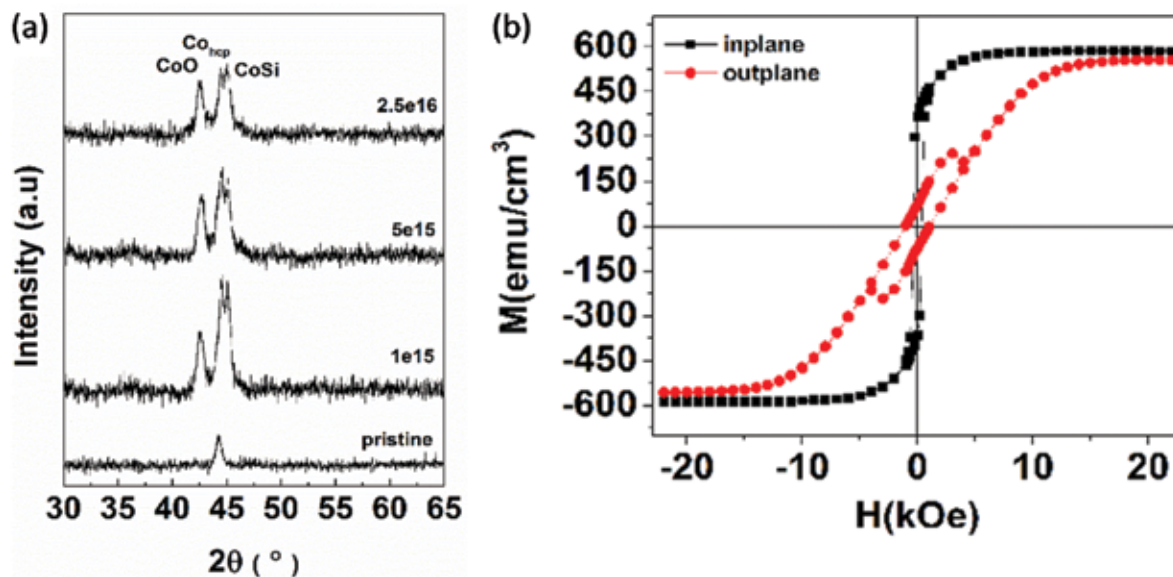


Figure 70 : (a) XRD pattern of pristine as well as ion implanted Co embedded in alumina matrix thin films at different fluences (b) hysteresis curve recorded at room temperature for pristine sample.

The XRD patterns of pristine as well as implanted samples are shown in Fig. 70(a). The appearance of peak at  $2\theta = 45.05^\circ$  corresponds to (013) peak of  $\text{Co}_2\text{Si}$  indicating the diffusion of cobalt into Si substrate. Further, increase in fluence results in a small decrease in intensity of  $\text{Co}_2\text{Si}$  peak. This may be attributed to the formation of  $\text{CoSi}$  due to more diffusion of cobalt into Si substrate. However, the most intense peak of both  $\text{CoSi}$  and  $\text{Co}_{\text{hcp}}$  comes at the same position. Therefore, profile fitting of XRD pattern can be used to estimate the relative percentage of  $\text{CoSi}$  and  $\text{Co}_{\text{hcp}}$  present in the system. The magnetic studies performed at room temperature (shown in Fig. 70(b)) depict the existence of uniaxial magnetic anisotropy.

## REFERENCES

- [1] Y. K. Koet al., Mater. Chem. Phys. 80 (2003) 560
- [2] T. Reith, J. M. Shaw and C. M. Falco, J. Appl. Phys. 99 (2006) 08N506
- [3] M. Y. Lee and P. A. Bennett, Phys. Rev. Lett. 75 (1995) 4460
- [4] R. N. Das, A. Bandyopadhyay and S. Bose, J. Am. Chem. Soc. 84 (2001) 2421

### 5.2.36 Study of low energy ion beam induced modifications in the properties of semiconducting nanowires

R. P. Chauhan, Chetna Narula and Pallavi Rana

Department of Physics, National Institute of Technology, Kurukshetra-136119, Haryana, INDIA

One-dimensional nanostructures can be utilized to use their properties which may be unrealizable or formidable to achieve in larger devices due to the reduced device size and ideal material properties. II–VI wide band gap semiconductor nanostructure materials serve as the promising materials due to their direct and rather large band gap and consequently their effective utilization in various nanoscale solid-state devices [1,2]. Ion implantation is a large scale and standard technique for the reconstruction of materials properties and surfaces [3,4].

Cadmium Selenide ( $\text{CdSe}$ ) nanowires of 80 nm diameter were implanted with 250 keV Al ions to fluences  $5 \times 10^{11}$ ,  $1 \times 10^{12}$ ,  $5 \times 10^{12}$  and  $1 \times 10^{13}$  ions/cm<sup>2</sup>. X-Ray Diffraction (XRD) pattern was recorded using a Ni-filtered  $\text{Cu K}\alpha$  radiation ( $\lambda = 1.54 \text{ \AA}$ ). The diffraction peaks in all the samples were in good agreement with the standard data for  $\text{CdSe}$  (JCPDS card no. 77-2307) and could be indexed to hexagonal structure with lattice constants as  $a = 4.299 \text{ \AA}$  and  $c = 1.6306 \text{ \AA}$ . It is observed that there is no deviation in the ' $2\theta$ ' positions of the peaks in the ion implanted

samples. However, an additional peak corresponding to the plane (220) was observed at all fluences with greater crystallinity at the last fluence which is attributed to the diffraction peak of aluminium (JCPDS card-04-0787). It is also observed that there is a minute variation in the values of crystallite size at initial fluence. As the fluence reached to a value of  $1 \times 10^{13}$  ions/cm<sup>2</sup>, the crystallite size is increased by about 4 nm in both the cases. A typical morphology of 80 nm diameter CdSe nanowires is shown in Fig. 71(I). The synthesized pristine nanowires exhibit cylindrical shape with regular and smooth edges. The electrical properties of pristine and ion implanted samples were also examined by using probe station and Keithley 2400 series source meter. At first three fluence, I-V curves of pristine and the Al implanted samples showed non-linear symmetric behaviour but 80 nm CdSe nanowires implanted at a fluence of  $1 \times 10^{13}$  ions/cm<sup>2</sup> exhibited pronounced linearity and displayed good ohmic contact with a substantial rise in current (Fig. 71(II)).

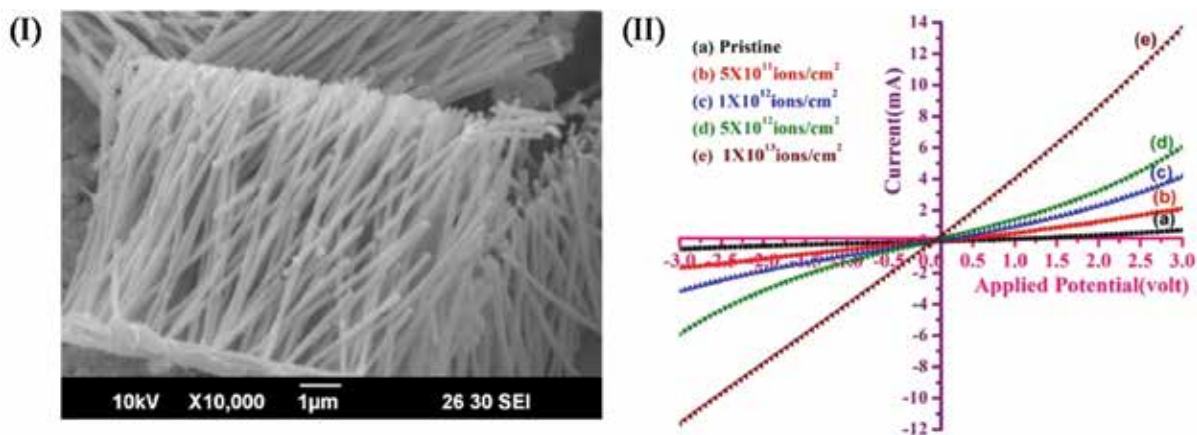


Figure 71 : (I) SEM image of pristine CdSe nanowires (80nm), and (II) I-V curves for pristine and implanted CdSe nanowires

In another study, effects of implantation with 250 keV protons on electrical and optical properties of CdSe nanowires of 80nm were studied for different fluences. I-V characteristics (IVC) for pristine and proton implanted CdSe nanowires at different fluences were measured to assess the modifications in IVC of implanted nanowires. The electrical conductivity was calculated using slope of the graphs. Implantation led to substantial change in the electrical conductivity at all doses as compared to pristine. The optical band gap values obtained from Tauc plot are 2.51 eV for pristine and 2.47 eV, 2.25 eV, 2.36 eV and 2.42 eV corresponding to fluences  $5 \times 10^{11}$ ,  $1 \times 10^{12}$ ,  $5 \times 10^{12}$  and  $1 \times 10^{13}$  ions/cm<sup>2</sup> respectively. This variation may be attributed to the decrease in the number of defects and increased crystallite size.

## REFERENCES

- [1] S. Park, S. Kim, G.J. Sun, D.B. Byeon, S.K. Hyun, W.I. Lee and C. Lee, Journal of Alloys and Compounds 658 (2016) 459-464
- [2] P.Rana and R. P. Chauhan, Journal of Materials Science: Materials in Electronics 25, no. 12 (2014) 5630-5637
- [3] A. Johannes, H.H. Moritz and C. Ronning, Semicond. Sci. Tech. 30.3 (2015) 033001
- [4] R.P.Chauhan and P.Rana, Journal of Radioanalytical and Nuclear Chemistry 302(2) (2014) 851-856

### 5.2.37 Low energy ion beam irradiation of GaAs nanostructures and study of their transport properties

Onkar Mangla<sup>1,2</sup>, Savita Roy<sup>2</sup>, S. Annapoorni<sup>1</sup>, K. Asokan<sup>3</sup>

<sup>1</sup>Department of Physics and Astrophysics, University of Delhi, Delhi-110007, India

<sup>2</sup>Physics Department, Daulat Ram College, University of Delhi, Delhi-110007, India

<sup>3</sup>Inter-University Accelerator Centre, Aruna Asaf Ali Marg, New Delhi-110 067, India

Low energy ion beam irradiation of gallium arsenide (GaAs) nanostructures fabricated on silicon substrates using high fluence ions in modified dense plasma focus device has been done. GaAs nanostructures were irradiated at low energies of 100 keV and 200 keV with fluence in the range of  $1 \times 10^{13}$  to  $5 \times 10^{15}$  ions/cm<sup>2</sup> in order to reach a depth of ~ 12-20 nm. In order to investigate the effect of ion irradiation on the transport properties of the samples, hall measurements have been carried out at IUAC on ECOPIA HMS-3000 Hall Effect measurement system. It shows that the conductivity of the nanostructures which is n-type for as-deposited samples [1] has been changed to p-type at ion fluence greater than  $1 \times 10^{14}$  ions/cm<sup>2</sup>. The changes in conductivity type and carrier concentration with ion fluence at both 100 keV and 200 keV energies are presented in Table 5.2.3. The carrier concentration is found to decrease with increasing ions fluence. This suggests the possibility of decrease in excess arsenic content found in as-deposited samples [1]. The decrease in the arsenic content results in formation of pure GaAs nanostructured thin films with suppressed EL2 defect concentration [2,3].

**Table 5.2.3: Transport properties of ions irradiated GaAs nanostructures.**

Energy	Fluence (ions/cm <sup>2</sup> )	$1 \times 10^{13}$	$1 \times 10^{14}$	$5 \times 10^{14}$	$1 \times 10^{15}$	$5 \times 10^{15}$
100 keV	Conductivity type	n-type	n-type	p-type	p-type	p-type
	Carrier Concentration (cm <sup>-3</sup> )	$1.45 \times 10^{19}$	$1.10 \times 10^{19}$	$4.84 \times 10^{18}$	$3.05 \times 10^{17}$	$1.23 \times 10^{17}$
	Conductivity ( $\Omega$ -1cm <sup>-1</sup> )	$3.75 \times 10^3$	$3.95 \times 10^1$	5.92	1.71	1.27
200 keV	Conductivity type	n-type	p-type	p-type	p-type	p-type
	Carrier Concentration (cm <sup>-3</sup> )	$2.08 \times 10^{17}$	$1.33 \times 10^{17}$	$2.97 \times 10^{13}$	$2.62 \times 10^{12}$	$1.03 \times 10^{12}$
	Conductivity ( $\Omega$ -1cm <sup>-1</sup> )	$2.85 \times 10^3$	$2.21 \times 10^2$	$2.94 \times 10^1$	5.75	2.29

## REFERENCES

- [1] O. Mangla, S. Roy, M.P. Srivastava, Adv. Sci. Eng. Med. 6 (2014) 1200
- [2] N.A. Naz, U.S. Qurashi, M.Z. Iqbal, J. Appl. Phys. 106 (2009) 103704
- [3] H.-P. Komsa, A. Pasquarello, Phys. Rev. B 84 (2011) 075207

### 5.2.38 Investigation of Blistering Process in Hydrogen Implanted GaSb for Potential Layer Transfer Applications

Ravi Pathak<sup>1</sup>, U. Dadwal<sup>1,2</sup>, and R. Singh<sup>1,2</sup>

<sup>1</sup>Department of Physics, Indian Institute of Technology Delhi, Hauz Khas, New Delhi-110016, India

<sup>2</sup>Nanoscale Research Facility (NRF), Indian Institute of Technology Delhi, Hauz Khas, New Delhi-110016, India

Gallium antimonide (GaSb) is a direct bandgap compound semiconductor with higher electron mobility. Therefore, it has promising applications in optical electronics and high frequency devices. In addition, the heterogeneous integration of GaSb-based electronics with III-V semiconductors can be carried out using ion-cut process. Ion-cut comprises of ion implantation and direct wafer bonding where a thin layer of a crystalline semiconductor can be transferred to a foreign substrate. In this process, semiconductor sample (wafer) is implanted by light ions such as hydrogen with a definite energy and fluence. Hydrogen implanted wafer (host) is subjected to cleaning followed by a direct wafer bonding between the host and handle wafers. The bonded wafer pair is then annealed at elevated temperatures. This leads to the formation of hydrogen in-built pressure within the damage region of host wafer which eventually results in the transfer of its thin layer onto a handle wafer.

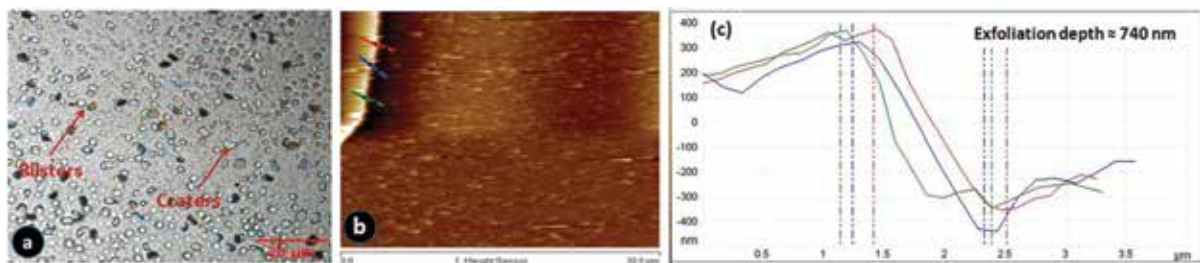


Figure 72 : (a) Nomarski optical image and (b) atomic force microscopy of the GaSb sample after post-implantation annealing at 300 °C for 30 min. (c) Atomic force microscopy sectional analysis at the marked lines of the Figure (b)

In the present work, GaSb samples were implanted with the hydrogen ions of energy 100 keV and fluence  $1 \times 10^{17}$   $\text{cm}^{-2}$ . The implantation was carried out at room temperature. Hydrogen implanted samples were then subjected to annealing at different temperature and time for studying the blistering kinetics. The samples were characterized using optical microscopy, atomic force microscopy, and stylus profilometry (Fig. 72). It has been found that in the as-implanted state, no surface blistering occurred. However, post-implantation annealing between 250 and 450 °C for 30 min showed the formation of surface blisters and craters. The lateral size of the blisters varied from 2 to 3  $\mu\text{m}$ . Surface exfoliation was also observed after post-implantation annealing at the same blistering parameters. The depth of the exfoliated region, which corresponds to the thickness of the transferred layer, was measured about 740 nm using atomic force microscopy sectional analysis. The root mean square surface roughness for the exfoliated region was about 12 nm for a scan area of  $10 \times 10 \mu\text{m}^2$ . This study can help in defining favorable conditions for the successful layer transfer of GaSb using ion-cut process.

### 5.2.39 Effect of 100 keV $\text{N}^+$ -ion irradiation on diamond films

B. Varalakshmi<sup>1</sup>, K. Asokan<sup>2</sup>, Sunil Ojha<sup>2</sup>, and V.V.S.S. Srikanth<sup>1</sup>

<sup>1</sup>School of Engineering Sciences and Technology, University of Hyderabad, Hyderabad, India

<sup>2</sup>Inter-University Accelerator Centre, Aruna Asaf Ali Marg, New Delhi-110 067, India

Low Energy Ion Beam Facilities (LEIBF) at IUAC was used to implant nitrogen ions into different kinds of diamond thin films (micro and nano-crystalline). These films were deposition on Si substrates by using microwave chemical vapour deposition (MWCVD) technique. This study is aimed at identifying the ideal diamond thin films as high energy facing surfaces and also to see if any new stable carbon nitride phases forms. A 100 keV  $\text{N}^+$ -ion beam [1] was implanted with doses of  $1 \times 10^{16}$  and  $1 \times 10^{17}$  ions/ $\text{cm}^2$ . Before and after implantation, the phase characteristics of the films were investigated by Raman scattering. Raman scattering results presented in Fig. 73 clearly show graphitization of the surface after implantation. It was also found that the structurally disordered  $\text{sp}^2$  phase increased with  $\text{N}^+$ -ion dose. RBS showed the presence of nitrogen as well as carbon in implanted diamond films.

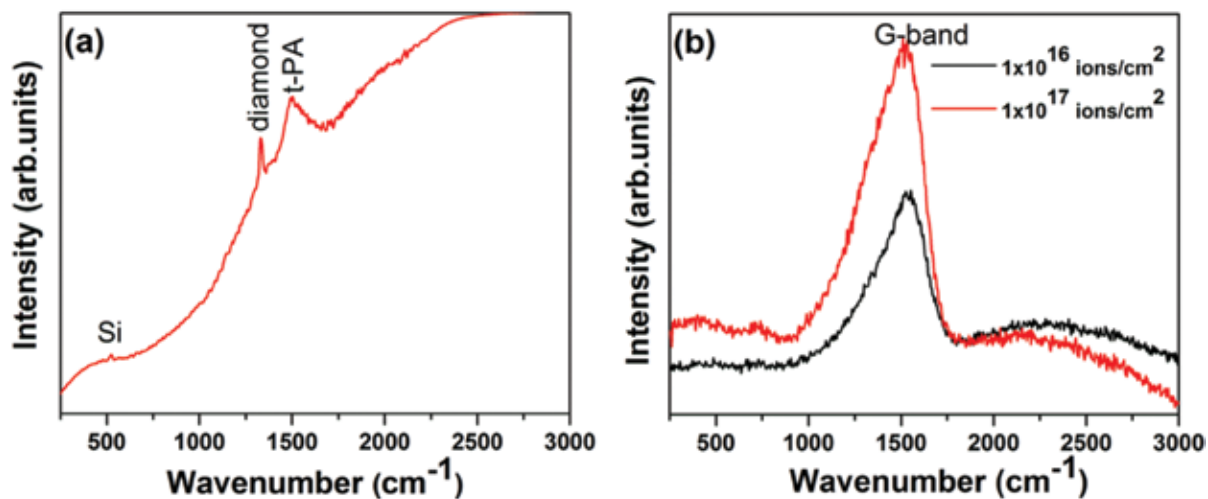


Figure 73 : Raman spectra of (a) pristine and (b) irradiated diamond thin film.

#### 5.2.40 Ion implantation on TiO<sub>2</sub> films

R. Lavanya<sup>1</sup>, D. Silambarasan<sup>1</sup>, K. Iyakutti<sup>2</sup>, K. Asokan<sup>3</sup> and V. Vasu<sup>1</sup>

<sup>1</sup>Thin film Laboratory, School of Physics, Madurai Kamaraj University, Madurai-625021, India.

<sup>2</sup>Department of physics & Nanotechnology, SRM university, Kattaankulathur-603203, India.

<sup>3</sup>Inter-University Accelerator Centre, Aruna Asaf Ali Marg, New Delhi-110 067, India

The implantation of the nickel (Ni) and carbon (C) ions to the TiO<sub>2</sub> photocatalysts was carried out with the energy of 200 keV and fluences of  $1 \times 10^{15}$  and  $5 \times 10^{15}$  ions/cm<sup>2</sup>. The ion implantation was performed at room temperature with an incidence angle of 0 degree. The C and Ni ions implanted samples with two different ion fluences are denoted as TiO<sub>2</sub> +  $1 \times 10^{15}$  C, TiO<sub>2</sub> +  $5 \times 10^{15}$  C, TiO<sub>2</sub> +  $1 \times 10^{15}$  Ni and TiO<sub>2</sub> +  $5 \times 10^{15}$  Ni, respectively. After implantation, these films were annealed at 450 °C for 1h in air atmosphere.

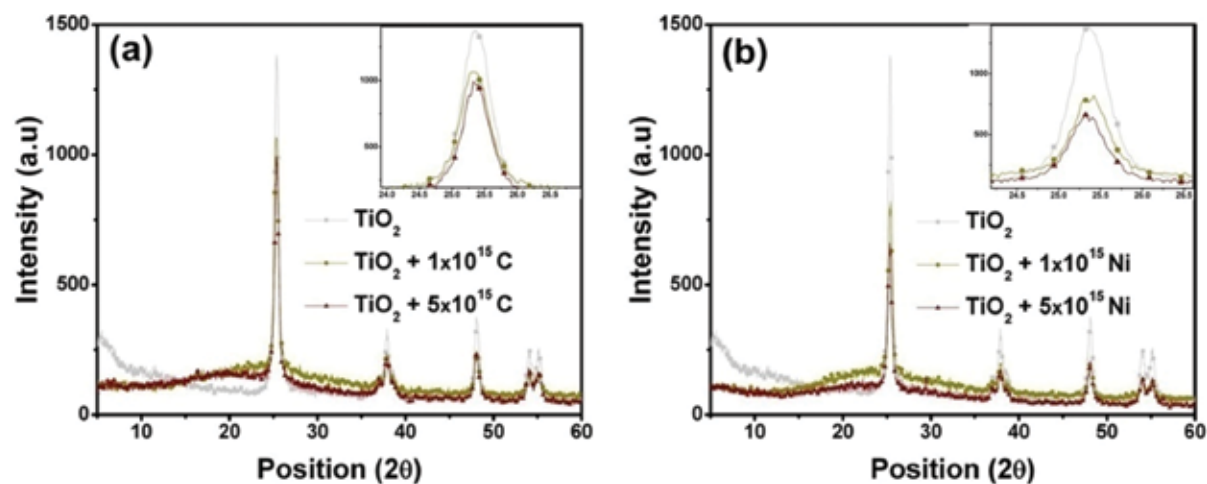


Figure 74 : XRD patterns of TiO<sub>2</sub> samples implanted with (a) carbon and (b) nickel ions (Insets show the magnified view of (101) peak indicating shift in peak position) at different ion fluences

Fig. 74 (a) and (b) show XRD pattern of the pure and implanted  $\text{TiO}_2$  samples. The prepared  $\text{TiO}_2$  nanopowder (Fig. 74(a)) shows six pronounced peaks, those are indexed with the polycrystalline tetragonal anatase  $\text{TiO}_2$ . The result matches well with the standard data (JCPDS card no. 21-1272). The diffraction peaks appearing at  $2\theta$  of  $25.36^\circ$ ,  $37.89^\circ$ ,  $48.09^\circ$ ,  $54.0^\circ$ ,  $55.15^\circ$  correspond to (101), (004), (200), (105) and (211) orientations, respectively. There is no additional peak observed after implanting with either 'C' or 'Ni' ions, even after increasing the ion fluence, which showed that the implanted ions are highly dispersed on  $\text{TiO}_2$  or normal XRD was not sensitive enough to detect such minor changes to  $\text{TiO}_2$ . This indicates that the doping process did not induce the formation of separate impurity phases and that the specific dopant could be considered to be fully incorporated into  $\text{TiO}_2$  lattice. It is clear from the insets of Figure that the intensity of the most intense peak (101) (at  $2\theta$  of  $25.36^\circ$ ) decreases with increasing fluence which can be ascribed to a weak damaging process and hence the crystallinity of  $\text{TiO}_2$  film is destroyed upon ion irradiation. Moreover, the (101) peaks of implanted samples were slightly shifted to lower diffraction angle as compared to that of pristine  $\text{TiO}_2$ . This slight shift implies the doping of carbon or nickel atom in the  $\text{TiO}_2$  lattice.

The results about structural properties suggest that the carbon and nickel ion implanted films do not possess any change in the crystal phase. However, the crystallinity of  $\text{TiO}_2$  film is declined upon ion irradiation. The other characterizations and measurements are in progress.

#### 5.2.41 Defects and junction characteristics of ion irradiated ZnO

S. Pal<sup>1</sup>, A. Sarkar<sup>2</sup>, P. Kumar<sup>3</sup>, D. Kanjilal<sup>3</sup>, D. Jana<sup>1</sup>

<sup>1</sup>Department of Physics, University of Calcutta, Kolkata -700009, India.

<sup>2</sup>Department of Physics, Bangabasi Morning College, Kolkata - 700009, India.

<sup>3</sup>Inter-University Accelerator Centre, Aruna Asaf Ali Marg, New Delhi-110 067, India

Zinc oxide (ZnO) is direct wide band gap semiconductor (3.37 eV at RT) which shows n-type semiconductivity due to presence of some native defects [1-2]. Its ability to form rectifying Schottky junctions with metals is one characteristic that promotes its use in diodes, UV detectors, gas sensors etc. Apart from that, low-resistance Ohmic contacts to ZnO are also needed for optical and piezoelectric applications. In this work, we report the defect induced changes in behavior of metal semiconductor junction (Au/ZnO). Defects have been created by 1.2 MeV Ar ion irradiation using the Low Energy Ion Beam Facility at IUAC. From SRIM calculation [3] it is understood that the maximum range of 1.2 MeV Ar ions in ZnO is  $\sim 1 \mu\text{m}$ . As the pellets are about  $\sim 250\text{-}300 \mu\text{m}$  thick, only sub surface modification is expected due to irradiation. I-V characteristics of unirradiated and irradiated samples have been recorded by two contacts from the samples, made by gold deposition. Fig. 75(a) shows the I-V characteristics (logarithmic plot) of all ZnO samples. It is clearly seen that the nature of I-V curve of unirradiated ZnO is asymmetric which means the metal semiconductor junction is showing rectifying behaviour i.e. Schottky like. This asymmetric nature continues to become symmetric with increasing fluence and with high fluence irradiation ( $1 \times 10^{16}$  ions/cm<sup>2</sup>) the curve becomes symmetric which means the junction becomes more and more ohmic. The changes in nature of junction could be better viewed from the I-V plots (Fig. 75(b)) where the forward currents have been scaled off. Fig. 75(b) clearly shows the increasing of leakage current with increasing fluence and the I-V curve becomes straight line for high fluence irradiated sample signifying a good ohmic contact. Another interesting fact is also revealed from the I-V plots (Fig. 75(b)) that the sheet resistance of low fluence ( $1 \times 10^{14}$  ions/cm<sup>2</sup>) irradiated sample increases by one order of magnitude than unirradiated sample whereas for high fluence irradiated sample four orders of magnitude decrease in sheet resistance is seen. The nature of contacts and sheet resistance depends on the type of defects present in the sub surface region and also with the concentration of the defects. Previous reports showed that the defects associated with oxygen vacancies ( $V_o$ ) are responsible for ohmic contacts and zinc vacancy ( $V_{zn}$ ) related defects are responsible for blocking contact [4]. Irradiation creates all possible types of native defects inside ZnO lattice. XPS and Raman studies clearly reveal that concentration of  $V_o$  has been increased with increasing fluence.  $V_{zn}$  plays an important role in reducing the conductivity of the low fluence irradiated samples although the effect is suppressed in high fluence irradiated sample. Besides that, low temperature photoluminescence and XPS also shows the significant increase of zinc

interstitial ( $I_{Zn}$ ) related defects in high fluence irradiated sample for which sharp decrease of its sheet resistance have been noticed.

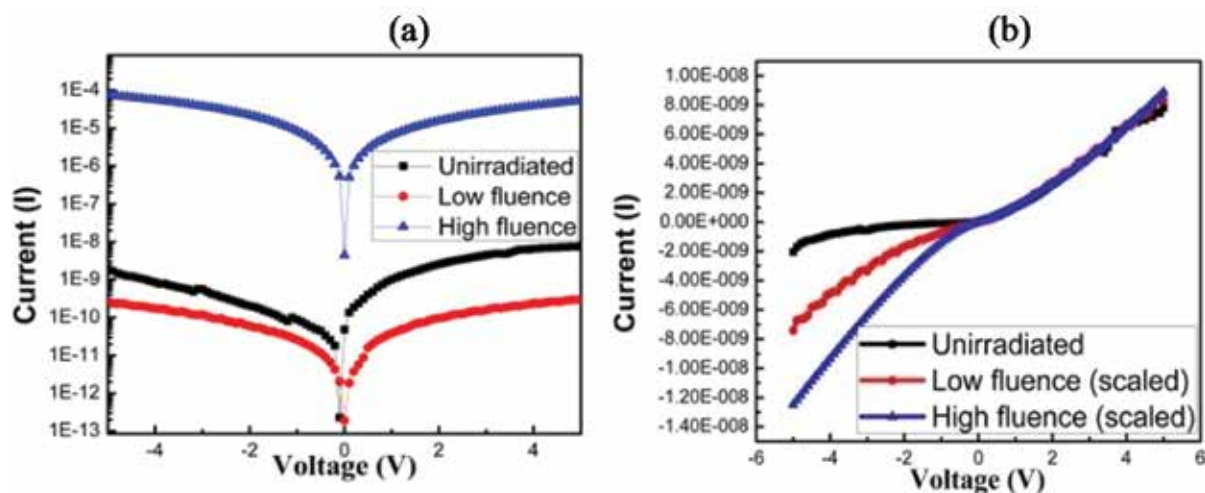


Figure 75 : (a) I-V characteristics (logarithmic plot) of all ZnO samples, (b) I-V curve of all ZnO samples (Forward currents have been scaled)

## REFERENCES

- [1] C. Klingshirn et al., Phys. Stat. Sol. (b) 247 (2010) 1424
- [2] S. Dutta et al., Prog. Mater. Sci. 54 (2009) 89
- [3] J.F. Ziegler et al., Stopping Power and Ranges of Ion in Matter, Pergamon, New York, 1985.
- [4] L. J. Brillson and Y. Lu, J. Appl. Phys. 109 (2011) 121301

### 5.2.42 Low energy ion beams reduced graphene oxide

K Hareesh<sup>1</sup>, K Asokan<sup>2</sup>, D Kanjilal<sup>2</sup>, V N Bhoraskar<sup>1</sup>, S D Dhole<sup>1</sup>

<sup>1</sup>Department of Physics, Savitribai Phule Pune University, Pune-411007, India

<sup>2</sup>Inter-University Accelerator Centre, Aruna Asaf Ali Marg, New Delhi-110 067, India

Graphene oxide (GO) is considered as a analogues of graphene which exhibits many oxygen functional groups such as carboxyl, epoxy and hydroxyl groups on its basal plane and edges, introducing  $sp^3$  defect sites and distorting the intrinsic conjugated  $\pi$  system that lowers the overall strength and conductivity [1]. GO can be reduced by many methods like Hydrazine, Thermal, Chemical doping, and by irradiation method [2]. Irradiation method is termed as clean and efficient method to reduce the GO compared to other conventional chemical methods [2]. In this work, we have irradiated GO by low energy ion beams viz. 100 keV  $H_2^+$ , 200 keV Ar and 350 keV  $N_2^+$  ions at different fluences.

Fig. 76(a) shows the high resolution C1s XPS spectrum of GO indicating the presence of C-C (284.5 eV), C-O (286.6 eV) and C=O (288.4 eV). Fig. 76(b) shows the high resolution C1s XPS spectrum of GO after 350 keV  $N_2^+$  ion irradiation. It can be observed from Fig. 76(b) that the intensities of oxygen functional groups decreased after irradiation indicating the reduction of graphene oxide [2]. Similar type of results are also observed in case of 100 keV  $H_2^+$  and 200 keV Ar ion beam irradiated GO confirming the reduction of GO.

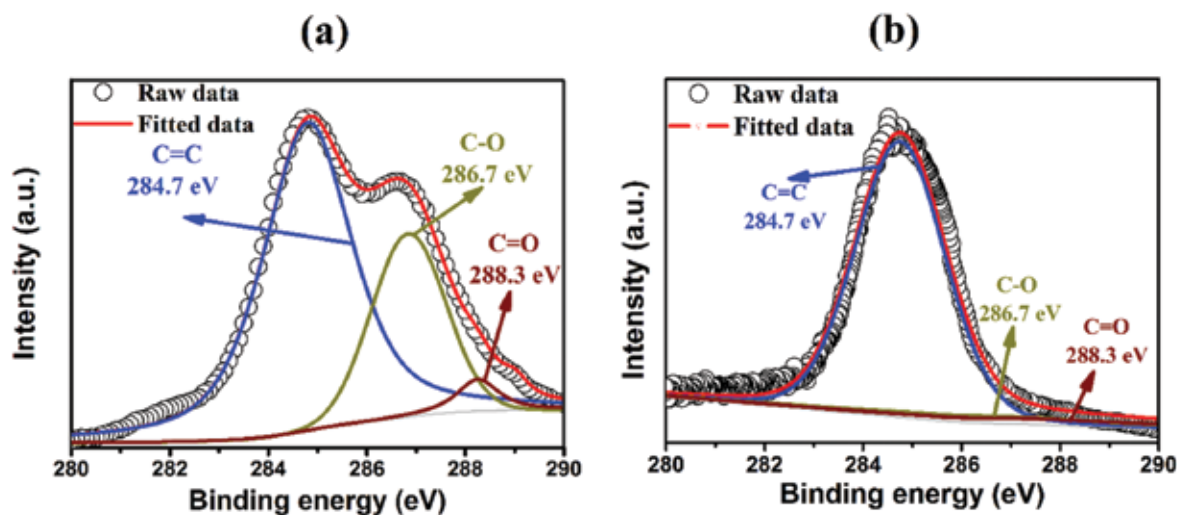


Figure 76 : Analysis of C1s spectra of (a) pristine GO and (b) 350 keV N ions irradiated GO at a fluence of  $5 \times 10^{15}$  ions/cm<sup>2</sup>.

## REFERENCES

- [1] Chen D et al., Chem. Reviews 112 (2012) 6027-53
- [2] Hareesh K et al., J. Phys. D: Appl. Phys. 48 (2015) 365105

### 5.2.43 Low Energy Ion Beam Induced Change in Structural and Optical Properties of SrTiO<sub>3</sub>

Vishnu kumar<sup>1</sup>, K. Asokan<sup>2</sup> and S. Annapoorni<sup>1</sup>

<sup>1</sup>Department of Physics and Astrophysics, University of Delhi, Delhi, India

<sup>2</sup>Inter-University Accelerator Centre, Aruna Asaf Ali Marg, New Delhi-110 067, India

Perovskite based oxynitrides, AB(O,N)<sub>3</sub> is an emerging class of solids. They have improved properties analogous to those of perovskite oxides. AB(O,N)<sub>3</sub> can be represented as nitrogen substituted perovskite oxides. Only a limited number of perovskite oxynitrides have been synthesized so far. These perovskite oxynitrides are becoming increasingly relevant for energy conversion and storage. For instance, the photo-catalytic activity in the visible light region has been reported for SrTaO<sub>2</sub>N, BaTaO<sub>2</sub>N, CaTaO<sub>2</sub>N and LaTaO<sub>2</sub>N.

Strontium titanate thin films are used as a substrate material for growth of other thin films. Also they can be used as insulating layers in dynamic random access memories etc. It is a well-known dielectric material with a high dielectric constant of 300. It is well known that on ion irradiation or implantation, structural distortion occurs in the system. The advantage of using ion irradiation is that due to the strong localized heating effects, drastic modifications in the material properties can be induced.

The Strontium titanate thin films were deposited on quartz substrates using RF magnetron sputtering (HINDHIVAC, Model 12" MSPT) of a Strontium titanate target in Ar+O<sub>2</sub> environment. The film thicknesses were estimated by using profilometer and Rutherford Back Scattering at IUAC. The Films were annealed at 700 °C in the presence of Ar+O<sub>2</sub> gas for 5 hours. The annealed films were subjected to 50, 60, 70 and 80 keV N<sup>+</sup> ion beam with different fluences of  $1 \times 10^{14}$  to  $5 \times 10^{16}$  ions/cm<sup>2</sup> to investigate the structural, dielectric and optical properties. Some of irradiated samples were characterized by X-Ray Diffractometer (PANalytical) with CuK<sub>α</sub> radiation ( $\lambda = 0.15406$  nm) operating at 45 kV and 40 mA, UV-Visible spectroscopy. As can be seen from Fig. 77(a), all the peaks in XRD pattern diminish and the most intense peak (110) is found to shift towards left after subjecting the sample to low energy ion irradiation. Energy band gaps, evaluated from UV-vis spectra shown in Fig. 77(b), corresponding to non-irradiated, fluence of  $1 \times 10^{15}$  and  $1 \times 10^{16}$  are 3.55, 3.57, 3.61 eV respectively. Therefore, band gap is found to increase with increase in fluence.

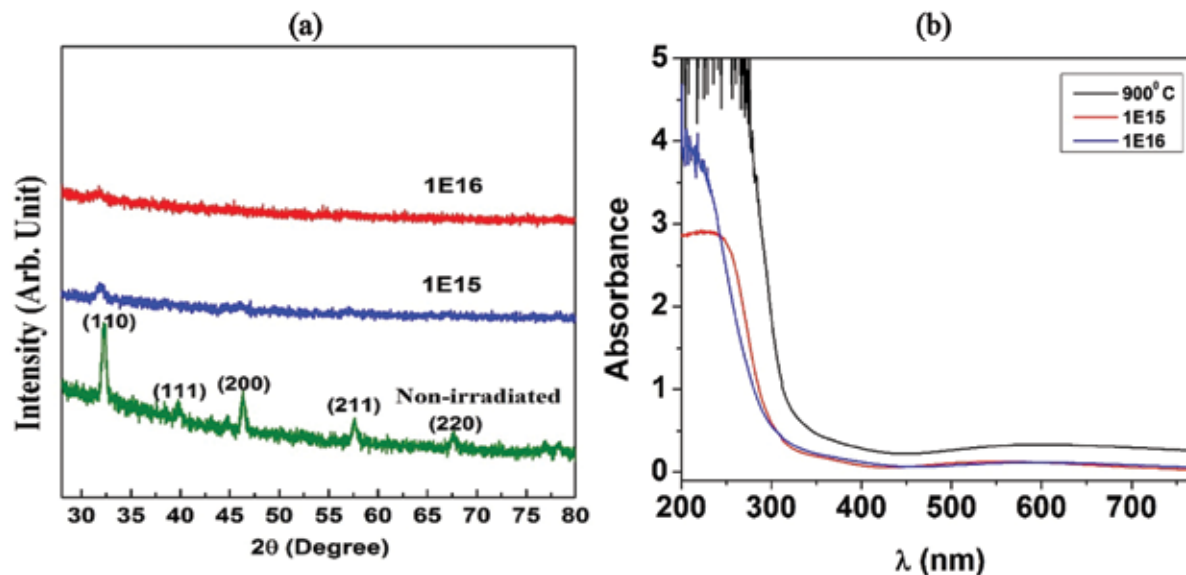


Figure 77 : (a) XRD pattern of STO thin films, and (b) UV-Visible spectra of STO thin films.

## REFERENCES

- [1] D. Kan et al., Nature Mater. 4 (2005) 816
- [2] C M Liu et al., J. Phys. D: Appl. Phys. 40 (2007) 7318
- [3] H. Stocker et al., Scripta Materialia. 86 (2014) 1

### 5.2.44 Low Energy ionirradiation Stability of Nano-Crystalline Cubic Zirconia Films

Parswajit Kalita<sup>1</sup>, Santanu Ghosh<sup>1</sup>, Devesh K. Avasthi<sup>2</sup>

<sup>1</sup>Department of Physics, Indian Institute of Technology Delhi, New Delhi, India.

<sup>2</sup>Inter-University Accelerator Centre, Aruna Asaf Ali Marg, New Delhi-110 067, India

The radiation stability of nano-crystalline cubic Zirconia films was investigated under 41 keV He ion irradiation. Stabilizer free cubic ZrO<sub>2</sub> films, with an average grain size ~ 10 nm, were grown on Si (100) substrates using electron beam assisted thermal evaporation at Target Lab, IUAC New Delhi. For thickness and composition analysis, the as-deposited films were characterized by RBS, using a 4 MeV He<sup>+</sup> ion beam at IUAC, New Delhi. The films were then irradiated with 41 keV He<sup>+</sup> ions at room temperature in the broad fluence range  $1 \times 10^{15}$  to  $1 \times 10^{17}$  ions/cm<sup>2</sup> using the table-top accelerator facility at IUAC, New Delhi. These ions were chosen to simulate alpha particles (produced during fission events) because of the similar electronic energy loss in zirconia. Although the cubic structure was retained upon irradiation, a slight reduction in crystallinity in the irradiated films was detected as compared to the as-deposited film (Fig. 78). No bulk amorphization was however observed for any of the fluences and hence these films are radiation tolerant to alpha particles. AFM of the irradiated films also did not show any major surface damage upon irradiation. The average surface roughness was however found to decrease after irradiation which might be attributed to sputtering from the film surface upon irradiation.

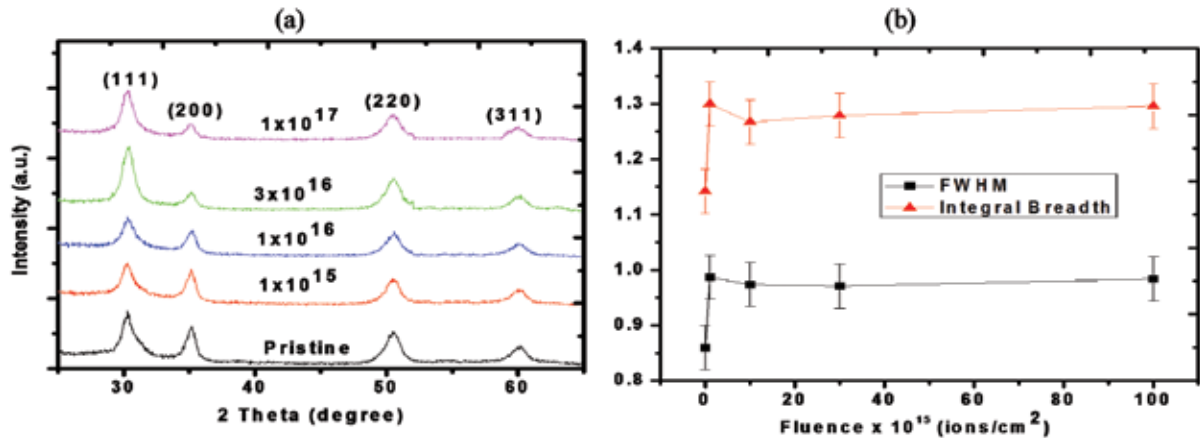


Figure 78 : (a) GXR D patterns of the 41 keV He irradiated ZrO<sub>2</sub> films and (b) FWHM and Integral Breadth of the most intense (111) peak as a function of fluence.

### 5.2.45 Magneto-resistance study of low energy irradiated superconductor/ferromagnetic thick films

S. Tripathy<sup>1</sup>, B. Sahoo<sup>1</sup>, K.L. Routray<sup>1</sup>, K. Asokan<sup>2</sup> and D. Behera<sup>1</sup>

<sup>1</sup>Department of Physics and Astronomy, NIT Rourkela 769008

<sup>2</sup>Inter-University Accelerator Centre, Aruna Asaf Ali Marg, New Delhi-110 067, India

Vortex dynamics in high temperature superconductors (HTSCs) gives information for many important properties such as the critical current density, quantized flux trapping, vortex flow and activation energy [1,2]. This aspect of activation energy has been studied through various techniques such as DC electrical resistivity, remnant magnetization and AC susceptibility [3]. The intrinsic and extrinsic properties of have been modified due to substitution at different crystallographic sites, by making composite to YBa<sub>2</sub>Cu<sub>3</sub>O<sub>7- $\delta$</sub>  (YBCO) and irradiating with low and high energy ion beams.

In the present work we have focused on the combined effect of La<sub>2-x</sub>Sr<sub>x</sub>MnO<sub>8</sub> (LSMO) inclusions and defects introduced due to ion irradiation on YBCO thick films prepared by diffusion reaction technique. YBCO is irradiated with 100 keV O, C and N ions to fluence of 5 × 10<sup>15</sup> ions/cm<sup>2</sup> and its composites are irradiated with only oxygen ions. These were subjected to varying magnetic field to observe the resistive dissipative. Fig. 79(A)-(C) show temperature dependence of resistance for oxygen, carbon and nitrogen irradiated samples under the influence of magnetic field (0-8 T) respectively. In all the irradiated samples, though T<sub>c</sub> onset has not been affected rather the T<sub>c0</sub> (R=0) shows large variation under the magnetic field. Particularly, samples irradiated under nitrogen ions show higher degradation at the intra- and intergranular region. The normal state behavior of the nitrogen ion irradiated sample shows semiconducting nature for the resistive transition (Fig. 79(C)). A double transition in T<sub>c</sub> has been observed for carbon and nitrogen ion irradiated samples (Fig. 79(B) and (C)). Implantations of low energy ions in the present study may affect in general, the links between intergrain boundaries. Nitrogen may be reactive or inert depending upon how it is bonded in the system. If it acts as inert, it will break the links or make weak links between the grain boundaries, at higher dose, it can even make it insulator.

The semiconducting nature of the curve with nitrogen ion may be due to segregating the holes in the crystal. In general, nitrides are of insulating nature and possibly in superconductors it will destroy the connectivity. In case of carbon ion, it is mostly passive and it can occupy vacancies of oxygen and may enhance the superconducting properties. In case of YBCO, oxygen can occupy the vacancies and may have relatively soft towards superconducting properties at low doses. In Fig. 79(D), we have shown the variation activation energy of YBCO/LSMO (1 and 2 wt.% samples irradiated with 100 keV oxygen ion and subjected to magnetic field with a fluence of 5 × 10<sup>15</sup> ions/cm<sup>2</sup>. As has been observed (Fig. 79(D)) : activation energy decreases with magnetic field

as reported [3]. However, these observed variations are different for the two types of samples. The behavior of the LSMO to YBCO suggests that grain boundary scattering plays an important role in the transport properties [4]. Particularly LSMO 2 wt.% shows higher activation energy as compared to LSMO 1 wt.% sample.

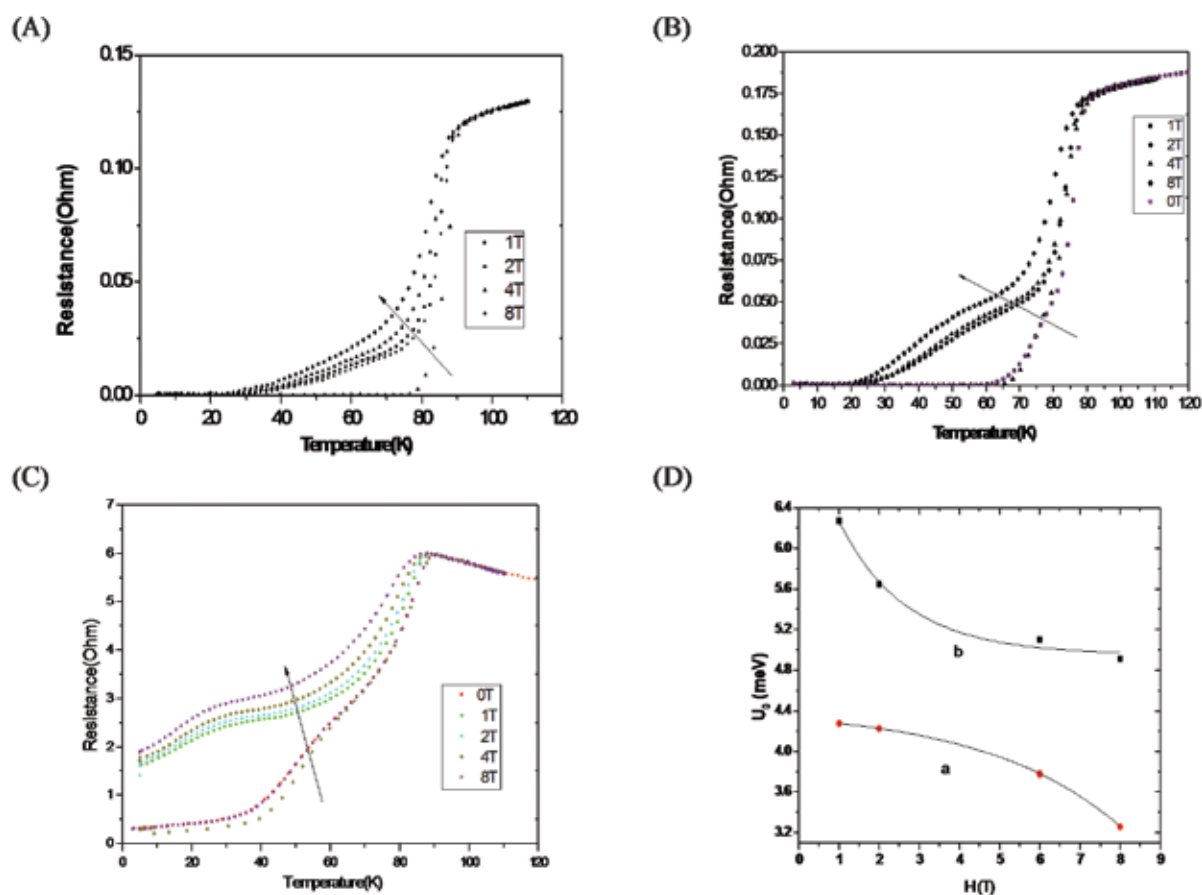


Figure 79 : Temperature dependent resistance of YBCO irradiated (A) with 100 keV Oxygen under the influence of varying magnetic field, (B) with 100 keV Carbon under the influence of varying magnetic field and (C) with 100 keV Nitrogen under the influence of varying magnetic field. (D) Activation energy vs. magnetic field in (a) YBCO+LSMO 1wt % and (b) YBCO+LSMO 2wt % samples

## REFERENCES

- [1] A. Mohanta, D. Behera, Solid State Communications 150 (2010) 1325
- [2] A. Kujur and D. Behera, Journal of Magnetism and Magnetic Materials, 377 (2015) 34
- [3] S.L. Liu, J. Supercond. Novel Magn. 21 (2008) 199
- [4] B.S. Blagoev, T.K. Nurgaliev, V. Strbik, E.S. Mateev, and A.J. Zaleski, Bulg. J. Phys. 40 (2013) 337

### 5.2.46 Carbon and Proton ion implantation in $Al_2O_3$ OSL phosphor for medical dosimetry

Mini Agarwal<sup>1</sup>, K. Asokan<sup>2</sup>, Pratik Kumar<sup>1</sup>

<sup>1</sup>Medical Physics Unit, IRCH, AIIMS, New Delhi- 110029, India

<sup>2</sup>Inter-University Accelerator Centre, Aruna Asaf Ali Marg, New Delhi-110 067, India

This work seeks to investigate doping effect of carbon in alumina substrate (single and poly crystalline) and In-lab made alumina via Sol-gel and SCS (Solution combustion synthesis) based methods and also commercially available alumina using ion-beam which may change the properties of the substrate and thus may produce  $Al_2O_3:C$  OSL phosphor. Also the proton beam effect on the same phosphor was to be investigated to compare the CW- OSL decay curve shapes and also to obtain the high sensitivity phosphor. It is an easy method which may make  $Al_2O_3:C$

cheaper. Ion beam implantation method has been found to change the physical and electronic properties of material [1-2]. This method is well suited to materials like insulators where small numbers of implanted particles can create the major changes in the optical or physical properties. By performing suitable implantations at different energies, it is possible to obtain a desired distribution of impurity such as a uniformly and homogeneous doped region. The effect of ion beam in the samples can be seen from the Fig. 80 - 82.

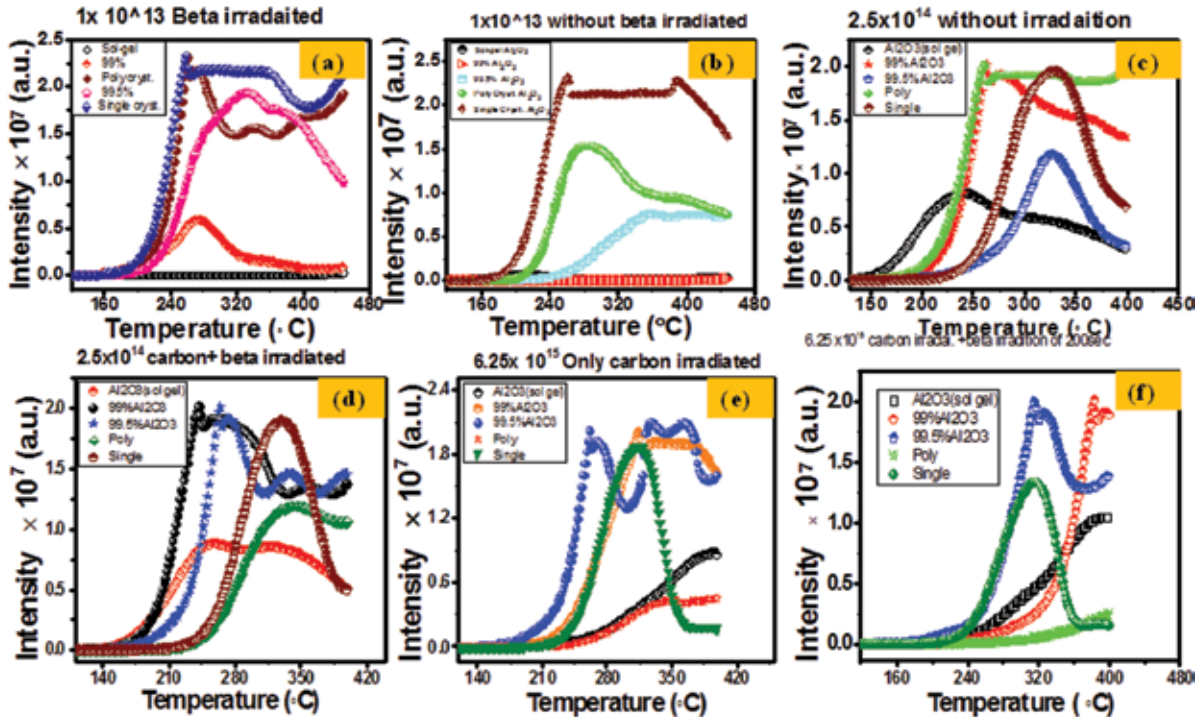


Figure 80 : Characteristic CW-OSL decay curve of  $\alpha$ - $\text{Al}_2\text{O}_3$  (micro-cryst. Nano cryst. Sol-gel and SCS based and single and poly crystalline) for carbon ion beam of 500 keV at  $1 \times 10^{13}$ ,  $2.5 \times 10^{14}$  and  $6.25 \times 10^{15}$  fluence ; (b, c and e) shows only carbon ion implantation and (a, d and f) shows the carbon + beta irradiation effect on  $\alpha$ - $\text{Al}_2\text{O}_3$  phosphors.

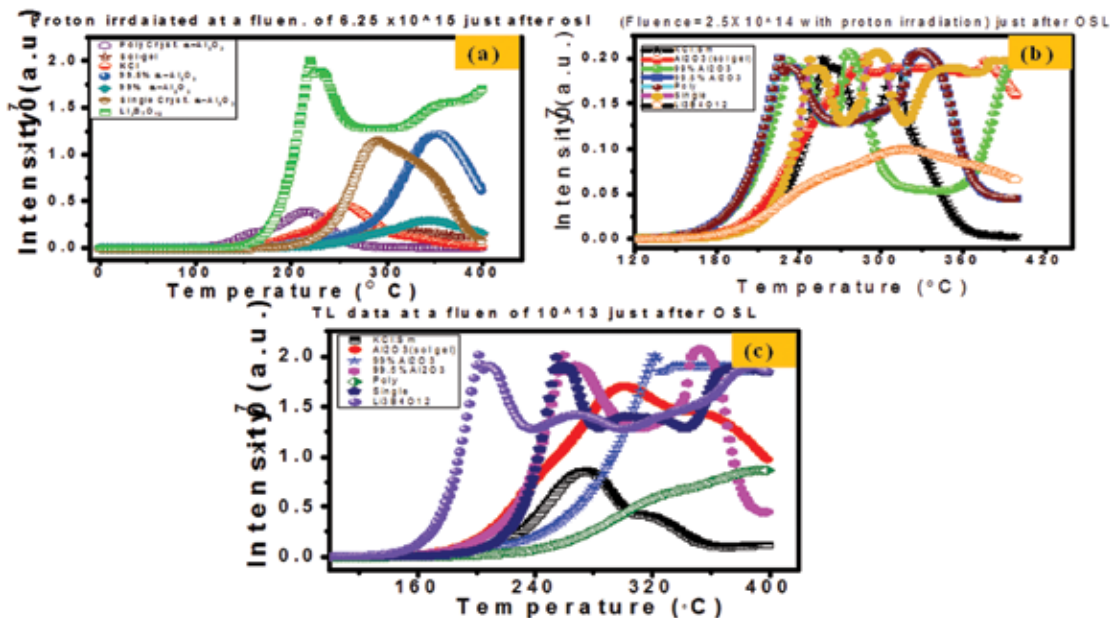


Figure 81 : TL just after CW-OSL decay curve of  $\alpha$ - $\text{Al}_2\text{O}_3$  (micro-cryst. Nano cryst. Sol-gel and SCS based and single and poly crystalline),  $\text{kCl:Sm}$  and  $\text{Li}_3\text{B}_7\text{O}_{12}$  for Proton ion beam of 250 keV; (a), at  $6.25 \times 10^{15}$  fluence; (b) at  $2.5 \times 10^{14}$  fluence ; and (c) at  $1 \times 10^{13}$  fluence.

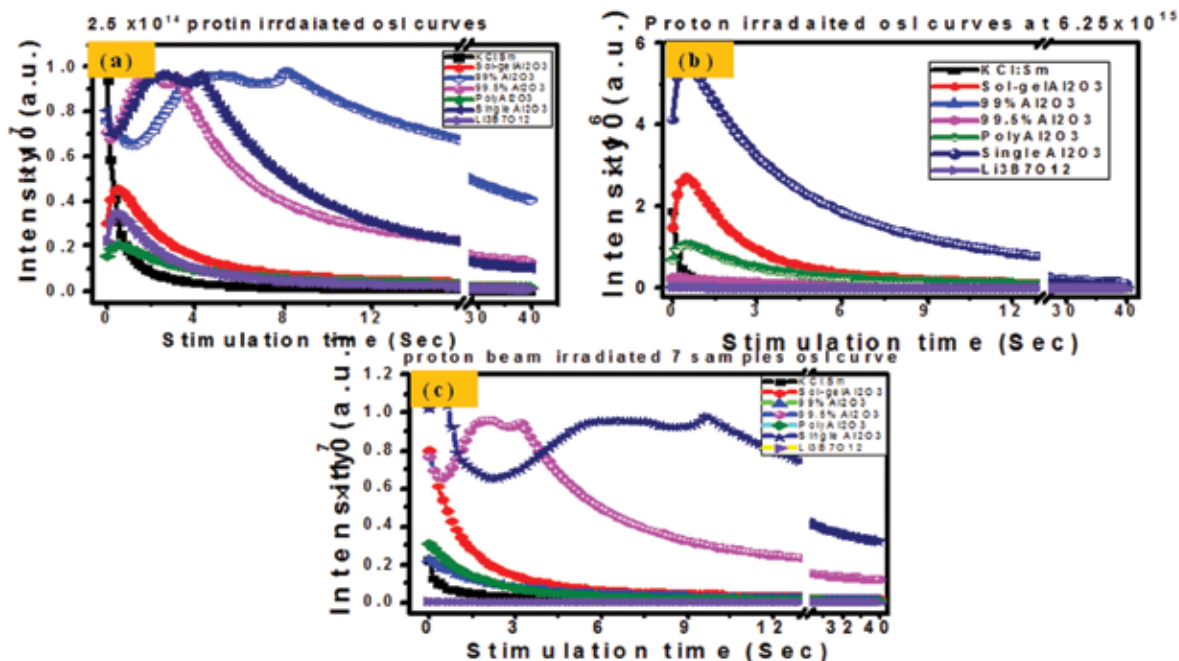


Figure 82 : CW-OSL decay curve of  $\alpha$ - $\text{Al}_2\text{O}_3$  (micro-cryst. Nano cryst. Sol-gel and SCS based and single and poly crystalline),  $\text{KCl:Sm}$  and  $\text{Li}_3\text{B}_7\text{O}_{12}$  for Proton ion beam of 250 keV; (a), at  $6.25 \times 10^{15}$  fluence; (b) at  $2.5 \times 10^{14}$  fluence ; and (c) at  $1 \times 10^{13}$  fluence.

In conclusion this work aims at to develop new and improved OSL material and also to characterize them so that they may be suitably used for medical radiation dosimetry. Also, the goal of this work is to investigate the suitability of these materials for dosimetry of heavy charge particle (HCP) as TLDs are not well placed for accurate dosimetry of HCPs [3-9] which are gaining ground as newer modality of cancer treatment.

## REFERENCES

- [1] S. J. Pearton et al., Ion implantation doping and isolation of GaN. *Applied Physics Letters*. 67 (1995) 1435
- [2] R. H. Dennard et al., Design of ion implanted MOSFETs with very small physical dimensions. *IEEE journals & Magazines*. 1974.
- [3] Janet Sisterson (ed). Review of ion beam therapy. *Particles Newsletter*. 25 (2000) 14.
- [4] S. P. Lochab, N. Salah, P. D. Sahare, R. S. Chauhan and R. Ranjan, *Nucl. Instrum. Methods B* 254 (2007) 231
- [5] Yang B, Xie L, Xu Y and Townsend P D, *Nucl. Instrum. Methods B* 187 (2002) 408
- [6] O. P. Geiß, M. Kramer and G. Kraft, *Nucl. Instrum. Methods B* 142 (1998) 592
- [7] P. Olko, P. Bilski, M. Budzanowski, and A. Molokanov, *Radiat. Prot. Dosim.* 110 (2004) 315
- [8] J. L. Massillon, I. Gamboa-deBuen and Brandan M E., *J. Appl. Phys.* 100 (2006) 103521
- [9] R. Gaza, E. G. Yukihara, S. W. S. McKeever, *Radiation Measurements* 38 (2004) 417

### 5.2.47 Effect of Hydrogen Ion Implantation on Cholesterol Sensing Using Enzyme-Free Laponite-Montmorillonite Electrodes

Nidhi Joshi<sup>1</sup>, Abhimanyu Sharma<sup>2,3</sup>, K. Ashokan<sup>3</sup>, Kamla Rawat<sup>2,3</sup> and D. Kanjilal<sup>3</sup>

<sup>1</sup>School of Physical Sciences, Jawaharlal Nehru University, New Delhi 110067, India

<sup>2</sup>Special Center for Nanosciences, Jawaharlal Nehru University, New Delhi 110067, India

<sup>3</sup>Inter-University Accelerator Centre, Aruna Asaf Ali Marg, New Delhi-110 067, India

Ion irradiation experiments were performed on Laponite-Montmorillonite/Indium Tin Oxide (L-MMT/ITO) films using 20 keV  $\text{H}_2^+$  ion beam with variable fluence ranging from  $10^{12}$  –  $10^{16}$  ions/cm<sup>2</sup> and the electrochemical

profiling of these irradiated electrodes were done using Cyclic Voltammetry (CV) and Electrochemical Impedance Spectroscopy (EIS) (Fig. 83). Scanning electron microscopy (SEM) (Fig. 84), X-ray diffraction (XRD) and Fourier transform Infrared spectroscopy (FTIR) were used for pre and post-irradiation morphology study and binding analysis. FTIR spectroscopy indicated the implantation of low-energy  $H_2^+$  ions resulting in the formation of new bonds. The enhanced cholesterol sensitivity of irradiated films upto fluence of  $10^{13}$  ions/cm<sup>2</sup> was observed due to morphological changes taking place in L-MMT films. Close to 20% enhancement in cholesterol sensitivity was noticed, when the ion fluence was  $\approx 10^{13}$  ions/cm<sup>2</sup> (Fig. 83(b)). The sensitivity for cholesterol detection of the L-MMT electrode formed through  $H_2^+$  ion implantation clearly exhibited a strong dependence on the fluence of the ion beam. The radiation-induced enhanced sensitivity can be proposed as a platform for development of a more effective enzymes-free strip sensor.

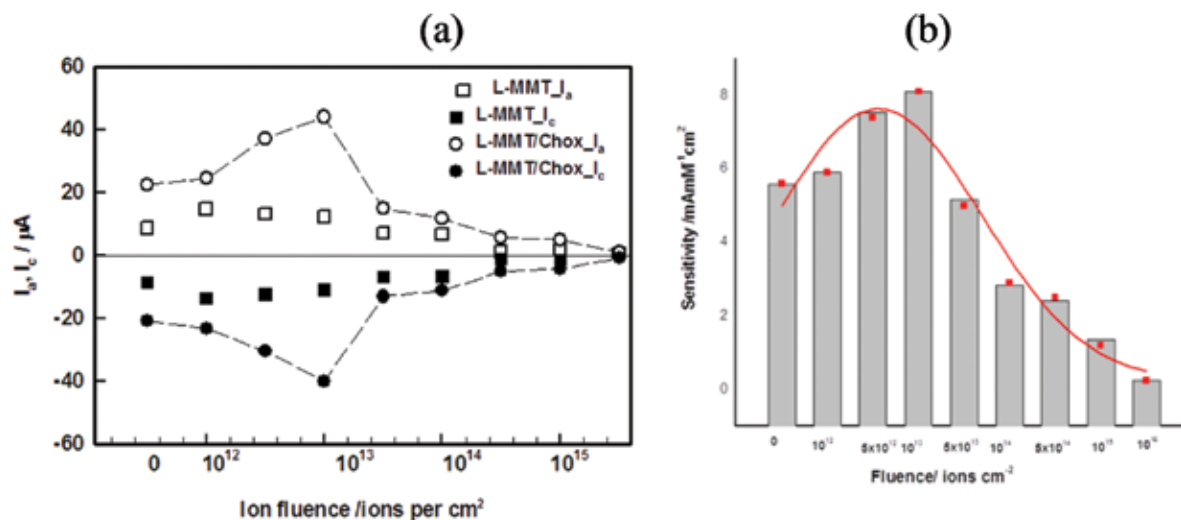


Figure 83 : Anodic and cathodic peak current as a function of ion fluences of  $H_2^+$  ion beam in the absence and presence of cholesterol. Sensitivity of L-MMT/ITO electrode for different irradiated electrode was shown, where the maximum sensitivity was noted for the  $H_2^+$  ion beam at the fluence of  $10^{13}$  ions/cm<sup>2</sup>.

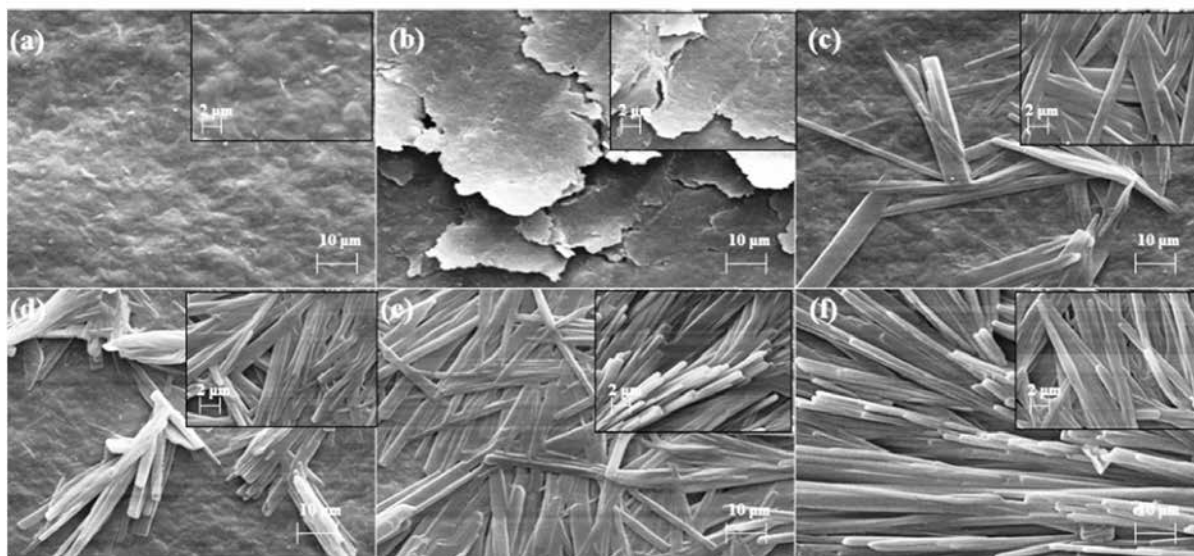


Figure 84 : SEM images for L-MMT/Chox/ITO irradiated with different fluence of hydrogen molecular ion beam. Figure depicts the (a) irradiated L-MMT/ITO thin film of ion fluence  $5 \times 10^{12}$  ions/cm<sup>2</sup> without cholesterol, (b) irradiated with  $H_2^+$  ion beam of fluence  $1 \times 10^{12}$ , (c)  $5 \times 10^{12}$ , (d)  $5 \times 10^{13}$ , (e)  $5 \times 10^{14}$  and (f)  $5 \times 10^{15}$  ions/cm<sup>2</sup> for L-MMT/Chox/ITO electrode.

### 5.2.48 Energy Independence and Thermoluminescence Properties of Eu Doped BaSO<sub>4</sub> Nanophosphor

Anant Pandey<sup>1</sup>, Kanika Sharma<sup>1</sup>, Shaila Bahl<sup>2</sup>, Pratik Kumar<sup>2</sup>, S. P. Lochab<sup>3</sup>

<sup>1</sup>Dept. of Physics, Sri Venkateswara College, University of Delhi, Dhaula Kuan, New Delhi-110021

<sup>2</sup>Medical Physics Unit, IRCH, All India Institute of Medical Sciences, New Delhi-110029

<sup>3</sup>Inter-University Accelerator Centre, Aruna Asaf Ali Marg, New Delhi-110 067, India

In this work, mainly the Thermoluminescence (TL) response of Eu doped BaSO<sub>4</sub> nanophosphor to different energies of gamma radiation has been studied along with a few other TL properties [1-2]. Various kinetic parameters have also been determined for the glow curve structures of the given phosphor irradiated with the same dose but different energies of gamma. BaSO<sub>4</sub> nanophosphor was prepared by the typical chemical co-precipitation method [3-5] and characterized using X-ray diffraction (XRD). The sample was then divided into two different sets containing a number of packets. One of the sets was irradiated with a very wide range i.e. 10Gy to 2kGy of gamma using 1.25 MeV of Co-60, while the other set was irradiated with 1Gy to 300 Gy of gamma using 662 keV of Cs-137. Thus, both the sets were exposed to an overlapping range of gamma radiation from 10Gy to 300Gy for two different energies. It was observed that the shape of the glow curve remained remarkably similar for the two different energies of gamma radiation. Further, the TL response curve also showed no substantial variation in linearity by changing the energies of the gamma radiation (Fig. 85). Therefore, it can be concluded that the given nanophosphor showed promising results as an energy independent TL phosphor. Further, the TL response curve also showed no substantial variation in linearity by changing the energies of the gamma radiation. Furthermore, the current nanophosphor showed an outstanding linear TL response over an extremely broad range of gamma radiation with response remaining linear for a dose as high as 2kGy of gamma radiation.

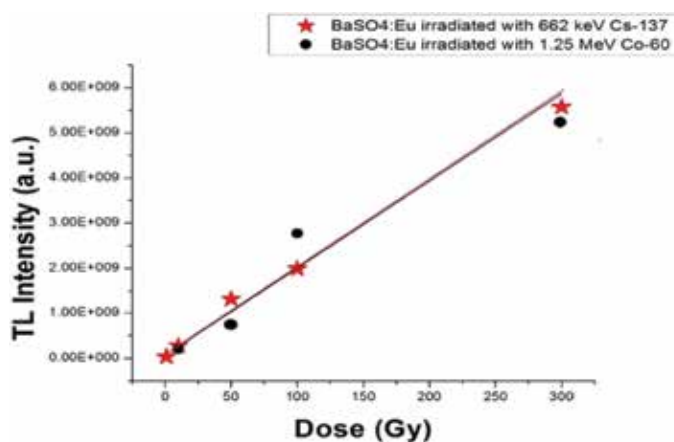


Figure 85 : TL response curve of Nanocrystalline BaSO<sub>4</sub>:Eu for different energies i.e. 662 keV Cs-137 & 1.25 MeV Co-60, but same dose range i.e. 10Gy -300Gy of gamma radiation. The nanophosphor exhibits energy independence.

### REFERENCES

- [1] S. W. S. McKeever et al., Thermoluminescence Dosimetry Materials: Properties and Uses. Nuclear Technology Publishing; Ashford (United Kingdom) (1995)
- [2] V. Kortov. Radiation Measurements 42 (2007) 576-581
- [3] S. Bahl et al., Journal of Luminescence 149 (2014) 176-184
- [4] R. Singh, M.K.Dhasmana, R.B.S. Rawat. Journal of Engineering and Science, 2(1) (2013) 16-19
- [5] N. Salah, S.S. Habib, Z.H. Khan, S.A. Hamed, S.P. Lochab. Journal of Luminescence 129 (2009) 192-196

### 5.2.49 Gamma ray induced thermoluminescence properties of Eu<sup>3+</sup> doped SnO<sub>2</sub> phosphor

M. Chowdhury<sup>1</sup>, S. K. Sharma<sup>1</sup>, S. P. Lochab<sup>2</sup>

<sup>1</sup>Department of Applied Physics, Indian School of Mines, Dhanbad-826004, India

<sup>2</sup>Inter-University Accelerator Centre, Aruna Asaf Ali Marg, New Delhi-110 067, India

Spectroscopic studies play a vital role in characterizing the specific luminescence properties such as photoluminescence and thermoluminescence. The rare earths are usually incorporated in the material as divalent or trivalent cation for the realization of optically active materials in photonics and optoelectronic applications.

Incorporation of  $\text{Eu}^{3+}$  ions in  $\text{SnO}_2$  has been extensively studied due to their high stability in oxide matrices and high quantum yield. In the present studies, we have reported the thermoluminescence (TL) properties of  $\text{Eu}^{3+}$  doped  $\text{SnO}_2$  prepared by combustion method. The thermoluminescence (TL) studies were carried out after irradiating the sample by  $\gamma$ -rays in the dose range 100 Gy to 1 kGy. Kinetic parameters such as order of kinetics, trap depth and frequency factor associated with the glow peak were also calculated.

The TL response of the phosphor having the optimum concentration of  $\text{Eu}^{3+}$  (3 mol%) were studied over the  $\gamma$ -dose range from 100 Gy-1 kGy at a heating rate of  $5^\circ\text{C/s}^{-1}$  (Fig. 86(a)). It shows an asymmetric broad TL band between  $50^\circ\text{C}$  and  $400^\circ\text{C}$  with the peaks at around  $116^\circ\text{C}$  and  $300^\circ\text{C}$ . The maximum TL intensity was observed for 1kGy irradiated phosphor. For all the doses, there is no significant change in the position of peak temperatures. The TL intensity of glow curves increases linearly in the dose range 100 Gy–1 kGy as shown in the Fig. 86(b).

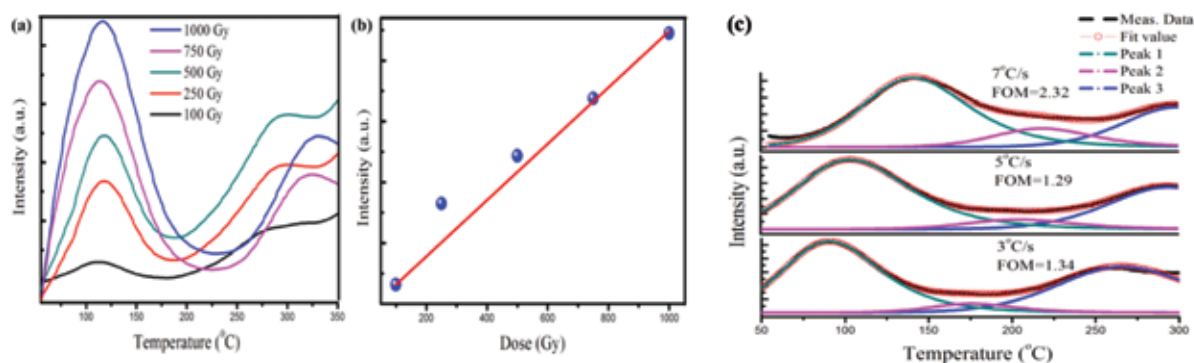


Figure 86 : (a) TL glow curves of  $\text{SnO}_2: \text{Eu}^{3+}$  (3 mol%) phosphor varying  $\gamma$ -dose (b) Intensity of glow peak as a function of  $\gamma$ -dose, (c) Deconvolution of TL glow curves

The TL glow curve is related to the trap levels lying at different depths in the band gap between conduction and valence bands of a solid. These trap levels were characterized by calculating different kinetic parameters such as trap depth, order of kinetics and frequency factor associated with these levels. The recorded glow curves of the prepared samples exposed to 1 kGy  $\gamma$ -irradiation dose at different heating rates 3, 5 and  $7^\circ\text{C/s}$  seem to be composite in nature as they exhibit a broad band. So, CGCD method was used to deconvolute the composite glow curve and to calculate the kinetic parameters using TLanal computer program. The fitted TL glow curves are shown in Fig. 86(c) and the values of trap depth and frequency factor of traps calculated by CGCD method are summarized in Table 5.2.4.

Table 5.2.4: Kinetic parameters by CGCD method

Heating rate	Peak 1		Peak 2		Peak 3	
	E (eV)	s <sup>(s-1)</sup>	E (eV)	s <sup>(s-1)</sup>	E (eV)	s <sup>(s-1)</sup>
3	0.53	$2.48 \times 10^6$	0.94	$4.88 \times 10^9$	0.82	$4.63 \times 10^6$
5	0.49	$5.61 \times 10^5$	0.83	$1.15 \times 10^8$	0.97	$7.34 \times 10^7$
7	0.63	$1.28 \times 10^7$	0.96	$2.34 \times 10^9$	1.17	$4.98 \times 10^9$

## REFERENCES

- [1] C. Furetta, Handbook of Thermoluminescence, 2nd ed., World Scientific, Singapore, 2003.
- [2] M. Chowdhury, S.K. Sharma, S.P. Lochab, Mater. Res. Bull. 70 (2015) 584–589.

### 5.3 RADIATION BIOLOGY RESEARCH

#### 5.3.1 High LET radiation induced effects on signaling pathways in human prostate cancer cell line

Pallavi Srivastava<sup>1</sup>, Chandra Mohini Chaturvedi<sup>1</sup>, Asitikantha Sarma<sup>2</sup>

<sup>1</sup>Department of Zoology, Banaras Hindu University, Varanasi

<sup>2</sup>Radiation Biology Lab, Inter-University Accelerator Centre, New Delhi

High LET Radiation (Carbon Ion Radiation) has significant biological advantages and in combination with radiomodulators, may result in further enhancement in the efficiency as well as cost effective. Radiomodulators are intended to enhance tumor cell death by altering one or more of the “5 Rs of radiotherapy”: Inherent cellular radiosensitivity, repair, reassortment, repopulation and reoxygenation.

Inhibitors of several enzymes involved in the repair of DNA strand breaks works as radiomodulator, are currently at various stages of the drug development process [1,2]. PNKP (polynucleotide kinase /phosphatase) plays vital roles in mammalian base excision repair, SSB repair, DSB repair and non homologous end joining (NHEJ) making it an attractive therapeutic target [3,4].

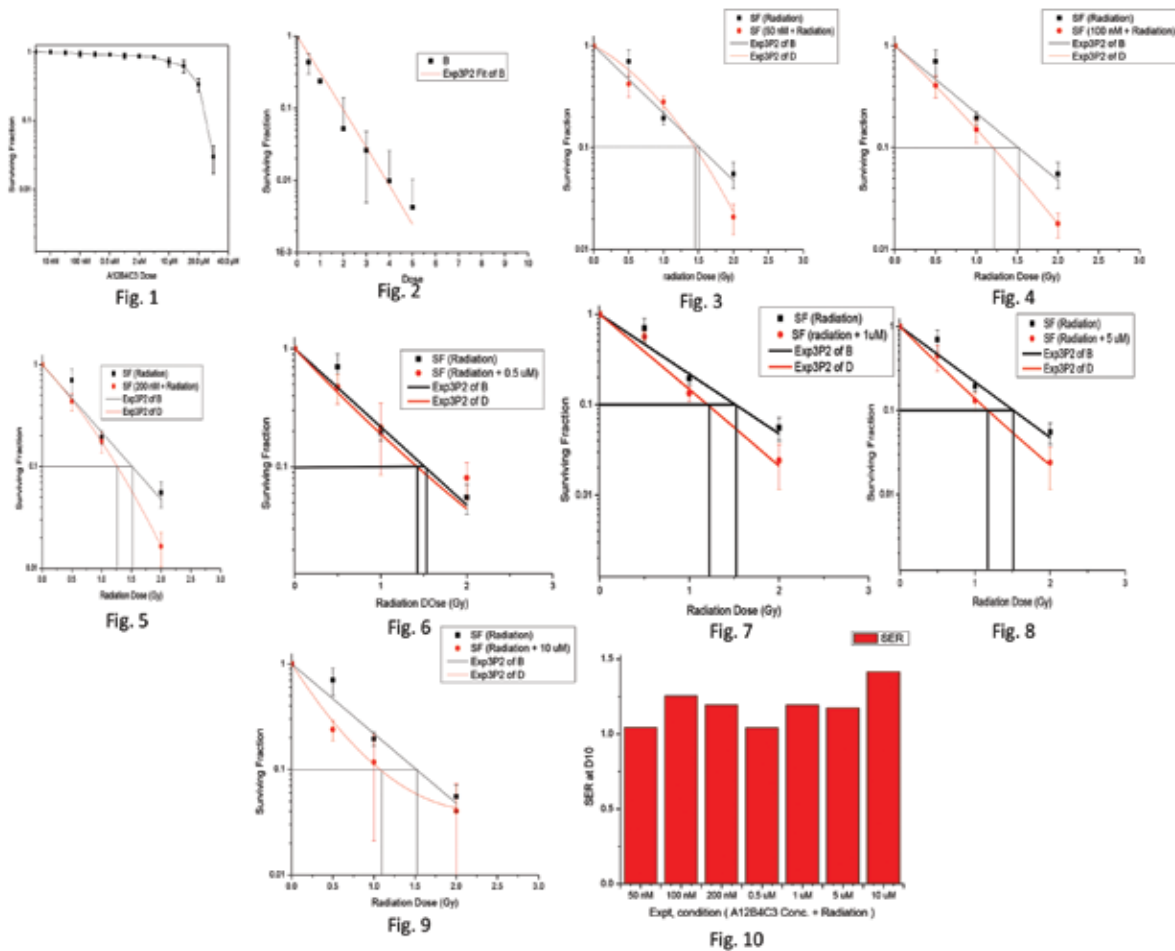


Fig. 87 : (1-9) Survival fraction (SF) curves of PC-3 Cell line  
 (10) Sensitizer enhancement ratio (SER) values determined from combination treatment (Radiation + ABC compound treatment)

So, in this study we are trying to suppress the DNA repair process by using PNKP inhibitor ABC (A12B4C3, Sigma Aldrich) in Prostate cancer cell line (PC-3) which may enhance the radiosensitivity by accelerating the apoptosis. Prostate cancer is the most frequently diagnosed tumor in men, accounting alone for 29% of incidence cases and it is the second most common cause of death due to cancer in men after lung cancer. One of the important reason for the use of charged particle beam in PCa radiotherapy is that it can three dimensionally deliver a large dose to the tumor, and allow the sparing of surrounding normal tissues [5].

The surviving fraction of PC-3 cells treated with  $^{12}\text{C}$ -ion radiation and ABC showed a dose dependent effect (Fig. 1, 2 of Fig. 87). For combination experiment, three doses of  $^{12}\text{C}$ -ion radiation and different doses (50 nM, 100 nM, 200 nM, 0.5  $\mu\text{M}$ , 1  $\mu\text{M}$ , 5  $\mu\text{M}$  and 10  $\mu\text{M}$ ) of ABC (Fig. 3-9 of Fig. 87) were used to determine surviving fraction. We found combined treatment (radiation + drug) has more radiosensitizing effect as compared to radiation alone. The sensitizer enhancement ratio (SER), an indicator of the radiosensitizing effect of a drug of interest, was calculated as the ratio of the  $D_{10}$  of cells treated with irradiation alone to the  $D_{10}$  of cells treated with irradiation plus drug. The lowest and highest SER is at 50nM and 10  $\mu\text{M}$  respectively (Fig. 10 of Fig. 87). In the present study, we are trying to reduce the radiation dose by using a non-toxic and moderate effect conc. of ABC which would contribute to evolve ABC as an efficient radiomodulator and cost effective heavy ion therapy. Further, we are trying to investigate the pathway responsible for cell death, which is under investigation.

## REFERENCES

- [1] D. Davidson, L. Amrein, L. Panasci, and R. Aloyz, Small molecules, inhibitors of DNA-PK, targeting DNA repair, and beyond, *Frontiers in Pharmacology* **4**, 1 (2013).
- [2] N. J. Curtin and C. Szabo, Therapeutic applications of PARP inhibitors: anticancer therapy and beyond. *Mol Aspects Med.* **34**, 1217 (2013).
- [3] M. Kramer and M. Scholz, Rapid calculation of biological effects in ion radiotherapy, *Phys. Med. Biol.* **51**, 1959 (2006).
- [4] C. R. Hunt, A. Gupta, and N. Horikoshi, Does PTEN loss impair DNA double-strand break repair by homologous recombination?, *Clin. Cancer Res.* **18**, 920 (2012).
- [5] P. Chatterjee, G. S. Choudhary, A. Sharma, K. Singh, W. D. Heston, J. Ciezki, E. A. Klein, and A. Almasan, PARP inhibition sensitizes to low dose-rate radiation TMPRSS2-ERG fusion gene-expressing and PTEN deficient prostate cancer cells. *PLoS One* **8**, e60408 (2013).

## 5.4 ATOMIC PHYSICS RESEARCH

### 5.4.1 Experimental evidence of beam-foil plasma creation during ion solid interaction

P. Sharma and T. Nandi

Inter University Accelerator Centre, ArunaAsaf Ali Marg, New Delhi 110067, India.

During the typical ion-solid collisions, the complex dynamic interactions between projectile ions and target atoms significantly alter the charge states of the corresponding atomic system. In the present work, charge state evolution of energetic projectile ions ( $^{56}\text{Fe}$ ,  $^{58}\text{Ni}$  and  $^{63}\text{Cu}$ ) during the passage from thin carbon foils has been revisited in the 1.51-2.69 MeV/u energy range using the x-ray spectroscopy technique [1]. Contributions from the bulk and the target surface in charge changing processes have been segregated by measuring the charge state distribution (CSD) of the projectile ions right at the ion-solid interaction zone. The measured projectile mean charge states (MCS) in the present work are found to be higher than the obtained MCS from empirical formalism [3] and experimental electromagnetic methods [4,5] as shown in the Fig. 88, which can be attributed to the multi-electron capture from the exit surface of the target [2]. Interestingly, CSD measured in the bulk exhibits Lorentzian profile in contrast to the well-known Gaussian structure observed using electromagnetic methods [4,5] and theoretical predictions [3,6], shown in the Fig. 88. The occurrence of such behaviour suggests that ion-solid collisions constitute high-density localized plasma in the bulk of the solid target, called beam-foil plasma. This beam-foil plasma is similar to the high-density solar and astrophysical plasma, which may have practical implications in various fields, in

particular, plasma physics and nuclear astrophysics. Further, present work suggests modification in the theoretical CSD predictions by incorporating plasma coupling effects during the ion-solid interactions.

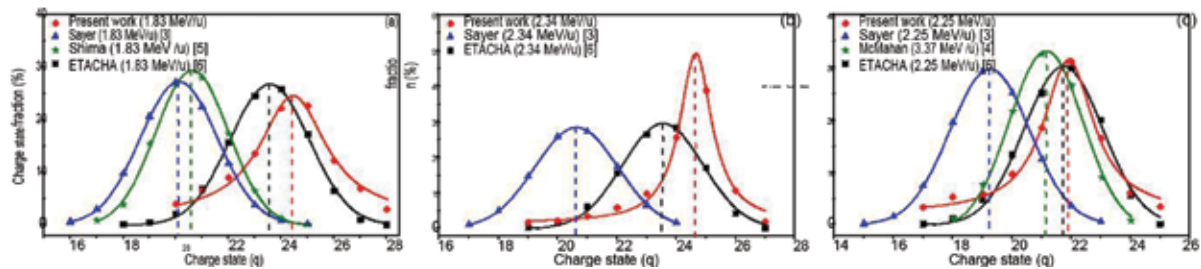


Fig. 88. Comparison of the charge state distribution and the mean charge states in the case of (a)  $^{63}\text{Cu}$  on  $^{12}\text{C}$  (b)  $^{58}\text{Ni}$  on  $^{12}\text{C}$  and (c)  $^{56}\text{Fe}$  on  $^{12}\text{C}$  at different beam energies. The Figure shows Lorentzian fit to the present work and Gaussian fit to all the others. Errors are embedded in the symbol itself. The vertical lines represent the mean charge states.

## REFERENCES

- [1] P. Sharma and T. Nandi, Phys. Lett. A 380, 182 (2016).
- [2] H. Brauning et al., Phys. Rev. Lett. 86, 991 (2001).
- [3] R. O. Sayer, Rev. Phys. Applique 12, 1543 (1977).
- [4] M. A. McMahan, R. F. Lebed, and B. Feinberg, Part. Accel. Conf. IEEE 1, 536 (1989).
- [5] K. Shima, T. Mikumo, and H. Tawara, At. Data Nucl. Data Tables 34, 357 (1986).
- [6] J. P. Rozet, C. Stphan, and D. Vernhet, Nucl. Instrum. Methods B 107, 67 (1996).

### 5.4.2 Shaking process during heavy ion-atom collisions

P. Sharma and T. Nandi

Inter University Accelerator Centre, ArunaAsaf Ali Marg, New Delhi 110067, India.

In the framework of sudden approximation limit, due to an abrupt change in the central potential and/or the electronic environment, orbital electrons of the corresponding atomic system may get excited (shake-up) or ionized (shake-off). Collectively, these processes are called shaking process [1]. Several works can be found in the literature discussing these sudden charge changing processes [2]. In earlier works e.g. [3], increased charge states of nuclear products have been observed. Similarly, in our laboratory, the formation of highly charged projectile/target-like fragment ions is observed during the heavy-ion nuclear reactions using x-ray spectroscopy technique. The detailed analysis revealed that such unusual ionization is due to the shake-off process, which occurs because of fast nuclear recoil and sudden change of nuclear charge. In the present theoretical work, we have discussed the collective role of nuclear recoil and charge change in the shake-off process during the heavy ion-atom collisions. Using non-relativistic hydrogen-like wave functions, shake-off probability for any atomic system can be defined as follows [4]

$$P_{\text{shake-off}} = \sum_{n',l',m'} |\langle n,l,m,Z | \exp(-ik.r) | n',l',m',Z \rangle|^2 = P_{\text{NCC}} + P_{\text{Recoil}} \quad (1)$$

Here,  $n, l, m$  and  $n', l', m'$  are the quantum numbers of the parent (nuclear charge,  $Z$ ) and daughter nucleus (nuclear charge,  $Z_0$ ), respectively and  $k$  denote the wave vector of the daughter nucleus.  $P_{\text{NCC}}$  and  $P_{\text{Recoil}}$  are the shake-off probability due to nuclear charge change and recoil, respectively. The shake-off probabilities have been calculated in the range of  $Z = 2 - 90$  using 105 non-relativistic hydrogenic wave functions. Interestingly, it is found that during the fast ion-atom collisions (MeV energy range) shake-off due to recoil plays a significant role in the charge changing processes, whereas in the slow collisions (keV energy range) change in nuclear charge shows dominance over the counterpart, as shown in Figure 89.

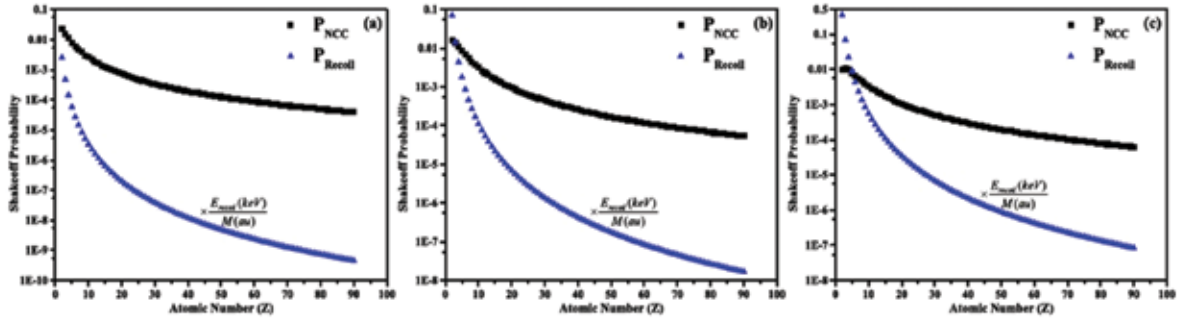


Fig. 89 : Shake-off probability versus atomic number ( $Z$ ) for a typical case of nuclear charge change  $\Delta Z (= Z' - Z) = 1$  for different quantum numbers ( $n, l, m$ ), (a) (1, 0, 0), (b) (2, 0, 0) and (c) (3, 0, 0).

## REFERENCES

- [1] B. Migdal, Qualitative Methods in Quantum Theory (Benjamin, London, 1977).
- [2] P. Sharma and T. Nandi, Nucl. Phys. A **941**, 265 (2015), and references therein.
- [3] N. K. Skobelev, Instruments Exp. Tech. **51**, 351 (2008).
- [4] L. Vegh, J. Phys. B - At.Mol. Phys. **16**, 4175 (1983).

### 5.4.3 Shakeoff ionization near Coulomb barrier during ion-atom collisions

P. Sharma and T. Nandi

Inter University Accelerator Centre, Aruna Asaf Ali Marg, New Delhi 110067, India

The effects of interaction responsible for any physical processes depend on the interaction range and the coupling constant, which are vastly different for electromagnetic and strong forces. Therefore, the atomic and the nuclear phenomena are not expected to interfere with each other. To explore the nuclear effects on atomic processes, if any, we have measured the projectile ion x-rays in the ion-atom collisions as a function of the beam energies around the Coulomb barrier. The variation of the projectile ionization with the ion-beam energies exhibits an unexpected jump resulting in a resonance type structure in the derivative spectrum near the Coulomb barrier as shown in Figure 90. Such behaviour cannot originate from primary atomic processes alone and therefore, indicates the interference of nuclear interaction. The long lived orbiting di-nuclear complex [1] is formed under the effect of the Coulomb as well as the nuclear potential, which gives rise to the shake-off ionization [2] of the projectile ion manifesting the resonance. At the barrier and above the barrier energies, the di-nuclear system formed disturbs the electron configuration of the ions, initiates shake-off ionization and pushes the ions in higher ionic stage thereby causing an increase in x-ray transition energy. The present finding has been validated with three asymmetric reactions, in inverse kinematics, viz.  $^{12}\text{C}(^{56}\text{Fe}, ^{56}\text{Fe})$ ,  $^{12}\text{C}(^{58}\text{Ni}, ^{58}\text{Ni})$  and  $^{12}\text{C}(^{63}\text{Cu}, ^{63}\text{Cu})$ . This study opens up new channels for interdisciplinary research comprising of atomic and nuclear physics.

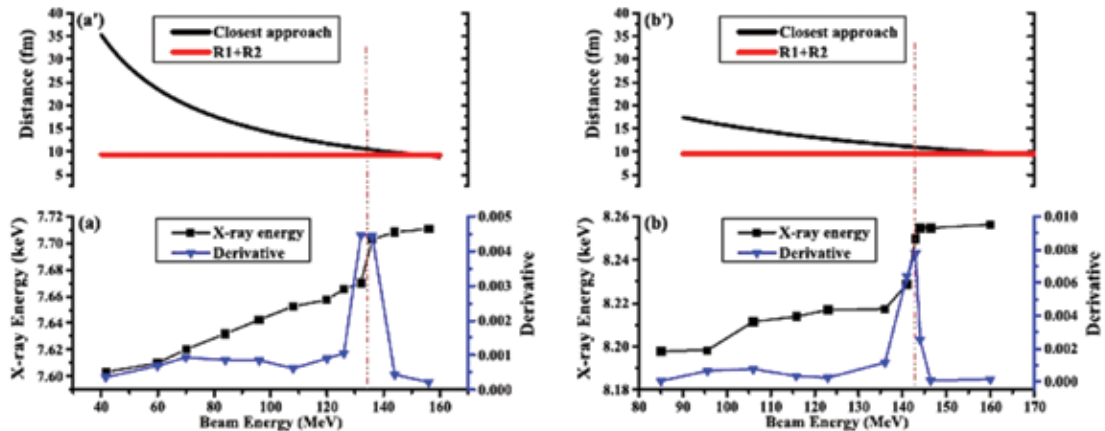


Fig. 90 : Centroid of the projectile x-ray energy peaks versus beam energies in lab frame (a)  $^{58}\text{Ni}$  and (b)  $^{63}\text{Cu}$  on C-foil and distance of closest approach and touching distance versus beam energy for two body systems of (a')  $^{58}\text{Ni}$  on  $^{12}\text{C}$  and (b')  $^{63}\text{Cu}$  on  $^{12}\text{C}$ . The distance of closest approach is calculated using the formulation given elsewhere [3]. Error bars are tiny and within the symbol size. All solid lines are to guide the eye only. The dash-dot vertical lines represent the centroid of the observed resonance-type structure.

## REFERENCES

- [1] S. J. Sanders, A. S. de Toledo, and C. Beck, Phys. Rep. **311**, 487 (1999).  
 [2] P. Sharma and T. Nandi, arXiv:1507.04171 (2015), arXiv:1507.04171.  
 [3] P. R. Christen and A. Winther, Phys. Lett. B **65**, 19 (1976).

## 5.4.4 X-ray spectroscopy around the pile-up region

G. Sharma<sup>1</sup>, D. Swami<sup>2</sup>, N.K. Puri<sup>1</sup> and T. Nandi<sup>2</sup>

<sup>1</sup>Dept. of Applied Physics, Delhi Technological University, Bawana Road, Delhi 110042, India

<sup>2</sup>Inter University Accelerator Centre, Aruna Asaf Ali Marg. New Delhi 110067. India

We have employed the Beer-Lambert principle of x-ray absorption to get rid of the pulse pile-up problem in high count rate detection of the true events and measure two-electron-one-photon [1-2] transition in K-shell, which is 104 times weaker than the most probable transition. The method used is capable of resolving the weak and the strong transitions provided the latter appears at the low energy side, and two types of transition are theoretically resolvable by the detector. We have successfully resolved these two kinds of transitions by reducing their intensity ratio using an Al absorber of suitable thickness as shown in Fig. 91. The technique also allows us to retrieve the actual intensities of the transitions with the knowledge of attenuation coefficient of the absorber and the detection efficiency as shown in Table 5.4.1. The energy of the spectral lines and the branching ratios of two-electron-one-photon (TEOP) to one-electron-one-photon transitions were also measured. In this report, we present the x-ray spectroscopy in the pulse pile-up region.

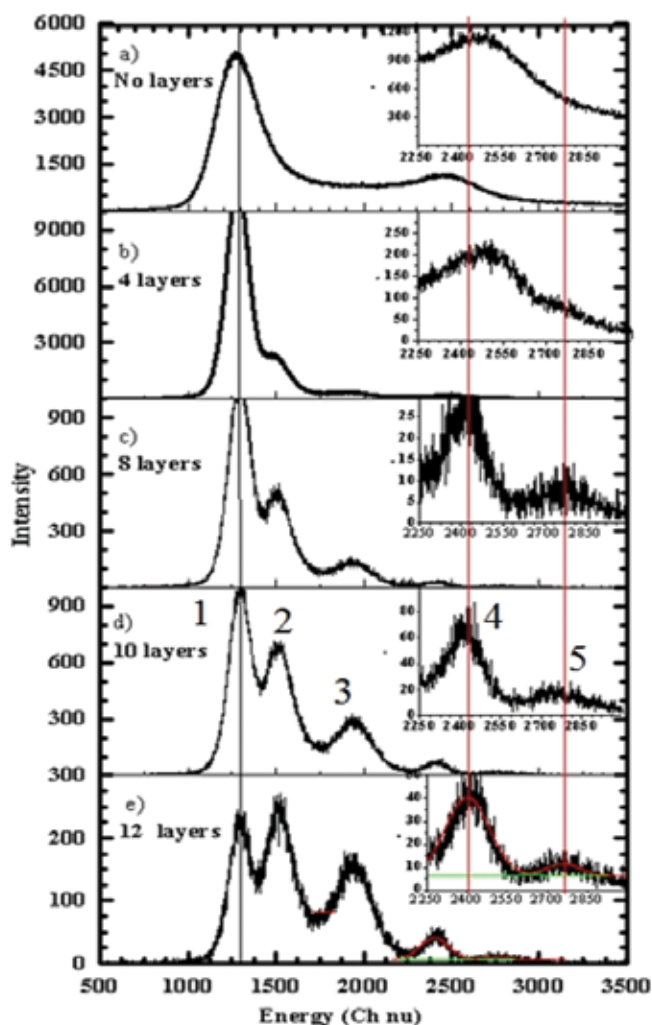


Fig. 91 : The x-ray spectra with the different absorber foil thickness: (a)-(e) represent the spectra taken with different numbers of Al absorber foils. The measured spectra show improvement on the resolution as a function of absorber foil thickness. For example, the spectrum with 10 layers shows five lines. The first four peaks (1-4) in Fig. 2(d) are assigned to He-like Ti from the projectile ions, He-like Cr, He-like Fe and H-like Co ions from the projectile-like ions. The last peak (5) is probably originated from TEOP transitions.

**TABLE 5.4.1. Attenuation (A) and detection efficiency ( $\epsilon$ ) corrected intensities: The x-ray intensities of the measured peaks with ten layers of Al absorbers ( $100 \pm 2 \mu\text{m}$ ) are corrected to have the actual intensities and the uncertainty is given in the 3rd column. The Figures in the 7th column indicate that pile-up effect is totally nullified and relative intensities as low as  $2.11\text{E}-05$  can well be measured.**

Channel number (keV)	Attenuated Intensity	% error	Trans. % (Al)	Total (A+ $\epsilon$ ) trans. %	Corrected Intensity	Intensity Ratio
1293.7 (4.73)	151959	1.3	0.20	0.02	753176786	1.00E+00
1508.7 (5.50)	149237	0.9	1.72	0.37	39808940	5.29E-02
2023.7 (7.36)	90878	0.4	8.13	4.06	2236592	2.97E-03
2482.5 (9.02)	11979	0.4	17.15	11.51	104111	1.38E-04
2748.0 (10.04)	5790	1.3	49.30	36.38	15915	2.11E-05

## REFERENCES

- [1] C. Stolleret. al., Phys. Rev. A **15**, 990 (1977).  
 [2] T. K. Mukherjee et al., Z. Phys. D **42**, 29 (1997).

### 5.4.5 Lifetime quenching due to surface wake field

G. Sharma<sup>1</sup>, D. Swami<sup>2</sup>, N. K. Puri<sup>1</sup>, and T. Nandi<sup>2</sup>

<sup>1</sup>Dept. of Applied Physics, Delhi Technological University, Bawana Road, Delhi 110042, India

<sup>2</sup>Inter University Accelerator Centre, Aruna Asaf Ali Marg, New Delhi 110067, India

The energy loss field in bulk of the foil is so large that it can blend the fine structure sub levels completely. However, the small surface wake field (SWF) [1] induced mixing leads to partial admixture of  $2s \ ^2S_{1/2}$  and  $2p \ ^2P_{1/2}$  levels in H-like ions so that it quenches the  $2s \ ^2S_{1/2}$  lifetime to a great extent [2]. In order to study this effect in various ion species, we have used the beam energy above the Coulomb barrier to obtain the spectrum from the projectile and the projectile-like ions in a beam-foil experiment as shown in Fig. 92 The four peaks observed can be assigned to He-like Ti, Cr, Fe and H-like Co ions [4] as the peak of radiative electron capture disappears from the delayed spectra. In fact, the x-ray lines from projectile-like ions are much weaker than the one from the projectile-ions; a special technique [3] is adopted to record them. Upper level lifetime measurements were carried out using the beam-foil time-of-flight technique with 110 MeV Ti ions with a flight distance of only 0-3 mm for the short lived levels as given in the Table 1. The lifetimes obtained cannot be attributed to a pure metastable state in the corresponding ions. Hence, effect of the Stark mixing of closely spaced  $1s2p \ ^3P_1$  and  $1s2s \ ^3S_1$  in the He-like ions and  $2p \ ^2P_{1/2}$  and  $2s \ ^2S_{1/2}$  in the H-like ions need to be considered. The prescription, given elsewhere [2], have been followed to obtain the SWFs, which fall in the order of  $10^7$  V/cm. It is thus much smaller than the field required for complete mixing ( $\sim 10^{10}$  V/cm) of the above mentioned states. Further, the results show that the SWF decreases linearly with the atomic number of the corresponding ion species.

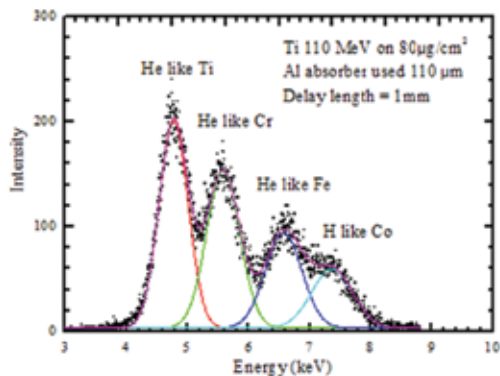


Fig. 92 : The x-ray spectrum of 110 MeV Ti on 80  $\mu\text{g}/\text{cm}^2$  C target. The lines from projectile ion and projectile like ions are resolved using 110  $\mu\text{m}$  Al absorber before the detector.

Table1: Measured ( $\tau$ ) and theoretical ( $\tau'$ ) lifetimes are compared. The mixing parameter  $\epsilon$  and corresponding SWF responsible for the mixing ( $E_f$ ) [2] are given.

Ion	E keV	$\tau$ (ps)	$\tau'$ (ns) [4]	$\epsilon$ $\times 10^{-2}$	$E_f$ (V/cm) $\times 10^{+07}$
Ti <sup>20+</sup> (1s2s <sup>3</sup> S <sub>1</sub> )	4.73	67.1	26.6	3.74	9.2
Cr <sup>22+</sup> (1s2s <sup>3</sup> S <sub>1</sub> )	5.50	61.9	10.7	2.63	6.4
Fe <sup>24+</sup> (1s2s <sup>3</sup> S <sub>1</sub> )	6.51	129.5	4.7	1.32	3.2
Co <sup>26+</sup> (2s <sup>2</sup> S <sub>1/2</sub> )	7.36	78.3	2.0	0.61	1.5

## REFERENCES

- [1] T. Nandi et al., Phys. Rev. Lett. **110**, 163203 (2013).
- [2] T. Nandi and B. P. Mohanty, J. Phys. B: At. Mol. Opt. Phys. **42**, 225402 (2009).
- [3] <https://arxiv.org/1512.08399>.
- [4] J. Hata and I.P. Grant, J. Phys. B: At. Mol. Phys. **14**, 2111 (1981).

### 5.4.6 L shell x-ray production cross-section measurements in high Z elements using 4-6 MeV/u fluorine ions

Sunil Kumar<sup>1,2</sup>, M. Oswal<sup>1</sup>, G. Singh<sup>1</sup>, Udai Singh<sup>2</sup>, N. Singh<sup>1</sup>, D. Mehta<sup>1</sup>, G. Lapicki<sup>3</sup> and T. Nandi<sup>4</sup>

<sup>1</sup>Department of Physics, Panjab University, Chandigarh 160014, India

<sup>2</sup>Department of Applied Sciences, Chitkara University, Himachal Pradesh 174103, India

<sup>3</sup>Department of Physics, East Carolina University, Greenville, North Carolina 27858, USA

<sup>4</sup>Inter University Accelerator Centre, Aruna Asaf Ali Marg, New Delhi 110067, India

We have measured the absolute L shell x-ray production cross-sections in <sup>78</sup>Pt, <sup>79</sup>Au, <sup>82</sup>Pb, <sup>83</sup>Bi, <sup>90</sup>Th, and <sup>92</sup>U natural targets ionized by adiabatic collision with the 4-6 MeV/u fluorine ions. The x-ray production cross-sections have also been calculated from the  $L_i$  ( $i = 1-3$ ) sub shell ionization cross-sections using the available theories. The multiple ionization effects have been considered in the single-hole fluorescence and Coster-Kronig (CK) yields calculations and incorporated in the ECPSSR and the ECUSAR theories. The theories are then called ECPSSR-MI and ECUSAR-MI, respectively. The results so obtained exhibit good agreement with the measured data, whereas, the FBA theory overestimates by a factor of two compared to the measured data.

The L shell x-ray production cross-sections in the elements with  $78 \leq Z \leq 92$  using the <sup>19</sup>F ions (charge states = 6<sup>+</sup>, 7<sup>+</sup>, 8<sup>+</sup>) in the energy range 76 – 114 MeV were measured. Heavy ions of F<sup>6+</sup> (76 MeV, 84 MeV), F<sup>7+</sup> (90 MeV) and F<sup>8+</sup> (98 MeV, 106 MeV and 114 MeV) were obtained from the 15 UD Pelletron accelerator at IUAC. Two silicon surface barrier (SSB) detectors at  $\pm 7.5^\circ$  to the beam direction were used to monitor the projectile ions. A Si(Li) solid state detector (thickness = 5 mm, diameter = 10 mm, 25  $\mu\text{m}$  Be window, ORTEC) in the horizontal configuration was placed outside the vacuum chamber at an angle of  $125^\circ$  to the beam direction. The energy resolution of the detector was  $\sim 200$  eV for the Mn  $K_\alpha$  x-rays. The target to the detector distance was 170 mm. The beam current was kept below 1 nA to avoid the pile up effects and the damage to the target. The spectra were collected for sufficiently long time so as to get good statistical accuracy.

**ECPSSR-MI VS ECUSAR-MI:** Both ECPSSR-MI [1] and ECUSAR-MI [2] represent the experimental data quite well. Nevertheless, we made a thorough comparison through the difference between experimental data

and theoretical estimations by standard error analysis techniques in Table 5.4.2. The lower average deviation dictates that the multi-ionization effect is better described by the ECUSAR-MI [2] theory. It means that the polarization effect of the inner shell electron of the target atom can be better represented by united and separated atom approximation as done in ECUSAR-MI [2], than the perturbed stationary state approximation as done in ECPSSR-MI [1].

**Table 5.4.2 : Normalized mean square deviation of the theoretical estimates with respect to measured values. The average deviation over six different target elements is also given.**

Theory	Target	Mean Square Deviation between Theory and Experiment			
		$Ll$	$L\alpha$	$L\beta$	$L\gamma$
ECPSSR	Pt	20.40	15.88	20.24	17.09
	Au	19.58	18.83	21.50	23.25
	Pb	23.08	18.83	19.79	15.78
	Bi	34.37	18.83	19.62	27.20
	Th	22.74	17.29	15.52	18.51
	U	43.74	16.12	17.61	20.93
	Average	27.32	17.63	19.05	20.46
ECPSSR -MI	Pt	21.86	9.45	11.18	9.67
	Au	14.48	13.99	15.48	17.34
	Pb	19.31	14.20	13.85	12.34
	Bi	28.59	13.59	13.70	23.73
	Th	19.51	12.73	10.79	13.82
	U	40.00	11.79	12.67	16.19
	Average	23.96	12.62	12.94	15.52
ECU-Si	Pt	18.53	14.64	22.11	19.89
	Au	16.39	15.91	19.23	21.38
	Pb	19.87	16.34	17.15	13.44
	Bi	29.77	15.39	17.03	24.27
	Th	21.59	14.87	13.32	16.56
	U	42.56	14.10	15.21	18.76
	Average	24.78	15.21	17.34	19.05
ECU-MI	Pt	25.27	10.32	5.09	8.06
	Au	9.33	9.52	11.13	14.14
	Pb	17.15	11.75	9.76	11.44
	Bi	23.45	9.25	10.55	20.92
	Th	17.39	9.62	8.73	11.86
	U	37.10	8.50	9.67	14.05
	Average	21.62	9.83	9.16	13.41

**SINGLE COLLISION VS. MULTIPLE COLLISIONS:** It may be noted that the measured x-ray production cross-sections are independent of any model, unlike the deduced ionization cross-sections, and thus the former can be directly compared with the other available data. The measurement with single collision condition is supposed to provide the correct data as done by Singh *et al* [3], however mostly the multiple collision conditions are adopted in the experiments like the present one. Typical thickness of the targets used in [3],  $5\mu\text{g}/\text{cm}^2$  for  $^{79}\text{Au}$  and  $10\mu\text{g}/\text{cm}^2$  for  $^{83}\text{Bi}$ , implies that on the average 1 and 2 collisions [4], respectively can take place. Whereas the target thickness used in this experiment is as large as  $120\mu\text{g}/\text{cm}^2$ , meaning about 30 collisions. The data have been compared for single collision [3], multiple collisions (present) and EUCSAR theory in the  $^{83}\text{Bi}$ , and  $^{79}\text{Au}$  targets. The energy range of [3] 60-98 MeV is closed to the energy range of the present experiments 76-114 MeV. Both the cross sections for few collisions as well as multiple collision data are compared in the Fig. 93. We can see that the difference between few and multiple collisions cannot be distinguished clearly. A fit with a polynomial function shows the trend of the variation of cross sections and hence it can be compared with the ECUSAR-MI [2] theory. The comparison shows a reasonable agreement between the experimental results and the theoretical prediction from ECUSAR-MI [2].

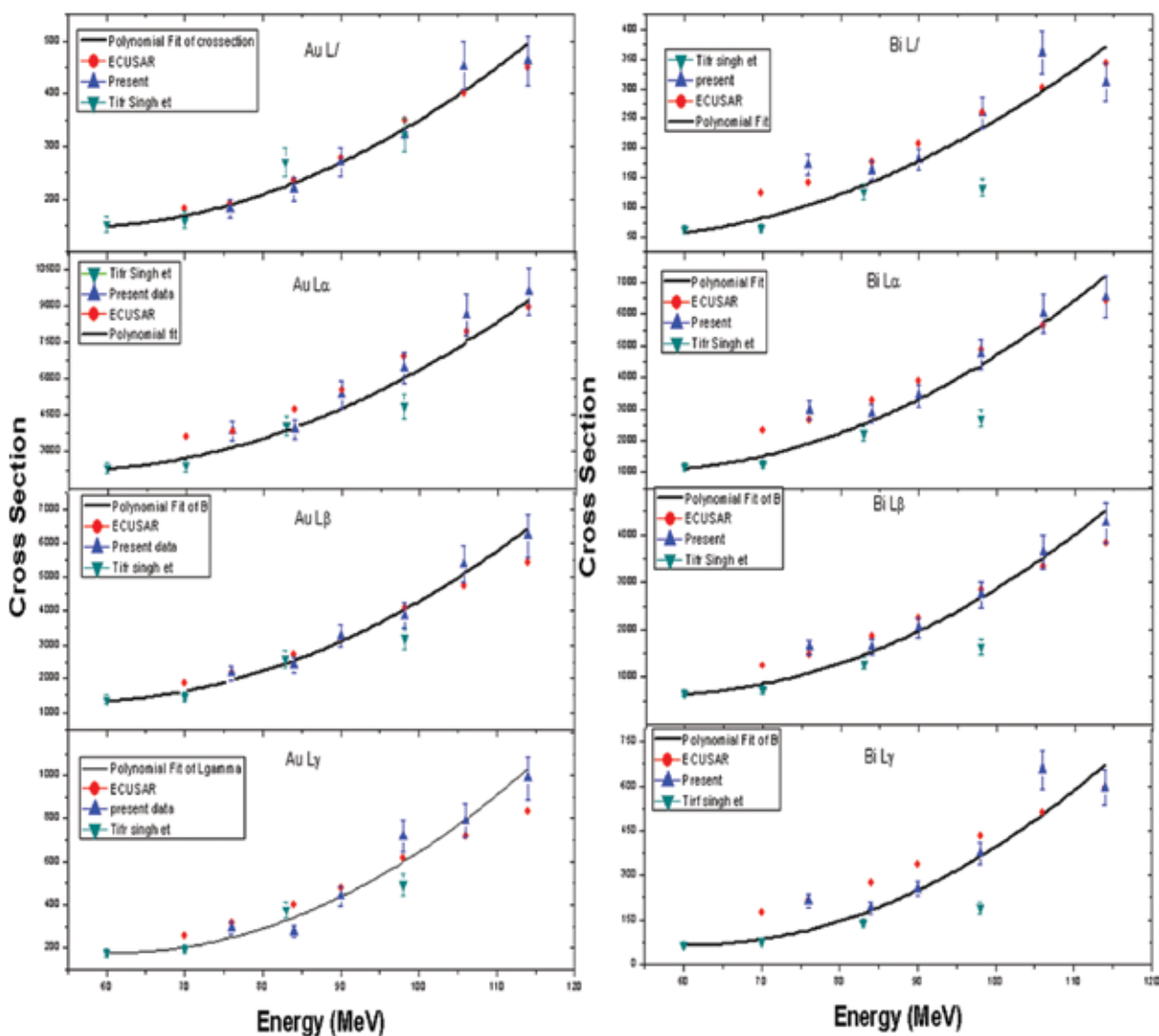


Fig. 93 : L-shell production cross sections from single collision conditions [3] as well as multiple collision conditions (present) are shown together and compared with ECUSAR-MI [2] predictions. The line is a polynomial fit to the experimental data.

## REFERENCES

- [1] W. Brandt and G. Lapicki, Phys. Rev. A **23**, 1717 (1981).
- [2] G. Lapicki, Nucl. Instrum. Methods B **189**, 8 (2002).
- [3] Y.P. Singh, D. Mitra, L.C. Tribedi, and P.N. Tandon, Phys. Rev. A **63**, 012713(2000).
- [4] J. H. McGuire, D. J. Land, J. G. Brennan, and G. Basbas, Phys. Rev. A **19**, 2180 (1979).

## 5.5 ACCELERATOR MASS SPECTROMETRY

### 5.5.1 Radiocarbon dating of a Harappan site using charcoal samples

Mayank N Vahia<sup>1,2</sup>, Pankaj Kumar<sup>3</sup>, Abhijeet Bhogale<sup>4</sup>, D C Kothari<sup>2,4</sup>, Sundeep Chopra<sup>3</sup>, Vasant Shinde<sup>5</sup>, Nilesh Jadhav<sup>5</sup> and Ranvir Shastri<sup>6</sup>

<sup>1</sup>Tata Institute of Fundamental Research, Mumbai 400005, India

<sup>2</sup>Department of Physics, University of Mumbai, Vidyaanagari, Mumbai 400098, India

<sup>3</sup>Inter University Accelerator Centre, Aruna Asaf Ali Marg, New Delhi 110067, India

<sup>4</sup>National Centre for Nanoscience and Nanotechnology, University of Mumbai, Mumbai 400098, India

<sup>5</sup>Deccan College, Yerawada, Pune 411006, India

<sup>6</sup>Haryana Department of Archaeology and Museums, Haryana, Panchkula, India

We have used charcoal samples excavated from the Harappan site of Rakhigarhi (29°17'19"N 76°06'47"E) near Delhi to date the site. The Site was excavated by a group led by Prof. Vasant Shinde of Deccan College. The samples were taken from different depths in a 25 meter trench. Two samples of carbon soot from each location in the trench were analysed for their carbon-14 to carbon-12 ratio. That was used to determine the date of the site. The results showed a high degree of consistency within the samples taken from the same depth and the variation of depth. The age of the samples varied from 4273 BP at 9.1 meters to 4616 BP at 20.6 meters. The results are consistent with the general expectation of the age of Harappan sites. The work has been accepted for publication in Current Science.

### 5.5.2 Developing chronological constraints for tectonic events in parts of the Himalaya

C.P. Rajendran, Anandasabari K.<sup>1</sup>, Jaishri Sanwal<sup>1</sup>, Pankaj Kumar<sup>2</sup> and Rajveer Singh<sup>2</sup>

<sup>1</sup>Jawaharlal Nehru Centre for Advanced Scientific Research, Bengaluru, Karnataka 560064, India

<sup>2</sup>Inter University Accelerator Centre, Aruna Asaf Ali Marg, New Delhi 110067, India

The Himalayan mountains, a product of India-Asia collision, is a locus of devastating earthquakes. The last few decades have witnessed a number of great earthquakes ( $M > 8.0$ ) -like the 1934 Bihar-Nepal and the 1950 upper-Assam earthquakes. Both had devastating impact on the mountainous and alluvial parts of the region. Two major issues stand out: one, identification of causative structure, and two, the recurrence pattern of great earthquakes. These issues are central to evaluating seismic risk in the Himalaya. Recent studies imply temporal variation in strain release leading to clustering of great earthquakes in time and space.

Our project is designed to conduct paleo-seismological studies in the selected locations in the Himalaya and its foot hills to determine ages, sizes and the extent of the earthquake ruptures. In addition to direct observation of fault offsets, we use liquefaction as earthquake proxy and generate dates to constrain the seismic events.

In the current work, all together 27 samples were processed to generate Radiocarbon AMS Chronology including Kashmir Himalaya. Nineteen samples were processed to date the seismic events and 8 samples for climatic studies in Kashmir Himalaya. The samples were pretreated using Acid-Base-Acid (A-B-A) pretreatment. In this method three main steps are designed to remove sedimentary and carbonates contaminations including the organic acid contaminations such as humic and fulvic acids, and dissolved atmospheric carbon dioxide that may have been absorbed during the base wash as suggested by Goh and Molloy (1972). Each acid or base wash was followed by a number of rinses with ultrapure MilliQ™ deionized water. After each rinse, samples were separated by centrifugation, settling, and decanting. After the final water rinse, samples were kept in deep freezer and then dried using freeze-dried prior to combustion and graphitization. The samples were finally ready for beam exposure.

In the initial phase we have received six dates from Imadhol and Ramkot sections near Kathmandu. On the basis of these results the chronology of liquefaction feature revealed evidence for a major event around AD 1450-1479 which also agrees with our previous results.

**Table 5.5.1 : Radiocarbon results from the IUAC, New Delhi**

<b>Ramkot A</b>				
<b>Sample Id</b>	<b>Renamed Id</b>	<b>Depth</b>	<b>Wall</b>	<b><sup>14</sup> C date</b>
Site A - 2 - D	RA - A - 2	90 cm	East Wall	1877 - 515 (BC)
Site A - 3 - D	RA - A - 1	70 cm	North Wall	3368 - 1639 (BC)

<b>Ramkot B</b>				
<b>Sample Id</b>	<b>Renamed Id</b>	<b>Depth</b>	<b>Wall</b>	<b><sup>14</sup> C date</b>
Site B - 2 - D	RA - B - 2	33 cm	East Wall	226 -376 (AD)
<b>Imadol Site A</b>				
<b>Sample Id</b>	<b>Renamed Id</b>	<b>Depth</b>	<b>Wall</b>	<b><sup>14</sup> C date</b>
Site A - 1 -D	IM - A - 1	90 cm	West Wall	1450 -1479 (AD)

<b>Imadol Site C</b>				
<b>Sample Id</b>	<b>Renamed Id</b>	<b>Depth</b>	<b>Wall</b>	<b><sup>14</sup> C date</b>
Site C - D2	IM - C- 4	60 cm	South Wall	1440 -1452 (AD)
Site C - D3A	IM - C- 5	80 cm	South Wall	1320 - 1406 (AD)

### **5.5.3 Vegetation and climate history of peninsular India – establishing late quaternary chronologies from diverse terrestrial sites using AMS dating of bulk sediments and pollen extracts**

Anupama Krishnamurthy<sup>1</sup>, Prasad Srinivasan<sup>1</sup>, Navya Reghu<sup>1</sup>, Pankaj Kumar<sup>2</sup>, Rajveer Sharma<sup>2</sup>, Sundeep Chopra<sup>2</sup> and Shreyas Managave<sup>3</sup>

<sup>1</sup>French Institute of Pondicherry, 11 St Louis Street, Puducherry 605001, India

<sup>2</sup>InterUniversity Accelerator Centre, Aruna Asaf Ali Marg, New Delhi 110067, India

<sup>3</sup>Department of Earth Sciences, Pondicherry University, Kalapet, Puducherry 605014, India

Accelerator mass spectrometers allow the measurement of  $^{14}\text{C}$  in very small quantities of carbon extracted from samples studied in the course of various applications. In paleo-environmental analyses, sediment cores are meticulously collected and preserved in specialized cold rooms for studying “multiple proxies” to help reconstruct the past environment. These can be collected from organically rich peat bogs and swamps but also from lakes, ponds and river deltas and floodplains.

Frequently, the quantity of sample collected is limited and has to be shared for various proxies – many of which will dissolve or completely use up the sample. In addition to this practical problem of small sample availability, there are also problems of organically poor sediments which will not yield much carbon for radiometric dating.

It is in this context that a method widely recommended for organically poor samples [1-6] is being tried and tested in India for the first time – namely, extraction of pollen rich residues for radiocarbon analyses.

The larger goal of our ongoing studies is to understand the changes that have shaped the evolution of the past environments and landscapes in peninsular India using biological proxies such as pollen and phytoliths. One of the key characteristics of peninsular India is the current diversity and heterogeneity. Be it climate (especially the monsoon), vegetation or topography, the marked west to east gradient is striking. Added to these “natural” factors of heterogeneity, the long history (and pre-history) of human and hominin occupation and modification of this land-cover add another dimension to this heterogeneity.

As a part of this project, commenced at the end of January 2016, measurements of the proportions of the carbon isotopes ( $^{12}\text{C}$ ,  $^{13}\text{C}$ ,  $^{14}\text{C}$ ) for a total of 25 to 30 samples are planned. Roughly half of these samples will be pollen-rich extracts and the other half organic bulk sediment. These samples are all collected at various terrestrial sites in peninsular India.

Among them, the first two samples measured are from an upper montane peat site in the Nilgiri hills [7]. These samples were processed in the routine manner followed for bulk sediments as they were organically rich.

We are now standardizing the protocol for pollen residue extraction following the method of Brown *et al.* [1]. In order to achieve the best pre-treatment, the pollen extraction procedure is being optimized using high purity reagents.

Pollen, an integral microscopic component of plants (Fig 94), provides a robust reconstruction of the past vegetation. In our opinion, directly dating the plants, represented by pollen grains, is an appropriate approach to identify the past land-cover and hence reconstruct past climate.

At present the samples chosen for this pollen extraction for radiometric dating, collected from a 1.3m trench at a site called CinnbabuSamudram in south-east India (Fig 95), are being analyzed.

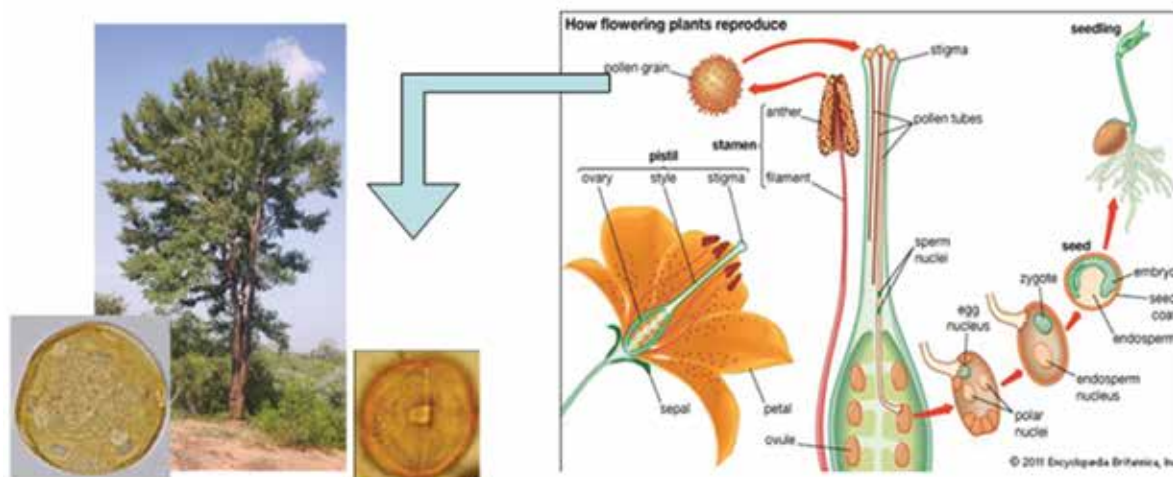


Fig 94 : Illustration showing microphotographs of pollen of *Hardwickiabinata* and *Dodoneaeviscosa*, two important dicotyledenous plants of south India, which are found frequently in fossil pollen records. On the right is an illustration of pollen in the life cycle of a plant.

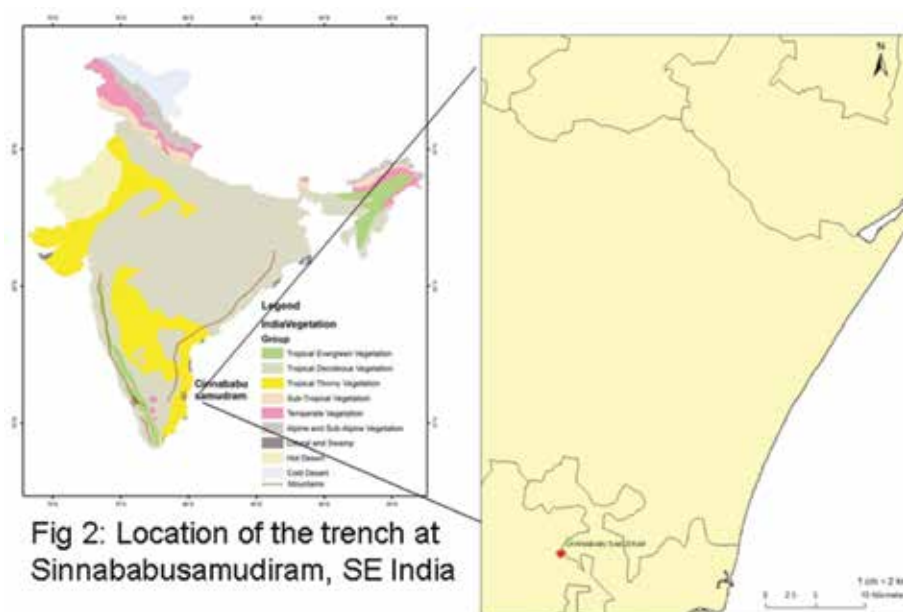


Fig 2: Location of the trench at Sinnababusamudiram, SE India

Fig 95 : Location of the trench at Cinnababu Samudram, south-east India.

## REFERENCES

- [1] T. A. Brown, G. W. Farwell, P. M. Grootes and F. H. Schmidt, Radiocarbon AMS dating of pollen extracted from peat samples, *Radiocarbon* **34**, 550 (1992).
- [2] M. J. Vandergoes, and C. A. Prior, AMS dating of pollen concentrates-a methodological study of late quaternary sediments from South Westland, New Zealand, *Radiocarbon* **45**, 479 (2003).
- [3] P. Atahan, K. Grice and J. Dodson, Agricultural and environmental change at Qingpu, Yangtze Delta region, China: a biomarker, stable isotope and palynological approach, *Holocene* **17**, 507(2007).
- [4] B. Albert, and J. Innes, Multi-profile fine-resolution palynological and micro-charcoal analyses at Esklets, North York Moors, UK, with special reference to the Mesolithic-Neolithic transition, *Vegetation History and Archaeobotany* **24**, 357 (2014).
- [5] Y. Zong, J. B. Innes, Z. Wang and Z. Chen, Mid-Holocene coastal hydrology and salinity changes in the east Taihu area of the lower Yangtze wetlands, China, *Quaternary Research* **76**, 69 (2011).

- [6] J. B. Innes, Y. Zong, Z. Wang and Z. Chen, Climatic and paleo-ecological changes during the mid-to late Holocene transition in eastern China: high-resolution pollen and non-pollen palynomorph analysis at Pingwang, Yangtze coastal lowlands, *Quaternary Science Reviews* **99**, 164(2014).
- [7] J. P. Sutra, Contribution palynologique à la connaissance de l'histoire de la végétation et du climat au cours des 30 derniers millénaires dans le massif des Nilgiri, Inde du Sud, Ph.D. thesis(unpublished), Université Aix Marseille III, France p. 174 (1997).

#### 5.5.4 Cosmogenic $^{10}\text{Be}$ dating of the samples collected from different locations to determine their palaeo-environmental implications

Meenakshi<sup>1</sup>, Amit Kumar<sup>1</sup>, Nishi Rani<sup>1</sup>, J.P. Shrivastava<sup>1</sup>, Pankaj Kumar<sup>2</sup>, Rajveer Sharma<sup>2</sup>, Sundeep Chopra<sup>2</sup> and G. S. Roonwal<sup>2</sup>

<sup>1</sup>Department of Geology, University of Delhi, Delhi 110007, India

<sup>2</sup>Inter University Accelerator Centre, Aruna Asaf Ali Marg, New Delhi 110067, India

Cosmogenic  $^{10}\text{Be}$ ,  $^{26}\text{Al}$  and  $^{14}\text{C}$  measurements were attempted with the samples collected from different locations (Table 5.5.2). Samples from different localities from Mandla lobe (Fig. 96) and Burzahama and Shankerpora sections in Karewas (Fig. 97) were collected to understand palaeo-environmental implications and dating of rocks.

Cosmogenic  $^{10}\text{Be}$  and  $^{26}\text{Al}$  are produced by cosmic ray spallation reaction on O, and Si atoms present in the structure of quartz crystals. Long half-life (~1.4 My for  $^{10}\text{Be}$  and 0.717 My for  $^{26}\text{Al}$  isotopes) permits long residence time before their ultimate decay to  $^{10}\text{B}$  and  $^{26}\text{Mg}$ , respectively. Being least altered and retentive mineral quartz is chosen for these studies.  $^{10}\text{Be}$ ,  $^{26}\text{Al}$  and its daughter products were used to examine soil erosion, soil formation from regolith, the development of lateritic soils (Palaeosols) and the age of Pleistocene climatic changes [1,2].

*M Series* samples were collected from Mandla lobe (eastern Deccan Traps) the volcanic eruption occurred at K/T boundary (63 My). They mark quiescent period between two successive volcanic eruptions and the exposure time of bole horizon was very less. Palaeosol samples were collected from two locations in Kashmir Burzahama (with BS initials in name) and Shankerpora (with SP initials) loess palaeosol profiles representing the cyclic glacial interglacial periods. Under successive warm humid conditions during interglacial periods the loesses deposited during cold dry conditions got transformed to the palaeosols [3].

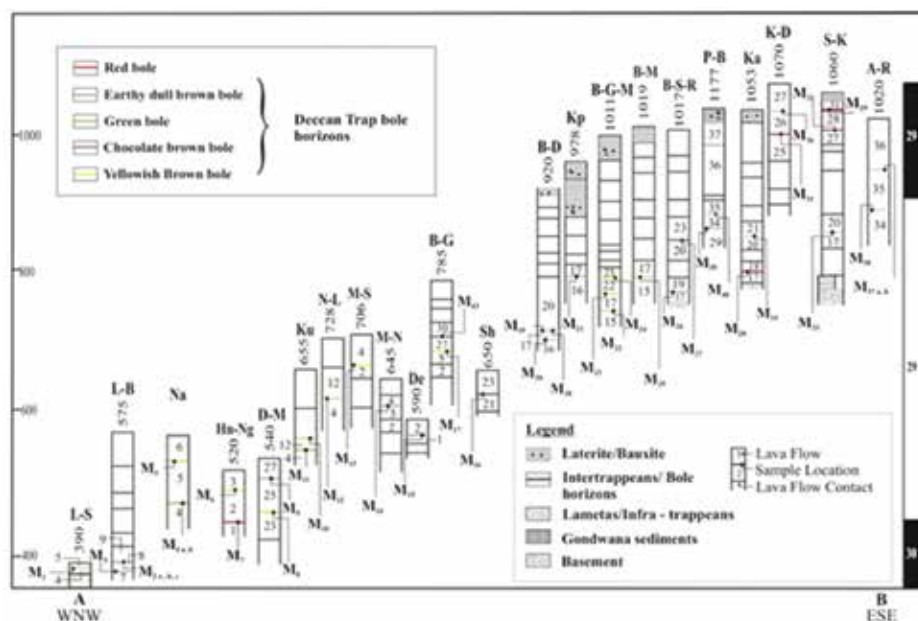
All the twelve samples were processed in the chemistry laboratory at IUAC. Samples were crushed (250-500 micron) and treated with 1:1 conc. HCl: MQ, 0.03%  $\text{H}_2\text{O}_2$  (acid bath). Further the reaction mixture was treated with  $\text{Na}_2\text{S}_2\text{O}_3$  which later on leached using the 1% HF reaction mixture and then passed through 11 micron Whatmann filter paper to collect the quartz. Then this separated quartz was treated with 4:1:1 HF:  $\text{HNO}_3$ : MQ for Microwave digestion which is passed through anion and cation columns after addition of the  $^9\text{Be}$  carrier (spike solution). Collected solution is allowed to precipitate at pH 8-10 in the form of  $\text{Be}(\text{OH})_2$ , which was converted into BeO by blowing in blue part of the flame for 1-2 minutes. BeO powder was loaded into the cathode tube after mixing with Nb for AMS measurement.

Two palaeosol samples were pretreated for  $^{14}\text{C}$  dating in graphitization lab at IUAC. After physical cleaning, samples were taken in the centrifuge tubes and then kept in oven for 8 hours with 1% HCl solution to remove carbonates and humic acid which later on washed with Milli Q water until it got pH 7. Afterwards samples were treated with 1% NaOH solution for 8 hours. Again it was made neutral by successive washing with milli Q water. Following the prescribed ABA (acid-base-acid) scheme [4], the samples were again put with 1% HCl solution for 8 hours to the oven and then made neutral repeating the same. Next this sample was kept in freezer for 20-30 minutes to achieve a temperature of 0-4 °C and then freeze dried in freeze drier at -80 °C for 10-12 hours. These dried samples were then graphitized and loaded into cathode capsule for  $^{14}\text{C}$  AMS measurements.

Remaining samples will be digested and processed for Be and Al and subsequently measurements will take place.

Table : 5.5.2

Sr. No.	Samples	Area and Location	Material Type	Treatment
1	M-4	Nagapahar (Mandla)	Bole samples	$^{10}\text{Be}$ and $^{26}\text{Al}$
2	M-9	Mohan Tola (Mandla)	Bole samples	$^{10}\text{Be}$ and $^{26}\text{Al}$
3	M-10	Kundam (Mandla)	Bole samples	$^{10}\text{Be}$ and $^{26}\text{Al}$
4	M-23	Garasarai (Mandla)	Bole samples	$^{10}\text{Be}$ and $^{26}\text{Al}$
5	M-24	Mohatra (Mandla)	Bole samples	$^{10}\text{Be}$ and $^{26}\text{Al}$
6	M-25	Bhalkoha (Mandla)	Bole samples	$^{10}\text{Be}$ and $^{26}\text{Al}$
7	M-34	Kapil Chabutra (Mandla)	Bole samples	$^{10}\text{Be}$ and $^{26}\text{Al}$
8	M-40	Badargarh Pahar (Mandla)	Bole samples	$^{10}\text{Be}$ and $^{26}\text{Al}$
9	BS-2B	Burzahama, Karewa	Palaeosolsamples	$^{14}\text{C}$
10	BS-3A	Burzahama, Karewa	Palaeosolsamples	$^{14}\text{C}$
11	BS-4A	Burzahama, Karewa	Palaeosolsamples	$^{10}\text{Be}$ and $^{26}\text{Al}$
12	SP-S-1B	Shankerpora, Karewa	Palaeosolsamples	$^{10}\text{Be}$ and $^{26}\text{Al}$
13	SP-S-5A	Shankerpora, Karewa	Palaeosolsamples	$^{10}\text{Be}$ and $^{26}\text{Al}$
14	SP-S-10A	Shankerpora, Karewa	Palaeosolsamples	$^{10}\text{Be}$ and $^{26}\text{Al}$

Fig. 96 : Locations of different bole samples with stratigraphic columns used for  $^{10}\text{Be}$  and  $^{26}\text{Al}$  dating.

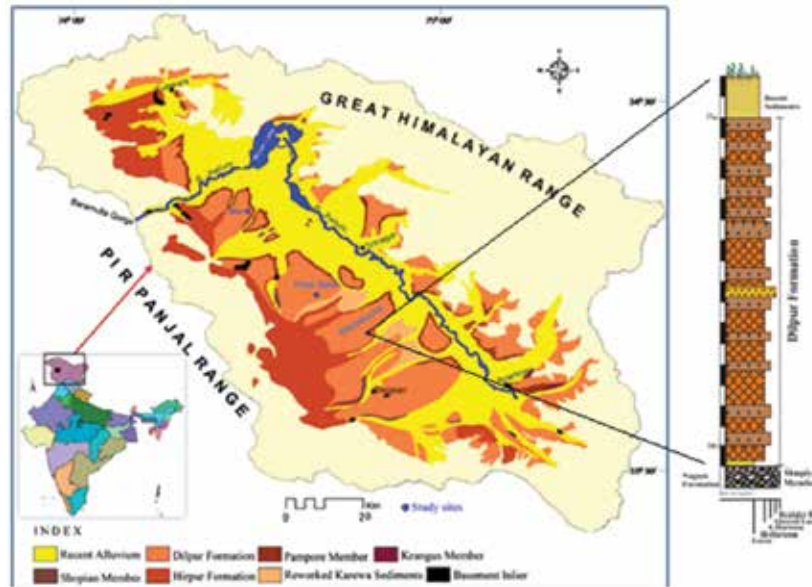


Fig. 97 : Locations of different palaeosol samples used for  $^{10}\text{Be}$  and  $^{26}\text{Al}$  dating.

## REFERENCES

- [1] J. P. Shrivastava and M. Ahmad, A review of research on late cretaceous volcanic-sedimentary sequences of the Mandla Lobe: implications for Deccan volcanism and the cretaceous/Palaeogene boundary, *Cretaceous Research* **26**, 145 (2005).
- [2] J. P. Shrivastava, Cosmogenic  $^{10}\text{Be}$  dating of the clay sediments associated with the intra-volcanic bole horizons of the Deccan Traps: palaeo-environmental implications and duration of volcanism at KTB (in press).
- [3] R. A. Dar, R. Chandra and S. A. Romshoo, Morphotectonic and lithostratigraphic analysis of intermontane Karewa basin of Kashmir Himalayas, India. *Journal of Mountain Science*, **10**, 731 (2013).
- [4] F. Brock, T. Higham, P. Ditchfield and C. B. Ramsey, Current pretreatment methods for AMS radiocarbon dating at the Oxford radiocarbon accelerator unit (ORAU), *Radiocarbon* **52**, 103 (2010).